NUREG/CR/0688
BNL-NUREG-50978

REACTOR SAFETY RESEARCH PROGRAMS

QUARTERLY PROGRESS REPORT

OCTOBER 1 - DECEMBER 31, 1978

Date Published - March 1979

DEPARTMENT OF NUCLEAR ENERGY BROOKHAVEN NATIONAL LABORATORY
UPTON, NEW YORK 11973

Prepared for the U.S. Nuclear Regulatory Commission
Office of Nuclear Regulatory Research
Contract No. EY-76-C-02-0016

NUREG/CR - 0688
BNL-NUREG - 50978
R-1,4,5,7,8

REACTOR SAFETY RESEARCH PROGRAMS

QUARTERLY PROGRESS REPORT

OCTOBER 1 - DECEMBER 31, 1978

HERBERT J. C. KOUTS, DEPARTMENT CHAIRMAN
WALTER Y. KATO, ASSOCIATE CHAIRMAN FOR REACTOR SAFETY

Principal Investigators:

Ashok K. Agrawal
Ralph J. Cerbone
Owen C. Jones, Jr.
Cesar Sastre
Donald G. Schweitzer
Daniel van Rooyen

Compiled by: Anthony J. Romano

Manuscript Completed - February 1979

DEPARTMENT OF NUCLEAR ENERGY
BROOKHAVEN NATIONAL LABORATORY, ASSOCIATED UNIVERSITIES, INC.
UPTON, NEW YORK 11973

Prepared for the
Reactor Safety Research Division
Office of Nuclear Regulatory Research
U.S. Nuclear Regulatory Commission
Contract No. EY-76-C-02-0016
FIN Nos.:
A-3014 A-3024
A-3015 A-3041
A-3016 A-3045
A-3208

NOTICE

Available from
U.S. Nuclear Regulatory Commission
Washington, D.C. 20555

Available from
National Technical Information Service
Springfield, Virginia 22161

FOREWORD

The Reactor Safety Research Programs Quarterly Progress Report describes current activities and technical progress in the programs at Brookhaven National Laboratory sponsored by the USNRC Reactor Safety Research Division. The projects reported each quarter are the following: Gas Reactor Safety Evaluation, THOR Code Development, Code Review, SSC Code Development, LMFBR and LWR Safety Experiments, Fast Reactor Safety Code Validation and Stress Corrosion Cracking PWR Steam Generator Tubing.

This report is the ninth of a series of quarterly reports which combines the reports of the individual projects mentioned above. The previous reports, BNL-NUREG-50624, BNL-NUREG-50661, BNL-NUREG-50683, BNL-NUREG-50747 BNL-NUREG-50785, BNL-NUREG-50820, BNL-NUREG-50883 and BNL-NUREG-50931 have covered the periods October 1, 1976 through December 31, 1978.

TABLE OF CONTENTS

TABLE OF CONTENTS

I. HTGR SAFETY EVALUATION

SUMMARY

Release of fission products from thermally failed TRISO coated UC_2 particles during a temperature ramp experiment up to 2600°C established that CsI was not present. However, fission products cesium and iodine were found to be present in several chemical forms. The cesium deposited at temperatures >1000°C, while the iodine band lay at 200-450°C.

Low flow experiments verified the formation of $CsCrO_4$ from CsI in experiments with air and chromium alloys. Dissociation of CsI was also found to occur with air only; the reaction appears to be facilitated by the presence of carbon steel.

Work has been initiated on the Cs_2O-graphite system. Preliminary results indicate that Cs_2O is readily reduced by graphite to form CO and Cs. Work on this system will continue within the temperature capabilities of the present furnace.

H451 graphite samples have been heated to 1600°C in both dry and humidified helium. The sample weight loss and the particle size distribution of the aerosol evolved during heating in dry helium have been measured. Most of the sample weight loss was found to occur during the initial heating period coincidently with the highest particle concentrations. Prolonged heating in pure helium did not contribute appreciably to the overall weight loss. The particles evolved initially are very small (0.02-0.03 μm diameter) and extremely monodisperse. This finding is consistent with a formation mechanism involving evaporation and condensation processes.

Subsequent heating of a sample to a lower temperature after outgassing in dry helium did not produce an initial burst of particles. The introduction of water vapor into the carrier gas consistently produced large quantities of CH4. At high temperature and high water vapor concentration, much coarser graphite aerosols were observed. Such particles are the result of destructive oxidation and are formed by physical degradation processes.

The attachment of fission products to Aitken nuclei could be of great importance during a reactor temperature excursion since they are in the best possible form to escape deposition.

A batch of 50 BISO coated ThO_2 fuel particles was heated to 2560°C for 1 hour to determine whether failure was likely for temperatures below the melting point of ThC_2. No failures were observed. This strongly indicates that internal pressurization within the particles, caused by CO formation when the liquid carbide is formed, is the principal cause of fuel failure.

A wet chemistry technique has been developed to measure the molybdenum concentration gradients in H451 graphite exposed to liquid Mo_2C. Compared to techniques used to date there is a significant increase in the detection of molybdenum and a decrease in the amount of scatter in the data.

A program has been initiated to obtain vaporization data up to 3000°C on simulated fission products, silicon carbide and uranium and thorium oxides and carbides in the presence of graphite. This program will be closely coordinated with the core heatup program.

No attack has so far been observed on fused quartz at 740°C from 1500 hours of exposure to cesium vapor at very low pressures ($<10^{-8}$ atm.). Attack has been observed on fused quartz at 800°C from exposure for 1900 hours to tellurium vapor at a pressure of 10^{-5} atm.

Long term high cycle fatigue testing proceeded on Incoloy 800H and Hastelloy X. The new data tend to confirm that at very long test times the oxidation of specimens exposed to a simulated HTGR helium environment becomes sufficiently significant to cause a decrease in the fatigue strength. At longer times the beneficial effects of the helium environment disappear and the fatigue strengths of the 2 materials in helium decrease to those obtained in air tests. Thermally aged specimens have been tested this period. For an aging time of 3000 hours in HTGR helium Incoloy 800H shows a drop in strength of about 20% compared to non-aged material. On the other hand, Hastelloy X is not affected by this aging treatment.

Creep-rupture testing of Incoloy 800H and Hastelloy X is continuing in air and in a simulated HTGR helium environment. The stress-rupture properties of Incoloy 800H at 649°C (1200°F) are similar for both environments. Slightly lower rupture strengths were observed for Incoloy 800H at 760°C (1400°F). However, the creep strengths of Incoloy 800H were not affected by the environments at both temperatures studied. For Hastelloy X, slightly lower stress-rupture strengths were observed when tested in helium at 760°C (1400°F) and at 871°C (1600°F). The creep strengths of Hastelloy X tested at either of the temperatures studied, seem to be unaffected by environment.

The first group of exposures of HTGR alloys to the simulated fission products I_2, Te_2, and CsI at elevated temperatures has been completed. Significant fission product deposition was observed on the samples and most showed evidence of corrosion when examined with the scanning electron microscope. Bend tests have been completed and metallographic studies are proceeding.

The Materials Test Loop functioned routinely during the quarter except for an 18 hour outage caused by a regionwide power failure near the end of the 3 month period. This was the first shutdown since the MTL was put into service 18 months ago. During the quarter the performance of the loop exceeded its own record from any previous reporting period.

A study was initiated to develop an optimal design for a large scale graphite oxidation loop. Such a loop would expose 10 inch diameter graphite samples to helium at 1800°F and at 50 atmospheres. The impurity levels would be monitored and controlled and the overall design is predicated on a 5% depletion in water vapor concentration as the helium traverses the sample. A quotation for an engineering design of the helium circulator was obtained from Mechanical

Technology, Inc. ($130,000). A budgetary estimate for the fabrication, assembly, testing and delivery of the circulator, motor, exciter, controls, etc. was also received ($660,000).

The Helium Impurities Loop was used to study the thermodynamics of reactions involving helium impurities with the retort material. A model has been formulated which is consistent with experimental observations in the fully oxidized and fully reduced conditions of the loop investigated so far. Experiments to determine hydrogen diffusion rates through the boundaries of the loop have been performed and the results have been correlated.

The Helium Afterglow Monitor has arrived from LASL and is currently being repaired. Additional instrumentation was ordered for the "quartz" loop and infrared absorption detectors were purchased to monitor water vapor levels in the loops.

Irregularities have been observed in the effects of burnoff and flow rate on the oxidation rate of PGX graphite. The oxidation rate of one specimen was observed to decrease with long term exposure to $H_2O + H_2$ ($P_{H_2}/P_{H_2O} = 10$) in He while the reaction rates of other specimens continuously increased with increasing flow rate. Generally, however, the behavior of specimens toward long term exposure to H_2O/H_2 mixtures and to variable flow rate was as expected.

Some evidence is provided which indicates that removal of iron from graphite is greatly facilitated by a high concentration of the impurity.

No effect of compressive prestress on the ultimate compressive strength of oxidized PGX graphite has been found. Specimens were prestressed up to 0.75 σ_c and oxidized up to 5% burnoff in a He atmosphere containing 2% H_2O + 20% H_2 maintained at 680°C.

Small scale depressurization experiments have thus far shown little or no effect of container vessel shape on overall mixing behavior. Binary gas sampling for some selected runs confirm mixing behavior that has been observed visually. Mathematical modeling of rapid depressurizations within the small scale experimental model using the RICE code is continuing. Numerical problems have been identified and means for modifying the code are being investigated.

The ORIGEN code has been used to calculate the fission product inventories generated in HEU and MEU fissile fuel particles. These have been compared with the results of GA-A13886 and GA-A14980 and reasonable agreement is obtained for the major fission products.

Fabrication of the three-dimensional vibrations test rig has been completed, and shake tests of three-dimensional block arrays will commence shortly. An evaluation of the forces induced in the core elements during a seismic event has been undertaken. The OSCVERT code is being used for this analysis. The development, debugging, and proof-testing of the OSC3D code continues.

1. Fission Product Release and Transport

1.1 The Release and Transport of Fission Products from Thermally Failed HTGR Fuel (F. B. Growcock, S. Aronson, R. D. Taylor)

The study of the chemical states of fission products released from thermally failed HTGR fuel was continued. The thermochromatographic technique employed (Castleman, 1967) was modified to permit investigation of relatively non-volatile species, as described in the previous quarterly progress report (Growcock, 1978). However, the design of the high temperature region, wherein the fuel particles are inductively heated, proved unsatisfactory. Diffusion of released fission products out of the graphite susceptor into the surrounding carbon black insulation precluded detailed analysis of the data.

An experiment designed to alleviate this problem was conducted this past quarter. A tantalum tube, kindly donated by C. L. Smith of General Atomic Co., was used as an inner liner for the H451 graphite susceptor; it ran the length of the high temperature region (2500°C-800°C) and extended several centimeters into the low temperature region (800°C-25°C). The tantalum was expected to serve as a barrier for the low levels of fission products released from the H451 graphite crucible positioned within its walls. The graphite susceptor was kept to serve as a physical barrier to impurities in the carbon black insulation that would tend to migrate through the tantalum into the fission product stream. A tapered joint between the high and low temperature regions provided a gas tight fit to prevent back diffusion of fission product gases from the low temperature region into the carbon black insulation. The crucible was also modified to ensure that the particles did not move during heating. An H451 graphite plug was placed in contact with the crucible to serve as a target for the optical pyrometer. A pyrex trap, designed to fit the 0.63 cm slit of the gamma detector, was packed with activated charcoal and maintained at -196°C; it was attached to the exit tube of the low temperature region via a greaseless joint. The extended preparatory procedure used previously for packing the reactor was followed.

Three TRISO-coated UC_2 particles, previously irradiated at GA, were re-irradiated in the BNL HFBR (nominal flux $\sim 10^{14}$ neutrons/cm^2-sec) for 1 hour to regenerate short lived radionuclides; this has an insignificant effect on the fuel particle fission product inventory, yet is an effective method for tagging many of the elements of interest. As in the previous experiment, only quartz was used in the low temperature region. Airco high purity He was passed over a gettering furnace at 150 cm^3/min. to reduce O_2 and H_2O to 0.1 ppmv. The crucible was heated to 1700°C over a period of several hours, then taken up to 2500°C at a rate of 200°C/hour. The gamma activity of the particles was monitored directly; although the gamma activity decreased continuously with increasing temperature (apparently an artifact), fuel particle failure could be noted by a sudden drop in gamma activity. Failure of all 3 particles did not occur at 2500°C, so the temperature ramp was continued until they did fail at an apparent target temperature of 2600°C.

The activated charcoal trap showed considerable activity at low gamma energies. Very low levels were observed above 80 keV, however. The 512 keV transition, arising from ^{85}Kr, gave a maximum activity of $\sim$20 counts/10 min.

(background ~2-5 counts/10 min.)

Since interest has been focused on the chemical forms of fission products Cs and I, the activities of ^{137}Cs and ^{131}I along the thermochromatograph were measured. The results are plotted in Figures 1.1 and 1.2. The absence of definite peaks for the 2 radionuclides in the temperature range 500-650°C (55-75 cm) indicates that no CsI was present. This is consistent with the results from the first experiment with unreirradiated fuel particles (Growcock, 1978) in which no deposition below 1000°C was observed. However, this is contrary to some expectations (e.g. Gotzmann, 1974). Elemental fission product inventory estimates give a weight ratio of cesium to iodine of ~19/1 (Skalyo, 1978), i.e. <5% of the cesium may be chemically bound to the iodine. The sensitivity of the Ge(Li) detector to ^{137}Cs is better than 0.01% so there is little doubt about the result. Equilibrium calculations for the dissociation of CsI(g) monomer give $K_{eq} \sim 5 \times 10^{-4}$ at 2500°C, while a slightly lower value is obtained for the dimer (Feber, 1977). Given that the partial pressure of CsI is sufficiently low, a significant amount of decomposition of CsI can be anticipated.

The complex ^{137}Cs spectrum (Figure 1.1) was not expected. A temperature profile of the high temperature region was attempted in a dry run prior to insertion of the fuel particles, using a W/26% Re thermocouple. The target temperature was increased to 2500°C, while the hot zone in the low temperature region was kept at 800°C. At high target temperatures (>1500°C) the thermocouple began to give readings that were considerably lower than the optical pyrometer values. However, the profile established up to that point left no doubt that below 25 cm the temperature was >1000°C. Dissection of the high temperature region showed that all the activity beyond the "heated region" was confined to the tantalum tube. It was noted that the tube became welded to the graphite susceptor. The gamma spectrum of the tube was also obtained for comparison with Figure 1.1. It is essentially identical to Figure 1.1, but the shoulders at 15-17 cm and 22-24 cm are absent. Further analysis of the gamma spectrum is desirable.

Deposition of iodine at 200° to 450°C (Figure 1.2) was not completely unexpected. Previous thermochromatographic work with irradiated metallic fuels heated to lower temperatures than employed here showed that 2 distinct iodine peaks were formed in the above mentioned temperature range (Castleman, 1970). The authors interpreted the peaks to be physically adsorbed uranium iodide compounds. In our work Ta is present also, which might form volatile iodides. The quartz tube in the region 200°-450°C is currently being divided into 3 sections and prepared for neutron activation analysis to ascertain the identities of the deposits.

The next experiment will incorporate a carbon steel liner in the low temperature region to examine its effect on fission product deposition. A few further minor modifications of the apparatus are planned.

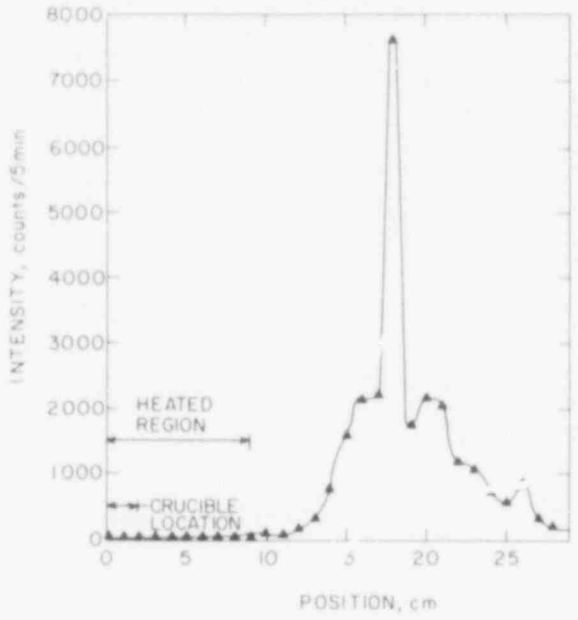

Figure 1.1. Deposition profile of ^{137}Cs released from thermally failed TRISO UC_2 particles. Substrate is Ta maiutained in a temperature gradient of 2600°C to 1000°C.

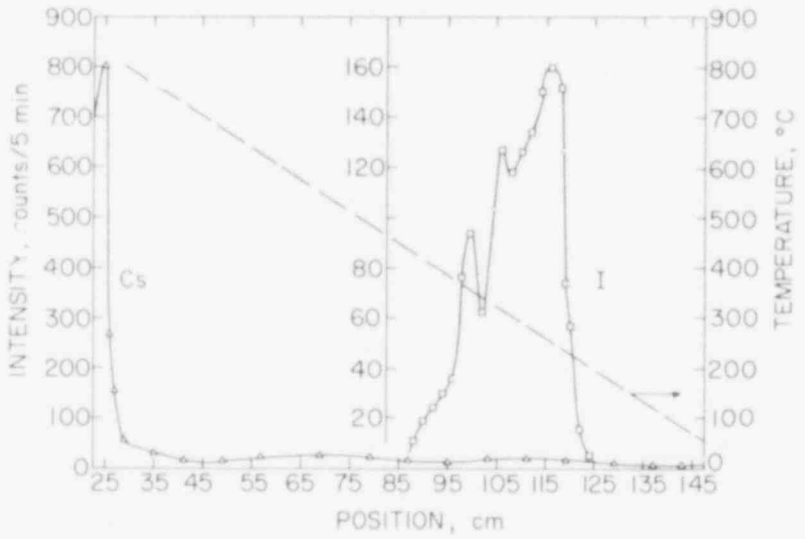

Figure 1.2. Deposition profiles of ^{137}Cs and ^{131}I released from thermally failed TRISO UC_2 par icles. Substrate is fused quartz maintained in a temperature gradien' of 800°C to 25°C.

1.2 The Reaction of CsI with HTGR Materials (F. B. Growcock, J. Plevritis)

In carbide fuels, such as may be used in an HTGR, fission product iodine may be chemically bound to fission product cesium as CsI (Fitts, 1971; Aitken, 1975; Götzmann, 1974). The release of CsI during a core heatup accident will result in its exposure to materials in the primary coolant system and, if sufficiently volatile, to the steam generator system. The volatility of fission product iodine could be enhanced by decomposition of CsI; the interaction of iodine so formed with HTGR materials is a problem which has not been fully answered (Chandra, 1976; Farmer, 1977).

Preliminary work on the stability and reactivity of CsI toward stainless steel 304 in various gaseous environments indicated that solid CsI at 530-630°C decomposes in 10% O_2 in He (Tang, 1977). CsI appeared to be stable at lower oxygen potentials (e.g. H_2O or CO/CO_2 mixtures in He). Further work indicated that the reaction which is probably occurring under those conditions is (Aronson, 1978):

$$2CsI(g) + 2O_2(g) + Cr(s) \rightleftarrows Cs_2CrO_4(s) + I_2(g)$$

Formation of a chromate salt was indicated also for Incoloy 800, Hastelloy X and chromium powder, but was not formed in the presence of iron or nickel powder.

This work has been continued and will be discussed in greater detail in a forthcoming informal report. The experimental arrangement of Aronson (1978) was modified slightly so that (1) the Cr-Al thermocouple was isolated from the reactants with a well placed in contact with the metal substrate and (2) greaseless joints were used. Typically a reaction was begun by raising the reactor temperature to the desired value (~20 min.); quenching was accomplished by removing the reactor from the furnace. A low flow rate of 25 cm^3/min. was used which provided good mixing, yet little evaporation of the ethanol (~2% for a 2-hour run). The metals were degreased and usually preoxidized in air for 1 hour. Both the CsI and metal were placed in a quartz cup which for most experiments was maintained at 600°C; generally the CsI was separated from the metal by small quartz rods. In one experiment, designed to reproduce the results of Aronson, et al (1978), stainless steel 304 turnings were mixed with the CsI powder. A comparison of the I_2 evolution from the solid mixture run with that from the gas/solid reaction is shown in Figure 1.3.

The results of the gas/solid reaction of various materials are shown in Figure 1.4. The metals used were in the form of turnings. The Hastelloy X, S.S. 304 and Incoloy 800 were machined differently than the carbon steel and 1Cr-1/4Mo steel; turnings of the latter material were much thicker and coarser than the former. Although all the Hastelloy X samples were of the same approximate weight, the rate of I_2 evolution and total amount formed varied considerably. However, the rates of runs 1 and 2 for Hastelloy X and the rates of the S.S. 304 and Incoloy 800 at long times are strikingly similar. Also, the rates of Hastelloy X run 3 and S.S. 304 after ~1 hour are quite similar. A rather low rate was obtained for the 1Cr-1/4Mo steel, which was expected considering its low Cr content. However, the similar rate obtained for carbon steel was not expected. Washing the metal turnings in H_2O removed $CrO_4^=$ from all except carbon steel.

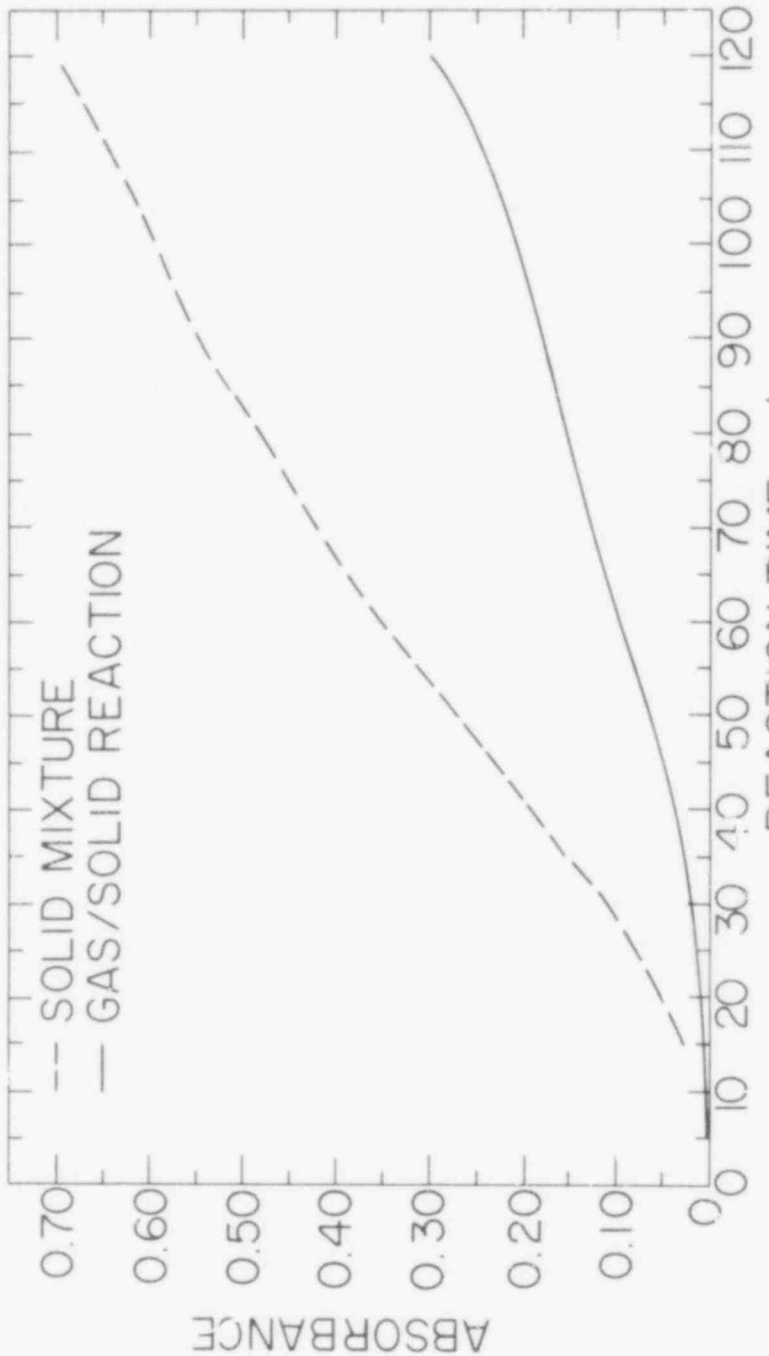

Figure 1.3. I_2 evolution from the reaction of CsI and air with S.S. 304 at 600°C.

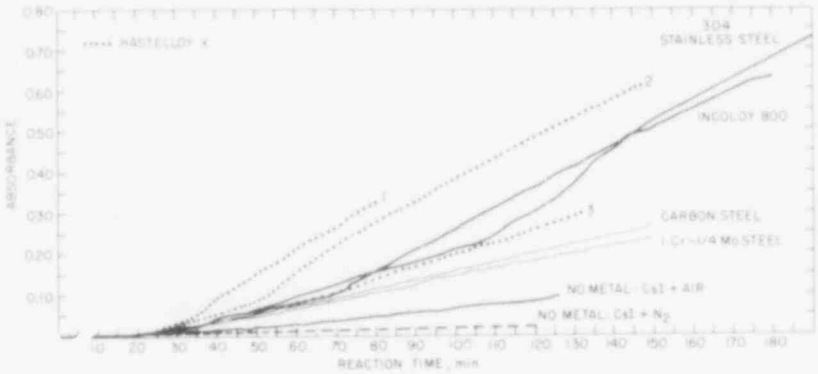

Figure 1.4. I_2 evolution from the reaction of CsI(g) and air with various materials at 600°C.

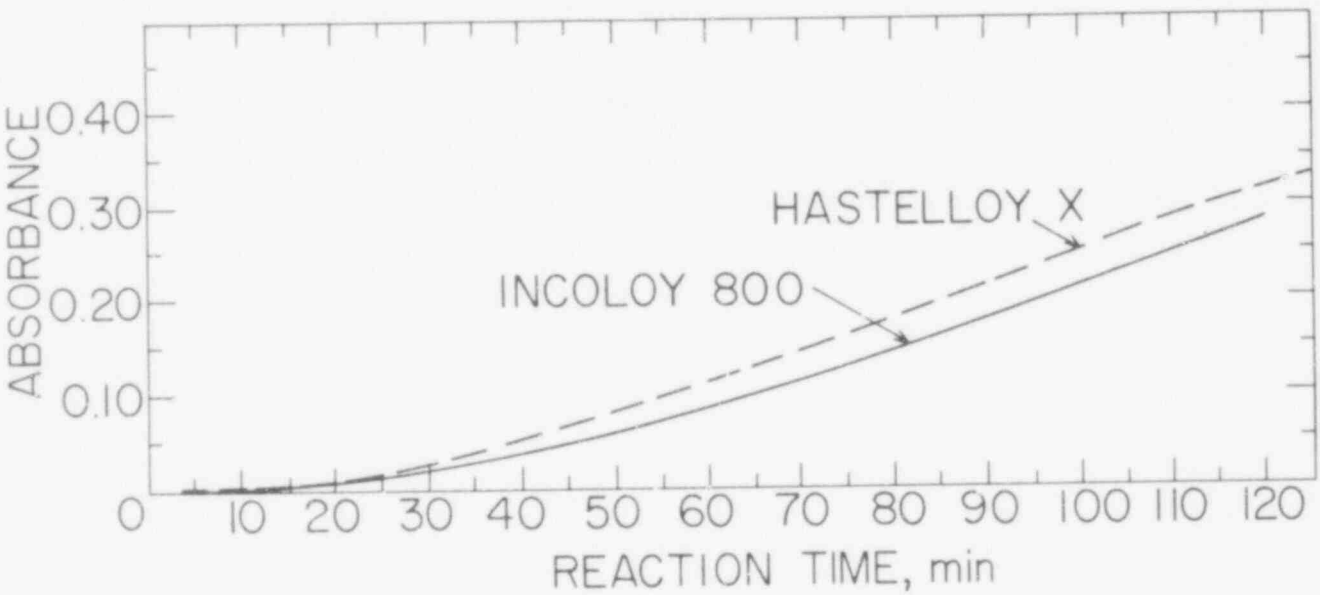

Figure 1.5. I_2 evolution from the reaction of CsI(g) and air with stock rod specimens of Hastelloy X and Incoloy 800 at 600°C.

Long induction periods were noted for all the runs, including that without metal. No induction period was noted for the CsI + N_2 run with no metal, and no effect was observed when the flow rate was increased by X10; however, the absorbance was too low to say with assurance that it was absent. A high flow rate run with Hastelloy X showed that diffusional flow was probably the cause of the long induction periods. In fact, the experimental conditions are such that P_{I_2} in the reactor is virtually constant, so that equilibrium is closely approached. Thus, a given value for the rate of I_2 evolution corresponds to a value of P_{I_2} in the reactor which is only a little lower than its equilibrium value.

The rate of I_2 evolution in the CsI + N_2 run was quite low, probably on the order of the experimental uncertainty. A similar run with He in place of N_2 gave an absorbance of 0.015 at 2 hours, compared with 0.020 for the N_2 run. An almost identical rate was obtained with Hastelloy X, CsI and 2.0% H_2O + 20% H_2 in He. Likewise, a run with Hastelloy X, CsI and N_2 gave about the same result as the run without metal.

The experiment with CsI + air in the absence of metal gave rise to a low rate, but definitely higher than the experimental uncertainty. This is consistent with the carbon steel result. The results from these 2 experiments indicate that a reaction, other than the aforementioned formation of $CsCrO_2$, may occur between CsI and O_2. The carbon steel (Fe_2O_3) may simply be an active surface upon which the reaction is facilitated, i.e. a catalyst.

Tang, et al (1977) observed no decomposition of CsI on quartz exposed to 30% O_2 in He. However, the reaction temperature was lower, 475-550°C; furthermore, these workers were looking for qualitative effects. Another argument against the present results is the apparent absence of a viable reaction. Formation of oxides appears to be contraindicated on thermodynamic grounds. Experimental evidence supports this: the pH of the solution obtained from washing some turnings was identical to that of distilled H_2O. It was expected that Cs_xO_y would form CsOH in H_2O if it had been generated. A mass balance of the reaction is currently being done with Hastelloy X and carbon steel. X-ray diffraction of the surface layers of a reacted carbon steel sample will also be done to help identify the cesium species presumed to be on its surface.

The almost equivalent rates of I_2 evolution observed for the high chromium steel turning samples in Figure 1.4 are also produced with stock samples. Sections of 1/2 inch Hastelloy X and Incoloy 800 rod were exposed to CsI + air at 600°C; the results are shown in Figure 1.5. Since these alloys contain similar amounts of Cr (22% for Hastelloy X and 20% for Incoloy 800 and S.S .304), differences in the slopes of the curves may be attributable to different active surface areas or different Cr activities produced by the variation in alloying constituents.

In Figure 1.6 the effect of reheating on the rate of I_2 evolution from Hastelloy X and Incoloy 800 turnings is illustrated. Similar induction effects are observed for the 2 heats with each specimen. The rate of I_2 evolution upon reheating Incoloy 800 is somewhat lower than in the original heat; the rate of I_2 evolution upon reheating Hastelloy X is considerably lower than in the

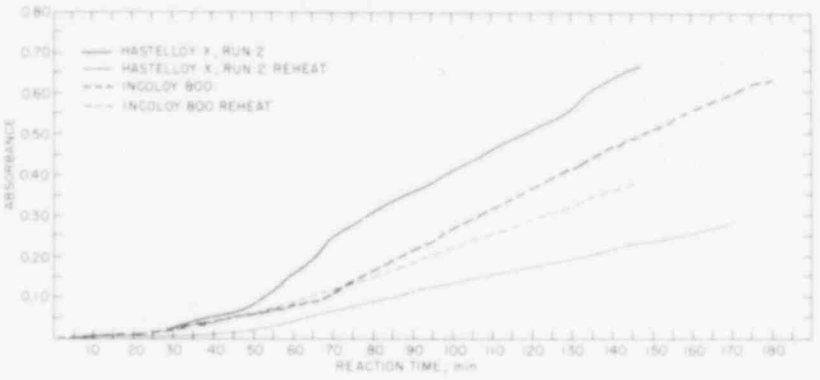

Figure 1.6. The effect of reheating on the rate of I_2 evolution during the reaction of CsI(g) and air with Hastelloy X and Incoloy 800 at 600°C.

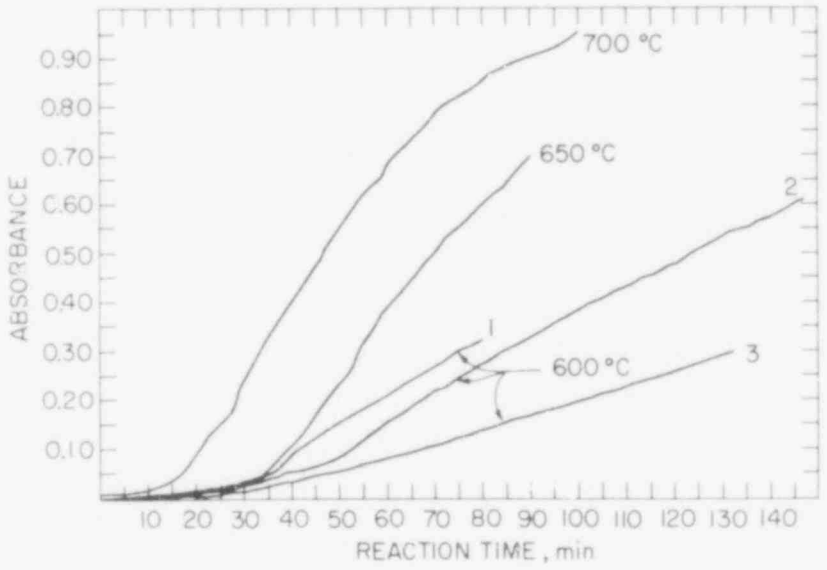

Figure 1.7. The effect of temperature on the rate of I_2 evolution during the reaction of CsI(g) and air with Hastelloy X.

original heat. Reactivities of high chromium alloys may be expected to decrease with time, even in the absence of thermal cycling, if spalling is not significant. At the high oxygen potentials used in this study, oxidation of all the major constituents occurs. Thus, reaction of Cr (actually Cr_2O_3) to give Cs_2CrO_4 depletes the amount of available chromium, resulting in a continuously decreasing activity, a_{Cr}. The partial pressure of I_2 above the specimen must consequently decrease also to maintain equilibrium.

The effect of temperature on the rate of I_2 evolution is shown in Figure 1.7 for 3 Hastelloy X specimens at 600-700°C. At 650°C and 700°C the effect of decreasing a_{Cr} on the rate of I_2 evolution is quite obvious from the curvature of the plots. CsI is molten at these temperatures, but the reactivity of CsI(g) should not be affected. Vapor pressure measurements yield interpolated values at 600, 650 and 700°C of 0.12, 0.54 and 2.5 torr, respectively (Scheer, 1962); recent calculations yield 0.079, 0.30 and 0.79 torr at the same temperatures, of which ~5% is the dimer, Cs_2I_2 (Feber, 1977). The maximum observed rates are in the approximate ratio 1:4.0:4.0 where the slope of run No. 3 at 600°C has been used for the comparison; this was considered valid since it was performed immediately prior to the 650° and 700°C runs. The vapor pressure ratio at 600°C to that at 650°C is quite similar to the I_2 evolution rate ratio. The relative rate obtained at 700°C is not in keeping with its relative vapor pressure. However, a brief induction period is observed, which could lead to a lowering of a_{Cr} more rapidly than with the other runs. Additionally, there may be considerable scatter in the rates of I_2 evolution (rates at 600°C varied by <40% from the mean).

Further work is planned in order to establish the equilibrium constant and reaction kinetics for the processes observed.

1.3 High Temperature Mass Spectrometer (S. Nicolosi, I. N. Tang, H. Munkelwitz)

SrO and SrO/graphite systems have been studied within the temperature capabilities of our mass spectrometer system. Since SrO is of such exceptional thermodynamic stability, the CO background pressure in the HTGR should oxidize the fission product Sr to SrO which has an extremely low vapor pressure. The presence of graphite may alter this equilibrium through the possible formation of a strontium carbide phase or adsorbed strontium. Such a consequence might enhance the release of fission product strontium. Our aim was to determine the susceptibility of SrO to reduction by graphite resulting in the evolution of elemental strontium vapor.

In the previous quarter, preliminary work was performed on the vaporization of pure SrO to determine if our apparatus could go to high enough temperature to observe a SrO signal and to determine the SrO fragmentation pattern in the mass spectrometer ionizer. The information on SrO fragmentation is needed for the interpretation of results from the SrO/graphite system. Preliminary results observed that the vapor over pure SrO may contain some Sr_2O dimers. This observation was of interest to us since the vapor pressure of SrO had been determined

only by a Langmuir vaporization method where the molecular species in the vapor were not identified. The vapor pressure was then calculated on the assumption that the vapor was predominantly monomer SrO. Thus, the presence of dimers would alter the calculations.

However, our observation of SrO dimers was only tentative. We were not able to make precise isotope abundance measurements due to the high background signal present. To overcome the background difficulties, the technique of a chopped molecular beam coupled with phase sensitive detection was deemed necessary. A molecular beam chopper, magnetically coupled to an external motor was designed and constructed. Since a synchronous motor was presently not accessible, a variable speed motor with poor speed control was used. With difficulty, we have obtained some degree of success with this motor. The chopper reference to the lock-in amplifier is supplied by a photodiode activated by a light beam that is chopped by holes drilled in the motor output shaft. With this apparatus we were able to achieve superb background rejection and a reasonably good mass spectrum of the signal from our SrO sample. Ion intensity and isotope ratio measurements show that our proposed $(SrO)^+_2$ species were actually Pb^+ and our proposed $(SrO)^+$ species were really Pb^{++}. Chemical analysis showed that our SrO sample contained impurity Pb at a level of 20 ppm. An attempt to boil off this metallic lead at high temperature resulted in the destruction of the furnace at 1130°C after approximately one hour. Although some basic components for a high temperature furnace were available, funds were not released for the construction of such a furnace. Thus, a new furnace, similar in design to the old one was constructed and has a temperature limitation of approximately 1000°C. Our studies of SrO were concluded by heating a mixture of SrO and graphite (.07 gram graphite and .09 gram SrO) to 835°C. The absence of any observable Sr bearing species indicates that at this temperature, SrO is not significantly reduced by C to Sr. Given the temperature limitation of our present furnace, we are unable to continue these studies of SrO systems.

Similar work has been initiated on the Cs_2O/graphite system with the aim of measuring the thermodynamic activity of Cs_2O in the presence of graphite.

A Cs_2O-graphite mixture (.4 gram Cs_2O and .09 gram graphite) was studied in the temperature range of 790-1020°K. Figure 1.8 shows observed values of IT (proportional to partial pressure) for CO and Cs vs. $10^3/T$. Assuming the relevant reaction to be:

$$Cs_2O_{(s,\ell)} + C_{(s)} \overset{1}{=} 2Cs_{(g)} + CO_{(g)}$$

the temperature dependence of the quantity:

$$K_1 = \frac{P^2_{Cs}\ P_{CO}}{a_{Cs_2O}\ a_C}$$

was studied and the results are shown to be $P_{Cs}{}^2P_{CO}$ and the activities are assumed to be unity. The ΔH calculated from our data at 1000°K are 159.6 kcal/mole. Based upon data from the JANAF tables (1971) for Cs, CO, and C; and from the Bureau of Mines Bulletin 542 for $Cs_2O_{(s,\ell)}$ the ΔH of this reaction

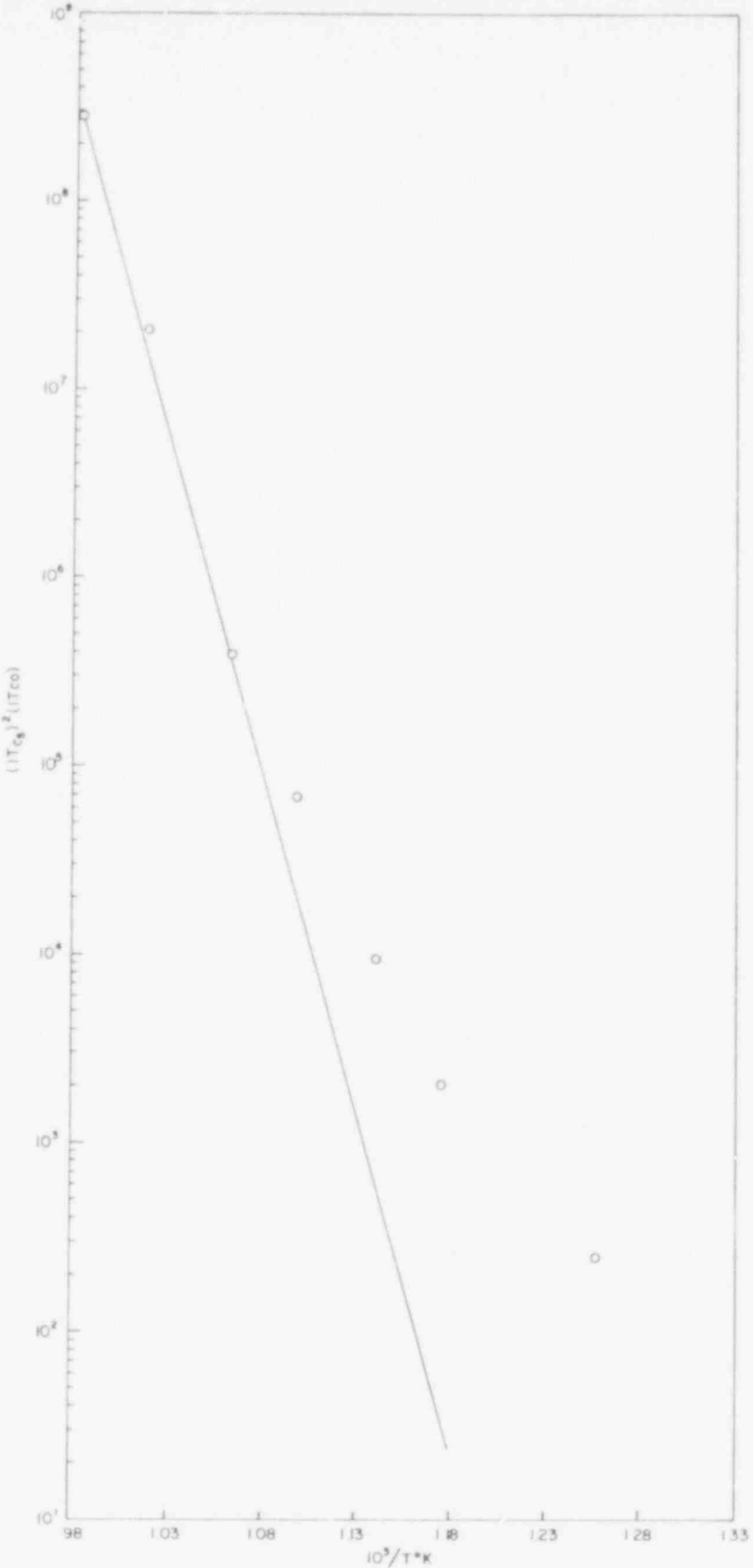

Figure 1.8. Intensities of CO^+ and Cs^+ as a function of temperature for the reaction $Cs_2O(s) + C_{graphite} = CO(g) + 2Cs(g)$.

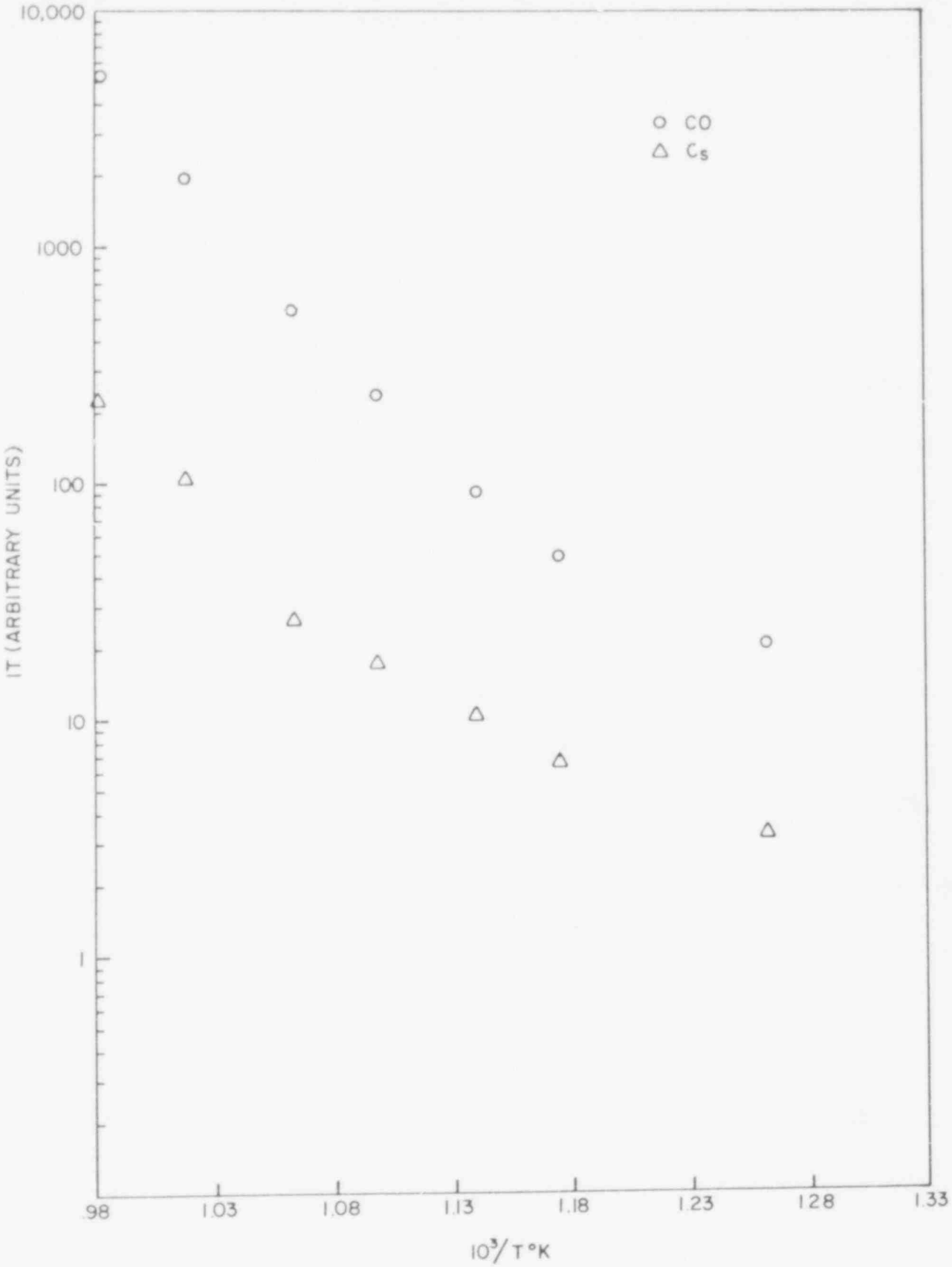

Figure 1.9. vant Hoff plot for the reaction of Cs_2O with graphite investigated with high temperature mass spectrometry.

is calculated to be only 77.23 kcal/mole. The discrepancy may be due to the estient furnace, we are unable to continue these studies of SrO systems. mate of ΔH for $Cs_2O_{(s,\ell)}$ and/or the effect of adsorption of Cs by graphite. In the latter case the system to be considered is:

$$Cs_2P_{(s,\ )} + C_{(s)} \overset{1}{=} 2Cs_{(adsorb)} + CO_{(g)}$$

$$2Cs_{(adsorb)} \overset{2}{=} 2Cs_{(g)}$$

In this case, the measured ΔH is ΔH_1 and 2 ΔH_2, and the ΔH_2 may be concentration dependent. Additionally, in Figure 1.9, the deviation from linearity at the lower temperatures is probably due to a change in heat capacity coupled with increasing contributions from background (since the mass spectrum was taken in the D.C. mode due to intermittent electronic problems with the lock-in amplifier). Work on this system will continue by varying the stoichiometry and by considering the effect of cesium adsorption by graphite.

1.4 Aerosol Formation from Graphite at High Temperature (I. Tang, H. Munkelwitz, S. Nicolosi)

Work continued on measuring the rate and extent of aerosol formation from core graphite samples heated to 1600°C in both dry and humidified helium. During the report quarter, emphasis was placed on the weight loss of H451 graphite specimens heated in dry helium as a function of temperature and heating duration. The particle size distribution of the aerosol evolved during heating in dry helium was also established by sampling with a diffusion battery.

When a new H451 graphite specimen was first heated in dry helium, condensation nuclei (CN) were invariably evolved. Initial CN concentrations were always in excess of 10^7 CN/cm^3 even at temperatures below red heat, and gradually decreased with time to a much lower concentration level. Increasing the temperature again produced a sharp increase in CN concentration, which then tapered off when the temperature was kept constant. Figure 1.10 shows the CN concentration change as a function of time for one graphite specimen heated at three different temperatures in dry helium.

At the end of each constant temperature period, the sample was cooled down and weighed. The results of sample weight loss as a function of sample temperature and heating duration are given in Table 1.1. Although the results are preliminary and quite limited, they indicate that at each sample temperature, most of the sample loss occurred during the initial heating period when the aerosol concentration was highest. Prolonged heating at the same temperature did not contribute appreciably to the overall weight loss.

The particles evolved during the initial degassing period were very small and not detectable using the light scattering instrument for particle size determination. Consequently, a Sinclair type diffusion battery was employed to obtain the size distribution of these condensation nuclei. The principle and application of this instrument have been described elsewhere.(Sinclair, 1972; 1975). In the present work, an iterative method was employed to derive the particle size information from the percent penetration data measured sequentially at each battery port. The fitting of the data was done on the BNL CDC

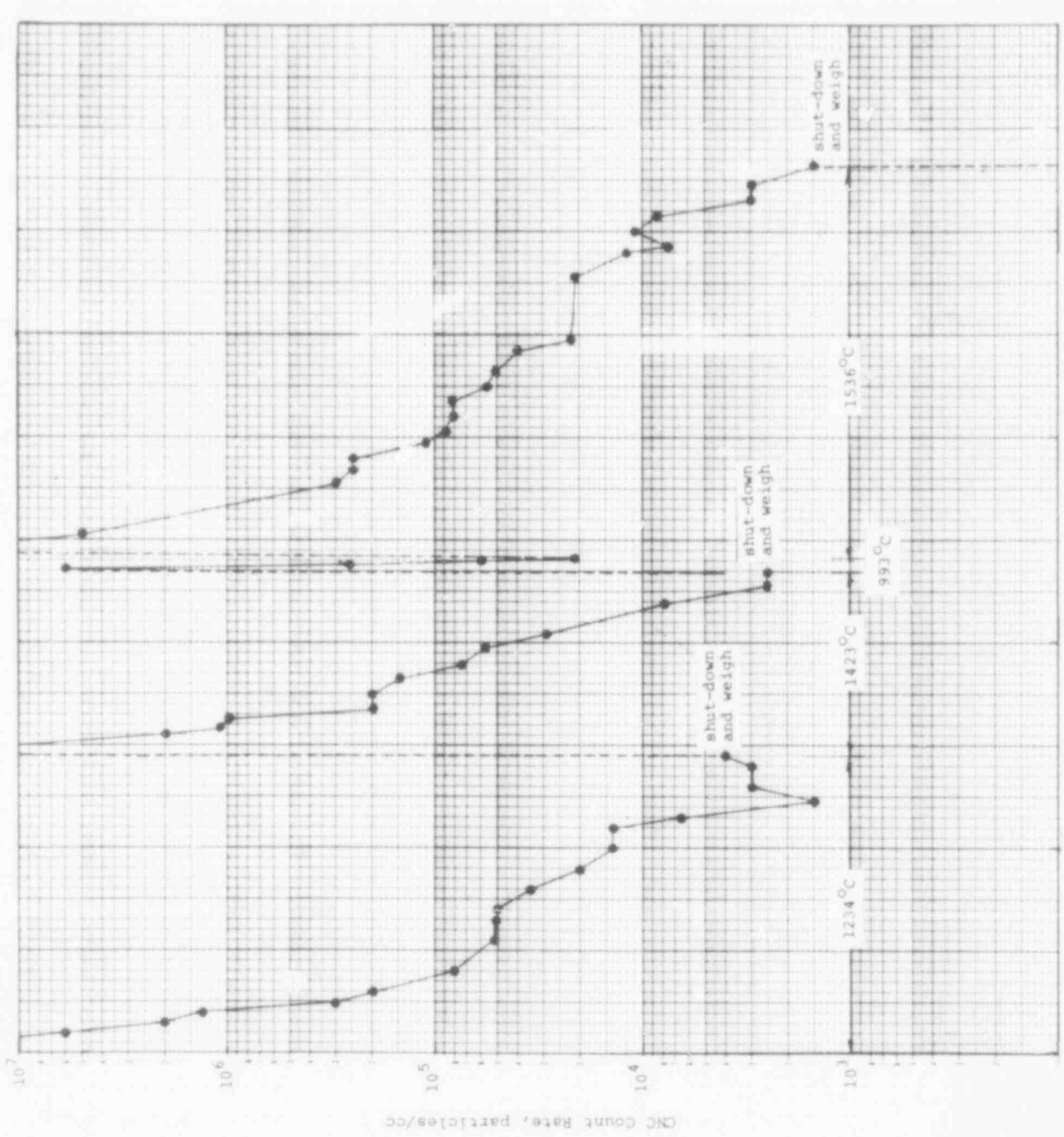

Figure 1.10. CN Concentrations as a function of time and sample temperatures during degassing in dry helium.

Table 1.1

Summary of Sample Weight Loss Data

Atmosphere	Temperature °C	Heating Duration Minutes	Weight Loss Percent
Dry He	1234	290	0.16
Dry He	1423	180	0.11
Dry He	1536	380	0.17
Dry He	1210	300	0.67*
Dry He	1400	330	
Dry He	1600	300	

*Total weight loss during the entire heating period at the specified temperatures.

7600 computer. Figure 1.11 shows the particle size distribution of the aerosol evolved during the first 15 minutes of heating in dry helium at 1010°C. This typical size spectrum indicates an extremely monodisperse aerosol that is consistent with a formation mechanism involving evaporation and condensation processes (LaMer, 1950). In the present system, the particle diameters were found to vary from 0.02 to 0.03 μm. Electron microscopic examination of the particles collected on copper grids with a thermal precipitator showed that these particles were quite unstable in the electron beam. Some of the particles evaporated quickly, leaving behind a residue. It is postulated that these particles are formed mainly from the volatilized residual binder material remaining in the graphite even after graphitization at high temperatures (Tingey, 1972).

A considerable amount of outgassing data has been reported for a variety of graphites (Eggleston, 1955; Asher, 1960; Redmond, 1960; Blakely, 1964). However, in all of these previous investigations only the gas content of graphite has been measured by heating a sample in vacuum and collecting the non-condensible gases for analysis. Typically, the evolved gases consist of H_2, CO, CO_2, H_2O, SO_2, N_2 and hydrocarbons (low molecular weights). No attempt was made by any of the previous investigators to look for the particulate matter that was also released with the gaseous species. In fact, the techniques employed by these investigators would not have been capable of monitoring aerosols since the particles emitted in vacuum would simply collect on the walls of the vessel. Redmond and Walker (1960) did a material balance and found that the evolved gases could account for only 50% of the sample weight loss. They noticed that considerable material was collected on the cool walls of the desorption chamber. An emission spectroscopic analysis indicated that this deposit was composed mainly of silicon, iron and magnesium.

Once a graphite sample was outgassed at a higher temperature, and subsequently heated at a lower temperature, there was either no change or a reduction in CN count rate, depending upon the degree of outgassing. However, addition of water vapor into the carrier gas invariably produced a brief burst of CN. Elec-

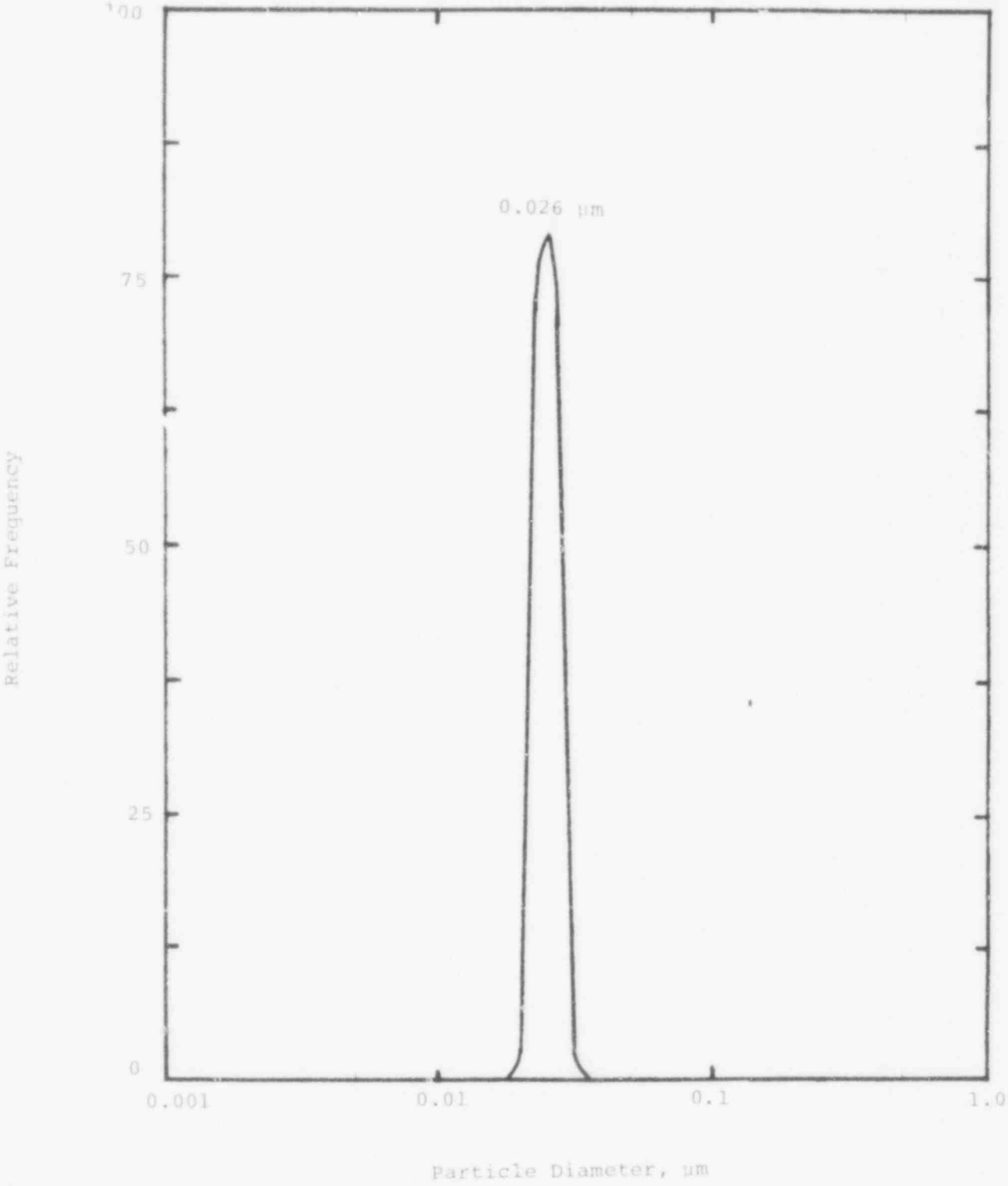

Figure 1.11. Particle size distribution of an aerosol evolved during degassing at 1010°C.

tron microscopic examinations of the particles collected from oxidation experiments revealed that these particles were stable, solid material. The morphology was entirely different from that of the particles emitted during degassing. Clearly, the solid particles were formed by physical degradation of the sample as a result of exhaustive oxidation. At high temperature and water vapor concentrations, much coarser graphite particles were observed to break off the heated specimen and deposit along the sampling tube leading to the CN counter. These large particles were not included in the data.

The attachment of fission products to Aitken nuclei may be of great importance in a reactor accident, since the deposition of these fission products would be controlled by the deposition behavior of the host aerosol. The Aitken nuclei are difficult to remove from the atmosphere as they are large enough to have low diffusion coefficients and yet are small enough to have a very low settling velocity under the influence of gravity. Fission products, therefore, attached to these nuclei are in the best possible form to escape deposition.

1.5 Experimental Studies of Core Heatup Phenomena (P. Soo, G. Uneberg, R. Sabatini, C. Sastre, D. G. Schweitzer)

The experimental HTGR Core Heatup Program was devised to obtain data on the behavior of fuel, fission products, control rod materials and graphite during hypothetical, nonmechanistic accidents in HTGR systems where temperatures are assumed to range up to the graphite sublimation regime (>3600°C). Very few experimental data are currently available on the physical and chemical interactions between these core materials so that fuel and graphite integrity and fission product migration rates are extremely difficult to quantify. Initial work in this program has involved relatively simple types of interactions between graphite and fuel, control rod and certain fission product species. This is considered necessary to obtain basic interaction data before more complex and prototypic experiments are initiated. Work is currently proceeding on molybdenum migration in H451 graphite, and heatup of BISO and TRISO coated fuel particles to determine their thermal stability.

1.5.1 Fuel Particle Testing

A batch of 50 BISO coated ThO_2 particles (Run 10578) was placed in a small capped crucible made from H451 graphite and heated in the induction furnace at an initial rate of about 2000°C/h to a temperature of 2560°C. The particles were maintained at this temperature for 1 hour after which the power was switched off and the fuel allowed to cool naturally.

This experiment was designed to determine whether significant fuel particle failure would occur for temperatures below the melting point of the liquid ThC_2 (2650°C). All work to data indicates that the principal failure mechanisms center on the rapid evolution of CO which forms when the oxide fuel is reduced to the liquid carbide according to the following reaction:

$$ThO_2 + 4C \rightleftharpoons ThC_2\ (liq.) + 2CO$$

The CO pressure builds up to a value high enough to rupture the pyrolytic carbon

coatings and the liquid fuel escapes.

Detailed scanning electron microscope studies revealed no trace of cracks or holes in the carbon coatings which confirms that failure is indeed initiated by internal gas pressure. Mechanisms of failure have been described in previous reports.

1.5.2 Molybdenum Migration in H451 Graphite

Work is progressing on the molybdenum diffusion experiments. Run 42078, in which Mo_2C was heated to 3000°C for 8 hours in a H451 graphite susceptor, has been analyzed using a wet chemical technique. First, the graphite susceptor is cut into slices of known thickness; then the individual slices are dried, weighed and ashed. The ashing is accomplished by exposing the sample to an oxygen plasma inside an LFE Corportion Model 302 low temperature asher. This process leaves a residue of inorganic ash which contains the trioxide of molybdenum and the oxides of other metals which may have been present in the graphite. This residue is then dissolved in a known amount of 10% NH_4OH solution and the absorption spectrum is taken with a Beckman Model 26 ultraviolet spectrophotometer, using 50 mm pathlength quartz cuvettes. The absorption intensity at 230 nm ($\varepsilon \sim 10{,}000$ liters/mole-cm) is then compared with that of solutions of MoO_3 of known concentration. Data points were obtained from a distance of 5 mm from the melt (21 ppm) to 55 mm from the melt (3 ppm). The Mo diffusion profile is shown in Figure 1.12. The wet chemical results are in general agreement with the results obtained using the proton microprobe.

The microprobe results, however, have not been absolutely quantified and the technique shows considerable scatter among the data points. The scatter might indicate that Mo is migrating preferentially along the grain boundaries in the graphite. The small beam diameter of the microprobe would enhance this effect and give rise to apparent scatter in the data.

The X-ray fluorescence technique indicates Mo concentrations about 3 orders of magnitude greater for identical distances from the Mo_2C melt. It is now believed that the X-ray fluorescence results, obtained from an offsite laboratory, are questionable and a new evaluation of this technique is required.

An analysis of the wet chemical results is in progress to obtain estimates of the diffusion rates of molybdenum in graphite.

1.6 High Temperature Vaporization Studies of HTGR Fuel Components and Fission Products (S. Aronson - Brooklyn College)

Data dealing with the physical and chemical reactions associated with the consequences of core heatup in HTGR environments are sparse. Information is needed on the vaporization and diffusion behavior of the fuel, coatings and fission products and on the interaction of these various chemical substances with each other and with graphite. We plan to obtain vaporization data up to 3000°C on simulated fission products, silicon carbide, and uranium and thorium oxides and carbides in the presence of graphite. This program will be closely coordinated with and will provide base data for the core heatup program in the

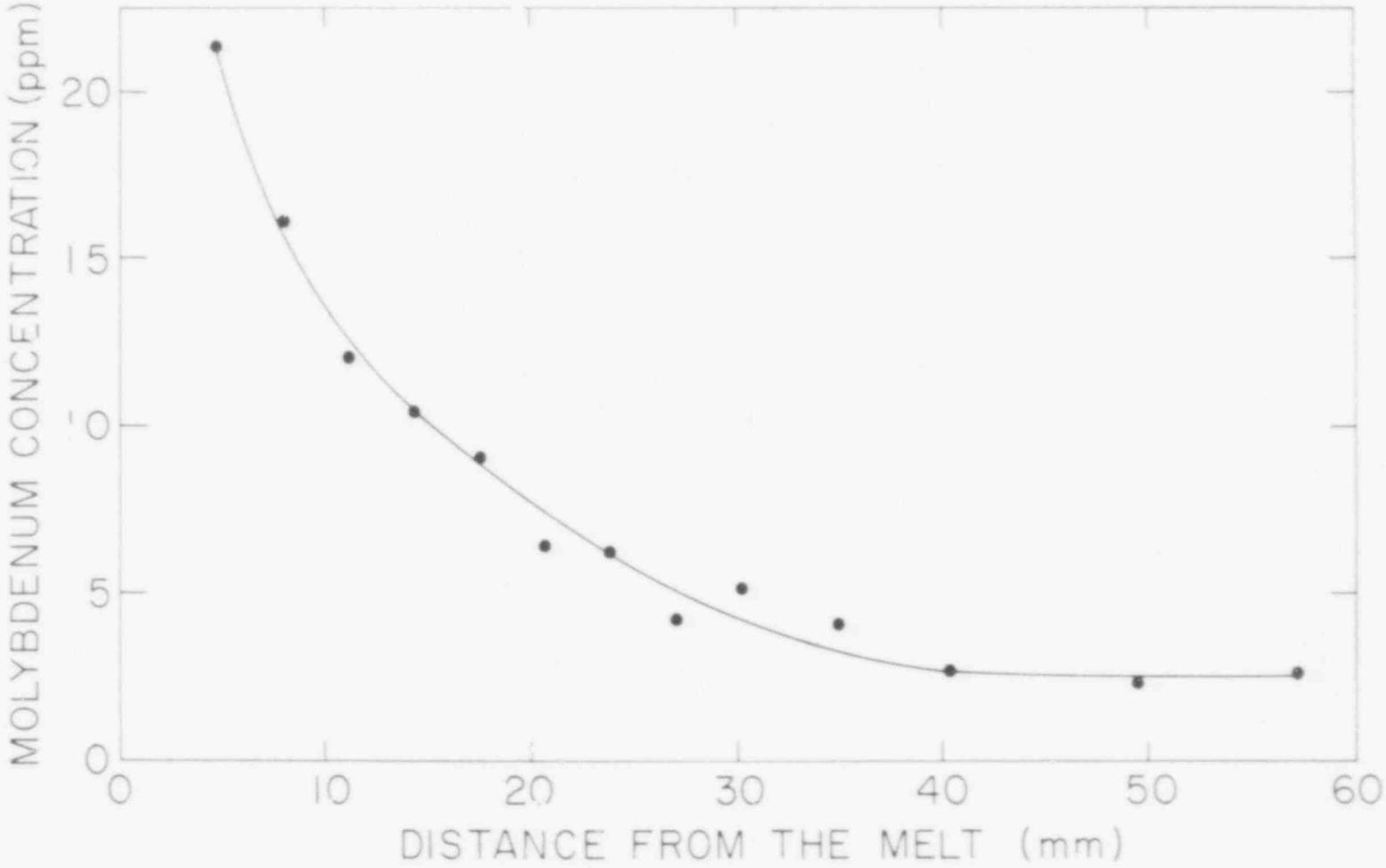

DIFFUSION OF Mo INTO H451 GRAPHITE. An H451 GRAPHITE SUSCEPTOR CONTAINING Mo_2C WAS INDUCTIVELY HEATED TO 3000 °C FOR 8 HOURS. THE RESULTS ARE FROM A WET CHEMICAL ANALYSIS OF RUN 42078.

Figure I.11

HTGR Safety Group at BNL.

The program will involve several interconnected components:

1. An experimental study will be made of the gas pressures (primarily CO and CO_2) generated by mixtures of graphite, ThO_2 or UO_2, SiC and one or more simulated fission product such as Sr, Zr, Mo, Cs and Ce. This study should yield information useful in elucidating the nature of the interactions of UO_2 or ThO_2 fuel with fission products at high temperatures. The experimental data will be compared with whatever information is available in the literature on the systems investigatged. The QUIL computer code developed at LASL and implemented at BNL will be extensively used in these calculations.

2. Measurement of the vapor pressure and heat of vaporization of a single simulated fission product mixed with graphite will be made in cases where this basic information is useful in making calculations concerning the mixed fission product system. The effectiveness of different experimental techniques for making vapor pressure measurements at high temperatures will be compared during this study.

3. Fuel failure mechanisms which have been proposed (Smith, 1974; Lindemer, 1974) will be reexamined. The phenomena of kernel migration, fission product gas pressure, the interaction of fission products with the SiC layer and CO-CO_2 diffusion and CO decomposition will be considered on the basis of the most recent data available in the literature and generated through the program described above.

1.7 Interaction of Cesium and Tellurium With Fused Quartz (S. Aronson, J. Klahr - Brooklyn College)

A long term test was begun on the interaction of fused quartz with cesium vapor. The temperature of the liquid cesium reservoir is 40°C corresponding to a cesium vapor pressure of 10^{-8} atm. The temperature of the fused quartz tube ranges from 40°C in the vicinity of the cesium reservoir to 740°C at the center of the furnace. No attack was observed visually after 1500 hours of exposure. A second capsule has been assembled which consists of a stainless steel tube sealed inside a fused quartz tube. The stainless steel tube which holds the cesium reservoir adjacent to its one closed end, extends from the cesium reservoir to within 2 inches of the other end of the fused quartz tube. The purpose of this arrangement is to concentrate the attack of the cesium vapor on the fused quartz region in the hot zone in the center of the furnace. It has been reported (Milstead, 1966) that cesium does not react with stainless steel. The cesium reservoir will be heated to 100°C (10^{-6} atm.) for the first test of this type.

It has been observed that tellurium attacks fused quartz (see Section 2.3). Two fused quartz tubes containing tellurium powder have been prepared. Long term tests will be run in which the temperatures of the tellurium reservoirs will be 400°C (10^{-6} atm.) and 300°C (10^{-4} atm.), respectively.

PUBLICATIONS

GROWCOCK, F. B., et al., "Thermochromatographic Investigations of Fission Product Transport and Chemistry," BNL-NUREG-25331, in Proc. U.S.-Japan Seminar on HTGR Safety Technology, Fuji, Japan, November 24-25, 1978, Vol. I.

SOO, P., et al., "Very High Temperature Behavior of HTGR Core Materials," BNL-NUREG-25323, in Proc. U.S.-Japan Seminar on HTGR Safety Technology, Fuji, Japan, November 24-25, 1978, Vol. III.

TANG, I. N., MUNKELWITZ, H. R. and NICOLOSI, S. L., "Aerosol Formation from Core Graphite Heated in Dry and Moist Helium," BNL-NUREG-25330, in Proc. U.S.-Japan Seminar on HTGR Safety Technology, Fuji, Japan, November 24-25, 1978, Vol. I.

REFERENCES

AITKEN, E. A., EVANS, S. K. and RUBIN, B. F. in Behavior and Chemical State of Irradiated Ceramic Fuels, IAEA, Vienna, 1974, pp. 269-85.

ARONSON, S., et al., "The Interaction of CsI with High Chromium Alloys in the Presence of Oxygen," J. Inorg. Nucl. Chem., in press.

ASHER, R. C., "The Degassing of Graphite," in Proc. US/UK Meeting on the Compatibility Problems of Gas-Cooled Reactors, ORNL, February 24-26, 1960, TID-7597, p. 504.

BLAKELY, J. P. and OVERHOLSER, L. G., "Outgassing Behavior of EGCR Moderator Graphite," ORNL-3560, 1964.

CASTLEMAN, A. W., Jr. and TANG, I. N., Nucl. Sci. Eng. 29, 159 (1967); J. Inorg. Nucl. Chem. 32, 1057 (1970).

CHANDRA, D., "Reaction of Primary Circuit Metal with Volatile Fission Products and Impurities in a Gas-Cooled Reactor - A Review and Guideline for Safety Research," BNL Internal Memo, 2/17/76, HTGR-MF-29.

EGGLESTON, E. R., et al., "Graphite Outgassing," NAA-SR-Memo-1240, January 21, 1955.

FARMER, F. R., Ed., Nuclear Reactor Safety, Academic Press, New York, 1977.

FEBER, R. C., "Thermodynamic Data for Selected Gas Impurities in the Primary Coolant of High Temperature Gas Cooled Reactors, April 1977, Los Alamos Scientific Laboratory, LA-NUREG-6635.

FITTS, R. B., LONG, E. L. and LEITNAKER, J. M., ORNL-TM-3385, 1971.

GOTZMANN, O. and OHSE, R. W., Behavior and Chemical State of Irradiated Ceramic Fuels, IAEA, Vienna, 1974, pp. 255-68.

GROWCOCK, F. B., et al., "Fission Product Release from HTGR Fuels," in Reactor Safety Research Programs Quarterly Progress Report, July 1-September 30, 1978, Brookhaven National Laboratory, BNL-NUREG-50931, December 1978.

LaMER, V. K., INN, F. C. Y. and WILSON, I. B., "The Methods of Forming, Detecting and Measuring the Size and Concentration of Liquid Aerosols in the Size Range of 0.01 to 0.25 μm Diameter," J. Colloid Sci. 5, 471 (1950).

LINDEMER, T. B. and deNORDWALL, H. J., "An Analysis of Chemical Failure of Coated UO_2 and Other Oxide Fuels in the HTGR," ORNL-4926, 1974.

MILSTEAD, C. E. and ZUMWALT, L. R., "Cesium Plateout on Stainless and Carbon Steels, GAMD-7525, 1966.

REDMOND, J. P. and WALKER, P. L., Jr., "Gas Content of Graphites," Nature 186, 72 (1960).

SCHEER, M. D. and FINE, J., J. Chem. Phys. 36, 1647 (1962).

SINCLAIR, D., "A Portable Diffusion Battery; Its Application to Measuring Aerosol Size Characteristics," Amer. Ind. Hyg. Assn. J. 33, 729 (1972).

SINCLAIR, D., et al., "Experimental Verification of Diffusion Battery Theory," presented at the 68th Annual Meeting of the Air Pollution Control Association, Boston, Mass., June 15-20, 1975.

SKALYO, J., Jr., "Fission Fragments and Activation Products in EOL Fuel Particles," BNL Internal Memo, 9/12/78, HTGR-MF-61.

SMITH, C. L., "Fuel Particle Behavior Under Normal and Transient Conditions," GA-A12971, 1974.

TANG, I. N., et al., "A Study of Fission Product Transport and Deposition Using Thermochromatography," Proc. Japan-U.S. Seminar on HTGR Safety Technology, Brookhaven National Laboratory, September 15-16, 1977, BNL-NUREG-50689.

TINGEY, G. L. and MORGAN, W. C., "Graphite for Helium-Cooled Rectors - A Review," BNWL-1687, Battelle Pacific Northwest Laboratories, Richland, Washington, 1972.

2. Materials, Chemistry, and Instrumentation

This program covers the evaluation of four main categories of materials: (1) metallic materials, (2) graphites, (3) PCRV, and (4) other materials. Included in (4) are control rod materials and thermal barrier insulation. At this time, however, the major emphasis is centered on metals. The objectives of the work are to critically review available materials data pertinent to HTGR safety, identify areas where information is sparse or unavailable, and to design and initiate experiments to yield data which will permit accurate assessments to be made of materials related safety problems.

2.1 Fatigue of Structural Materials (P. Soo, J. Chow, R. Sabatini)

The current effort on fatigue is focused mainly on the high cycle fatigue regime to evaluate the behavior of components subjected to rapidly oscillating stresses. Tests are conducted in air and a simulated HTGR helium environment under load control at a cycling rate of 40 Hz.

2.1.1 In-Helium High Cycle Fatigue Testing

Incoloy 800H and Hastelloy X are currently being evaluated. The simulated HTGR helium environment contains 40 μatm. H_2O, 200 μatm. H_2, 40 μatm. CO, 20 μatm. CH_4 and 10 μatm. of CO_2. Air tests are also being carried out to check the effects of helium against a known standard environment. Chemistries of the 2 materials are given below:

	C	P	S	Mn	Si	Cr	Ni	Mo	Fe	Others
Incoloy 800H (Ht. HH7427A)	0.05	NA	0.003	0.67	0.46	19.83	32.17	NA	Bal.	0.65 Cu 0.43 Ti 0.39 Al
Hastelloy X (Ht. 4-2809)	0.11	0.021	0.008	0.50	0.41	20.67	Bal.	8.86	18.66	2.10 Co 0.55 W

NOTE: NA = not analyzed. All concentrations in weight percent.

Long term tests were continued during this reporting period but only a small amount of additional information has been obtained. Figures 2.1 and 2.2 show the data obtained to date.

Incoloy 800H shows inconsistent behavior for the two test temperatures. At 649°C (1200°F) there is a clear indication that the helium environment gives a lower fatigue strength, viz. 217.2 MPa (31.5 ksi) versus 237.9 MPa (34.5 ksi) for air. At 760°C (1400°F), however, the air environment gives a substantially lower fatigue strength. For cycles to failure (N_f) larger than 10^8 there seems to be a tendency for the helium curve to show an accelerating decrease in the fatigue strength with time.

In the case of Hastelloy X (Figure 2.2) the only tests carried out in the simulated HTGR helium environment were at 871°C. For the shorter test times

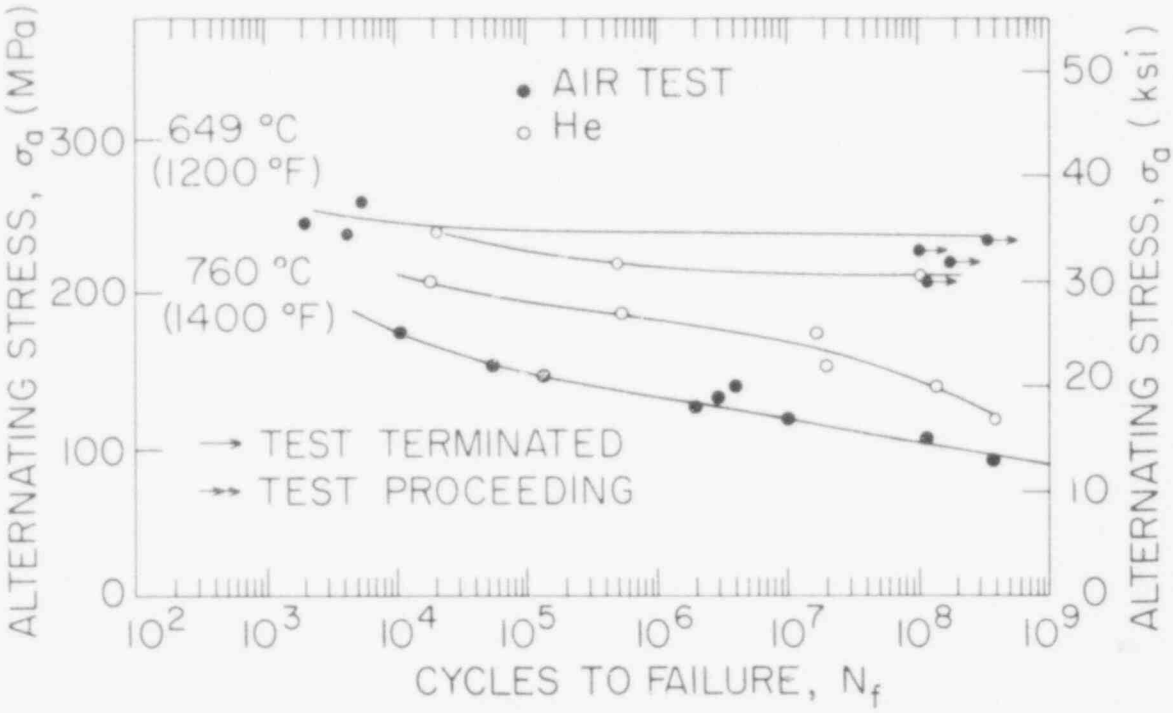

EFFECT OF A HELIUM ENVIRONMENT ON THE HIGH – CYCLE FATIGUE OF INCOLOY–800H

Figure 2.1

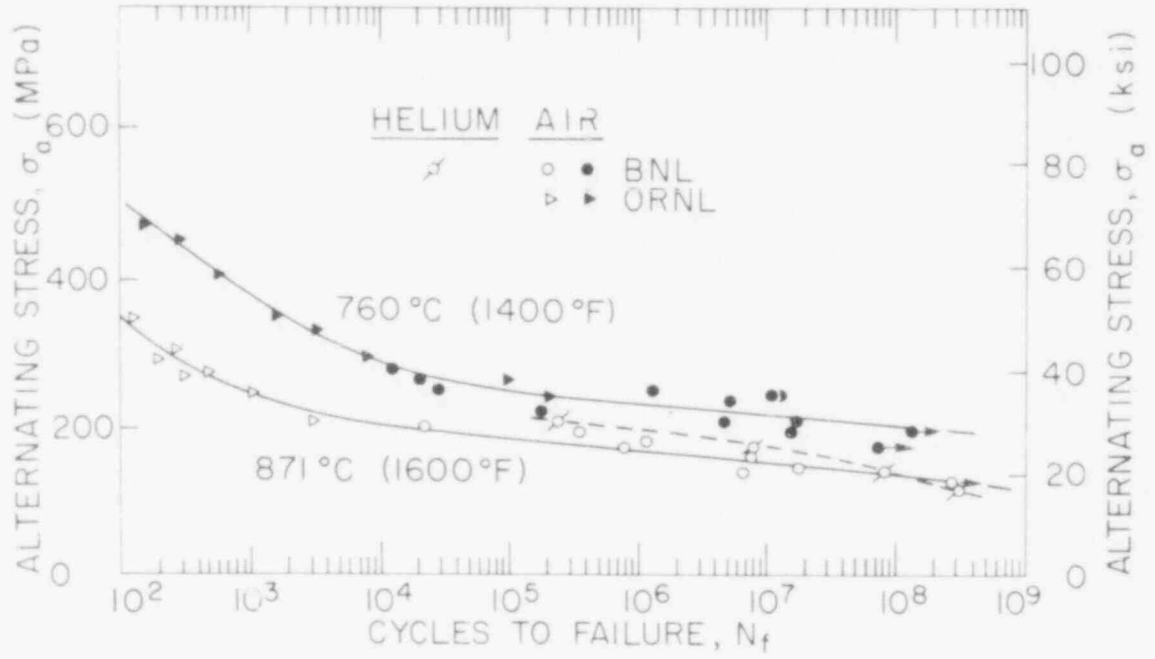

THE EFFECT OF A HELIUM ENVIRONMENT ON THE HIGH-CYCLE FATIGUE STRENGTH OF HASTELLOY-X

Figure 2.2

helium gives a higher fatigue strength compared to the air environment. However, after approximately 10^8 cycles the two curves converge and the fatigue strengths become comparable.

One explanation of the environmental effect is that air gives lower fatigue strengths because of the rapid formation of an oxide scale. At the higher stress levels this scale cracks easily and leads to early fatigue failure. Evidence to support this model was given recently by Soo (1978).

In the case of helium tested specimens the oxide scale forms much more slowly. Only at the longer test times will surface oxidation lead to an accelerated decrease in strength as shown in Figure 2.1.

Since the 649°C (1200°F) data for Incoloy 800H shown in Figure 2.1 are not consistent with the proposed oxide embrittlement model, it is possible that the slow oxidation rates at this lower temperature do not cause a sufficiently thick or brittle scale to give a pronounced effect. Hence, some other mechanisms could be controlling the fatigue strength of Incoloy 800H at 649°C (1200°F).

Some metallographic observations have been made of the microstructure of a fatigued Hastelloy X specimen (MHF-16) which was tested in air at 760°C (1400°F) at an alternating stress of 234.4 MPa (34.0 ksi). The specimen failed after 5.5 x 10^6 cycles. The scanning electron micrograph in Figure 2.3 shows a thin, irregular oxide scale which was shown to be rich in chromium. Immediately beneath the scale the metal appears to be filled with small pores, which could be areas from which small precipitates have been etched out. Carbides of the M_6C type are often observed to be present in this area. It is believed that this is an area where the chemical composition has been significantly changed from the starting value because of the diffusion of metallic elements into, and also out of, the scale region. At 871°C (1600°F) this area has been observed to undergo recrystallization and the precipitation of additional phases.

Beneath this layer, a second region is observed which consists of etched planes lying parallel to the surface. These are slip planes which were formed by surface grinding which occurred in the preparation of the specimen. During the fatigue process a second phase, most likely $M_{23}C_6$, precipitates on the slip planes and this gives rise to the irregular etching characteristics.

Figure 2.4 shows the types of carbides which develop during fatigue testing. The small particles at the grain boundaries are likely to be $M_{23}C_6$ whereas the fine precipitates within the grains are probably of the M_6C prime type (Lyman, 1972). Two types of large carbide particles are observed which are distinguishable by their color as observed with the scanning electron microscope (SEM). The most common is light gray in color and the other is medium gray. The difference in contrast is brought about by the "atomic number effect." This is caused by the larger numbers of secondary electrons which are generated when the SEM electron beam impinges on elements of high atomic number. Since these secondary electrons are responsible for image formation, phases containing large fractions of heavy elements are lighter in color. The large light gray carbides are thus likely to be M_6C (Lyman, 1972) and many are probably primary carbides present after the initial heat treating of the specimens. Smaller M_6C parti-

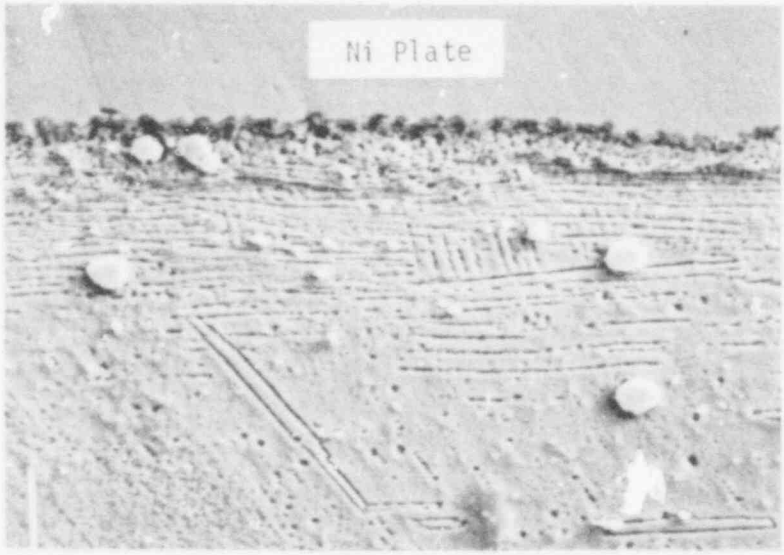

Figure 2.3. Scanning electron micrograph of Hastelloy-X specimen (MHF-16) fatigue tested in air at 760°C (1400°F) at an alternating stress of 234.4 MPa (34.0 ksi). Cycling rate was 40 Hz and cycles to failure were 5.5×10^6. Magnification 1000X.

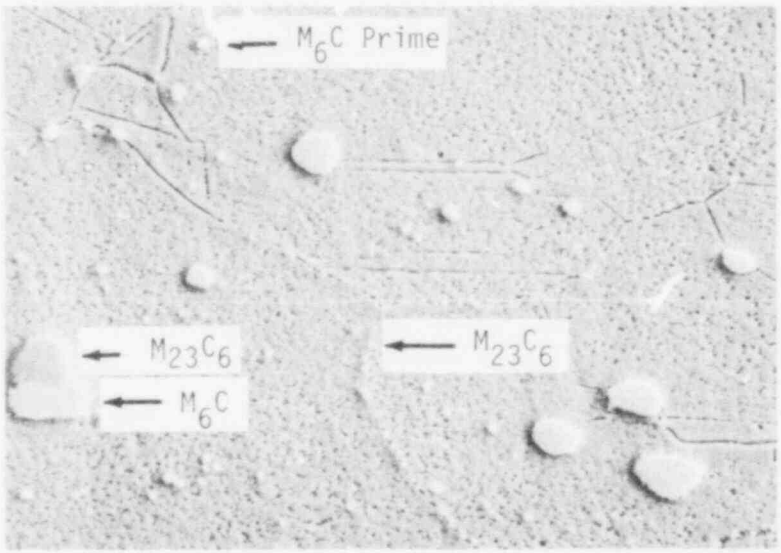

Figure 2.4. Scanning electron micrograph showing various carbides present in Hastelloy-X specimen (MHF-16) fatigued in air at 760°C (1400°F) at an alternating stress of 234.4 MPa (34.0 ksi). Cycling rate was 40 Hz and cycles to failure were 5.5×10^6. Magnification 1000X.

icles could have formed from the M_6C prime described above. The medium gray phase is also thought to be a carbide. It seems to always exist in close association with the M_6C, often as attached particles (Figure 2.4). Frequently, the darker carbide is observed to transform into M_6C, as shown in Figure 2.5. Nucleation points are at small particles on the surfaces of the carbide. Probably the darker carbide is $M_{23}C_6$ since it has been shown to commonly exist in this temperature range (Decker, 1969).

Some approximate measurements have to be made of the chemical compositions of various carbides shown in Figure 2.6 and the results are given in Table 2.1. Carbide particles A, C and D are relatively close in composition which is consistent with their tentative identification as M_6C or M_6C prime. Carbide B, however, is greatly different and, compared to the other carbides, is found to be deficient in Mo and Ni. This is shown more clearly with the scanning electron microscope/microprobe (SEMM) scans given in Figure 2.7.

2.1.2 High Cycle Fatigue of Alloys Aged in an HTGR Helium Environment

Batches of Incoloy 800H and Hastelloy X have been thermally aged in the helium environment described in the previous section in order to determine how long term corrosion affects fatigue strength. By preaging specimens in simple furnaces prior to testing, considerable machine time is saved since the specimens are not exposed within the fatigue unit itself.

Figures 2.8 and 2.9 show preliminary data obtained for 3000 hour aged specimens. Comparisons are made with unaged specimens tested in air and in helium. The aged Incoloy 800H shows a decrease in fatigue strength of approximately 20 percent compared to unaged material tested in helium. However, the strength is still considerably higher than unaged material tested in air. In the case of Hastelloy X aged and unaged specimens tested in the helium environment show very similar fatigue strengths. For the shorter test times air gives lower fatigue strengths but, at longer times ($N_f \geq 10^8$) the air and helium fatigue strengths are comparable.

To define the effects of thermal aging in helium some preliminary work has been carried out on an Incoloy 800H specimen (MNF-194) which was preaged for 3000 hours at 760°C (1400°F) prior to testing in helium. The specimen was cycled at 40 Hz at an alternating stress of 158.6 MPa (23.0 ksi). Failure occurred after 5.5×10^5 cycles. The fractograph in Figure 2.10 shows that crack propagation occurs in a uniform manner similar to that for unaged material. However, higher magnification examination shows that in the Stage II crack propagation region a fine precipitation is present (Figure 2.11). This was probably brought about by the thermal aging process and attempts will be made shortly to determine the nature of this phase.

A pronounced oxide scale was formed by the aging process and fatigue cycling causes significant spallation to occur as shown in Figure 2.12. The metal immediately beneath the scale appears to be embrittled as shown by subscale cracking initiated during fatigue (Figure 2.13). This effect is not observed in unaged material. Additional examinations are being carried out to confirm these observations.

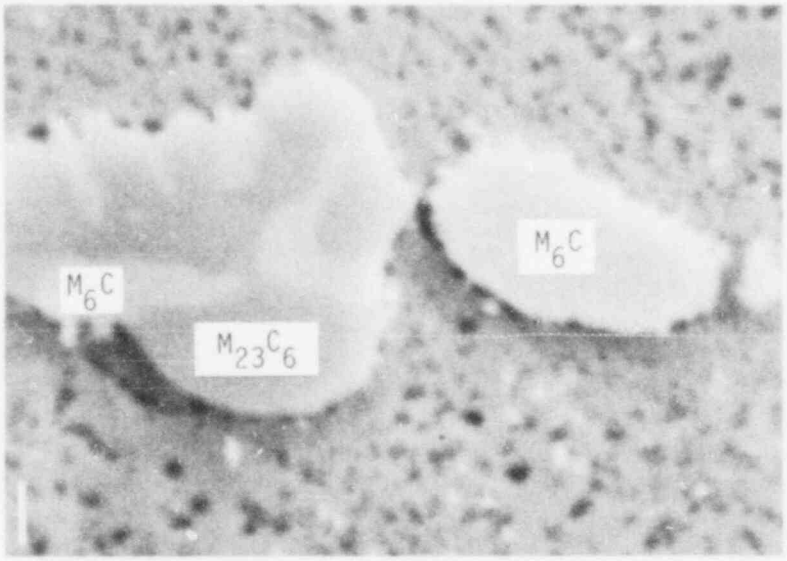

Figure 2.5. Scanning electron micrograph showing gray carbide phase in Hastelloy-X (probably $M_{23}C_6$) transforming to M_6C during fatigue testing at 760°C (1400°F) at an alternating stress of 234.4 MPa (34.0 ksi). Cycling rate was 40 Hz and cyles to failure were 5.5×10^6. Magnificati~n 6000X.

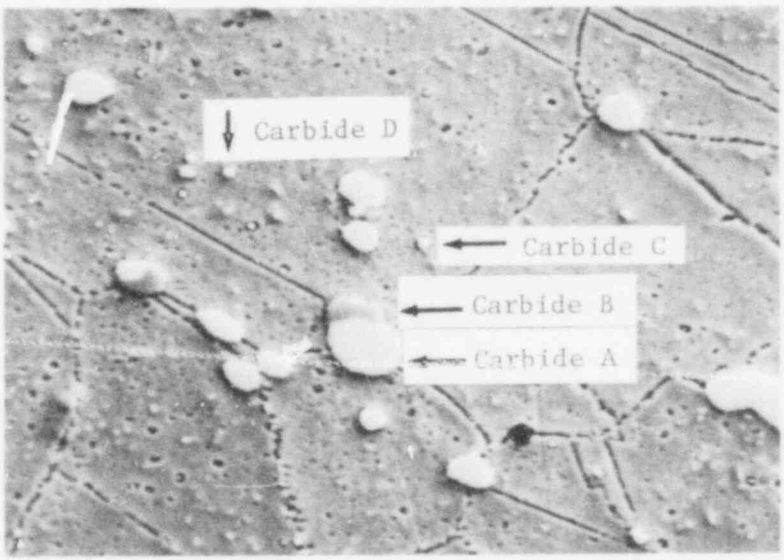

Figure 2.6. Identification of carbides in Hastelloy-X specimen (MHF-16) fa igued in air at 760°C (1400°F) at an alternating stress of 234.4 MPa (34.0 ksi). Cycling rate was 40 Hz and cycles to failure were 5.5×10^6. Magnification 1000X.

Table 2.1

Approximate Compositions of Carbides in a Hastelloy X Fatigue Specimen[1] Obtained by Scanning Electron Microscope/Microprobe Analyzer

	Concentration (wt. percent)[2]					
Element	M_6C[3]	Carbide A[4]	Carbide B[5]	Carbide C[6]	Carbide D[6]	Avg. in Alloy[7]
Ni	21	22	6	26	--	48.1
Fe	7	7	5	10	--	18.7
Cr	14	14	58	15	--	20.7
Mo	62	65	30	43	37	8.9
W	6	7	2	4	--	0.6
Co	1	----	-----	-----	--	2.1
Mn	0.2	0.1	0.2	0.3	--	0.5
Si	2	2	0.01	0.01	--	0.4
C	----	----	-----	-----	--	0.11

NOTES:

(1) Specimen tested at 760°C (1400°F) at an alternating stress of 234.4 MPa (34.0 ksi). Cycling rate was 40 Hz and failure occurred after 5.5×10^6 cycles.
(2) Approximate concentration of an element obtained from the expression: (X-ray counts from carbide/counts from matrix) X average concentration of element in alloy.
(3) Values for M_6C carbide in control specimen heat treated at 1176°C (2150°F) for 0.5 hour followed by water quench.
(4) M_6C type.
(5) Probably $M_{23}C_6$ type.
(6) Probably M_6C prime type.
(7) Alloy vendor analysis.

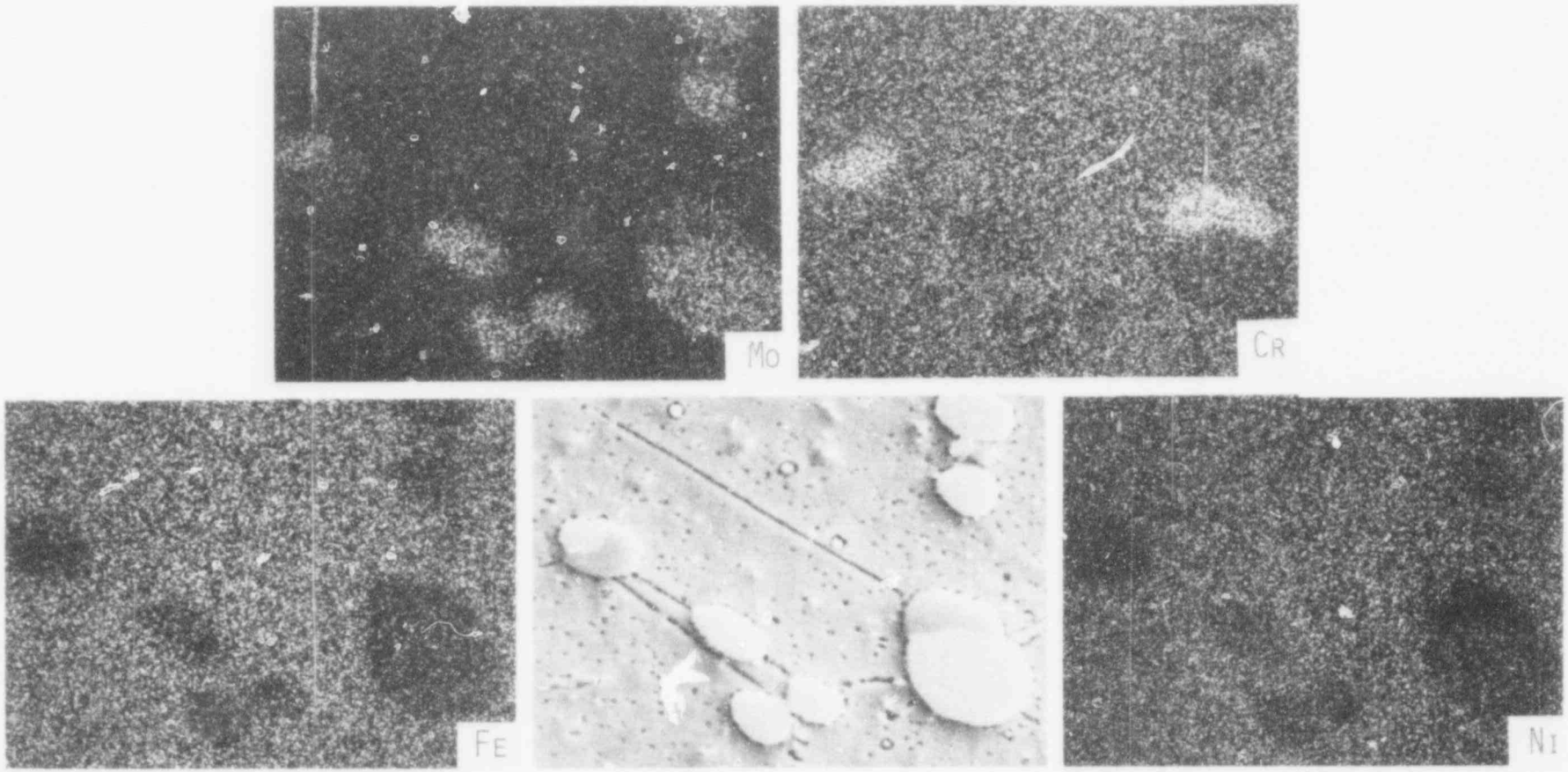

SCANNING ELECTRON MICROSCOPE MICROPROBE ANALYSIS OF CARBIDE PARTICLES IN A HASTELLOY-X FATIGUE SAMPLE TESTED AT 760°C (1400°F) AT AN ALTERNATING STRESS OF 234.4 MPa (34.0 ksi) AT 40 Hz FOR 38 HOURS. MAGNIFICATION 500X

Figure 2.7

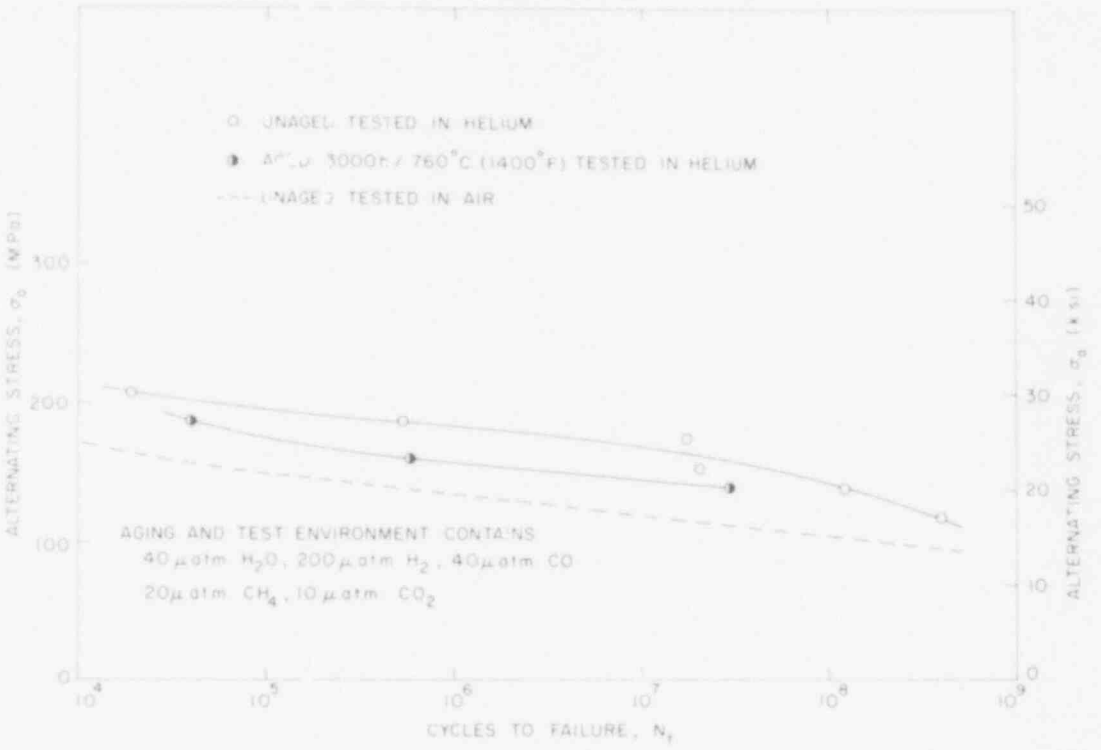

EFFECT OF THERMAL AGING IN HELIUM ON THE HIGH CYCLE FATIGUE OF INCOLOY 800H AT 760°C

Figure 2.8

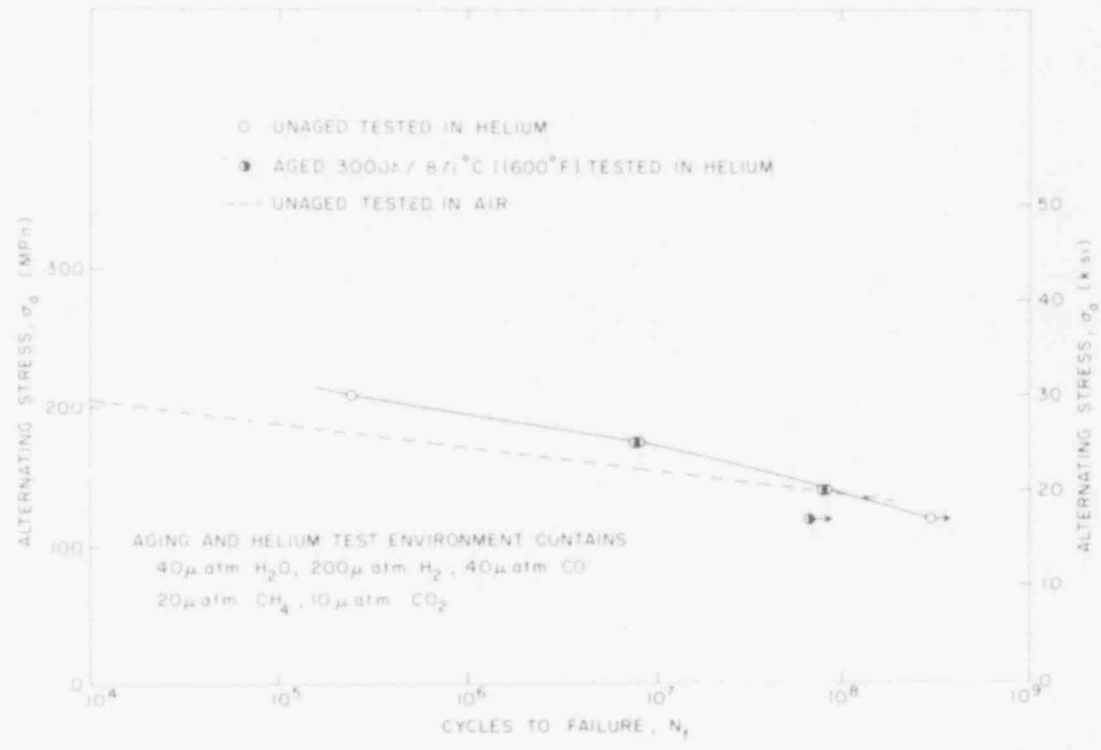

EFFECT OF THERMAL AGING IN HELIUM ON THE HIGH CYCLE FATIGUE OF HASTELLOY X AT 871°C

Figure 2.9

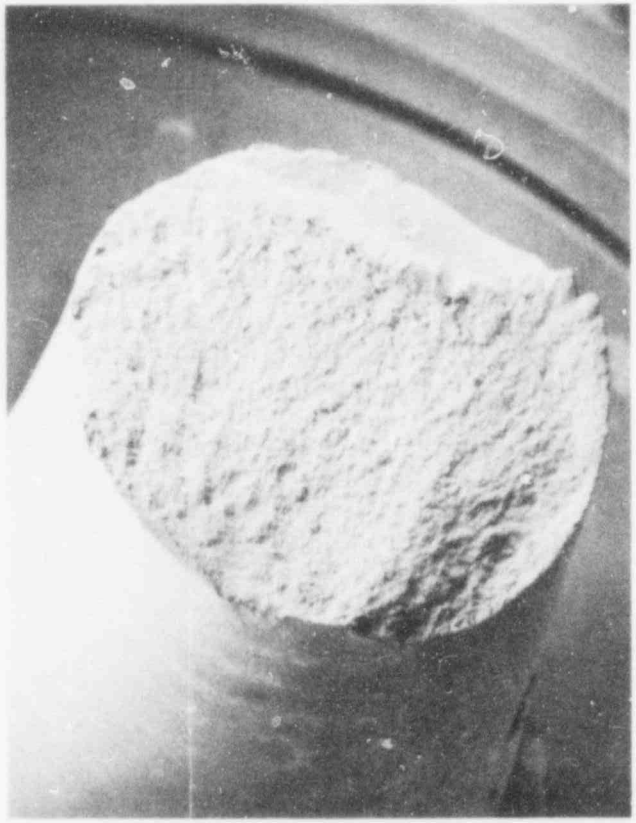

Figure 2.10. Fractograph of an Incoloy-800H specimen (MNF-194) thermally aged in HTGR helium for 3000 hours at 760°C (1400°F) and tested in HTGR helium at an alternating stress of 158.6 MPa (23.0 ksi) at 760°C (1400°F); N_f is 5.5 x 10^5. Magnification 12X.

Figure 2.11. Fine precipitation in the fracture surface of an Incoloy-800H specimen (MNF-194) thermally aged in HTGR helium for 3000 hours at 760°C (1400°F) and tested in HTGR helium at an alternating stress of 158.6 MPa (23.0 ksi) at 760°C (1400°F); N_f is 5.5 x 10^5. Magnification 500X.

Figure 2.12. Scale spallation on surface of an Incoloy-800H specimen (MNF-194) thermally aged in HTGR helium for 3000 hours at 760°C (1400°F) and tested in HTGR helium at an alternating stress of 158.6 MPa (23.0 ksi) at 760°C (1400°F); N_f is 5.5 x 10^5. Magnification 100X.

Figure 2.13. Subscale cracking near the surface of an Incoloy-800H specimen (MNF-194) thermally aged in HTGR helium for 3000 hours at 760°C (1400°F) and tested in HTGR helium at an alternating stress of 158.6 MPa (23.0 ksi) at 760°C (1400°F); N_f is 5.5 x 10^5. Magnification 600X.

2.2 Creep Rupture Properties of Primary Circuit Structural Materials in Air and Helium (J. Chow, P. Soo)

Many of the HTGR primary components are inaccessible for replacement and have to last for the design life of the reactor. Therefore, the long term structural integrity of these components is an important safety consideration. In an HTGR the primary circuit materials are exposed to helium with impurities such as water which is present due to water influx from the steam generators. In this phase of our program, an elevated temperature testing effort has been established to study the long term mechanical behavior of some critical alloys in a prototypic HTGR helium environment.

The helium environment for the mechanical testing is being supplied from the Materials Test Loop (MTL) and conists of helium with 40 μatm. H_2O, 200 μatm. H_2, 40 μatm. CO, 10 μatm. CO_2 and 20 μatm. CH_4. It is believed that this "wet" environment simulates that which could exist in an operating HTGR.

At the present time, 20 lever arm creep rupture units are being used to test HTGR materials. During the last quarter, 11 test units were run with helium retorts and the balance of the units were used for in-air tests.

The creep testing program has been concentrated on Hastelloy X which is the thermal barrier cover plate material in the highest temperature zones and on Incoloy 800H which is widely used in the construction of the steam generator. Materials from commercial heats of these 2 alloys being tested are given in Section 2.1. Both of these alloys were purchased in the form of 1/2 inch diameter rods

Prior to machining of the test specimens the Incoloy 800H alloys was solution treated by heating to 1149°C (2100°F) and water quenched. The Hastelloy X specimens were heated to 1176°C (2150°F) for 1/2 hour and water quenched. In order to eliminate heat-to-heat variations the in-air and in-helium test specimens were made from single reference heats.

2.2.1 Incoloy 800H

Creep rupture testing of Incoloy 800H at 649°C (1200°F) and 760°C (1400°F) in the simulated HTGR helium environment and in air is continuing. The updated stress-rupture curves and creep rate curves are shown in Figure 2.14 and Figure 2.15, respectively. The lines are drawn through the in-air test data which are represented by solid points. The in-helium tests are represented by open circles. Also shown are the minimum expected values obtained from Code Case 1592 of the American Society of Mechanical Engineers (ASME) Boiler and Pressure Vessel Code.

In Figure 2.14 the in-air rupture test data points are only slightly above the Code Case 1592 expected minimum. For Incoloy 800H, the strength is highly dependent upon the carbon content. Since the heat of Incoloy 800H that we are testing contains 0.05 w/o C it is at the lower limit of the H grade.

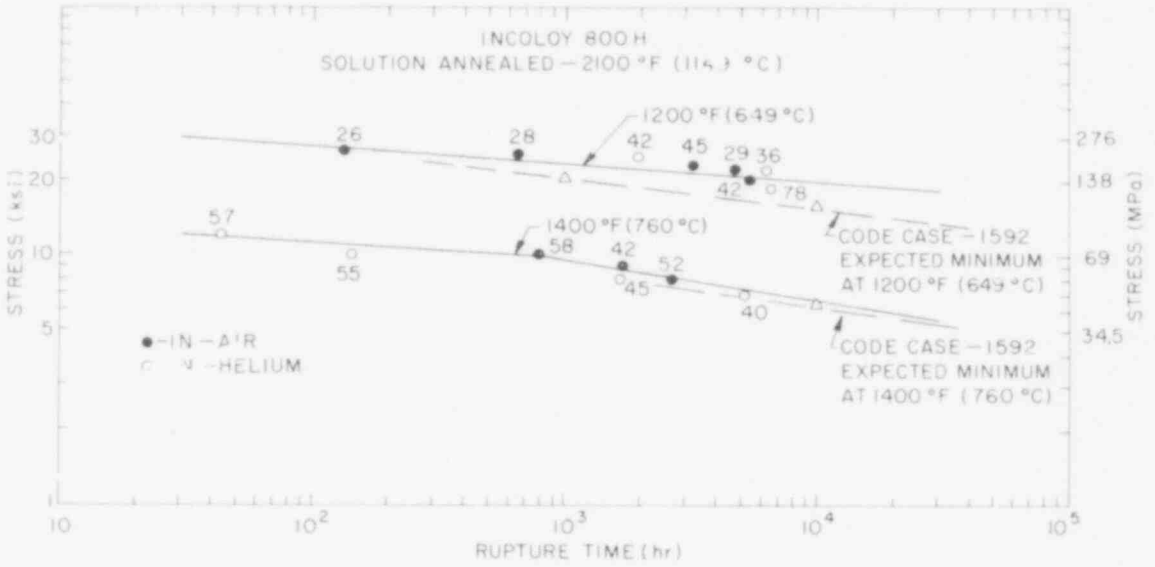

STRESS RUPTURE PROPERTIES INCOLOY 800H TESTED AT 1200°F (649°C) AND 1400°F (760°C) IN AIR AND IN HTGR HELIUM

Figure 2.14

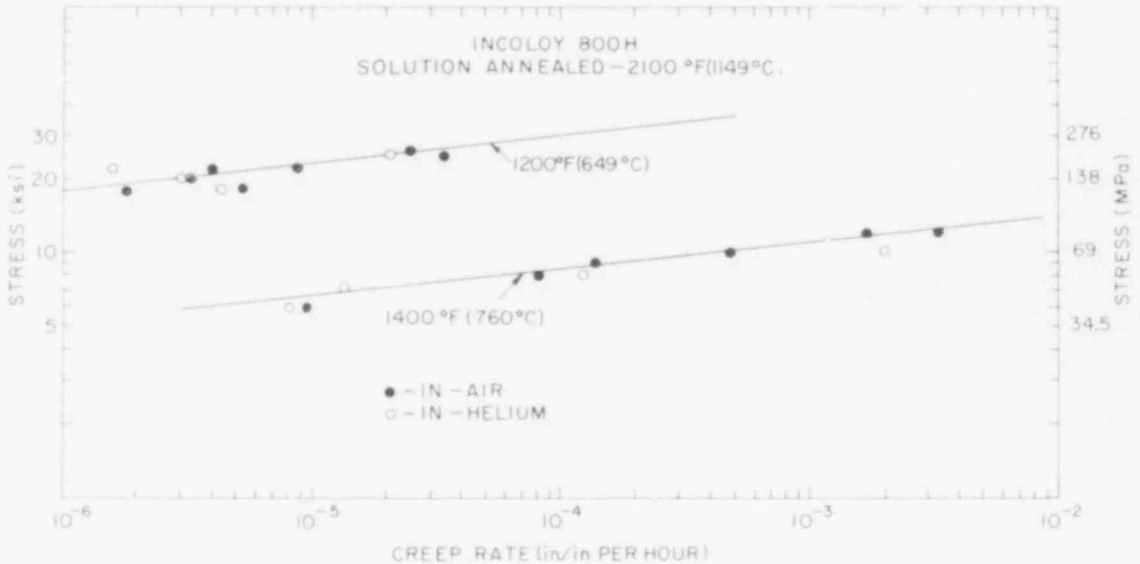

CREEP STRENGTHS OF INCOLOY 800H AT 1200°F (649°C) AND 1400°F (760°C) TESTED IN AIR AND IN HTGR HELIUM

Figure 2.15

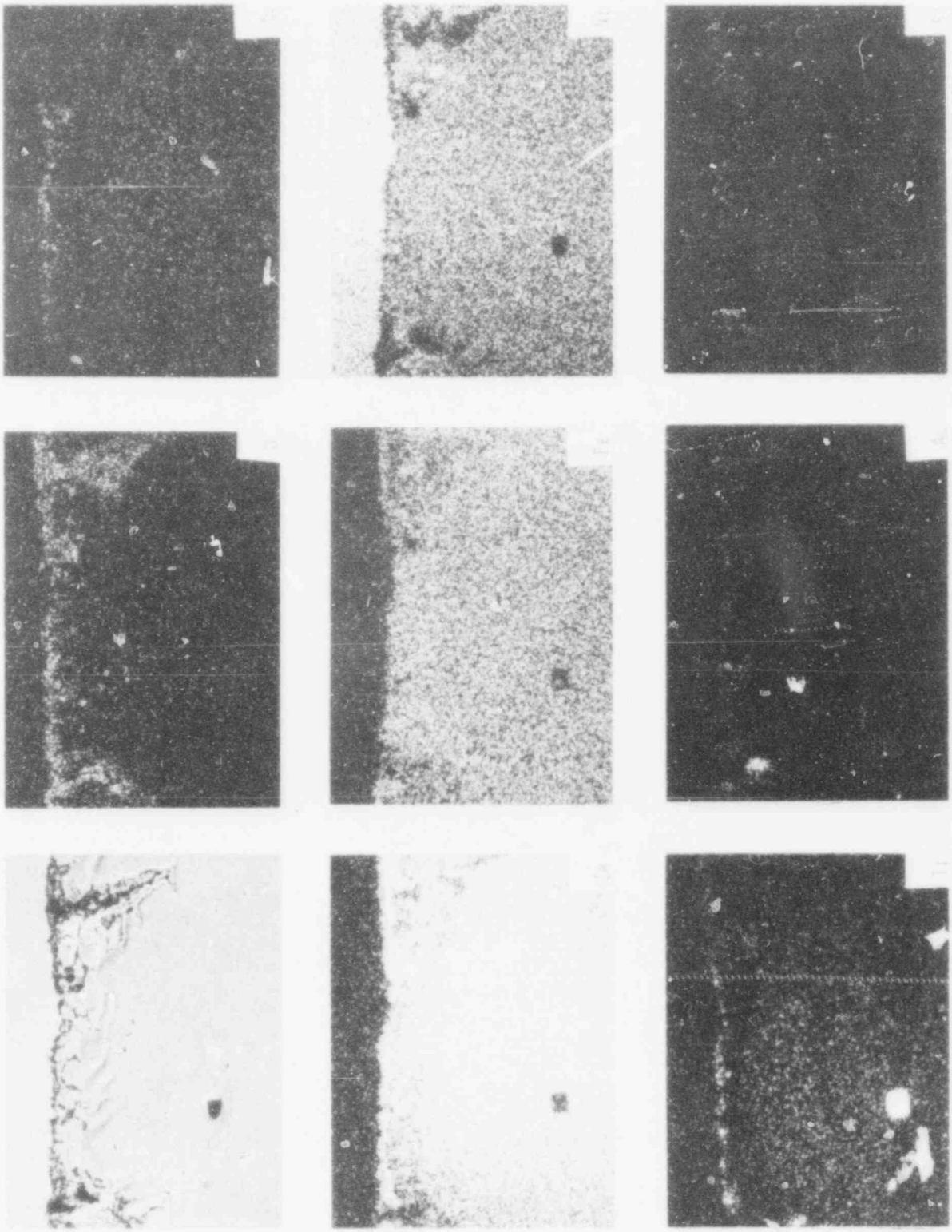

Figure 2.16. SCANNING ELECTRON MICROPROBE ANALYSES OF INCOLOY 800H STRESS RUPTURE TESTED AT 760°C (1400°F) IN AIR. SPECIMEN RUPTURED AFTER 2604 HOURS UNDER A STRESS OF 55.1 MPa (8Ksi) 450X

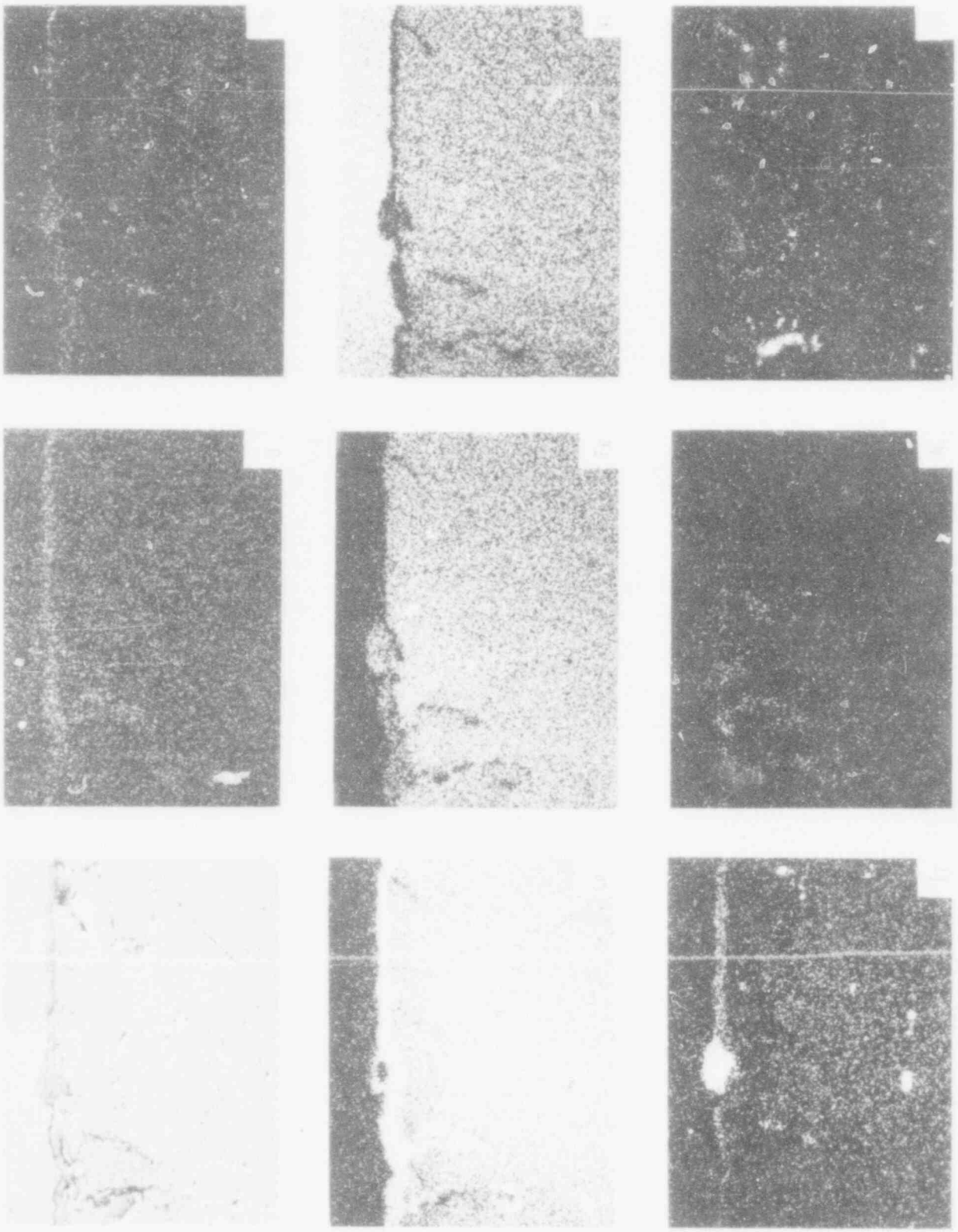

Figure 2.17. SCANNING ELECTRON MICROPROBE ANALYSES OF INCOLOY 800H STRESS RUPTURE TESTED AT 760°C (1400°F) IN HELIUM. SPECIMEN RUPTURED AFTER 5136 HOURS UNDER A STRESS OF 48.23 MPa (7 Ksi) 450 X

At 649°C (1200°F), for test time up to about 7000 hours, there appears to be no difference in rupture strengths for the two environments. However, at 760°C (1400°F), two rupture points at 1628 and 5176 hours lie slightly below the in-air test line. The ductilities of the specimens, shown in terms of percentage elongation in parentheses next to the data points, do not seem to be detrimentally affected by the helium environment.

Long term tests at 649°C (1200°F) stressed at 82.7 to 124 MPa (12.0 to 18.0 ksi) are under way both in air and in helium environments. Some of these tests have gone beyond 10,000 hours of testing. Long term tests at 760°C (1400°F) stressed at 34.5 and 41.4 MPa (5.0 and 6.0 ksi) are also under way.

Figure 2.15 gives the creep strengths obtained for Incoloy 800H at 649°C (1200°F) and 760°C (1400°F). There is no apparent difference in the minimum creep rate for the air and helium test environments. It is possible that the small surface-to-volume ratio used in the test specimens would require a longer test time in order to show environmentally induced differences in properties.

A comparison has been made of 2 Incoloy 800H specimens tested in air and helium at 760°C (1400°F). The stress levels were comparable but the helium specimen was exposed to the test environment for 5136 hours whereas the air specimen was exposed to only 2604 hours. Nevertheless, there were basic similarities in their corrosion behavior which are shown in Figures 2.16 and 2.17, and summarized below:

- The predominant oxide was that of chromium but titanium oxide was also clearly observed in the bulk of the scale.
- Manganese oxide seems to form a thin layer on top of the chromium and titanium oxides.
- Aluminum and silicon are also oxidized. However, it is not certain whether these elements are oxidized in the same location as the chromium or some other area, below the chromium.
- Manganese, chromium, aluminum and silicon are also oxidized along intergranular regions.
- The oxidation of magnanese, chromium and titanium results in the formation of a zone beneath the oxide scale which is depleted of these elements.

2.2.2 Hastelloy X

Figure 2.18 presents the stress-rupture data for Hastelloy X at 760°C (1400°F) and 871°C (1600°F). At both of these temperatures, the in-helium test points either lie on the line which is drawn through the air test points or slightly below. This indicates a detrimental effect of testing in helium on the rupture strength. The most convincing data that illustrate the environmental effect are the two tests performed at 871°C (1600°F) at a stress of 41.4 MPa

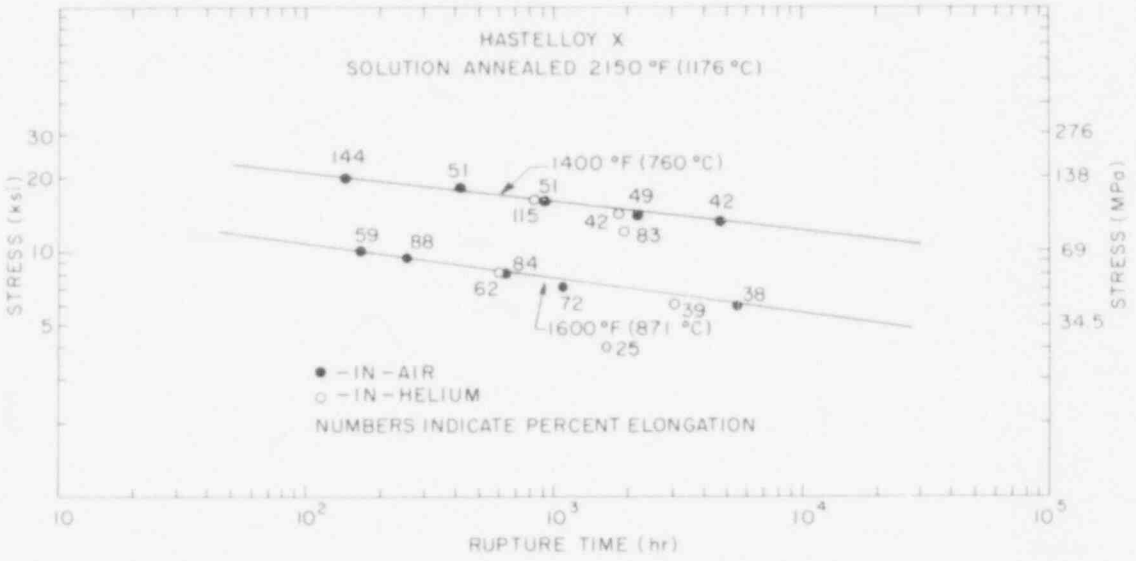

STRESS RUPTURE PROPERTIES OF HASTELLOY X AT 1400 °F (760 °C) AND 1600 °F (872 °C) TESTED IN AIR AND IN HTGR HELIUM

Figure 2.18

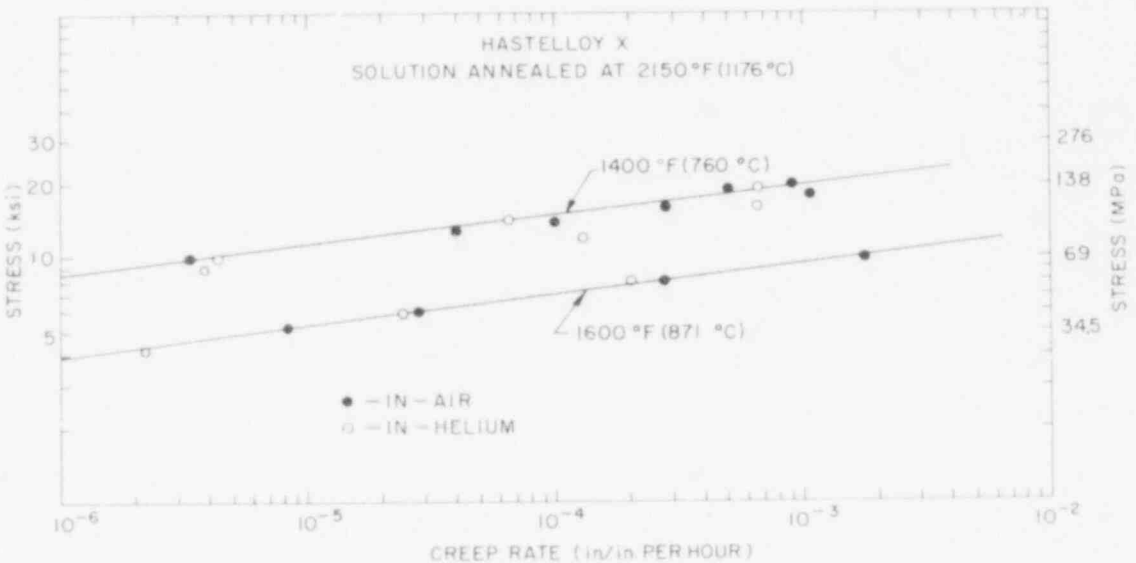

CREEP STRENGTHS OF HASTELLOY X AT 1400 °F (760 °C) AND 1600 °F (871 °C) IN AIR AND IN HTGR HELIUM

Figure 2.20

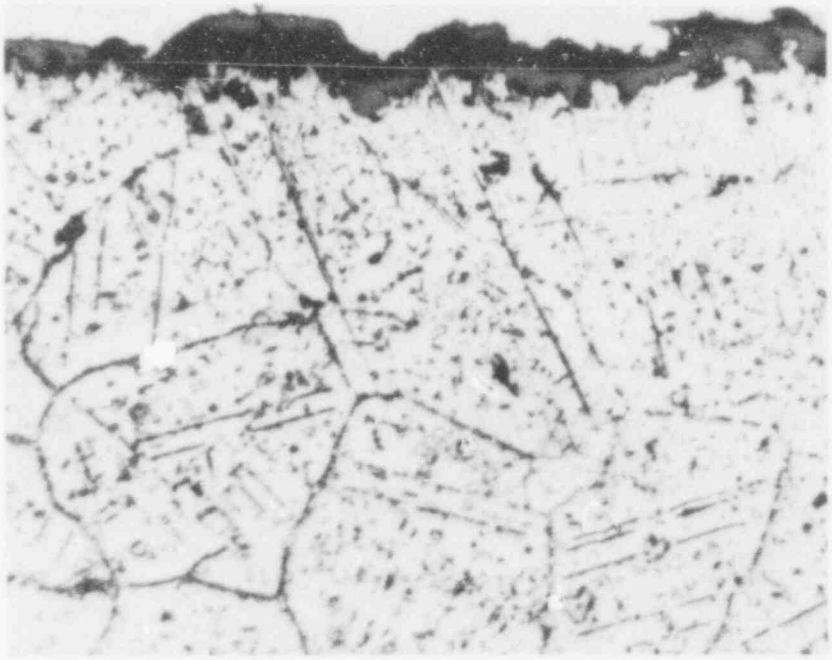

(A)

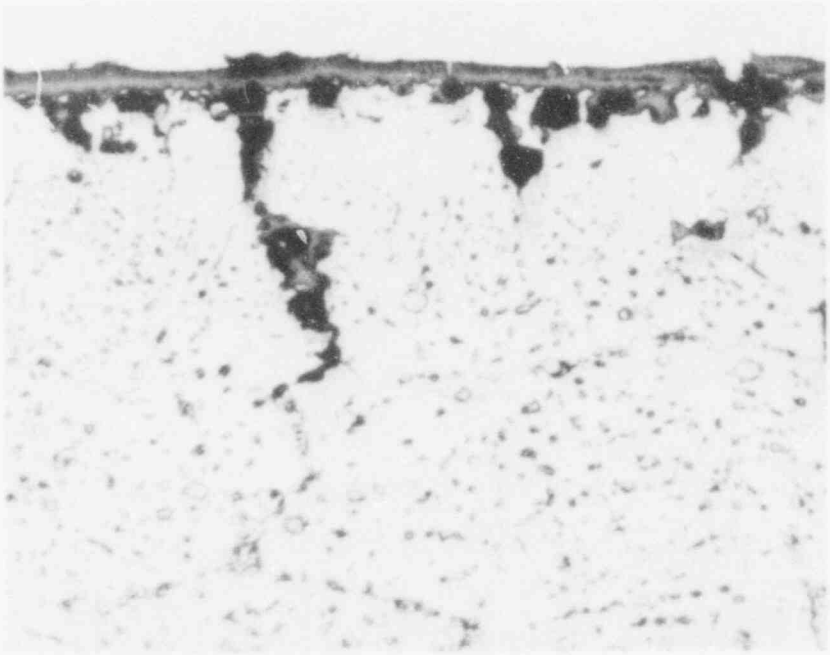

(B)

Figure 2.19. Hastelloy X creep specimens fractured at 871°C (1600°F), 41.4 MPa (6.0 ksi); (A) ruptured in air after 5543 hours, (B) ruptured in HTGR helium after 2986 hours. The air specimen had a thicker oxide scale and showed more intergranular precipitation in the matrix. The alloy depleted zone is thicker in the specimen tested in helium. Mag. 500X.

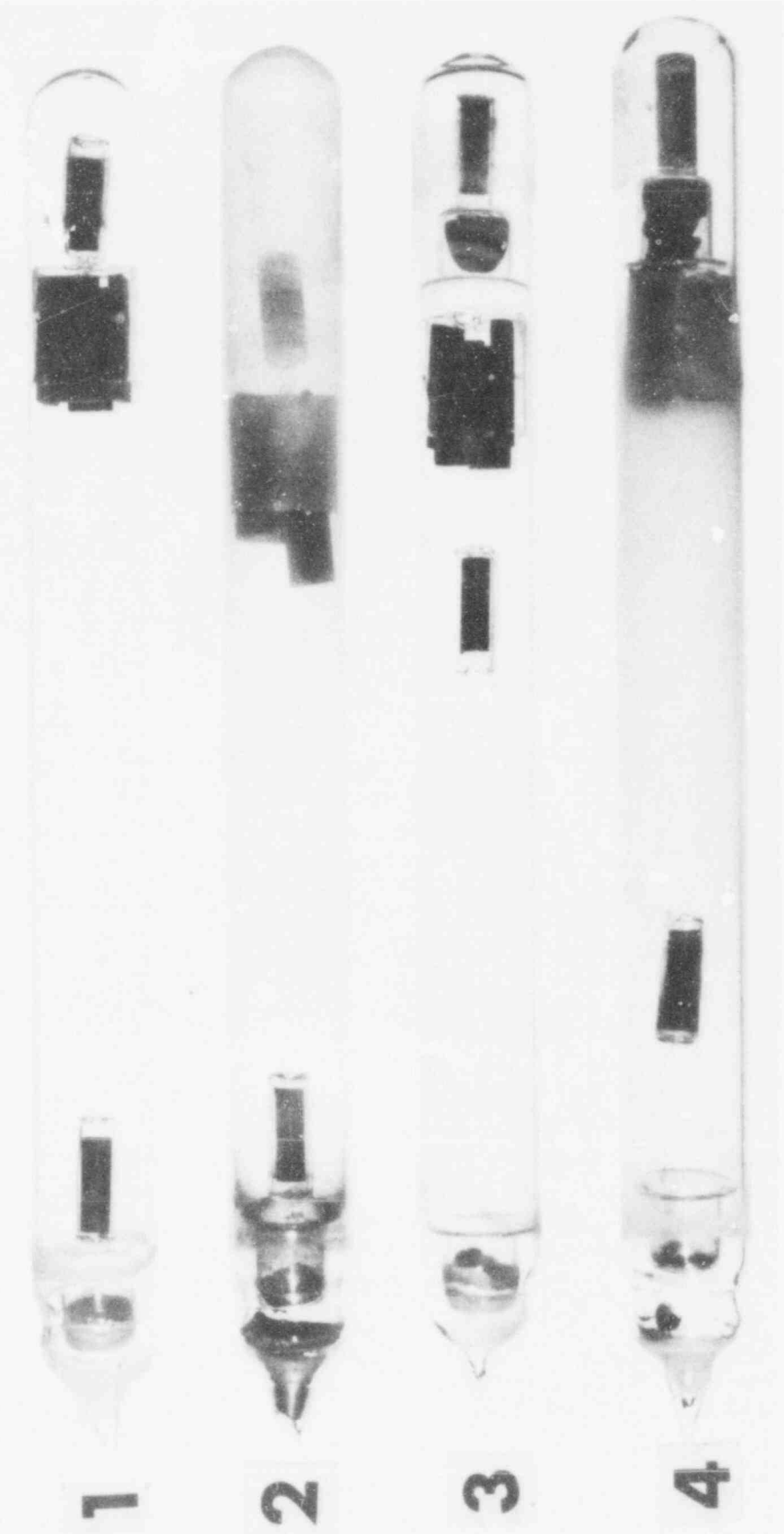

Figure 2.21. Test capsules after long term aging at approximately 800°C; Capsule 1 contains CsI, Capsule 2 contains Te, Capsule 3 contains CsI with 10^{-14} atm. O_2 and Capsule 4 contains Te with 10^{-14} atm. O_2.

(6.0 ksi). The air test failed after 5543 hours whereas the helium test ruptured after 2986 hours. However, the ductilities were very similar, 38% for the air test and 39% for the helium test.

During this quarter, a test at 871°C (1600°F) in helium stressed to 27.56 MPa (4.0 ksi) fractured after only 1665 hours. This test was meant to be a long term evaluation of the effect of the helium environment and projected to last 15,000 to 20,000 hours. The specimen broke with 25% elongation and only 14% reduction of area. Metallographic studies on the specimen are under way to see if the cause of the premature failure can be established. Also, this test will be repeated.

Figure 2.19 shows metallographic sections for the 2 specimens described above. The oxide layers on both specimens seem to be quite adherent; however, the one for the air test is thicker and showed more cracking along the gauge length. This could be because the oxide is inherently more brittle or because a thicker layer cracks more readily under stress. The alloy depleted zone appears to be thicker and there is less grain boundary precipitation in the specimen tested in helium. As in the case of Incoloy 800H, continuing metallographic and scanning electron microprobe studies on additional specimens are being made to establish the influence of the 2 environments on the morphology of the oxide scale and subsurface microstructure of Hastelloy X.

Figure 2.20 shows the minimum creep rate data for Hastelloy X. For tests lasting up to 9000 hours at 760°C (1400°F) and up to 7000 hours at 871°C (1600°F), no differences in rate have been observed for the two environments.

Long term tests at 760°C (1400°F) under stresses of 69.0 and 55.1 MPa (10.0 and 8.0 ksi) and at 871°C (1600°F) under stress of 34.5 and 27.6 MPa (5.0 and 4.0 ksi) are under way.

2.3 Effect of Fission Product Interactions on the Mechanical Properties of HTGR Metals (S. Aronson, J. Chow, P. Soo)

This program was initiated to determine the effect of long term (>1000 hours) exposure of HTGR alloys (Type 304 stainless steel, Hastelloy X, Incoloy 800, Inconel 718) to iodine, tellurium, cesium iodide and cesium under conditions similar to those occurring during normal HTGR operation. Exposures have been completed on 5 groups of samples. Information on the test conditions is given in Table 2.2.

The test capsules used in the first 4 tests are shown, after exposure, in Figure 2.21. The fused quartz tube in Test 3, for example, contains from left to right a fused quartz crucible containing tellurium powder, a magnet encapsulated in fused quartz, a quartz holder with the 4 metal samples, a fused quartz crucible holding a nickel-nickel oxide mixture and, finally, a second quartz encapsulated magnet. Parts of the fused quartz tubes in Tests 2 and 4 became cloudy with a loss of transparency indicating that tellurium attacks fused quartz (see Section 1.7)

Table 2.2

Exposure of HTGR Alloys to Simulated Fission Products

Test No.	Simulated Fission Product	Fission Product Vapor Pressure (atm.)	Temperature of Metal Samples °C	Exposure Time (hours)
1	CsI	10^{-5}	790	1896
2	Te_2	10^{-5}	770	1992
3	CsI	10^{-5}	730	1825(1)
4	Te_2	10^{-5}	800	1850(1)
5	I_2	10^{-3}	800	1173

NOTE: (1) This capsule contains a Ni-NiO mixture maintained at 800°C to give an oxygen partial pressure of 10^{-14} atm.

All the metal samples in the 5 tests were strongly corroded. In Test 5, the iodine source was completely used up in attacking the metal samples. A heavy deposit of reddish-black crystals was found at a location in the quartz tube at which the temperature was maintained at 200-300°C. It is apparent that metal iodides were vaporised from the metal samples and condensed at this location. These crystals have been collected and submitted for chemical and X-ray diffraction analysis.

The scanning electron micrographs in Figure 2.22 show preliminary data obtained from Capsule No. 2 in which Type 304 stainless steel, Incoloy 800, Hastelloy X and Inconel 718 were exposed at an average temperature of 770°C to tellurium vapor at a partial pressure of about 10^{-5} atmospheres. The surfaces shown were initially polished through 600 grit silicon carbide papers and finally polished on "Microcut 600 grit soft" paper lubricated with kerosene.

For the Type 304 stainless steel, Incoloy 800 and Hastelloy X there is a large amount of surface deposition which is easily spalled away if handled. Beneath the deposited layer the original metal surfaces are identifiable by the polishing scratches. In the case of Type 304 stainless steel, however, there does appear to be significantly more corrosion of the metal and the polishing marks are not usually observed. This is an anticipated result since this material is usually the least resistant to corrosion of the 4 materials evaluated.

There is also a significant deposition of small particles on top of the deposited layers for the 3 materials. These take the form of fine granular deposits or whisker type growths.

Inconel 718 behaves differently from the first 3 materials insofar as general deposition of corrosion products is not seen. The polished surface maintains high integrity but there is localized corrosion as shown in Figure 2.22.

Work has recently been completed on bend tests on the above samples and on others exposed to different fission product species. Metallographic analyses will be carried out during the next quarterly period and will be described in the next report.

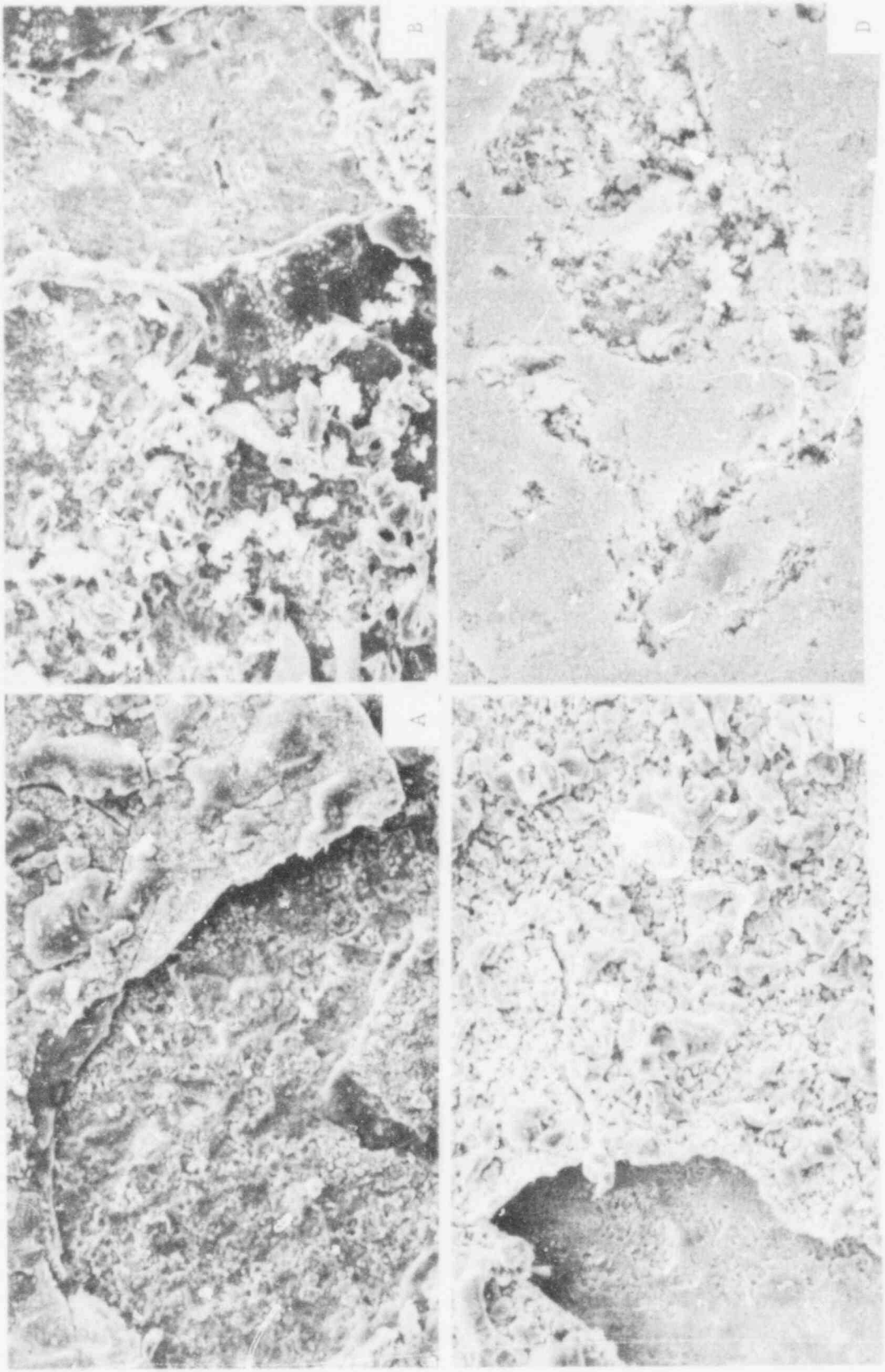

Figure 2.22. Corrosion of polished metal surfaces exposed to tellurium vapor at 750°C for 1800 hours: (A) Type 304 Stainless Steel, (B) Incoloy 800, (C) Hastelloy X, (D) Inconel 718. Magnifications 500X.

2.4 Materials Test Loop (L. Epel)

The Materials Test Loop (MTL) functioned routinely during the last quarter, supplying helium with controlled amounts of impurities to 3 high cycle fatigue machines, 11 creep testing machines, and 4 aging retorts. The only noteworthy incident during the 3 month interval was a regionwide power failure that caused the first interruption in steady operation since startup 1 1/2 years ago. The total length of time that the MTL was shut down was approximately 18 hours and it was readjusted to design levels within an hour or 2 after startup.

The MTL behavior during this quarter is summarized in Table 2.3, which shows the 3 month averages and standard deviations of each of the 5 controlled impurity concentrations together with the desired levels of each. As can be seen from inspection of this table, the average impurity levels were quite close to the design concentrations and the standard deviations were also reasonably small, except perhaps for hydrogen; even there, however, the coefficient of variation was just 22.5.

Table 2.3

Impurity Concentrations in the MTL (ppm)

Impurity	Desired	Average	Standard Deviation
Carbon Dioxide	10	11.0	2.8
Carbon Monoxide	40	39.8	3.3
Hydrogen	200	198.9	44.8
Methane	20	19.1	2.9
Water Vapor	40	42.3	6.0

2.5 Large Scale Graphite Oxidation Loop (L. Epel)

Work has begun to design a large scale graphite oxidation loop to be used initially for exposing 10 inch diameter PGX samples to high temperature, high pressure, contaminated helium. Because the major capital equipment item is the circulating pump and motor, a quotation for an engineering design of a helium circulator was requested from Mechanical Technology, Inc. of Latham, New York. Also, a budget figure for fabrication, assembly, testing and delivery of the final design circulator (including motor, exciter, controls, etc.) was requested. The engineering design effort, which would be approximately 6 months long, was estimated to cost about $130,000 on a cost plus fixed fee basis. The budgetary estimate for the circulator-motor assembly stands at $660,000. These figures apply to a circulator having the following characteristics:

Inlet Pressure	735 psia
Outlet Pressure	760 psia
Inlet Temperature	1000°F
Flow (at inlet conditions)	600 ft^3 helium/min.

In order to develop the most economical design, 3 variations the nominal

configuration are being considered in the design study. These variations will necessitate differences in other capital equipment items such as electrical heaters, heat exchangers, piping, etc. but may lead to a less expensive overall system than the "nominal" one based on the circulator specifications given above. In all of the designs the test section conditions are assumed to be the same, namely 1800°F helium at 735 psi, experiencing a 5% reduction in water vapor concentration as it passes over the graphite specimen. These conditions result in the following calculated helium flow rates for the nominal case and its 3 variations:

Case	Pump Inlet Press. psia	Pump Inlet Temp. °F	Pump Inlet Flow cfm
Nominal (Case 1)	735	1000	600
Case 2	735	200	270
Case 3	50	1000	2270
Case 4	50	200	1025

Each of these variations will be considered separately in the study to determine the optimal economic design for the graphite oxidation loop.

2.6 Helium Impurities Loop (L. Epel)

The Helium Impurities Loop (HIL) has been run during the quarter to gain further insight into the thermodynamics and kinetics of chemical reactions of helium impurities with the alloy which comprises the retorts. Additional experiments were performed to study the diffusion rate of hydrogen through the walls of the loop and to obtain a preliminary idea of absorption and desorption rates of hydrogen in the metal walls.

The Helium Afterglow Monitor, developed at LASL, has arrived at BNL and work has started on repairing the vacuum system. A quartz plate that rests between the "glow tube" and the monochrometer was found to be cracked and a new one is being made.

Additional instrumentation has been ordered for the HIL and for the "quartz loop" so that experiments can proceed in both systems simultaneously. Also, infrared absorption detectors have been purchased to replace the "Panametrics" moisture monitors, the latter having been found to be unreliable.

More specifically, the metallurgical condition of the HIL under oxidizing and reducing atmospheres is becoming better undersood. The H_2/H_2O ratios observed when water is present in the loop are entirely consistent with a model of chromium, iron and nickel oxidation which asserts that the chromium and the nickel oxide activities are much less than unity at equilibrium. It happens that at the retort temperature of the HIL the free energy of formation of iron oxide and of water vapor are numerically close so that it is the competition between iron and hydrogen that determines the measured H_2/H_2O ratios. Under these conditions chromium is essentially completely oxidized while nickel is immune to any free oxygen in the system (Epel, 1978).

Similarly, when the HIL is in a very reduced state, following hydrogen firing, the H_2/H_2O ratios yield information from which inferences can be drawn concerning which constituents of the stainless steel retorts are still oxidized and which are not. The thermodynamics of the system together with the observed H_2/H_2O ratios implies that the chromium remains oxidized while the iron is essentially completely reduced during hydrogen firing. Since chromium oxide will not give up its oxygen to CO (the free energy change is positive for this reaction), the observedd conversion of CO to CO_2 following a CO injection must be a disproportionation reaction. This expectation was confirmed by the mass balances done in the HIL when it was in a reduced state.

The experimental observations in the HIL are consistent with thermodynamic predictions if equilibrium conditions are assumed, at least for the highly oxidized and highly reduced system. A systematic method of predicting the oxidizing, reducing, carburizing, decarburizing, or sooting potential of various impurity combinations is being studied (Gurry, 1950; Noda, 1978). If a self-consistent, predictive model can be generated, however, it will still only apply to equilibrium conditions. The kinetics of various processes in the HIL need further study.

Some experiments aimed at estimating hydrogen diffusion rates through the HIL boundaries were completed. The time behavior of hydrogen concentration in the HIL following massive injections of hydrogen was observed at normal HIL operating conditions for two levels of H_2 concentration an order of magnitude apart. Both tests resulted in exponential decay with time of the hydrogen in the HIL, the half lives agreeing with one another within about 5%.

The quartz loop has been used during the quarter to investigate the possibility of forming free carbon monoxide with a mechanism other than disproportionation. Thermodynamically it is possible to oxidize the chromium in stainless steel by exposure to CO to form a stable oxide and free carbon. At 1000°K, the temperature of the reaction zone in the loop, the standard free energy change for the reaction $2Cr + 3CO = Cr_2O_3 + 3C$ is -62.8 kilocalories. The standard free energy changes for the oxidation of iron and nickel by carbon monoxide are positive. Assuming unit activities for all of the solids in the above reaction, the computed final CO pressure is 27 μatm. This is very close to the final CO pressure observed in the quartz loop after it was charged initially with 7000 μatm. There was no buildup of CO_2 or other impurities as the CO became depleted, indicating that the reaction shown above was the one involved.

2.7 Characterization of PGX Graphite (F. B. Growcock, M. Eto, J. Heiser, G. Uneberg)

During this quarter, the study of PGX graphite in the following areas was continued: oxidation kinetics, removal of iron from impure graphite and effect of oxidation on ultimate compressive strength. The study of gas transport at elevated temperatures has not yet finished the apparatus construction phase; it will not be discussed. A similar status exists for a study on the effects of tensile and compressive stresses on oxidation rate and ultimate tensile and compressive strengths of PGX graphite. This task arose from preliminary work done at BNL on the effect of tensile stress on the oxidation rates of HTGR graphites (Growcock, 1978a); although no effect was found from this and other

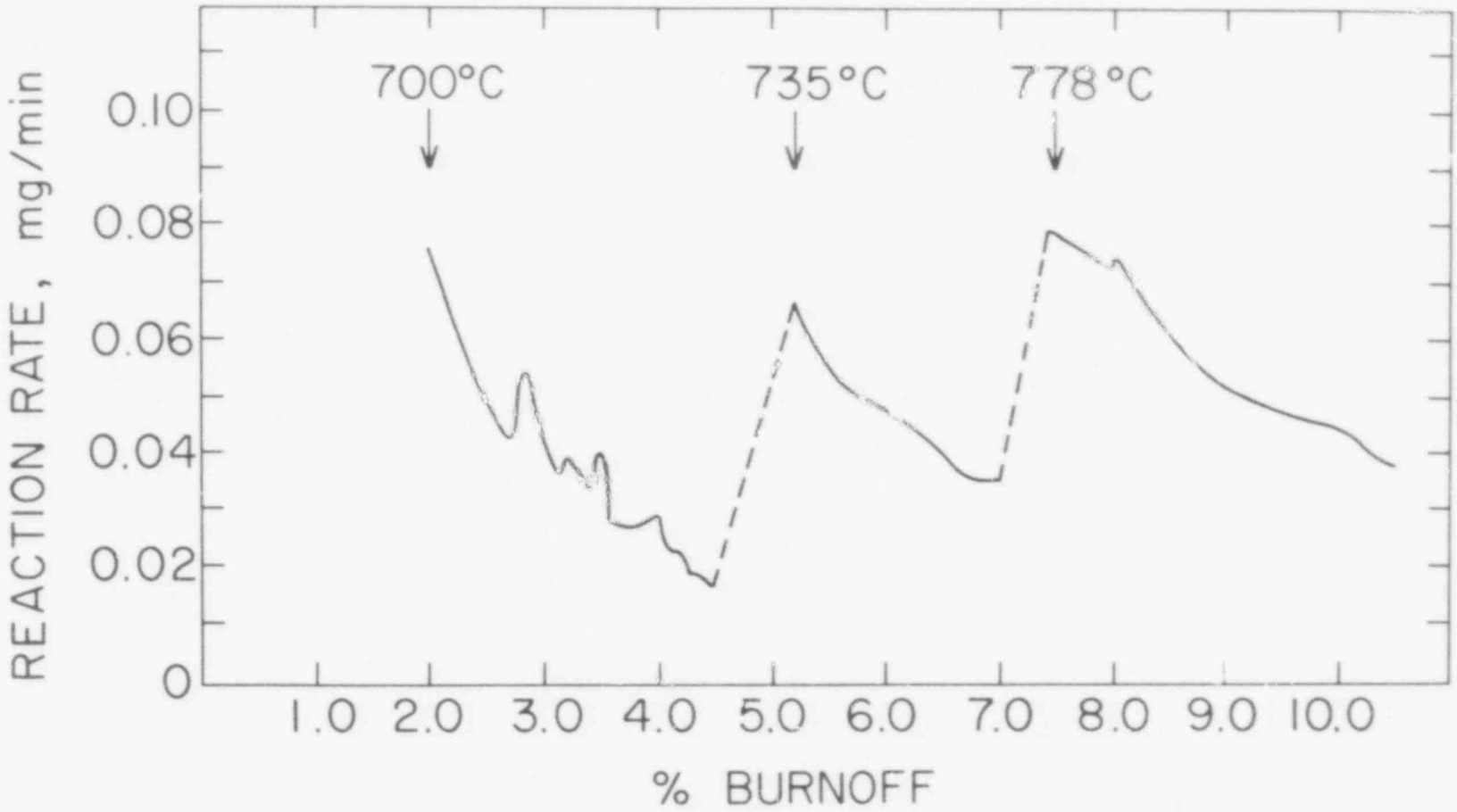

Figure 2.23. The effect of burnoff on the oxidation rate of a PGX graphite specimen containing <100 ppm iron in He containing 0.63% H_2O + 6.3% H_2.

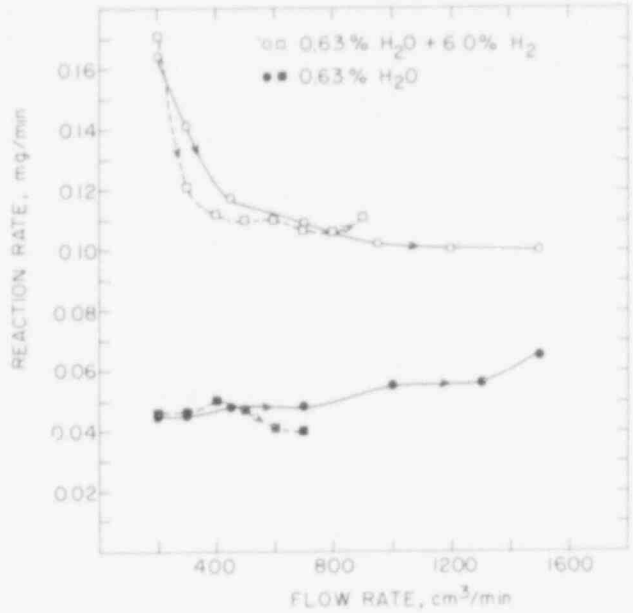

Figure 2.24. The effect of flow rate on the oxidation rate of a PGX graphite containing <100 ppm iron.

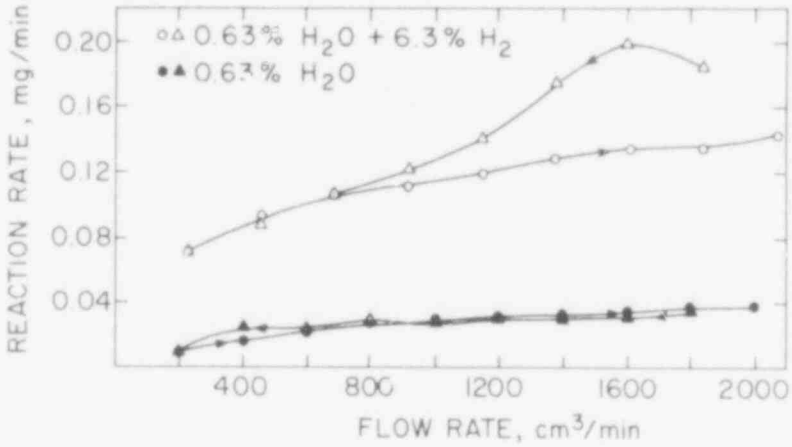

Figure 2.25. The effect of flow rate on the oxidation rate of a PGX graphite specimen containing ~400 ppm iron.

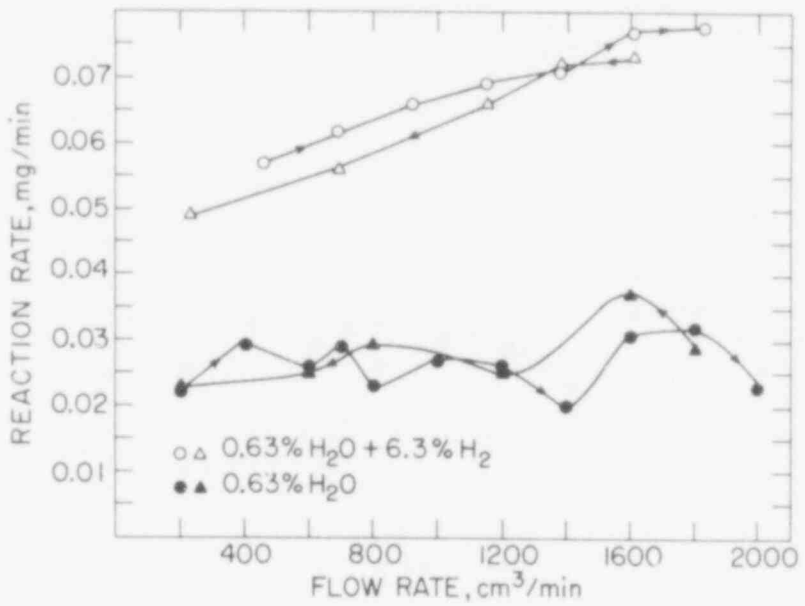

Figure 2.26. The effect of flow rate on the oxidation rate of a PGX graphite specimen containing >1000 ppm iron.

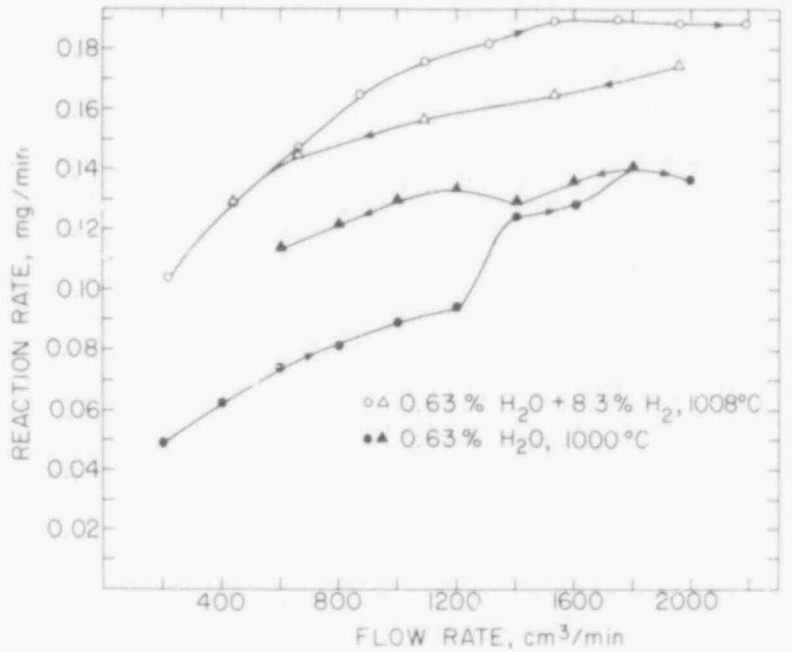

Figure 2.27. The effect of flow rate on the oxidation rate of a H451 graphite specimen.

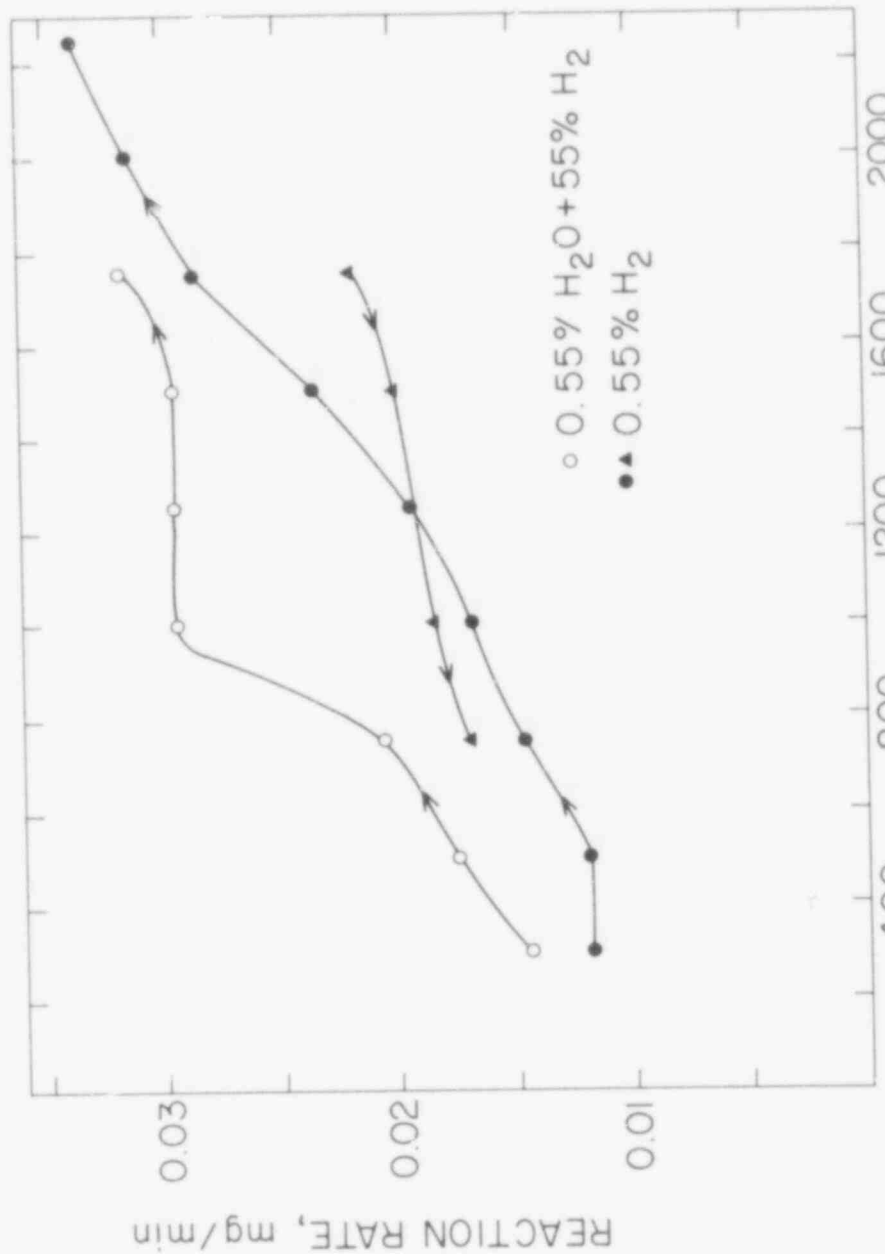

Figure 2.28. The effect of flow rate on the oxidation rate of a H451 graphite specimen.

similar studies (Kubaschewski, 1976 and Thrower, 1977), the results from the original study (Krefeld, 1973) are potentially significant enough so that an exhaustive investigation seems worthwhile.

Two new tasks were added this quarter: investigation of PGX graphite strength loss in non-oxidizing gaseous environments and the effects of tensile and compressive prestresses on oxidation rate and ultimate tensile and compressive strengths of PGX graphite.

2.7.1 Oxidation Kinetics of PGX Graphite

The effect of burnoff on the oxidation rate of an axial PGX graphite specimen obtained from the midlength (ML) of BNL log 2 was determined by thermogravimetry. The specimen was shown to contain <100 ppm iron by Mossbauer spectroscopy. It was exposed to 0.63% H_2O + 6.3% H_2 in He at a total flow rate of 1500 cm^3/min. Data were obtained at increments of ~0.08% burnoff. The results are shown in Figure 2.23. The oxidation rate is observed to decrease with increasing burnoff up to ~10% over the temperature span 700-778°C. This result is contrary to previous observations wherein the oxidation rate increased with burnoff (Growcock, 1977). The effect of burnoff on reaction rate has often been attributed to the process of pore development. However, it is difficult to explain the data in Figure 2.23 in these terms. Workers at General Atomic have, on occasion, obtained results similar to the above, which they ascribe to slow adsorption of hydrogen onto active sites (GA, 1978). This phenomenon has been observed by the same workers with H327 and H451 graphites. An alternative explanation is the slow reduction of catalytically active metal oxide impurities. Insufficient information at this time precludes further discussion of the phenomenon. It should be noted also that the oxidation rate data in Figure 2.23 exhibit some erratic behavior. This is consistent with previous observations of oscillatory rate behavior during the oxidation of PGX graphite.

The effect of flow rate on the oxidation rate of PGX graphite was also investigated thermogravimetrically. The results are given in Figures 2.24 to 2.26 for specimens containing <100 ppm to >1000 ppm iron. Similarly obtained plots for H451 graphite specimens are shown in Figure 2.27 and 2.28. Although smooth curves are drawn through the data, no functional relationship is assumed. The curves generated with added H_2 were obtained after those without added H_2. The arrows indicate the direction in which the flow rate was changed.

The large hysteresis observed for some of the runs was not expected. The overall trends, however, follow the presumption that at a sufficiently high flow rate the rate of weight loss should approach a constant value corresponding to a negligible reduction in the reactant concentration. The curves with added H_2 displayed in Figure 2.24, however, show the same kind of trend as that obtained with burnoff in Figure 2.23. The oscillatory behavior noted previously appears in the run without added H_2 in Figure 2.26. All the PGX graphite runs were obtained with specimens at relatively large burnoffs (>5%), whereas the H451 graphite runs were obtained at burnoffs of ≤1%. The H_2O run with the first H451 specimen (Figure 2.27) showed two abrupt increases in the reaction rate during the course of the experiment, which we cannot explain. The runs with the second H451 specimen (Figure 2.28) gave rise to a continuously increasing

oxidation rate with increasing flow rate. Again, we are without explanation. Such an effect has, however, been observed by others (Blakely, 1965 and Burnette, 1978) for ATJ and H327 graphites, respectively. The curve with added H_2 in Figure 2.28 is higher than the curve generated in the absence of added H_2. This appears to be contrary to the expected inhibitory effect of H_2. However, measurements obtained at 1750 cm^3/min. at the end of the experiment gave reaction rates of 0.0316 mg/min. with added H_2 compared to 0.0406 in the absence of added H_2. The apparent discrepancy of these curves can probably be ascribed to the effect of burnoff.

2.7.2 Removal of Iron from Impure Graphites

Samples of PGX graphite containing <100 ppm iron were ground and sieved to <50 μm diameter particles, homogeneously blended with reduced iron powder of similar size and pressed into 1/4 inch thick pellets. It was found that exposure to ~0.1 torr I_2 in He at 750°C for 24 hours was sufficient to decrease the iron concentration in a 40% iron specimen to <100 ppm, while that of a 10% iron specimen was decreased to ~0.1% and that of a 0.2% iron specimen was decreased to ~0.1%. The increasing difficulty in removing iron from specimens containing progressively lower amounts of iron can be attributed to the potential for forming a lamellar compound of graphite, iron and iodine. An unknown spectrum was clearly observed after exposure of the 0.2% iron specimen to I_2, while it was definitely absent in the case of the 40% iron specimen. In specimens containing large amounts of iron, the atom ratio C/Fe may be so low as to preclude the C-C bonding necessary to form a lamellar compound. Additionally, removal of iron is facilitated as the reaction progresses due to the open porosity brought about by removal of the iron; this effect is expected to become pronounced at high concentrations of iron.

The difficulty in reproducing the unknown spectrum with iron-rich specimens leads to difficulty in identification of the species. X-ray diffraction usually requires a sample which is concentrated to $\geq$5%. Consequently, methods are being sought to separate graphite from the supposedly lamellar compound. It should be noted that there are no published reports of the existence of graphite-iron-iodine lamellar compounds, whereas extensive documentation is available on fluorine and chlorine compounds.

2.7.3 The Effect of Oxidation on the Ultimate Compressive Strength of PGX Graphite

A new flow system has been designed to study the effect of burnoff on the ultimate compressive strength of graphites. It is hoped that a similar design can be used in the 5 foot long, 4 inch I.D. tube furnace whose arrival is awaited.

Three right cylindrical 1.5 inch diameter times 3.0 inch length graphite specimens are suspended end-to-end in a 2 inch quartz tube within a resistance furnace. A preheater raises the temperature of the gas to the inlet furnace temperature. Flow rates as high as 50 liters/min. can be accommodated before the temperature profile along the specimens is significantly affected. Axial ML specimens from BNL log 2 have been found to have reactivities at least an order of magnitude greater than those used previously from BNL log 1 (Growcock, 1978b). To minimize secondary reactions and conversion of H_2O, reaction temperatures

will necessarily be limited to <900°C.

Preliminary oxidations have been done on several specimens at 850°C using 0.07% H_2O + 0.7% H_2 in He. Inspection of the specimens revealed the absence of large pits; indeed, they appear to exhibit uniform surface burnoff. Experiments will be done at several temperatures and H_2O concentrations, with H_2/H_2O = 10-20. Reaction rates will be monitored by intermittent analyses of the product gases via gas chromatography. Weight and compressive strength of oxidized specimens will be determined. One series of specimens will be machined to >2 times "L" (expected diffusion length) and subsequently compression tested.

2.7.4 Effect of High Temperature Exposure of PGX Graphite to Non-Oxidizing Gases

Loss of bulk material during the oxidation of PGX graphite under presumed diffusion-limited conditions may occur via wormholing. Alternatively, oxidized metallic impurities distributed in the bulk of the graphite may be reduced by the graphite and H_2/CO yielding H_2O and CO_2, which can oxidize the graphite itself. Further loss of bulk material may occur from the desorption of CO and CO_2. Experiments are now under way to test these possibilities.

The first series of experiments involve axial ML PGX graphite specimens from BNL log 2. Three sizes of right cylindrical specimens are being used: 0.75 inch diameter times 1.5 inch length, 1.5 inch diameter times 3.0 inch length and 3.0 inch diameter times 3.0 inch length. These are exposed to a static purified He environment at 900-1000°C until the $H_2/CO/CO_2$ partial pressures are constant; the specimen weight loss is determined followed by measurement of ultimate compressive strength. In some cases specimens are exposed to several cycles of quenching, air refill, evacuation, helium refill and heating. Specimens will be weighed and compression tested at the end of the experiment. In the second series of experiments the procedure will be identical, but H_2/He mixtures will be substituted for pure He.

A manifolded vacuum station designed for $<10^{-6}$ torr has been built for interfacing the reactors to a mass spectrometer. The latter is to be used for all gas analyses. It is now operational and has been modified for these experiments. Results should be forthcoming soon.

2.7.5 The Effect of Compressive Prestresses on the Ultimate Compressive Strength of PGX Graphite

The impetus for this study came from the unpublished work of Imai and Sasaki of JAERI (1978). They prestressed samples of H327 grahite under compression up to 0.9 x σ_c and oxidized the specimens in air. At 430°C the reaction rate of a prestressed specimen was several times greater than that of virgin material; however, the effect became less pronounced with increasing temperature and disappeared above 590°C. Annealing at 1000°C after prestressing did not change this result, though annealing at 2000°C eliminated the effect.

Concern about this effect in HTGR graphites exposed to He containing H_2O and H_2 impurities has prompted a similar study with PGX graphite. However, the low reactivity of H_2O compared to air precludes using reaction temperatures

below 600°C in short term experiments. Since the interest lies in the effect of prestress on strength, oxidation rate is not being measured in preliminary tests, only ultimate compressive strength, σ_c.

Currently, 0.75 inch diameter times 1.5 inch length right cylindrical axial ML specimens from BNL log 2 are being exposed to prestresses up to 0.75 σ_c at 0.1 in./min. Total dimensional changes observed are several tenths of one percent. The specimens are oxidized (in the chemical reaction controlled regime) at 670°C with 2% H_2O + 20% H_2 in He flowing at 300 cm^3/min. Five specimens are oxidized at once in the same tube furnace; these are periodically removed, weighed and repositioned in the opposite order to average out any temperature gradient and H_2O conversion effects. The results to date are shown in Figure 2.29. No effect from prestressing PGX graphite up to 0.75 σ_c is observed. It should also be noted that no effect of prestressing on the average rate of weight loss has been observed either. Measurements up to 10% burnoff will be obtained soon.

2.8 Instrumentation and Control Systems (G. Uneberg)

The Nuclide Corporation mass spectrometer was installed at BNL this quarter. Acceptance testing has been completed and modifications to the inlet system are under way. A loss of power to the mass spectrometer during an outage in December caused pump oils to be backstreamed into the instrument. This caused some delay in the planned incorporation of the mass spectrometer into the graphite oxidation program.

Future reporting on the mass spectrometer will henceforth be described in the section on graphite oxidation.

PUBLICATIONS

ARONSON, S., et al., "Effect of Fission Product Interactions on the Corrosion and Mechanical Properties of HTGR Alloys," BNL-NUREG-25325, in Proc. of U.S.-Japan Seminar on HTGR Safety Technology, Fuji, Japan, November 24-25, 1978, Vol. III.

CHOW, J. G. Y., SOO, P. and EPEL, L., "Creep and Fatigue of Incoloy-800H in a High Temperature Gas Cooled Reactor (HTGR) Helium Environment," in Alloy 800, Proc. of the Petten International Conference, The Netherlands, March 1978, North Holland Publishing Co., 1979, pp. 331-36

CHOW, J. G. Y., SOO, P. and SABATINI, R., "The Effect of a Helium Environment on the Mechanical Properties of HTGR Primary System Metals," BNL-NUREG-25326, in Proc. of U.S.-Japan Seminar on HTGR Safety Technology, Fuji, Japan, November 24-25, 1978, Vol. III.

EPEL, L. G. and SCHWEITZER, D. G., "Chemical Reactions in the Helium Impurities Loop," BNL-NUREG-25324, in Proc. of U.S.-Japan Seminar on HTGR Safety Technology, Fuji, Japan, November 24-25, 1978, Vol. II.

GROWCOCK, F. B. and SKALYO, J., Jr., "Role of Impurity Iron in the Oxidation of PGX Graphite," American Ceramic Society 31st Pacific Coast Regional Meeting, San Diego, California, October 25-27, 1978 (copy of paper appears in

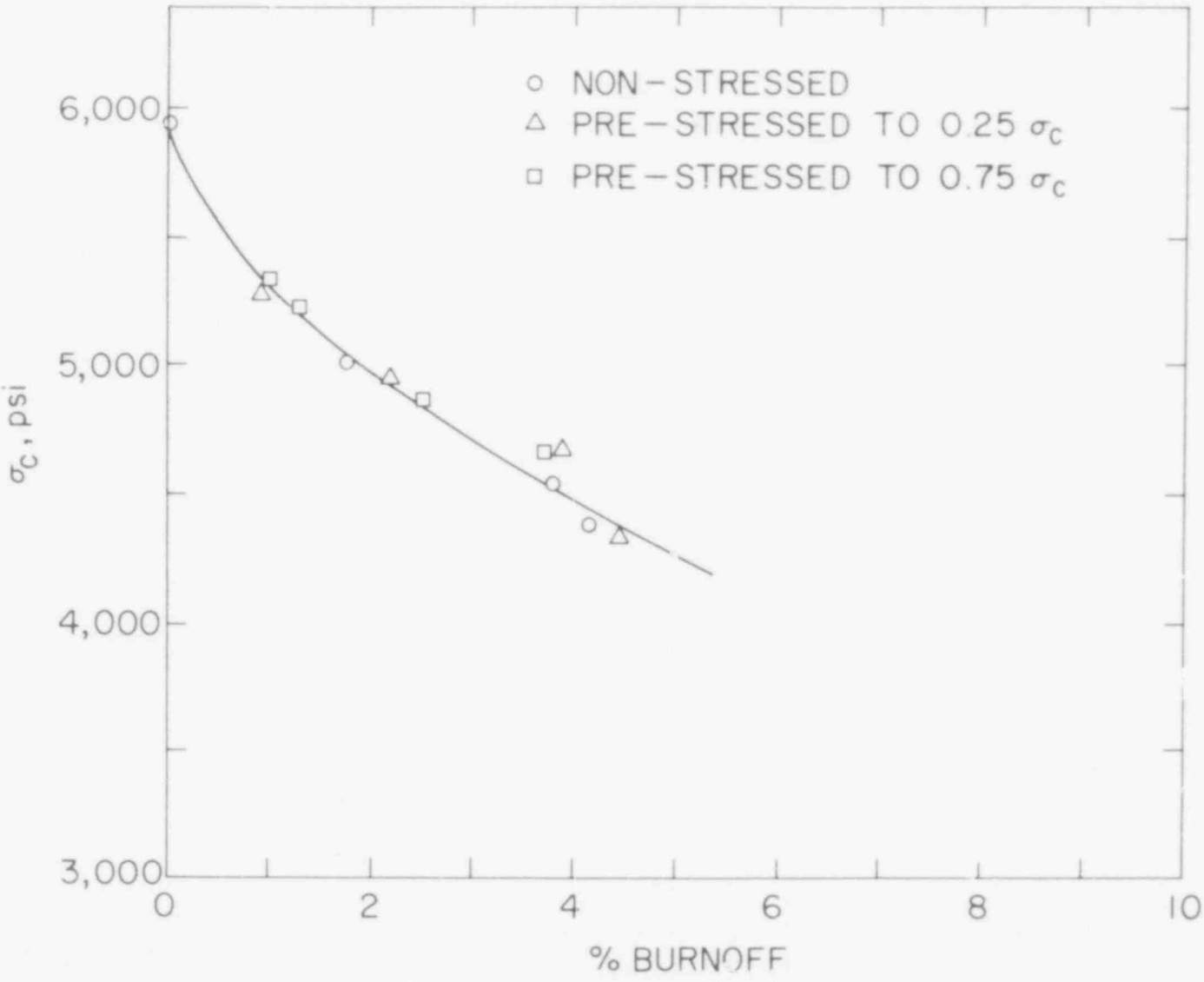

Figure 2.29. The effect of burnoff on the ultimate compressive strength of prestressed PGX graphite.

Fachinformationzentrum Energie, Physik, Mathematik GmbH).

GROWCOCK, F. B., et al., "Graphite Oxidation by Moisture," BNL-NUREG-25327, in Proc. of U.S.-Japan Seminar on HTGR Safety Technology, Fuji, Japan, November 24-25, 1978, Vol. II.

SOO, P. and CHOW, J. G. Y., "Correlation of Low-Cycle and High-Cycle Fatigue Data for Solution Annealed Incoloy-800," in Ailoy 800, Proc. of the Petten International Conference, The Netherlands, March 1978, North Holland Publishing Co., 1979, pp. 169-74.

SOO, P. and CHOW, J. G. Y., "Correlation of High Cycle and Low Cycle Fatigue Data for Some HTGR Structural Metals," BNL-NUREG-25333, in Proc. of the U.S.-Japan Seminar on HTGR Safety Technology, Fuji, Japan, November 24-25, 1978, Vol. III.

SOO, P. and CHOW, J. G. Y., "The Effect of Mean Tensile Stresses on the High Cycle Fatigue of Quenched and Tempered Type 422 Stainless Steel," BNL-NUREG-25332, in Proc. U.S.-Japan Seminar on HTGR Safety Technology, Fuji, Japan, November 24-25, 1978, Vol. III.

REFERENCES

BLAKELY, J. P. and OVERHOLZER, L. G., Carbon 3, 269 (1965).

BURNETTE, R. D., private communication.

DEKKER, R. F., "Strengthening Mechanisms in Nickel Base Superalloys," presented at The Steel Strengthening Mechanism Symposium, Zurich, Switzerland, May 5 and 6, 1969.

EPEL, L. G. and SCHWEITZER, D. G., "Chemical Reactions in the Helium Impurities Loop," BNL-NUREG-25324, Proc. of the U.S.-Japan Seminar on HTGR Safety Technology, Fuji, Japan, November 24-25, 1978, Vol. II.

GROWCOCK, F. B. and CHOW, J. G. Y., "Tensile Stress Corrosion of HTGR Graphites," Brookhaven National Laboratory Informal Report, BNL-NUREG-24672, July, 1978a.

GROWCOCK, F. B., "Characterization and Oxidation Kinetics of PGX Graphite," in Reactor Safety Research Programs Quarterly Progress Report, July 1-September 31, 1977, Brookhaven National Laboratory, BNL-NUREG-50747, December 1977.

GROWCOCK, F. B., SKALYO, J., Jr. and STEMP, L., "The Oxidation Kinetics of PGX Graphite," in Reactor Safety Research Programs Quarterly Progress Report, April 1-June 30, 1978, Brookhaven National Laboratory, BNL-NUREG-50883, August 1978b.

GURRY, R. W., "Composition of Atmospheres Inert to Heated Carbon Steel," Trans. AIME, Vol. 188, pp. 671-87, April 1950.

HTGR Generic Technology Programs Fuels and Core Development, Quarterly Progress Report for the period ending August 31, 1978, September, 1978, General Atomic Company, GA-A15093, UC77.

IMAI, H. and SASAKI, Y., Japan Atomic Energy Research Institute, Tokai-mura, Ibaraki-ken, Japan 319-11, private communication, December 10, 1978.

KREFELD, R., LINKENHEIL, G. and KARCHER, W., 11th Biennial Conf. on Carbon, 1973, Gatlinburg, Tennessee, ORNL-CONF-730601. KUBASCHEWSKI, preliminary report, KFA, Julich, Fed. Republic of Germany, October 22, 1976.

LYMAN, T., Editor, Metals Handbook, 8th Ed., Vol. 7, Amer. Soc. for Metals, 1972, p. 163.

NODA, T., et al., "Thermodynamic Analyses of Impure Helium for HTGR Material Testing," Proc. of U.S.-Japan Seminar on HTGR Safety Technology, Fuji, Japan, November 24-25, 1978.

SOO, P. CHOW, J. G. Y. and TIEFEL, T., "Fatigue of Structural Materials," in Reactor Safety Research Programs Quarterly Progress Report, April 1-June 30, 1978, BNL-NUREG-50883, August 1978, p. 41.

THROWER, P. A., "Studies of Mechanical Properties and Irradiation Damage Nucleation of HTGR Graphite," Pennsylvania State University, Progress Report, February 1, 1976 - January 31, 1977, ERDA Contract No. EY-76-5-02-2712.

3. Structural Evaluation

3.1 Core Seismic (J. Curreri, M. Subudhi, H. Goradia, P. Bezler, L. Lasker, M. Reich)

Construction of the three-dimensional vibrations test rig has been completed. The cross-sectional design of the apparatus is similar to that of the vertical array test rig. However, the three-dimensional aspects of the new design increase the complexity of the devices used to adjust dimensions that are to be varied. Testing with the new rig will commence shortly.

Two-dimensional analytical and test studies have established the general dynamic characteristics of vertical block arrays. This includes the conclusions reported in the last quarterly on the effects of a vertical preload and simultaneous horizontal and vertical excitations. Continuing these studies, we are presently performing an evaluation of the forces developed in a vertical block array subjected to a seismic excitation. The results will permit an assessment of the structural integrity of the core blocks and the relative importance of the clearance parameters used in the model.

A vertical block array consisting of three columns with nine blocks per column was used in the analysis. Each of the twenty-seven blocks has the three degrees of freedom consistent with the OSCVERT model. Clearance was provided between adjacent columns as well as between the columns and side walls. Each block has associated with it fourteen spring gap elements; two each per side, three each for the base and top surfaces, and four associated with the base and top surface dowel pins. The size of the array is almost half of the size of the maximum array we anticipate evaluating in a complete analysis (seven columns of nine blocks each). Program output includes a time history trace of each of the spring forces for each block, thereby enabling a detailed assessment of the block force dynamics.

The time excitation in the horizontal direction was decomposed from the spectral plot shown in Figure 3.1. On this figure the asterisk symbols depict the target spectrum while the numeral 1 indicates the spectrum of the acceptable time decomposition obtained after three iterations with the SIMEAR Code. Two separate analyses were made with the excitation being only vertical in one run and only horizontal in the second.

For each run the duration of the event was one second. Printouts of force were made for every 0.01 seconds. For the horizontal excitation run, the computer usage was 180 seconds.

Vertical excitation was found to produce only vertically acting forces of smaller magnitude than those induced by the horizontal excitation. Typical force time history traces generated in the horizontal run are shown in Figures 3.2a and 3.2b. Figure 3.2a depicts the force acting on the bottom surface dowel pin of the second block from the top of the right-most column. Figure 3.2b depicts the force acting on the upper dowel pin of that block. We are continuing to refine the output graphics so as to report the maximum forces on each block for any excitation.

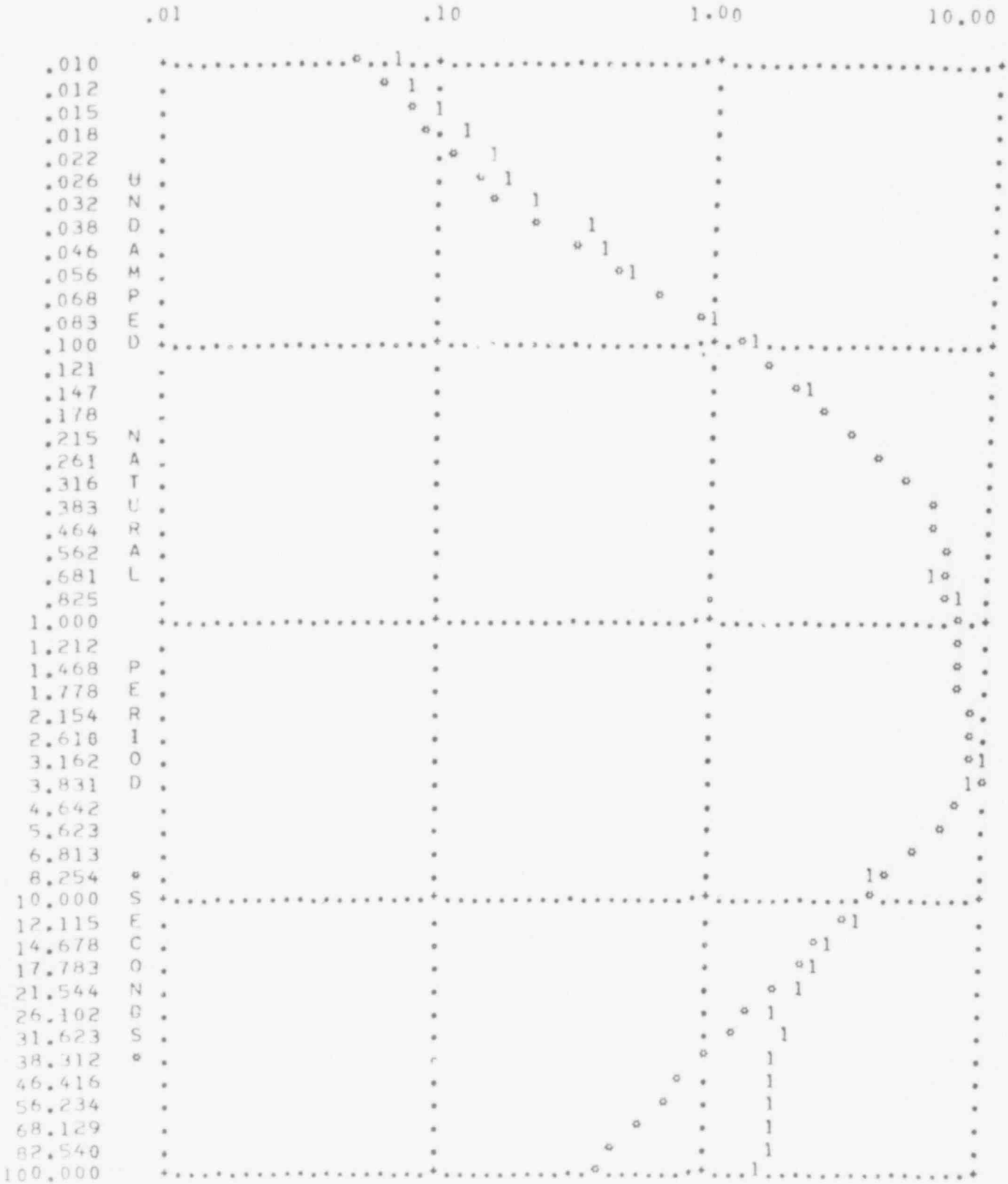

Figure 3.1. Spectrum - horizontal excitation

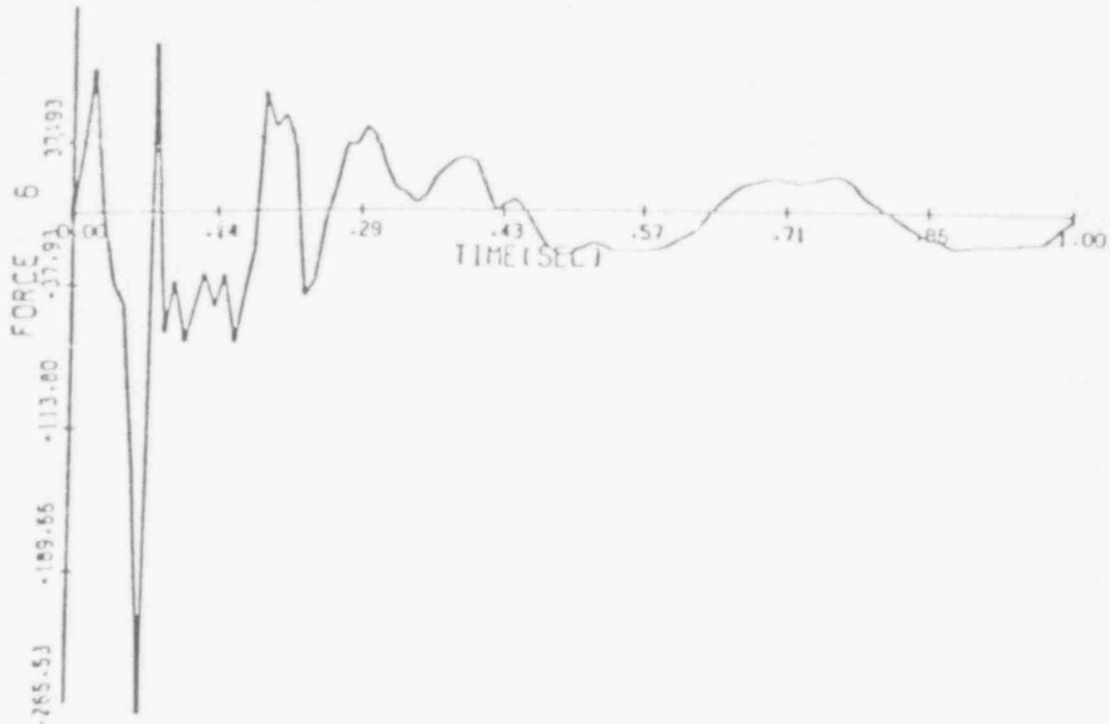

Figure 3.2a. Bottom surface dowel pin force

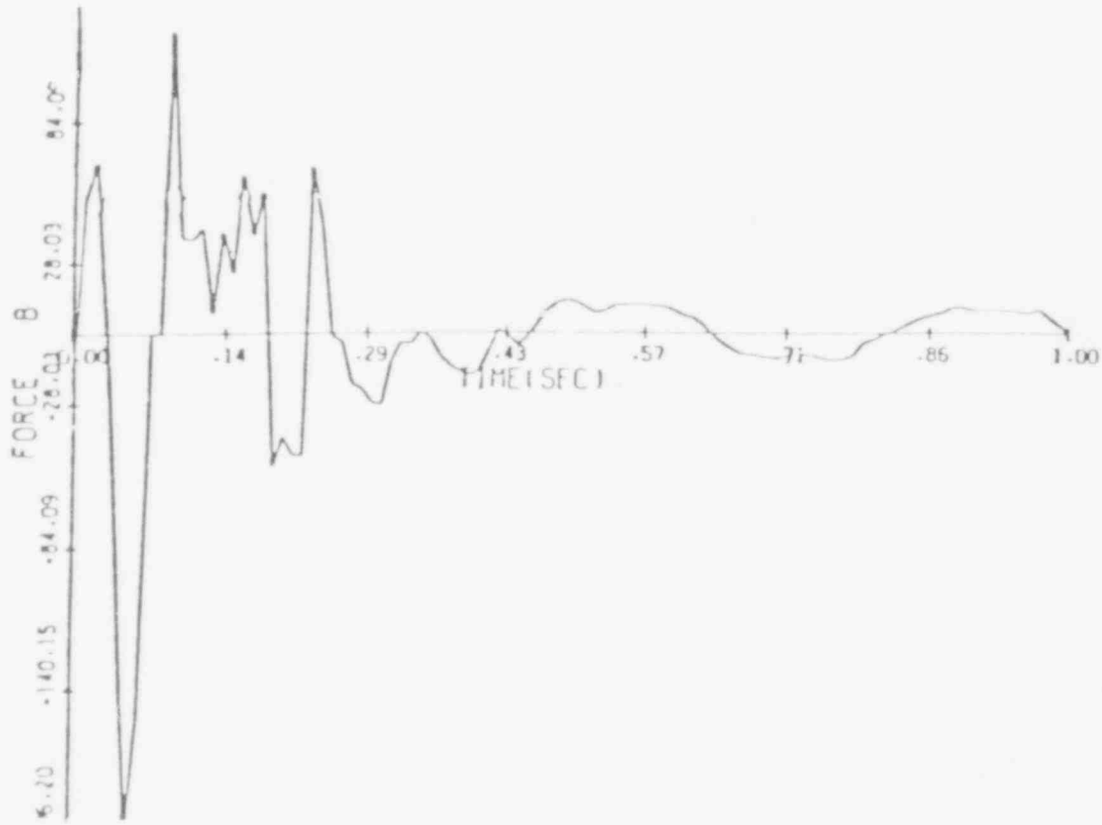

Figure 3.2b. Upper surface dowel pin force

3.2 Development of OSC3D Computer Code

The development, debugging, and proof-testing of the program OSC3D continues. The analytical study is directed towards an investigation of the nonlinear response of the reactor core blocks in the event of a seismic occurrence. The computer code is developed for a specific mathematical model which represents a vertical arrangement of layers of blocks as shown in Figure 3.3. This comprises a "block module" of core elements which would be obtained by cutting a cylindrical portion consisting of seven fuel blocks per layer. It is anticipated that a number of such modules properly arranged could represent the entire core. Hence, the predicted response of this module would exhibit the response characteristics of the core.

The basic block element employed is a finite discrete mass having five degrees of freedom, rotations about the vertical axis being excluded. The governing equations for each mass contain terms from the inertia effect, the restoring forces, and the surrounding wall input forces. This program sets up five second order ordinary differential equations for each mass, which are further broken into ten first order ODE's. The GEAR, multistep integration package for stiff ODE, is used for solving these equations.

A basic force algorithm is written for vertical force and for horizontal plane forces for a typical layer of blocks. Each layer of seven hexagonal blocks is arranged with one in the center surrounded by the remaining six. The entire module is contained in an eighteen-faced constraint wall. The wall can move with any assigned input history.

In any horizontal layer, as shown in Figure 3.4, there are sixty separate surfaces for potential contact between two adjacent surfaces. When such contact occurs, the blocks involved experience a compressive force between them. Since this force is equal and opposite in nature, it need not be calculated twice for individual surface points of contact whenever two adjacent blocks are involved. Each block face is simulated by two gapped-restoring elements attached at the top and bottom ends of the block. These restoring elements are arranged among the seven blocks in such a way that for any layer there exist thirty independent interelement forces to be calculated at each end of the block. In the case of vertical forces, each block has six vertical restoring elements at the six corner points. It should be noted that each restoring element has gap elements in the spring and exhibits only compressive action.

The presently operational version of the code is suitable for systems without dowel pins. For such systems, the results obtained with OSC3D were compared with those obtained from the two-dimensional code OSCVERT. As may be inferred from Figure 3.4, a wall motion on the flat side of a one layer, three-dimensional model may be simulated with a one layer, two-dimensional model of three blocks subjected to horizontal excitation. That is, block elements 3, 7, and 6 of the three-dimensional model should exhibit nearly the same response motions of the three elements of the two-dimensional model.

The results obtained for just such comparative runs are shown in Figure 3.5. For these runs, the input forcing function was horizontal sinusoidal wall motion

as shown in the upper curve. As can be seen from the lower curves, the response characteristics are indeed similar. The slight differences between the response motions are felt to be due to the coupling that occurs from elements 1, 2, 4, and 5 in the three-dimensional array. The nature of the spacial coupling that results for horizontal and vertical excitation for both single layer and multilayer systems are under consideration for future studies.

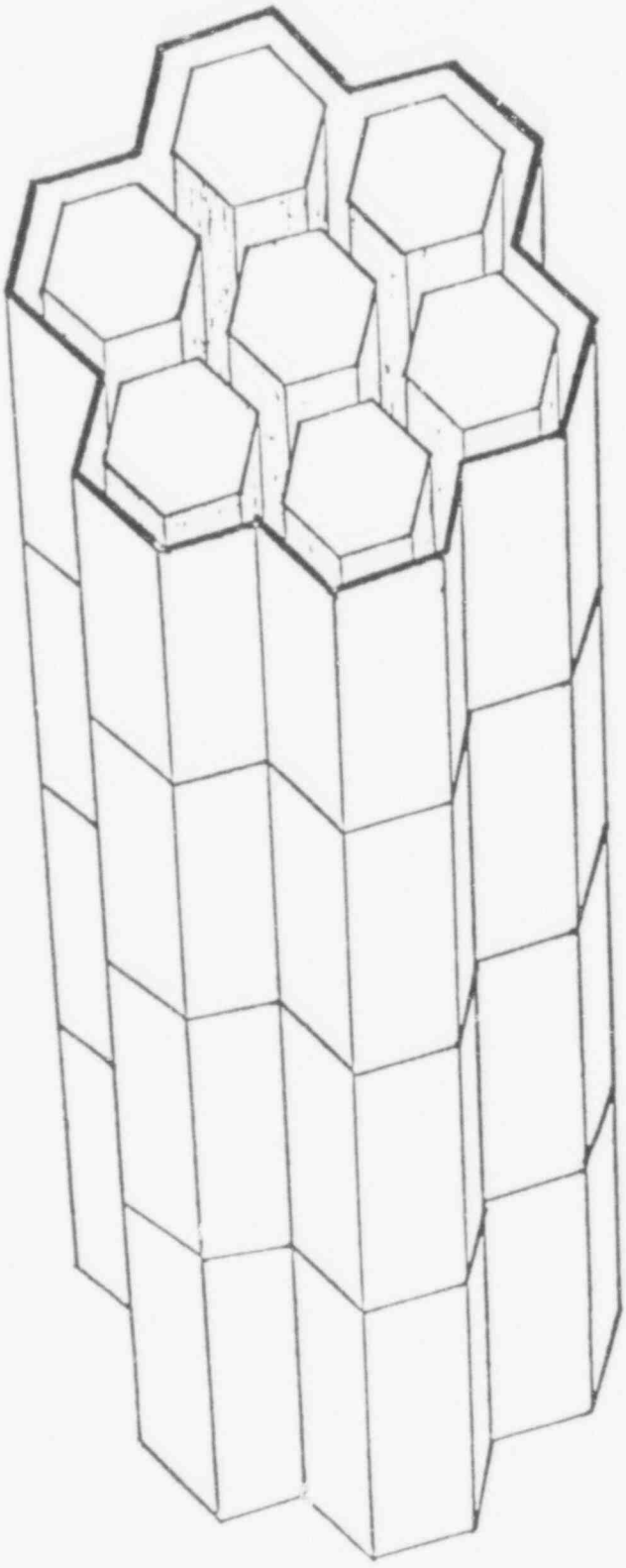

Figure 3.3. A block module of four layers

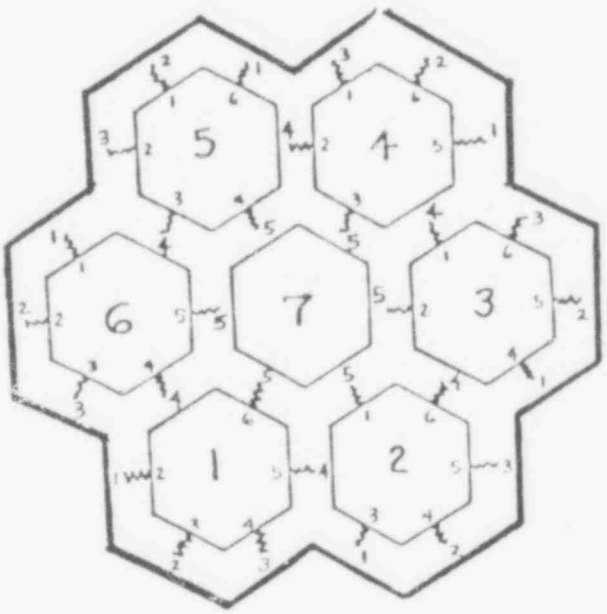

Figure 3.4. Horizontal arrangement of blocks with restoring elements

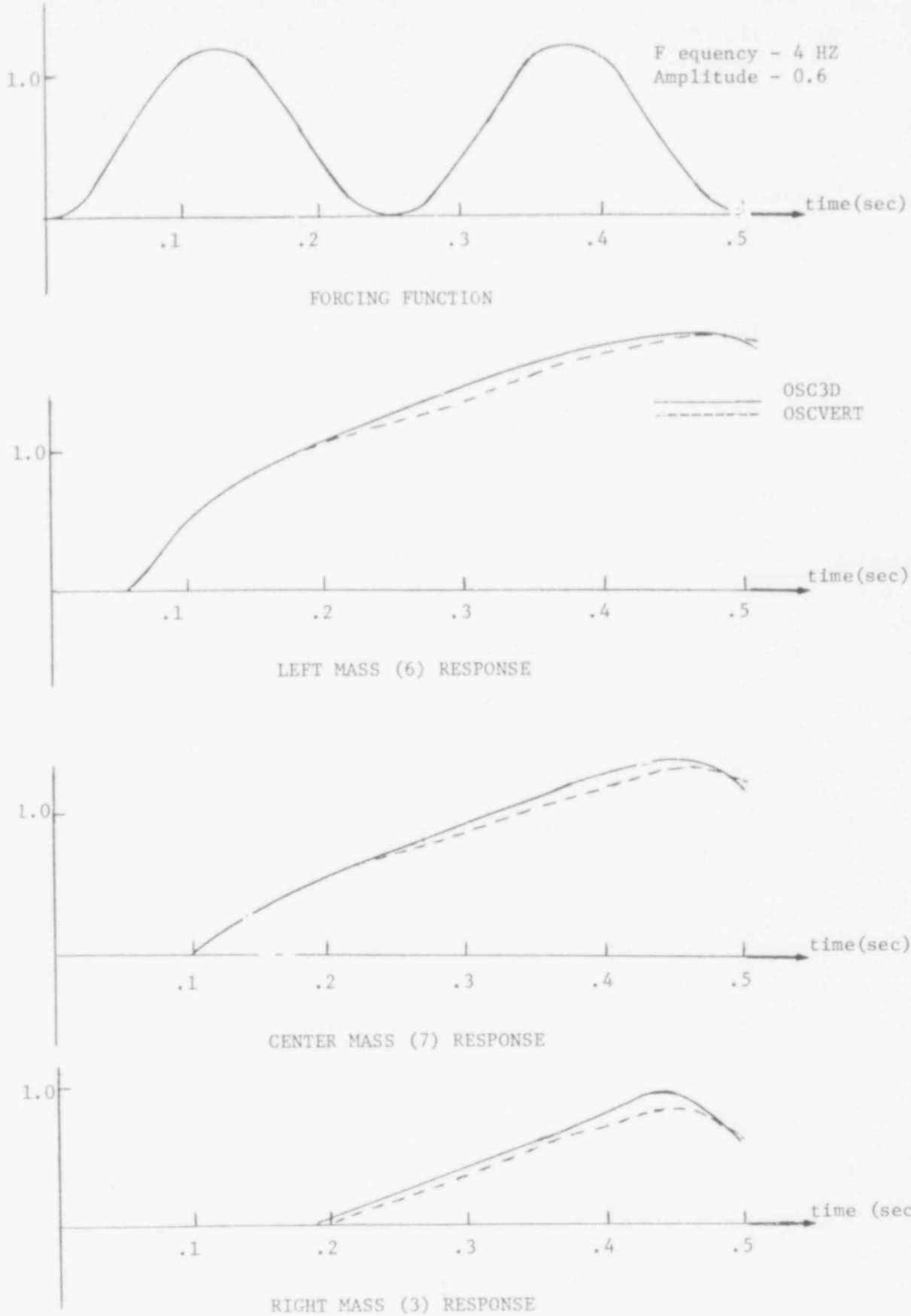

Figure 3.5. One, layer response, 2-D and 3-D models

PUBLICATIONS

The following is a list of publications during the current reporting period from this activity:

BEZLER, P., CURRERI, J., "HTGR Core Model Response to Simultaneous Horizontal and Vertical Excitations," Presented at the U.S.-Japan Seminar on HTGR Safety Technology, Volume IV, Fuji, Japan, November 24-25, 1978.

4. Analytical

4.1 HTGR Code Library

The LARC-2 code from Los Alamos is being converted to run at BNL and should be available for use shortly. However, at this time the plotting capabilities have been deleted and it will take more time to rewrite that section of the code for the BNL plotters.

The new version of the Los Alamos code CHAP has been received at BNL and conversion work has begun. However, we understand from LASL that this is not a final form of the code and that sections are to be replaced in the near future. In addition, two modules of the code are not available from LASL as yet. We have, so far, extracted the updated LASAN subset code from CHAP and converted that to run satisfactorily (apart from one feature) on the BNL system. The complete CHAP code will not fit on the BNL system and it may be necessary to wait until LASL releases the overlaid version of the code before work can continue at BNL.

Table 4.1 is a listing of our HTGR Safety Code Library to date.

4.2 Containment Vessel Gas Dynamics (J. Boccio)

During this period the project work has continued on both analytical and experimental investigation of containment vessel response to sudden depressurizations.

The experimental program and test apparatus, described in the January 1978 quarterly (Boccio, 1978a), has stressed the following during this reporting period:

- Effects on model containment vessel size on the overall mixing process.
- Effects of the jet impingement region geometry on the overall mixing process (region 2 in Figure 4.7 in above cited reference).
- Gas composition measurements.

To date, gaseous discharge within four containment vessel configurations have been observed, viz:

- CV #1: 18 in. diameter/18 in. high bell jar
- CV #2: 18 in. diameter/30 in. high bell jar
- CV #3: 18 in. diameter/18 in. high cylindrical chamber
- CV #4: 12 in. diameter/12 in. high cylindrical chamber.

Under similar test conditions visual observations made in the above four chambers, when selectively compared, were used to study the following effects:

Table 4.1

HTGR Safety Code Library

Program	Status	Proprietary	Function
CRECT	OP	NP	Corrects data on ENDF/B tape.
LISTFC	OP	NP	Lists data from ENDF/B tape.
RIGEL	OP	NP	Manipulates data on ENDF/B tape.
ENDFB2	OP	NP	Converts data on ENDF/B tape to binary.
FLANGE	OP	NP	Prepares thermal cross section transfer arrays.
GAND2	OP	NP	Prepares fine group fast, resonance, and thermal cross sections from ENDFB2 binary tapes.
GFE2	OP	NP	Prepares fine group fast cross sections from ENDFB2 binary tapes.
MAKE	OP	NP	Prepares fine group fast cross section tape from GFE2 for spectrum codes.
WTFG	OP	NP	Prepares fine group thermal cross section tape from GAND2 or FLANGE for spectrum codes.
PRINT	OP	NP	Reads the fast cross section tape produced by MAKE.
SPRINT	OP	NP	Reads the thermal cross section tape produced by WTFG.
GGC4	OP	NP	Prepares broad group cross sections from MAKE and WTFG tapes.
INTERP	OP	NP	Prepares broad group cross sections from MICROX output data tapes.
1-DX	OP	NP	Performs one-dimensional, diffusion theory, steady state calculations.

C = In the process of being converted to the CDC 7600.
OP = Operational on the BNL CDC 7600 system under Scope 2.
R = Recently received from General Atomic Co. or Argonne Code Center.
P = General Atomic Co. proprietary code.
NP = Not considered to be a proprietary code.
B = In the process of development at Brookhaven National Laboratory.
L = Recently received from Los Alamos Scientific Laboratory.
I = Inactive.

Table 4.1 Cont'd.

Program	Status	Proprietary	Function
FEVER-7	OP	NP	Performs one-dimensional, diffusion theory, burnup and reload calculations.
TEMCO-7	OP	NP	Computes reactor temperature coefficients from input cross section data.
BLOOST-7	OP	NP	Performs zero-dimensional reactor kinetics calculations.
GAKIT	OP	NP	Performs one-dimensional reactor kinetics calculations.
TWIGL	OP	NP	Performs two-dimensional light water reactor kinetics calculations.
TAC-2D	OP	NP	Performs two-dimensional, transient conduction analyses.
FLAC	OP	NP	Calculates steady state flow distributions in arbitrary networks with heat addition.
POKE	OP	P	Calculates steady state flow distributions and fuel and coolant temperatures in a gas cooled reactor.
PREPRO	OP	P	Prepares input data and source code revisions for RECA code.
RECA	I	P	Calculates time dependent flow distributions and fuel and coolant temperatures in the primary system.
CORCON	OP	P	Computes the temperature history and fission product redistribution following a loss of all convective cooling of the core.
SORSD	OP	P	Computes the release of volatile fission products from an HTGR core during thermal transients.
COPTWO	OP	NP	Analyzes the steady state graphite burnoff and the primary circuit levels of impurities.
OXIDE-3	OP	P	Analyzes the transient response of the HTGR fuel and moderator to an oxidizing environment.
SAMPLE	OP	NP	Propagates uncertainties in probability distributions by Monte Carlo technique.

Table 4.1 Cont'd.

Program	Status	Proprietary	Function
TAP	OP	P	Calculates the transient behavior of the integrated HTGR power plant.
SORSG	OP	P	Computes the release of non-volatile gaseous fission products from an HTGR core during thermal transients.
DIFFTA	OP	NP	Solves the steady state, two-dimensional diffusion equation by finite element method.
DIFFT1	OP	NP	Solves the time dependent, 2-D diffusion equation by the finite element method.
PDQ-7	OP	NP	Analyzes reactors in up to three space dimensions via diffusion theory.
SOSNCC	OP	NP	Calculates steady state natural convection flow rates during long term loss of power.
OSCIL	OP	NP	Simulates one-dimensional spring mass system for seismic analysis of HTGR core.
H-CON1	OP	NP	Calculates one-dimensional heat conduction for an HTGR fuel pin by finite difference method.
HYDRA-1	OP	NP	Computes thermal/hydraulic parameters for single phase liquid due to external heat source.
CONTEMPT-G	OP	P	Simulates temperature-pressure response of an HTGR containment atmosphere to postulated coolant circuit depressurization.
SOSSME	OP	NP	Solves the steady state one-dimensional momentum equation.
HAZARD	OP	NP	Analyzes gas layering and flammability in an HTGR containment vessel following a depressurization accident.
CIRC (formerly JETS)	OP	NP	Calculates fluid dynamics in an HTGR containment vessel following a depressurization accident.

Table 4.1 Cont'd.

Program	Status	Proprietary	Function
ORIGEN	OP	NP	Solves the equation of radioactive growth and decay for large numbers of isotopes with arbitrary coupling.
MOSBDA	OP	NP	Analyzes experimental data from Mössbauer spectrometer.
INREM	OP	NP	Calculates internal radiation doses.
EXREM	OP	NP	Calculates external radiation doses.
SODEMME	OP	NP	Calculates transient thermal hydraulic aspects of circulating gas systems.
KACHINA	OP	NP	Calculates fully interpenetrating fluid flows using Implicit Multifield (IMF) method, for handling different material fields.
SWIRL-S	OP	NP	Calculates fluid dynamics for two-dimensional steady state recirculating flows.
SWIRL-T	B	NP	Calculates fluid dynamics for two-dimensional time-dependent recirculating flows.
CHAP-1 (Jan. 1978)	OP	NP	Simulates the overall HTGR plant with both steady state and transient solution capabilities.
EVAP	OP	NP	Calculates evaporation and redistribution of fission products during a temperature transient.
BAAL	OP	NP	Calculates three-dimensional fluid flows at all speeds with an Eulerian-Lagrangian computing mesh.
LEAF	L	NP	Calculates fission product release from a reactor containment building.
SUVIUS	L	NP	Solves the behavior of fission gases in the primary coolant of a gas-cooled reactor.
FYSMOD	L	NP	Calculates the two-dimensional solution of HTGR core blocks subjected to external motion.
NONSAP-C	L	NP	Calculates static and dynamic response of three-dimensional reinforced concrete structures, in addition to creep behavior.

Table 4.1 Cont'd.

Program	Status	Proprietary	Function
LARC-1	C	NP	Calculates fission product release from BISO and TRISO fuel particles of an HTGR during the LOFC accident for single isotopes.
LARC-2	C	NP	Similar to LARC-1; in addition, handles release from isotope chains.
QUIL/QUIC	OP/C	NP	Solve complex equilibrium distributions in chemical environments.
FENG, RATE and SURF	OP	NP	Three codes which create or add to the reactions data library for QUIL and QUIC codes. Reactions added are of types Free Energy, Rate and Surface, respectively.
RICE	OP	NP	Solves transient Navier-Stokes equations in chemically reactive flows.
THGRAF	OP	NP	Calculates position and velocity of the thermochromatograph as a function of time for various models.
FPPROD	OP	NP	Performs simplified fission product production analysis.
LASAN-LASL	I	NP	A general systems analysis code consisting of a model independent systems analysis framework with steady state, transient and frequency response solution capabilities. There are two versions of the code available - the original LASL version and the converted BNL version.
LASAN-BNL	OP	NP	
CHAP-2 (Dec. 1978)	C	NP	Simulates the overall HTGR plant with both steady state and transient solution capabilities.

- CV #1/CV #2: Effects of Reynolds number based upon chamber length to the global mixing pattern.
- CV #1/CV #3: Effects of the jet impingement region geometry to the global mixing pattern.
- CV #3/CV #4: Effect of overall chamber size to the global mixing pattern.

Thus far visual observations made in the NH_3Cl seeded SF_6/He mixture could not show any noticeable differences of the effects of CV external geometry on overall stratification. That is stratification has been only observed at pressure ratios of 10 or lower, regardless of CV shape. Effects of containment vessel size and external geometry had only subtle effects on the mixing pattern which did not affect substantially the overall degree of final stratification. However, an order of magnitude change in scale size has not been tried, these observations must be considered as tentative.

Gas sampling within the CV #2 configuration has also been initiated during this reporting period. Gas samples were collected at several off axis locations within the vessel and at several pressure ratios. During one test run, two probes consisting simply of 1/8 inch steel tubing were inserted at various heights (% L) above the base plate -- one probe offset from the axis by 50%; the other by 75%. The gas collected in 100 ml sample bottles were then analyzed using a mass spectrometer. The table below, summarizing the data thus obtained, presents the mole fractions of helium (X_{He}) and sulfur hexafluoride (X_{SF_6}) in the SF_6/He mixture at four different heights (ℓ_1=0.75 L, ℓ_2=0.50 L, ℓ_3=0.25 L, ℓ_4=0.10 L) for three different He/SF_6 initial pressure ratios (P_{RV}/P_{CV}):

Pressure Ratio (psia/psia)		Probe Height				
(P_{RV}/P_{CV})		ℓ_1	ℓ_2	ℓ_3	ℓ_4	
(165/5)	$SF_6(X)$	.60	.61	.67	.60	.60
	He(X)	.39	.38	.30	.39	.40
(65/5)	$SF_6(X)$	.77	.77	.80	.81	.79
	He(X)	.23	.20	.20	.19	.21
(30/10)	$SF_6(X)$	.93	.96	.98	.99	.94
	He(X)	.06	.03	.02	.01	.06

The last column in the above table gives the analytical composition assuming complete mixing. As the data indicate a substantial degree of layering (or incomplete mixing) occurs for the 30/10 pressure ratio case only; the higher pressure ratio cases indicate complete mixing thus substantiating the earlier reported visual observations. Again, one cannot generalize these results until similar tests are conducted to investigate the effects of geometric scale size. In addition, as noted in General Atomic's Quarterly (July 1978), the sonic orifice (or underexpanded jet) discharge does not adequately simulate what GA now envisions as a upper plenum PCRV depressurization. For example, a depres-

surization through a steam generator concrete penetration plug (flow restrictor area of 100 $in.^2$) is envisioned as an annular jet of helium exhausting into, and filling, the compartmental space between the top of the PCRV and refueling platform and thence issuing into the CV as an isobaric jet or plume through the annular grating in the refueling platform. Resistance to the helium flow is provided by the omega seals and by the ring around the concrete plug containing the tendons which extend to the lower face of the PCRV. Thus, although the small scale tests do not correspond with what GA now considers for upper plenum PCRV gas release, it can indeed provide meaningful qualitative, and with additional instrumentation, quantitative data on the mixing processes within enclosed environs. Indeed, the notion of an isobaric jet discharge through the refueling platform floor appears to lend more credence to the possibility of gas layering due to a reduction of the effects of jet impingement with the upper levels of the CV on the overall mixing processes. Enhanced momentum and kinetic energy losses through flow restrictors, omega seals, and steam generator top cap geometry brings the buoyant forces, through the gradient Richardson number, into predominance at an earlier stage of the overall discharge process.

In this context, work is continuing with the small scale experiments to provide a data base for the evaluation and/or refinement of the RICE code (Boccio, 1978b). The RICE code is presently being used to numerically simulate the flow processes that occur within the small scale experiments. Many factors in the solution algorithm, governing equations, and code structure must be considered. Presently a simple eddy viscosity law is being used in the code. The main thrust in these initial calculations will be to investigate the effects on how the time advanced pressure is calculated. Presently, the continuity and momentum equations are coupled together and solved implicitly using the equation of state to relate the time advanced pressure to the time advanced density. After which, the energy and species continuity equations are solved explicitly. This treatment, therefore, assumes that changes in the fluid pressure in each computational cell are due primarily to density changes and that pressure changes due to changes in internal energy, temperature, and gas concentration are relatively small. Thus, considering the multispecies ideal gas equation of state, i.e.,

$$p = \rho RT \sum_{i=1}^{N'} Y_i/W_i$$

in which R is the gas constant, W_i is the molecular weight of species i, Y_i is the mass fraction (ρ_i/ρ), ρ and T the global density and temperature, the time advanced pressure $(t=n+1\Delta t)$ can be formally expressed as:

$$p = p^n + \left(\frac{\partial p}{\partial \rho}\right)^n (\rho^{n+1} - \rho^n) + \left(\frac{\partial p}{\partial T}\right)^n (T^{n+1} - T^n)$$

$$+ \sum_{i=1}^{N} \left(\frac{\partial p}{\partial Y_i}\right)^n (Y_i^{n+1} - Y_i^n)$$

In the code at present only the first two terms in the above expression are used where $(\partial P/\partial \rho)$ is taken as the square of local sound speed. Thus, pressure variations due to internal energy and composition are accounted for subsequent to the explicit solution of the energy and species continuity equations.

Preliminary experience using the RICE code has been presented elsewhere (Boccio, 1978b and Boccio, 1978c). Work is now continuing to experimentally verify the code and to incorporate into it the two equation turbulent kinetic energy analysis.

4.3 Fission Products (J. Skalyo, Jr.)

Various fuel cycles are being considered for HTGRs as discussed by Baxter, et al (1978). In effect, the HTGR concept appears to be adaptable to the various fuel cycles which are being considered for purposes of non-proliferation and/or conservation of uranium resources. The fission product inventory for the HTGR at any time is dependent on the particular fuel cycle, due to the varying ^{238}U content in the fuel with its resultant production and burning of ^{239}Pu. To study the major differences in fission product inventory that occur due to different fuel cycles, the ORIGEN code (Bell, 1973) has been used.

It is a simple one energy group code wherein the fast and resonance fluxes are taken as fixed ratios of the thermal flux. The input data for the code is therefore simple to prepare and the results that are obtained are useful for most purposes. This approach can be compared to the more accurate GA methodology of utilizing 9 energy groups in the GARGOYLE (Todt, 1969) code. The resultant calculational complexity requires a more complete knowledge of the flux spectrum which would require an extensive neutronic analysis.

In addition to scoping studies of fission product inventories, the code is expected to find use in the analysis of fission product experiments being performed on fuel kernels in our experimental program. Some of the experiments involve the temperature induced failure of irradiated fuel kernels which have been reirradiated for short times in the Brookhaven High Flux Beam Reactor.

The code results for a sample problem on an LWR fuel loading gave excellent agreement with the ORNL IBM-360 output; thus verifying proper conversion of the program. A calculation was then carried out using the ORIGEN HTGR Library to evaluate fission product inventory on an average spent fuel element for the HEU fuel cycle and the MEU fuel cycle. The results of an inventory at a time point 180 days following discharge from the core can be compared to the extensive lists calculated by GA in the reports GA-A13886 (Hamilton, 1976) and GA-A14980 (Zane, 1978). These two reports appear to be aimed at fuel reprocessing and hence give inventories following a period of storage. The ORIGEN code allows us more control over the output to analyze the fission product decay at short times (minutes and hours) following shutdown. This output is of direct use for accident studies.

The HEU fissile fuel particles in an average equilibrium fuel element are assumed to contain 6.18, 779, 2.36, and 49 grams of ^{234}U, ^{235}U, ^{236}U, and ^{238}U, respectively, and the fertile particles contain up to 8546 grams of ^{232}Th. This loading was inputted to the ORIGEN code and run at constant power over a four year repeated cycle of 11 months up and one month down. The power was varied until the heavy metal burnup of the fissile fuel amounted to 70.2%, to normalize to the same burnup assumed by GA. The procedure gives a 7.2% heavy metal burnup of the thorium; this is inconsistent with the GA evaluation of 4.1%. The ORIGEN code determined a thermal flux for each time period of the calculation. A recalculation using the evaluated thermal fluxes as input was then done with the ORIGEN code on a fuel loading consisting of the fissile material alone.

The fissile uranium particles give a chemical elemental content shown in column 1 of Table 4.2 at 180 days following discharge; the GA-A13886 results are shown in column 2. The results appear to be in good agreement for the major fission fragments and would give adequate results for most scoping studies. It is noted that GA-A13886 predicts that there is more U and less Pu than ORIGEN predicts. This may be, in part, the result of using the 1973 ORIGEN data library rather than the 1975 ENDF/B-IV library and also, in part, due to the simplified flux spectrum assumed in ORIGEN.

The LEU calculation was done similarly to the HEU calculation. Here, 2.343 kg of 9.3% enriched uranium and 3.405 kg ^{232}Th are in a fuel element initially and the power is chosen to obtain a heavy metal burnup of 25.5% in the fissile particles and 3.1% in the fertile particles. The GA-A14980 report was not available when these calculations were made. The fissile input loading of 2.343 kg was arbitrarily scaled by 0.66 of the given input loading (3.55 kg) in the report. This scale factor is an approximate correction for what appears to be an inconsistency in the charge and discharge mass of GA-A14980. The scale factor was chosen to get a comparison with the output of GA-A14980, Volume II.

The ORIGEN and GA-A14980 results are shown in columns 3 and 4 of Table 4.2, respectively. Again, the GA-A14980 results predict more U and less Pu than ORIGEN predicts. The results for the MEU case are also accurate enough for most purposes.

One of the obvious deficiencies in the trend of the disagreements between columns 3 and 4 is the comparison for Ru. The trend of columns 2 and 4 (both GA calculations) in the vicinity of Ru would seem to indicate a discrepancy. The major share of the 170 gram total for Ru is due to 141 grams of ^{100}Ru; the latter is derived from activation since ^{100}Ru is shielded in the main β-decay chain by ^{100}Mo. The production of ^{100}Ru by β-decay of ^{100}Tc must depend on a ^{100}Tc fission yield of 3.24×10^{-6} for ^{239}Pu or 2.38×10^{-7} for ^{235}U (Rose, 1976). At this point, one must assume that GA-A14980 is too high in its prediction of ^{100}Ru concentration by at least an order of magnitude.

A measure of confidence has been obtained in utilizing the ORIGEN code to make predictions needed by our experimental study of reirradiated fuel particles. Work on the incorporation of the 1975 ENDF/B-IV data library into the code is proceeding.

Table 4.2

Element Concentrations (grams per fuel element)

Element	1	2	3	4
Cm	8.64-01	9.48-02	4.64+00	9.97-01
Am	8.44-01	2.23-01	9.19+00	2.55+00
Pu	3.50+01	1.04+01	1.39+02	4.86+01
Np	2.63+01	1.41+01	1.10+01	8.56+00
U	1.88+02	2.20+02	1.59+03	1.85+03
Pa	1.16-05	9.80-06	9.21-06	1.30-06
Th	1.91-05	4.87-05	1.64-05	3.32-02
Ac	6.56-10	2.85-10	3.34-10	2.06-14
Ra	2.26-09	1.09-09	6.54-10	5.26-11
Fr	5.73-17	1.33-16	3.33-17	5.70-18
Rn	3.40-13	1.63-13	6.54-14	8.22-15
At	4.35-21	1.38-20	2.66-21	6.27-22
Po	4.62-15	3.41-11	2.47-15	3.70-08
Gd	5.61+00	2.12+00	2.59+00	1.63+00
Eu	2.72+00	1.58+00	3.22+00	1.61+00
Sm	1.07+01	9.40+00	1.15+01	8.23+00
Pm	3.86-01	1.12+00	1.12+00	1.54+00
Nd	7.25+01	7.23+01	5.92+01	5.31+01
Pr	2.08+01	2.05+01	1.86+01	1.52+01
Ce	5.51+01	4.75+01	4.47+01	3.59+01
La	2.14+01	2.12+01	1.88+01	1.60+01
Ba	2.70+01	2.56+01	2.18+01	1.98+01
Cs	3.96+01	4.46+01	4.20+01	3.89+01
Xe	8.93+01	8.98+01	8.03+01	6.39+01
I	3.13+00	2.43+00	4.23+00	2.05+00
Te	7.96+00	6.00+00	9.08+00	5.48+00
Sb	1.25-01	1.46-01	2.71-01	1.99-01
Sn	3.92-01	1.04-01	7.02-01	5.45-01
In	2.42-03	3.80-03	1.29-02	1.02-02
Cd	5.22-01	2.30-01	1.82+00	5.38-01
Ag	9.78-02	5.21-02	9.15-01	7.67-01
Pd	1.20+01	9.07+00	2.34+01	1.59+01
Rh	1.54+00	2.96+00	4.64+00	4.52+00
Ru	3.12+01	3.15+01	3.55+01	1.70+02
Tc	1.19+01	1.30+01	1.23+01	1.05+01
Mo	5.80+01	6.12+01	5.08+01	4.53+01
Nb	5.50-02	6.31-02	3.26-01	2.35-01
Zr	7.09+01	6.48+01	5.28+01	4.98+01
Y	1.01+01	1.04+01	6.53+00	5.89+00
Sr	1.89+01	2.11+01	1.22+01	1.30+01
Rb	7.24+00	1.21+01	4.65+00	3.84+00
Kr	7.85+00	9.82+00	5.21+00	6.09+00
Br	2.46-01	4.33-01	2.19-01	3.01-01
Se	9.85-01	1.05+00	7.58-01	7.51-01

Table 4.2 (Cont'd.)

1. ORIGEN results for HEU fuel element (only fissile particles).
2. GA-A13886 results for HEU fuel element (only fissile particles).
3. ORIGEN results for MEU fuel element (only fissile particles).
4. GA-A14980 results for MEU fuel element (only fissile particles).

4.4 A Study of Flammability Under the Influence of Large Ignition Sources (R. A. Strehlow, K. R. Sivier - University of Illinois)

During this quarter, assembly and shakedown of the combustion chamber [internal dimensions: diameter of 43.2 (17 inches) and height of 182.9 cm (72 inches)] system was completed and the first series of combustion tests in simple methane-air mixtures were made. The results of this work will be reported in a M.S. thesis presently being prepared. A description of the design, assembly, and initial operation of the experimental apparatus (including the initial methane-air flammability tests) is published separately as a M.S. Thesis, prepared by Paul Bailey (1978).

Briefly, the ranges of conditions investigated in these initial tests were:

1. Methane volumetric concentrations from 0 to 5.9%.
2. Stoichiometric methane-air ignition pockets (polyethylene plastic bags) with volumes from 0.135 to 0.66 ft^3 representing ignition-pocket-to-chamber volume ratios of 0.014 to 0.069.
3. Vertical locations of the ignition pocket (relative to the bottom of the chamber) from 30 to 152 cm (1 to 5 feet).

The ignition pockets were ignited remotely with a low intensity electric arc.

The most significant result from these initial tests was the excellent agreement found with the Cubbage and Marshall (1972) data for methane-air mixtures. This agreement serves to validate the present experimental setup.

With the completion of these initial tests, the program will now move into the investigation of more complex mixtures with the addition of carbon monoxide and hydrogen fuels. Parallel studies of conventional flammability limits (carried out in the 2-inch diameter flammability tube) and the effects of large stoichiometric ignition pockets (carried out in the combustion chamber will begin early in the next reporting period.

PUBLICATIONS

BOCCIO, J. L., et al., "HTGR Depressurization Analysis," BNL-NUREG-25334, in Proc. U.S.-Japan Seminar on HTGR Safety Technology, Fuji, Japan, November 24-25, 1978, Vol. I.

SASTRE, C., "HTGR Accident Delineation," BNL-NUREG-25329, in Proc. U.S.-Japan Seminar on HTGR Safety Technology, Fuji, Japan, November 24-25, 1978, Vol. I.

REFERENCES

BAXTER, A. M., MERRILL, M. H. and DAHLBERG, R. C., "The Use of Non-Proliferation Fuel Cycles in the HTGR," GA-A15049, October 1978.

BELL, M. J., "ORIGEN-The ORNL Isotope Generation and Depletion Code," ORNL-4628, May 1973.

BOCCIO, J. L., SKALYO, J. and TAKAHASHI, H., "HTGR Depressurization - Small Scale Model Experiments," in Reactor Safety Research Programs Quarterly Progress Report, January 1 - March 31, 1978, Brookhaven National Laboratory, BNL-NUREG-50820, May 1978a.

BOCCIO, J. L., "Containment Vessel Gas Dynamics - A Global Approach," in Reactor Safety Research Programs Quarterly Progress Report, July 1 - September 31, 1978, Brookhaven National Laboratory, BNL-NUREG-50931, December 1978b.

BOCCIO, J. L., et al. "HTGR Depressurization Analysis," presented at Japan-U.S. Seminar on HTGR Safety Technology, November 22-24, 1978, Fuji, Japan, BNL-NUREG-25334, November 1978c.

CUBBAGE, P. A. and MARSHALL, M. R., "Pressure Generated in Combustion Chambers by the Ignition of Air-Gas Mixtures," I. Chem. E. Symposium Series No. 33, 1972, p. 24.

HAMILTON, C. J., et al., "HTGR Spent Fuel Composition and Fuel Element Block Flow," GA-A13886, July 1976.

ROSE, P. F. and BURROWS, T. W., "ENDF/B Fission Product Decay Data," BNL-NCS-50545, August 1976.

TODT, F. W., "GARGOYLE II - An Infinite Medium Fuel Cycle Analysis Code with Fuel and Poison Searches," GA-9477, May 1969.

ZANE, G, GEORGHIOU, D. L. and EVERLINE, C. J., "LHTGR MEU Spent Fuel Element Definitions and Block Flows," GA-A14980, August 1978.

II. LMFBR SAFETY EVALUATION

SUMMARY

In the adiabatic gas injection simulation experiments, the test set up was completed and installed. Pressure drop and void fraction measurements were taken in the test column with bottom gas injection. The results for the average pool void fraction and for the flow regime transitions are compared with models existing in the literature.

An analytical model was developed to describe the transient dispersion characteristics of fuel-steel boiling pool systems under decay heating conditions, with boundary heat losses. With this model, the pressure-temperature history of the boiling pool systems are computed, as well as the spatial distribution of void fraction. Typical results for the average steel vapor fraction for a typical pool are presented. The pool average steel vapor volume fraction indicates the strong impact of the vapor region heat sink on the boilup process.

The experimental apparatus for the measurement of local heat transfer coefficients to inclined walls in a boiling pool was upgraded. Experiments were conducted at wall angles of 90°, 75°, and 60°. In addition, average pool void fraction measurements were performed, and general observations on the pool characteristics and flow regimes are also reported.

The Super System Code (SSC) development program consists of three series of codes: SSC-L, SSC-P, and SSC-S. During this quarter, the SSC-L code was used to analyze a flow coastdown transient in CRBRP to 1800 seconds. All computations were performed using the twelve-channel data set. This calculation took 1785 CPU seconds on CDC-7600 machine, which is slightly less than the simulation time. Major findings from this calculation are: (a) The interassembly flow redistribution is a very significant factor in affecting the maximum sodium temperature, (b) The hot channel temperature in blanket assembly for the EOEC fuel is higher than that in the fuel channel, (c) A minimum of five channels may be used in simulating in-core response, (d) When the interassembly flow redistribution is artificially suppressed, the hot channel blanket temperature will exceed sodium boiling point for an extended period of time.

The effects of uncertainties on decay heat and the scram delay-time were examined as a part of the run matrix calculations.

A pipe rupture calculation was also simulated. For the case of scram delay-time of 0.625 second, sodium in the peak channel was calculated to start boiling in another 0.7 second. This calculation is being continued to see if and when boiling may be terminated.

Models for the steam generator controllers were written. Some simplifications in calculational scheme were also made. Other PPS/PGS systems have been programmed and interfaced with the SSC-L code. Several test runs were also made.

Sodium pump characteristics were extended to include both the HAN and HVN curves during steady-state calculations.

The SSC-L code was exported to Babcock and Wilcox.

The SSC-P code initialization was completed. Input data and individual modules were upgraded and modified. The steady-state predictions by the SSC-P code are, in general, consistent with known and expected PHENIX operating values. Model equations describing transient primary system hydraulics for the hot pool concept have been formulated.

The SSC-S code effort was concentrated in defining various tasks and subtasks in the work plan. Literature search was also conducted for the in-vessel model to be used in the code.

The SSC Validation work during this quarter covered a number of areas. Intercomparison between SSC and IANUS continued. The FFTF primary loop specification and simulation was completed and comparisons between SSC and IANUS indicate general good agreement. The draft report on the evaluation of FFTF instrumentation vis-a-vis code validation requirements has undergone extensive review and revision. Finally, results of the SSC-BRENDA comparisons have been completed and reported.

1. Fast Reactor Assessment - Accident Sequence Studies (O. C. Jones, Jr. and N. Abuaf)

1.1 Hydrodynamic Characteristics of Two-Phase Dispersed Systems (T. Ginsberg, J. J. Barry; and J. C. Chen, Lehigh University)

The purpose of this task is to study the hydrodynamic dispersive behavior of two-phase pools under conditions prototypic of transition phase accident circumstances. Adiabatic gas injection simulation experiments are carried out with fluid-pair systems which bracket the hydrodynamic parameters of fuel-steel boiling systems.

1.1.1 Experimental Investigations

The adiabatic gas injection apparatus (Ginsberg 1978a) was completed and installed. This test facility was designed to provide a two-phase, gas-liquid, pool flow configuration in which to simulate the characteristics of volume-heated boiling pools. Gas is supplied from the bottom of the column through a porous plate. The immediate objective of the experiments with this apparatus is to evaluate the disturbance introduced to the flow field by cylindrical obstructions to the flow (Ginsberg 1978b). These results will be used to assess the usefullness of proposed experiments with volume-distributed gas injection.

The assembled gas injection column together with γ-ray source and detector holders and traversing apparatus are shown in Figs (1.1) and (1.2). Figure (1.1) shows the column, pressure taps and connecting lines, and the air supply manifold. The axial and transverse traversing mechanisms are also shown in Figs. (1.1) and (1.2). Figure (1.3) shows the flow control and monitor panels. On the left are air flow rotameters. On the right side the pressure port, selector valves, the pressure transducer, and the liquid makeup rotameters are shown (to maintain uniform liquid inventory with droplet carryover). A porous plate is located in the base of the column. Gas is bubbled through the plate.

Preliminary pressure drop and void fraction measurements have been made in the test column. A porous steel plate, 1/8-inch thick with 10 μ porosity (will filter 98% of particles whose diameters are greater than 10 μ) was used in these experiments. Results are presented in Figs. (1.4) and (1.5). The steady-state mixture momentum equation is utilized to obtain the void fraction. In the absence of acceleration effects, this equation is

$$\frac{dp}{dx} = -\rho_\ell g(1 - \alpha) \tag{1.1}$$

where p is the pressure, x is the axial distance, ρ_ℓ the liquid density, g the acceleration of gravity, and α the local void fraction.

In these bottom injection bubbling column tests, it is probably a good assumption (to be verified later with the γ-ray void measurements) that the

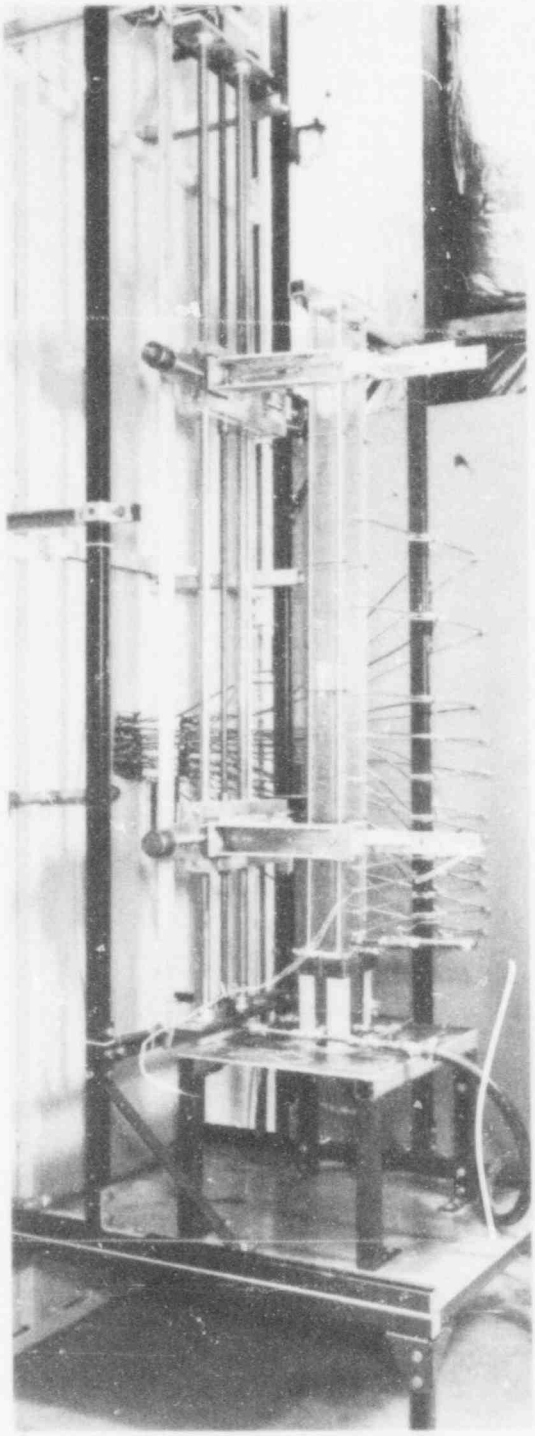

Figure (1.1) - Photograph of Gas Injection Test Column (BNL Neg. No 1-533-79).

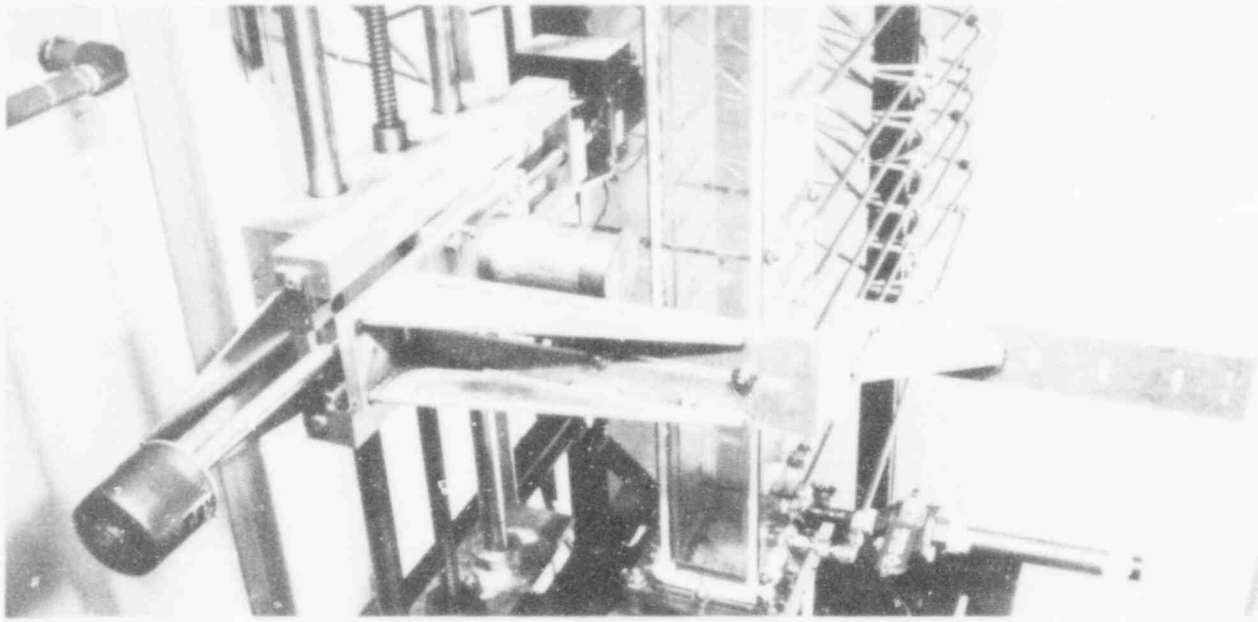

Figure (1.2) - Traversing Apparatus (BNL Neg. No 1-534-79).

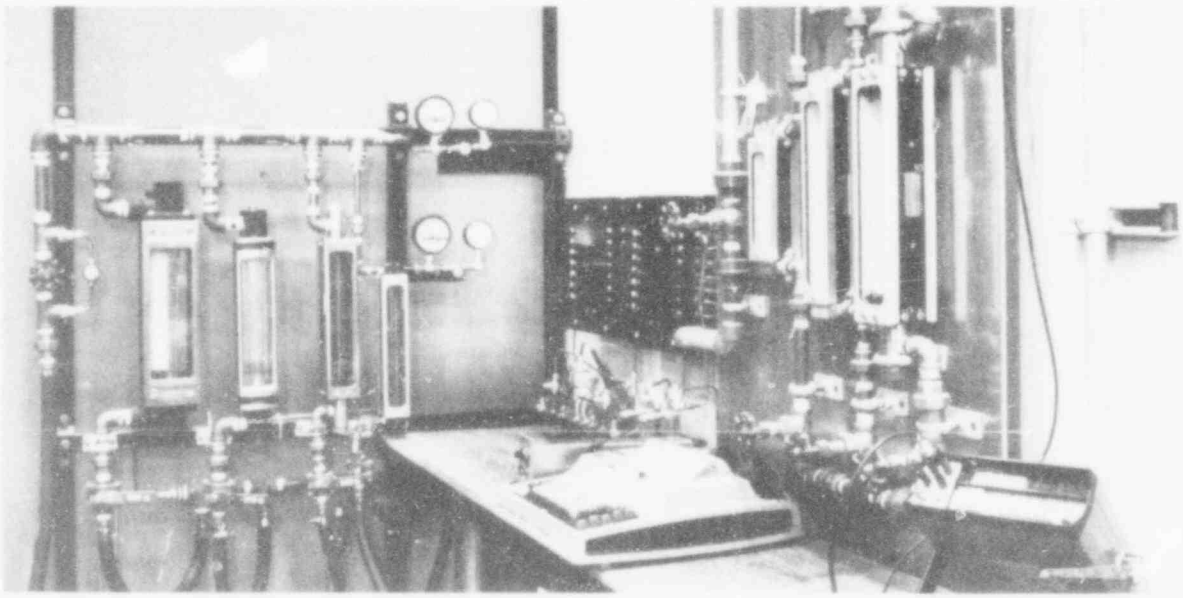

Figure (1.3) - Flow Control and Monitor Panels (BNL Neg. No 1-530-79).

area-averaged void fraction is independent of position. Equation (1.1) then, is integrated to give

$$\frac{p - p_1}{\rho_\ell g(1 - \alpha)H_o} = \frac{x_1 - x}{H_o} \quad (\text{or } P^* = X^*) \tag{1.2}$$

where H_o is the liquid height with no gas injection and the subscript '1' denotes a reference pressure tap location. The experiments were carried out for H_o = 0.3 m over a range of gas injection rates with dimensionless superficial vapor velocities j_g/U_∞ up to 1.5, where U_∞ is the bubble rise velocity in a infinite medium. For each j_g/U_∞, an average void fraction was computed using a linear least-squares analysis of the pressure data. The void fraction results are shown in Fig. (1.4). Presented with the data are predictions based upon bubbly flow, and churn-turbulent flow, drift-flux models (C_o is the distribution parameter). These results indicate:

(i) The bubbly flow model is a good representation of the data for small j_g/U_∞. While bubbly flows were observed up to $j_g/U_\infty \simeq .37$, the data departs from the bubbly ($C_o = 1$) model before a flow transition is abruptly observed. It is hypothesized that the departure is due to the onset of two-dimensional flow within the column.

(ii) A transition from bubbly to churn flow was observed in the range of j_g/U_∞ between 0.4 and 0.7. This is apparent in Fig. (1.4), and was also observed visually.

(iii) The Zuber-Findlay (Zuber 1965) churn-turbulent drift flux model with $C_o = 1.2$ does not adequately represent the data in the churn flow regime.

The computed least-squares void fractions were then used in Eq. (1.2) and, the dimensionless pressure data are shown in Fig. (1.5). Expressed in this form, the pressure data should be linear with x and independent of void fraction. The results lend support to this contention.

1.2 Liquid Dispersion in Internally Heated Boiling Pools (T. Ginsberg; J. C. Chen, Lehigh Uni.)

The objectives of this task are to conduct experiments and perform analysis to study the dispersive characteristics of internally heated boiling pools. Experiments using internal heat generation are used to simulate nuclear heating, and the two-phase boiling characteristics are studied in open and closed boiling systems with boundary heat losses.

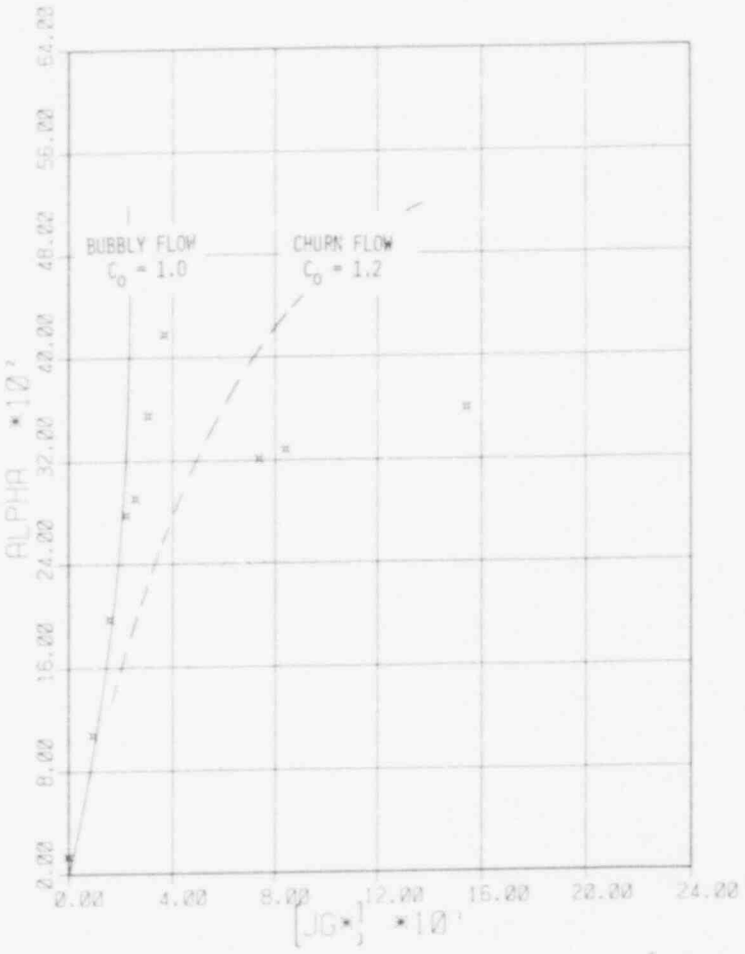

Figure (1.4) - Least-Squares Void Fraction
(BNL Neg. No 1-926-79).

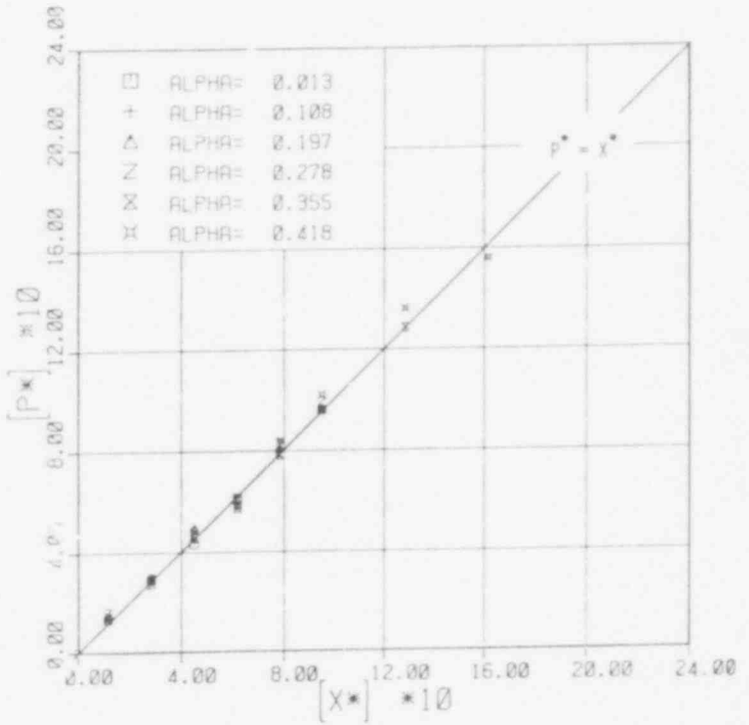

Figure (1.5) - Dimensionless Pressure Profiles
(BNL Neg. No 1-925-79).

I.2.1 Analytical Investigations

Arguments have been proposed which suggest that at decay-heating rates down to 1 percent of steady-state LMFBR power density, boiling pools of steel and molten oxide fuel are self-dispersive. Available evidence from experiments with simulation fluid systems, heated electrically and with microwave dielectric heating, suggest that if the energy available to the steel for vaporization is of decay heating magnitude, then there is a strong potential for dispersal of the mixture to the limits of the volume available to it (Ginsberg 1978).

In a closed boiling pool system with boundary heat losses, however, the energy available for vaporization may be significantly less than the decay heating rate, as a result of sensible heating and boundary losses (Dhir 1976). The potential for fuel dispersal may be greatly diminished when these effects are correctly modeled.

An analytical model has been developed which describes the transient dispersion characteristics of fuel-steel boiling pool systems under decay heating conditions, with boundary heat losses. In addition to pressure-temperature histories of boiling pool systems, the spatial distribution of steel vapor (void fraction) and molten fluid are computed. Local heat losses and sensible heating are included in the model for the vapor generation rate in the material balance equations.

A schematic diagram of a closed volume-heated boiling system is shown in Fig. (1.6). The pool is assumed bounded on all sides by stable fuel crusts (Fauske 1977). Molten fuel (heat source) and steel (vapor source) are assumed homogeneously mixed at the steel saturation temperature. The mixture is treated as an effective single-component, volume-heated, two-phase equilibrium boiling system. Thermodynamic properties are appropriately weighted.

In general, a pool would not boil up to fill the available volume. The system, therefore, was divided [see Fig. (1.6)] for purposes of identification of heat transfer mechanisms into an upper continuous steel vapor region and the two-phase molten mixture. It was assumed that the mode of heat transfer in the vapor zone is steel condensation limited (Rohsenow 1972; Gerstmann 1967) and is molten UO_2 boilup-enhanced natural circulation limited (Greene 1977) (to vertical boundaries) or boilup-enhanced conduction limited (Baker 1977) (downward direction) in the molten mixture region.

Additional assumptions are:

(i) The time scale for decay-heating transients are controlled by thermal inertia. Flow inertia and kinematic wave transport time scales are small compared to the thermal time scale.

(ii) One-dimensional drift flux modeling is an adequate description of the liquid-vapor void dyanmics.

(iii) The entire pool contents are at uniform temperature.

As a consequence of the first two assumptions, a quasi-steady, one-dimensional drift flux model was formulated. Mass and energy balance equations were formulated to characterize the transient thermodynamic behavior of the system. The vapor source term is computed on a transient basis and incorporates the effects of sensible heating and boundary losses.

Typical results are presented in Fig. (1.7) and Table (1.2) for a pool whose parameters are defined in Table (1.1). The heat transfer rate (h_p) to the boundaries of the two-phase molten region was taken as $10^4 W/m^2K$, representative of rates predicted by the correlations of Greene (1977) and Baker (1977). The condensation rate at the steel vapor region boundaries is highly uncertain due to the presence of noncondensibles and also possibly of a UO_2 liquid film from splashing of chugging liquid. This heat transfer rate, therefore, was treated parametrically.

Preliminary results for the pool-average steel vapor volume fraction, $\bar{\alpha}$, indicate the strong impact of the vapor region heat sink on the boilup process. The stronger the steel condensation rate, for a given power input, the greater the potential for the two-phase mixture to fill the available volume [indicated by $\bar{\alpha}_{MAX} = 0.7$ in Fig. (1.7)]. The reason for this behavior is represented in Table (1.2). Most of the available energy source is consumed in sensible heating, indicating nearly an adiabatic, constant-volume heating process with little attendant vaporization. As the condensation rate increases, the rate of pressurization decreases, less energy is consumed in sensible heat addition, and more energy becomes available for vaporization. The dispersal process is thus enhanced as the potential for condensation increases. For condensation rates greater than $2 \times 10^4 W/m^2K$ the calculations indicate that the two-phase mixture would disperse to the limits of the available volume. For the system of interest, unimpeded steel condensation rates of $10^5 W/m^2K$ are predicted with the methods of Rohsenow (1972) and Gerstmann (1967). The potential for dispersal to the limits of the available volume is, therefore, conceivable.

The transient pool dispersal model calculations indicate:

(i) The potential exists for dispersal of UO_2 steel pools to the limits of the available volume under decay heating conditions. However, only a fraction of the available decay heat source is useful for vaporization and fuel dispersal.

(ii) Mild pressurization rates of 0.1 atm/s are characteristic of transition phase closed-pool accident conditions.

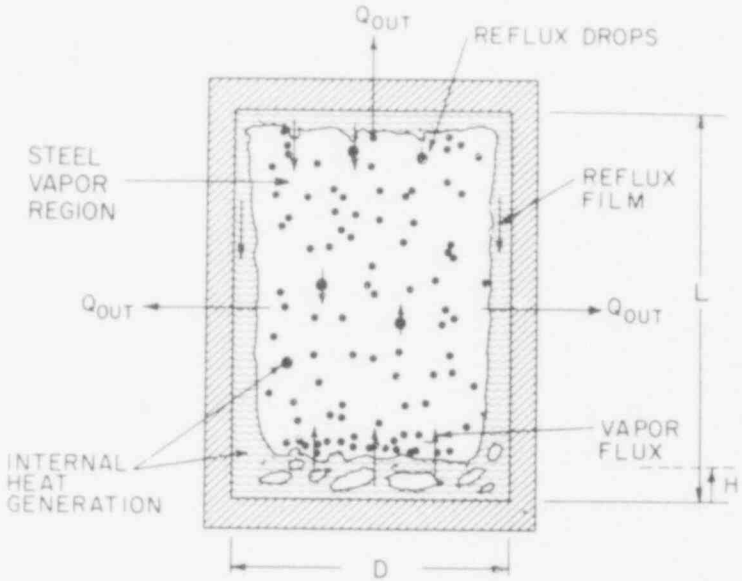

Figure (1.6) - Schematic of Closed Boiling System With Boundary Heat Losses (BNL Neg. No 1-837-79).

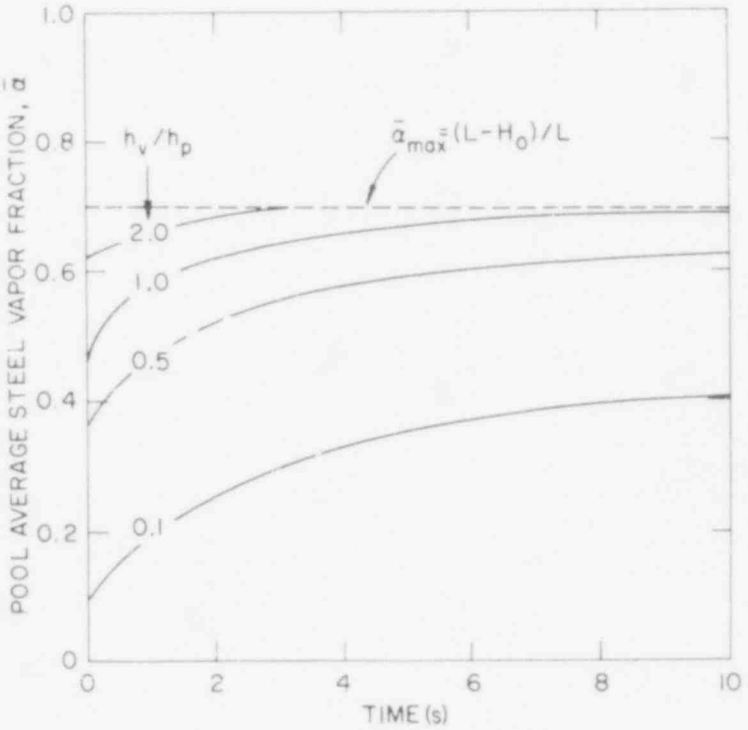

Figure (1.7) - Predicted Transient Steel Vapor Fractions (BNL Neg. No 1-838-79).

TABLE (1.1) - BOILING POOL PARAMETERS

Composition: Molten Oxide Fuel and Steel
Pool Diameter (D): 1.0 m
Pool Cavity Height (L): 1.0 m
Collapsed Liquid Level (H_o): 0.3 m
Mass Fraction Fuel: 0.678
Initial Pool Temperature: 3090 K
Boundary Temperature: 3063 K
Power Density: 8 percent of steady state LMFBR power density

TABLE (1.2) - CALCULATIONAL RESULTS

Vapor Condensation Coefficient h_v/h_p	Pressurization Rate (ATM/S)	Vaporization Rate Q_{VAP}/Q_{GEN}	Sensible Heating Rate Q_{SENS}/Q_{GEN}
0.1	.086	.003	.985
0.5	.085	.019	.970
1.0	.082	.037	.941
2.0	.079	.075	.894
2.5	.078	.094	.875

(iii) The most significant parameter affecting the dispersal process is the magnitude of the vapor condensation heat sink. There is also much uncertainty in this parameter.

Nomenclature

D	pool diameter
g	acceleration of gravity
h_p	two-phase mixture heat transfer rate
h_v	vapor condensation rate
H	height of two-phase mixture
H_o	collapsed liquid level
L	height of available pool volume
p	pressure
p^*	dimensionless pressure $\left[\equiv (p - p_1)/[\rho_\ell g(1 - \circ)H_o]\right]$
P_1	reference pressure
Q_{GEN}	heat generation rate
Q_{SENS}	sensible heating rate
Q_{VAP}	steel vaporization rate
U_∞	bubble terminal rise velocity
x	axial coordinate
X^*	dimensionless axial coordinate $[\equiv (x - x_1)/H_o]$
x_1	reference axial position
α	area-averaged void fraction [Eq. (1)]
$\bar{\alpha}$	average vapor volume fraction in mixture $[\equiv (H - H_o)/H]$
$\bar{\alpha}_{MAX}$	maximum vapor volume fraction $[\equiv (L - H_o)/L)$
ρ_ℓ	liquid specific gravity

1.3 Boiling Pools With Internal Heat Generation (G. A. Greene and C. E. Schwarz)

The purpose of this task is to study and characterize local boundary heat losses and void distributions in volume-heated boiling pools at power levels characteristic of PAHR conditions in an LMFBR. Experimentation under boiling conditions has begun at wall angles of 90^{o}, 75^{o}, and 60^{o}. Measurements are being made of local heat transfer, as well as pool-average void fraction.

1.3.1 Experimental Apparatus

Apparatus upgrade has been completed. Nonuniform flow patterns in the coolant flow have been eliminated. The coolant flow rate has been increased to 3.5-5. gpm. This has the effect of reducing the resistance to heat transfer in the coolant to a negligible level.

1.3.2 Measurement of Local Heat Transfer Coefficient

In the only previous investigation of local boundary heat flux from volume-boiling pools (Gustavson 1977), the local boundary flux was measured by calorimetric measurements through isolated coolant channels in a test wall, and the surface temperature was calculated by extrapolating an interior temperature across an electrical insulating teflon sheet. In this manner the local (segment-averaged) heat transfer coefficient could be measured in up to nine channels.

In the present investigation, the local heat flux and surface temperature are directly measured with no area averaging and no extrapolation of temperature across an insulating layer. Gold-plated microthermocouples are installed at 19 separate front-and-back locations, flush-mounted with the front and back surfaces of an electrically insulating boron nitride test wall, which is in direct contact with the boiling pool. Once steady-state conditions are determined in the pool and test wall, the ouput of each thermocouple, which are individually calibrated to within $\pm$ 0.1 ^{o}C, is time-integrated to determine the average temperature at each location. Simultaneously, the standard deviation of the thermocouple reading is recalculated at each sample. The final data is stored on magnetic tape. The local heat transfer coefficient from the volume-boiling pool is defined as

$$h(x) = \frac{k_{BN}(T_{front}(x) - T_{back}(x))}{a \cdot (T_{pool} - T_{front}(x))} \qquad (1.3)$$

where $h(x)$ is the local convective heat transfer coefficient, k_{BN} is the test wall thermal conductivity, a is the test wall thickness, $T_{front}(x)$, $T_{back}(x)$, and T_{pool} are the pool-side local surface temperature, back-side local surface temperature, and bulk pool temperature, respectively. In this manner, the problems associated with calorimetry, temperature extrapolation,

and contact heat transfer resistance are avoided. A sample of the local distribution of heat transfer coefficient vs. depth for run number 9013 is presented in Fig. (1.8).

1.3.3 Measurement of Pool-Average Void Fraction

The average void fraction is necessary for calculation of the boiling heat transfer correlation (Greene 1977), as well as for calculations of pool dynamics, neutronics, and multiphase solidification (Greene 1978). The average void fraction is defined as

$$\bar{\alpha} = \frac{H_B - H_o}{H_B} \tag{1.4}$$

where $\bar{\alpha}$ is the average void fraction, H_B is the boiling pool height, and H_o is the static pool height at the saturation temperature. This is necessary since the density of the nonboiling pool and thus the nonboiling depth, H_o, are a function of the pool temperature. In the experiments, H_o and H_B are determined with a traversable voltage probe. The probe is lowered to both the static and boiling pool until the circuit is closed and the voltmeter indicates pool voltage. In this fashion, an objective determination of the fluctuating pool surface is possible. The net power corresponding to the evaporative and boiling losses is calculated from the net flow rate of water necessary to replenish these losses from the pool. This flow rate is determined through a constant level weir to which the gross flow rate is measured and the overflow flow rate is subtracted to yield the net makeup flow rate. This flow rate is converted to a net volumetric power and is presented in dimensionless form as the dimensionless superficial vapor velocity, $j_{g\infty}/U_\infty$,

$$j_{g\infty}/U_\infty = \frac{\dot{Q}_B H_o}{\rho_v h_{fg} U_\infty} \tag{1.5}$$

The data for average void fraction vs. superficial vapor velocity is presented in Fig. (1.9).

1.3.4 General Observations

During the period the pool is in the bubbly flow regime, the pool is observed to be comprised of two distinct regions, a bubbly boiling region on top and an essentially single-phase nonboiling region at the bottom. As the net boiling power is increased, the thickness of the nonboiling region decreases. The bubbly flow regime pool is observed to swell, indicating a sensitivity of the pool boiling behavior or void fraction to fluctuations or changes in the net boiling power and/or heat losses to the boundaries. As

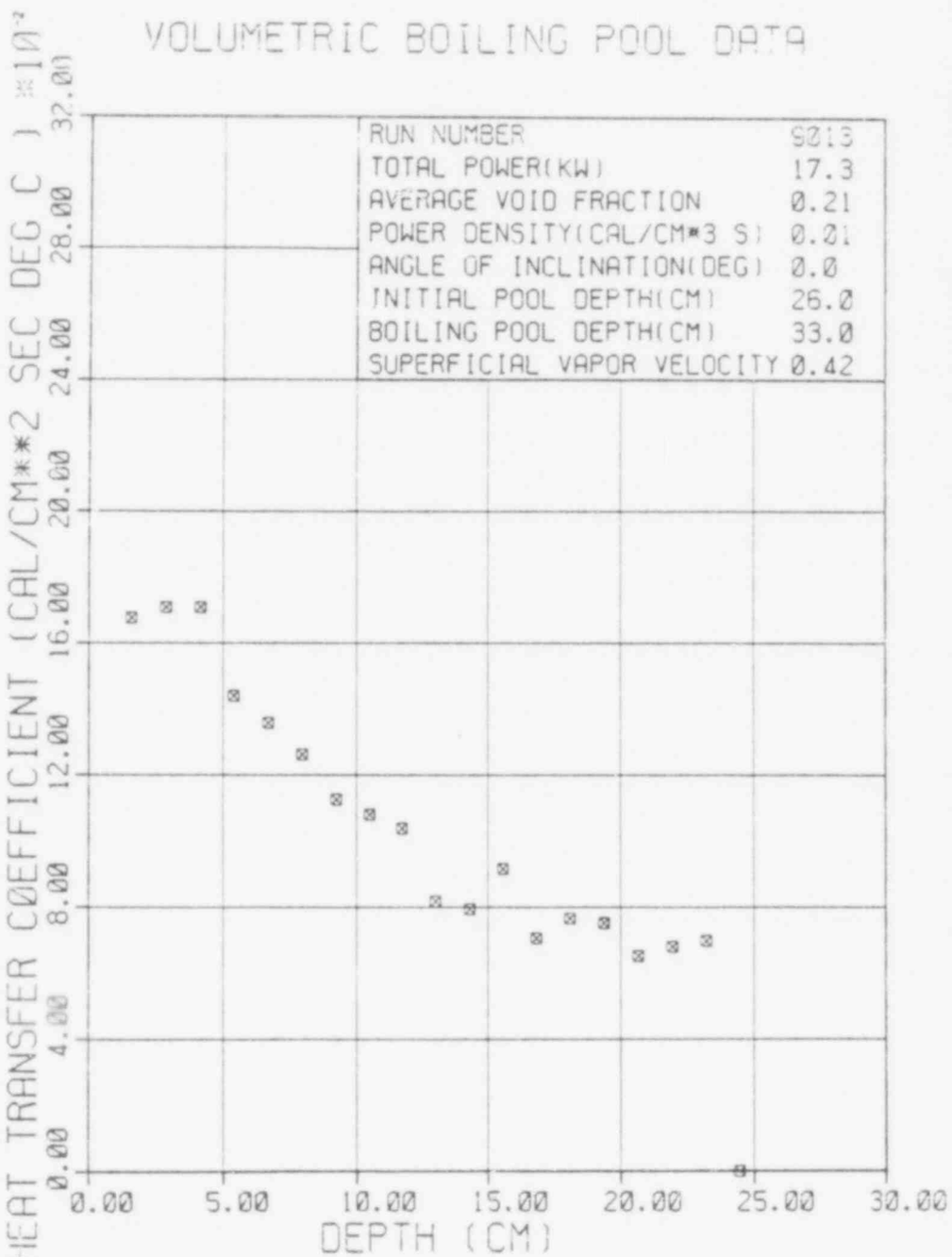

Figure (1.8) - Local distribution of boundary heat transfer coefficient from volume boiling pool, bubbly flow regime (Run No. 9013). (BNL Neg. No 1-1383-79).

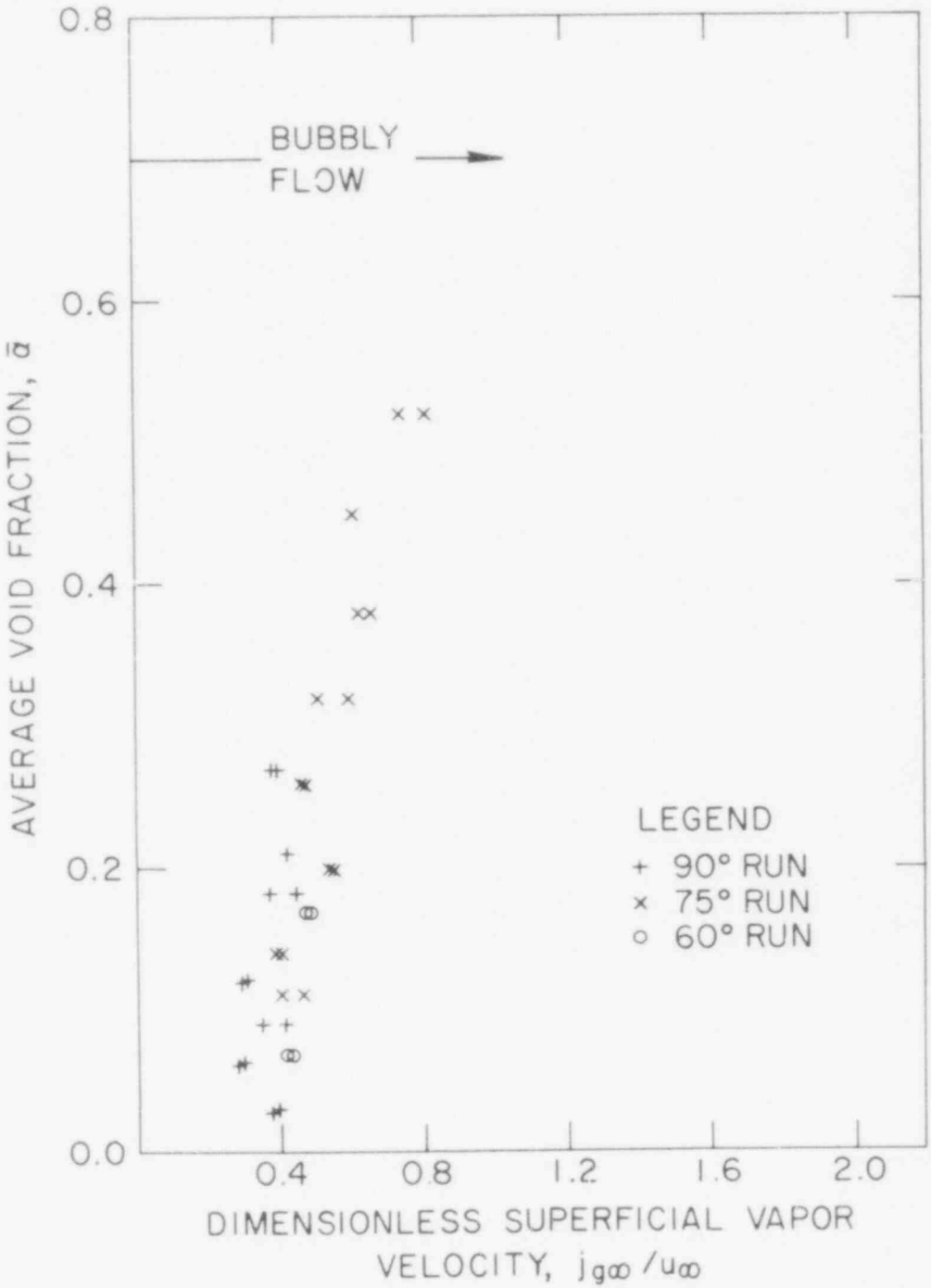

Figure (1.9) - Average void fraction vs. dimensionless superficial vapor velocity for bubbly flow regime in volume boiling pools. (BNL Neg. No 1-1296-79).

the power increases, the pool is observed to undergo flow regime transition to a churn-turbulent type flow regime in which boiling penetrates all the way to the bottom of the pool. This transition appears to occur at a value of $j_{g\infty}/U_\infty$ in the neighborhood of unity in agreement with observations of Ginsberg (1978) for subassembly like geometries. Additional experimental evidence is necessary to confirm this.

For a boiling UO_2 pool at the following conditions,

$$H_o \tilde{-} 30 \text{ cm}$$

$$\rho_v \tilde{-} 10^{-3} \text{ gm/cm}^3$$

$$h_{fg} \tilde{-} 64 \text{ cal/gm}$$

$$U_\infty \tilde{-} 24 \text{ cm/s}$$

$j_{g\infty}/U_\infty$ would equal unity for $\dot{Q}_{BOIL} \sim 0.5$ cal/cm^3/sec. This corresponds to less than .1 percent full power for a CRBR type core, indicating that for PAHR conditions, one would expect the boiling fuel pool to exceed the bubbly-churn turbulent transition by a wide margin for the majority of the accident sequence and the pool to exhibit churn-turbulent hydrodynamic behavior.

REFERENCES

BAKER, L. R., et al., "Post Accident Heat Removal Technology," ANL/RAS 77-2 (1977).

DHIR, V., et al., "Role of Heat Transfer and Other Variables on Fuel Compaction and Recriticality," Int. Meeting on Fast Reactor Safety and Related Physics, CONF-761001, 1172 (October 1976).

FAUSKE, H. K., "Assessment of Accident Energetics in LMFBR Core Disruptive Accidents," Nucl. Eng. & Des., 42, 19 (1977).

GERSTMANN, J. and GRIFFITH, P., "Laminar Film Condenstaiton on the Underside of Horizontal and Inclined Surfaces," Int. J. Heat and Mass Transfer, 10, 567 (1967).

GINSBERG, T., et al., "Reactor Safety Research Programs - Quarterly Progress Report: April - June, 1978", BNL-NUREG-50785 (February 1978).

GINSBERG, T., JONES, O. C. JR., and CHEN, J. C., "Volume-Heated Boiling Pool Flow Behavior and Application to Transition Phase Accident Conditions," ENS/ANS Topical Meeting on Nuclear Power Reactor Safety, Brussels, Belgium (October 1978).

GREENE, G. A., JONES, O. C. JR., and SCHWARZ, C. E., "Thermo-Fluid Mechanics of Volume-Heated Boiling Pools," Proceedings of the Third PAHR Information Exchange, ANL-78-10, BNL-NUREG-50759 (November 1977).

GUSTAVSON, W. R., CHEN, J. C., and KAZIMI, M. S., "Heat Transfer Characteristics of Internally Heated Boiling Pools," BNL-NUREG-50722 (September 1977).

ROHSENOW, W. M., "Film Condensation of Liquid Metals," Trans. CSME, 1, 5 (March 1972).

ZUBER, N. and FINDLAY, J. A., "Average Volumetric Concentration in Two-Phase Flow Systems," ASME J. Heat Transfer, 87, 453 (1965).

3. SSC Code Development (A. K. Agrawal)

The Super System Code (SSC) Development program deals with the development of an advanced thermohydraulic code to simulate transients in LMFBRs. During this reporting period, work on three codes in the SSC series was performed. These codes are: (1) SSC-L for simulating short-term transients in loop-type LMFBRs, (2) SSC-P is analogous to SSC-L except that it is applicable to pool-type designs, and (3) SSC-S for long-term (shutdown) transients occurring in either loop- or pool-type LMFBRs. Reference is made to the previous quarterly progress report (Agrawal, 1978a) for a summary of accomplishments prior to the start of the current period.

3.1 SSC-L Code (J. G. Guppy)

3.1.1 Flow Coastdown Transient in CRBRP (J. G. Guppy and A. K. Agrawal)

A flow coastdown transient to natural circulation was run for the CRBRP. The reactor was assumed to operate at full power (975 MW) prior to the loss-of-electric power (LOEP) at time zero. The reactor was scrammed at 0.75 s later. The three heat transport systems in CRBRP are represented by one equivalent loop. The primary loop consists of the piping from the vessel outlet to pump, pump to intermediate heat exchanger, intermediate heat exchanger to check valve, and finally piping from the check valve to vessel inlet. All core parameters used are for the end of equilibrium cycle (EOEC). These are taken to be the nominal design values as given in the CRBRP PSAR.

Results are presented for two models of the reactor core: (1) a four channel representation and (2) a twelve channel representation. A channel in SSC-L represents at least one assembly. The channel is characterized by a set of parameters such as the power generation, coolant flow rate and the hydraulic diameter. These parameters can then be chosen such that the assembly-averaged conditions are represented. Alternately, the channel can represent either a 'peak' or 'hot' channel in that assembly by adjusting power and flow characterizations. In the selection of channels for an SSC-L simulation, the grouping of assemblies can proceed along two general lines, i.e., according to (1) similar hydraulic characteristics or (2) similar thermal (power) characteristics. In this study, the assemblies were grouped by hydraulic characteristics.

In the four channel representation of the reactor core, the first channel models the peak fuel assembly explicitly. The actual orificing pattern, based on its location in the core, is used. The power generation and flow assignment to this channel is chosen to explicitly represent either an average channel in the peak fuel assembly, or a 'hot' channel. Because a channel in SSC-L represents at least one assembly, all of the 217 pins in Channel 1 are operating at the same power and flow conditions. The second channel represents the 'average' of the remaining 197 fuel assemblies. An equivalent orificing pattern for this channel was defined. Of the remaining two channels, the third models all (150) of the radial blanket assemblies which surround the core, and the fourth models all of the primary and secondary

control systems assemblies. As SSC-L specifically takes into account a bypass channel, all unassigned flow and/or power is assigned to this channel. The radial shield assemblies are lumped with the bypass channel in this sample problem. Alternately, the radial shield assemblies can also be represented by another channel.

For the second model of the CRBRP core (the twelve channel case), the selection of channels were based on the explicit representation of each of the nine orifice zones (five orifice zones for fuel assemblies and four orifice zones for blanket assemblies), one 'hot' channel each in the fuel and blanket assemblies and the last channel to model all primary and secondary control assemblies. Thus, the twelve channels are:

- Channel 1 - Hot channel in fuel assembly (same as Channel 1 in the four channel model),
- Channels 2 through 6 - Average fuel assembly in each of the five fuel orifice zones,
- Channel 7 - Hot channel in radial blanket assembly,
- Channels 8 through 11 - Average radial blanket assembly in each of the four blanket orifice zones, and
- Channel 12 - Average channel representing all primary and secondary control assemblies (same as Channel 4 in the four channel model).

The transient investigated here is a loss of electric power (LOEP) event from full power and full flow conditions. All pumping power (including pony motor power) is assumed lost at time t = 0 and the loop flow rates then coast down to natural circulation conditions. The scram rods are inserted at 0.75 s.

As mentioned earlier, in addition to the explicit treatment of the orifice zone, other deterministic uncertainties can be applied to a particular channel to make it represent either the average pin in a peak assembly or the hot channel. For the four channel model, results will be presented for two combinations: Channel 1 representing either an average pin in the peak fuel assembly or a hot fuel channel. The specifications for the hot channel are obtained by applying direct and statistical contributions to an average pin in the peak fuel assembly. Direct contributions are included from factors such as uncertainty in (1) power level measurement and control system deadband, (2) inlet flow maldistribution, (3) flow maldistribution within an assembly. The statistical contributions are 3-σ uncertainties from factors such as temperature variation, nuclear data, fissile fuel maldistribution, and coolant flow area. For the twelve channel in-core model, results for only one configuration are presented. In this case, Channels 1 and 7 represent the hot fuel and blanket channels, respectively.

To demonstrate the effect of the interassembly transient flow redistribution model on the in-vessel coolant temperatures, the LOEP event for these three core representations was run with and without this flow redistribution calculation being computed. When the flow is artifically not allowed to redistribute (a physically unreal situation), the fraction of total flow assigned to each channel is maintained constant (equal to the initial value) throughout the transient. The fraction of total coolant flow in a channel during transient is explicitly computed when the flow redistribution model is turned 'on.' This model couples the coolant flow in a channel with all other channels through common pressure points in the lower and upper reactor plena. Thus, the coolant flow in a channel is determined by the heating rate and frictional losses in that channel, as well as the flow rate in all other channels.

The results of the LOEP event for six different cases will be presented. These six cases are summarized in Table 3.1. These case numbers are referred to on subsequent graphs and in the discussion of results. The initial (steady-state) power and flow fractions assigned to each channel as well as the type of assembly and number of assemblies represented by each channel for each case are indicated in Table 3.2. Pre-transient or steady state values for power, flow rates and temperature rise data that may be derived from our channel power and flow fractions are given in Table 3.3. The linear power in the average channel represents the total power generated in either fuel or blanket zone per unit height. The term 'peak power' denotes power peaking in the axial direction.

In all cases, the primary loop flow rate responded as typified by Figure 3.1. As seen, the flow rate decreases rapidly initially, until the pump rotor stops at around 60 seconds. A small undershoot occurs at which time the flow rate reaches a minimum. As the onset of natural circulation is reached, the flow rate increases slightly before establishing a fairly constant value.

In Figure 3.2, the responses of the normalized flow rate ($W_{channel}(t)/W_{channel}(0)$) in each of the four channels as well as the normalized total flow rate ($W_{total}(t)/W_{total}(0)$) are shown for Case 1. One can see that, when the transient interassembly flow redistribution is calculated, the normalized flow rates distribute themselves around the total flow rate. The hotter channels tend to suck more flow at the expense of the cooler channels. An effect of this transient redistribution of core flow will be to 'flatten' radial temperature profile across the core. This temperature flattening has been observed in EBR-II natural circulation tests. Other results of the four-channel representation are included in an informal report (Guppy, 1978).

The response of the CRBRP for the flow coastdown transient was also studied using a more detailed in-core representation. As noted earlier, the entire core was modeled by twelve channels. The specific power and flow characterizations, prior to initiating transient, for various channels are noted in Table 3.2. For the cases reported in here, an explicit treatment of hot fuel (Channel 1) and hot blanket (Channel 7) channels was done with and without interassembly flow redistribution, Cases 5 and 6, respectively. As

Table 3.1

Identification of Cases Run for CRBRP LOCP Event

Case	Number of in-core Channels	Channel 1 Represents	Channel 7 Represents	Flow Redistribution Calculations
1	4	Average pin in peak fuel assembly	N/A	On
2	4	Average pin in peak fuel assembly	N/A	Off
3	4	Hot fuel channel	N/A	On
4	4	Hot fuel channel	N/A	Off
5	12	Hot fuel channel	Hot blanket channel	On
6	12	Hot fuel channel	Hot blanket channel	Off

N/A - not applicable

Table 3.2

Initial Channel Power and Flow Fractions
for the Various Cases

Channel Number	Power Fraction*/Flow Fraction**/Assembly Type and Number***for		
	Cases 1,2	Cases 3,4	Cases 5,6
1	0.0060/0.0046/F-1	0.0067/0.0033/F-1	0.0067/0.0033 /F-1
2	0.883 /0.786 /F-197	0.8823/0.7873/F-197	0.3325/0.2996 /F-65
3	0.104 /0.135 /B-150	0.104 /0.135 /B-150	0.3473/0.3085 /F-78
4	0.007 /0.060 /C-19	0.007 /0.060 /C-19	0.1398/0.1231 /F-36
5			0.0446/0.0390 /F-12
6			0.0181/0.0171 /F-6
7			0.0020/0.00076/B-1
8			0.0192/0.0485 /B-36
9			0.0183/0.0376 /B-30
10			0.0413/0.03134/B-41
11			0.0232/0.0168 /B-42
12			0.0070/0.060 /C-19
Bypass	- /0.0144/Bypass	- /0.0144/Bypass	- /0.0144 /Bypass

*Power fraction is initial fraction of 964 MW.

**Flow fraction is initial fraction of 5224 kg/s.

***F=Fuel assembly, B=Blanket assembly, C=Control assembly.

Table 3.3

Steady-State Power, Flow and Temperature Rise Data for the Various Cases

Parameter		Fuel Assembly	Blanket Assembly
Linear Power in Average Channel	(kW/m)	20.95	6.74
Peak Power in Average Channel	(kW/m)	26.60	12.61
Peak Power in Peak Assembly	(kW/m)	35.55	--
Peak Power in Hot Channel	(kW/m)	39.70	36.37
Coolant Flow in Average Channel per Assembly	(kg/s)	20.56	4.70
Coolant Flow in Peak Assembly per Assembly	(kg/s)	24.03	--
Coolant Flow in Hot Channel per Assembly	(kg/s)	17.24	3.97
Temperature Rise in Average Channel	(K)	164.0	112.3
Temperature Rise in Peak Assembly	(K)	190.3	--
Temperature Rise in Hot Channel	(K)	296.2	383.6

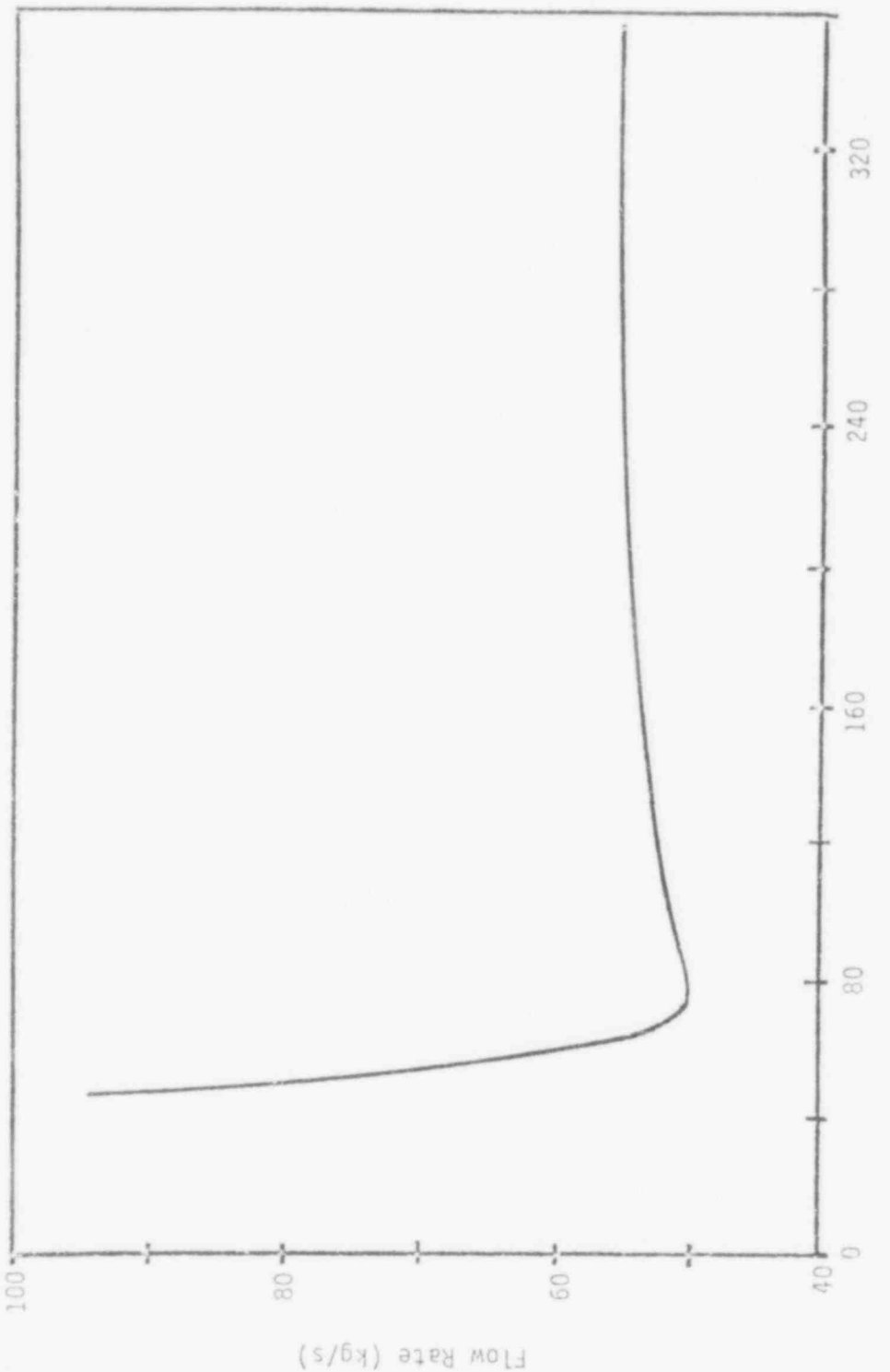

Figure 3.1. Flow Rate in each Primary Loop for the LOEP Event.

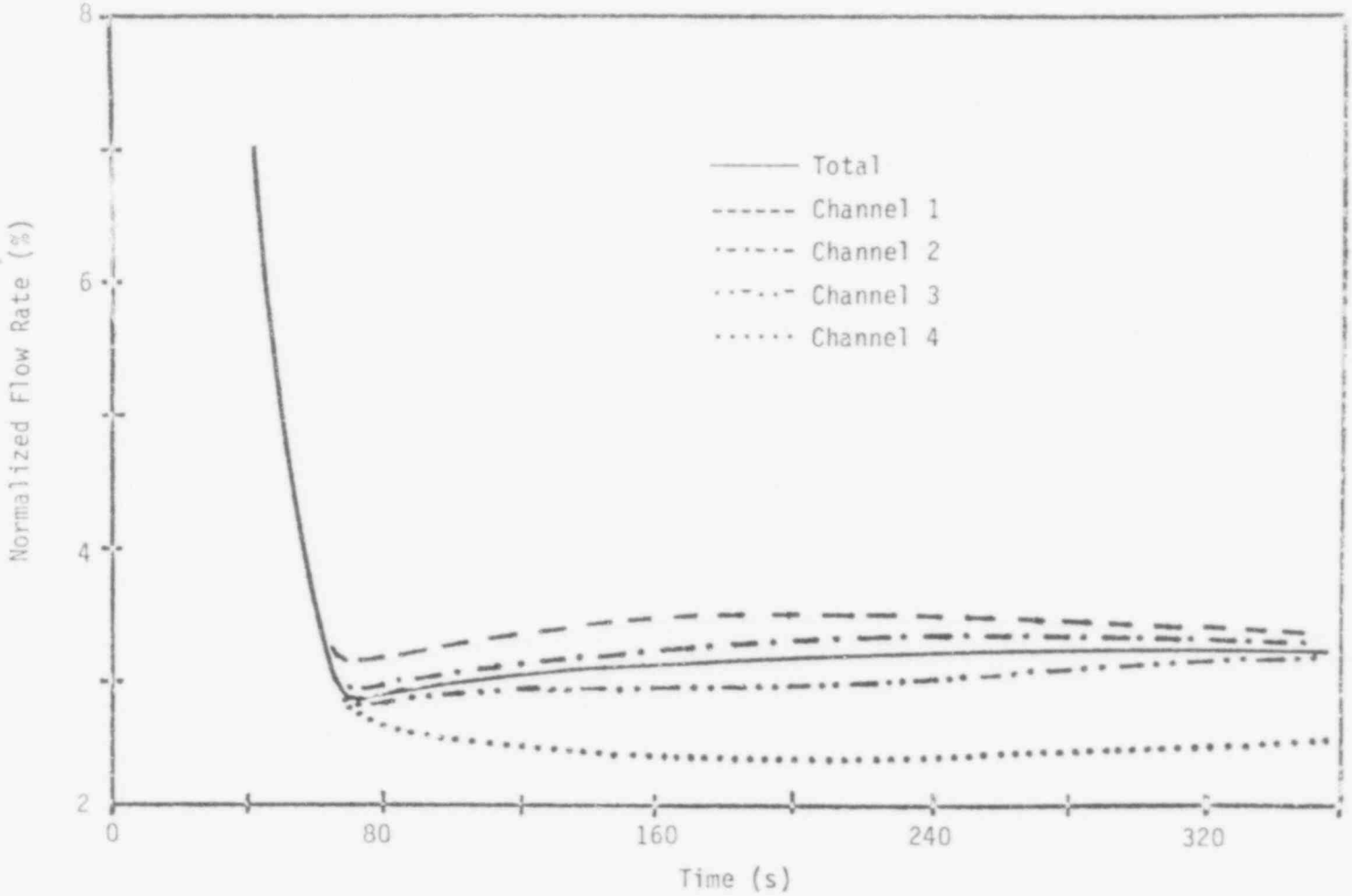

Figure 3.2. Normalized In-Vessel Flow Rates for Case 1.

indicated in Table 3.2, Channel 1 for Cases 5 and 6 corresponds indentically to Channel 1 for Cases 3 and 4 (i.e., hot fuel channel). The power and flow rate of the remaining fuel assemblies are assigned to five fuel assemblies (one for each CRBRP fuel orifice zone). The power and flow rate of the blanket assemblies are assigned to a hot blanket channel representation and to four remaining blanket assemblies (one for each CRBRP blanket orifice zone) in Cases 5 and 6.

The influence of the more detailed model on the maximum hot fuel channel sodium temperature is shown in Figure 3.3 for this LOEP event. The maximum coolant temperatures in the hot channel (Channel 1) for Cases 3 and 5 (i.e., for a four and twelve-channel representation) are displayed in this figure. As seen, the difference between the two cases is almost negligible (less than 5 K at maximum). Since the power in Channel 1 is identical for the two cases, the differences in temperature are due to the small differences in channel flow rate. An important conclusion that can be drawn here is that the prediction of the hot fuel channel temperature is not sensitive to the degree of detailed representation of the remaining fuel assemblies.

A hot channel in blanket assembly was also modeled with the twelve channel representation of the reactor core. For the end-of-equilibrium cycle (EOEC) conditions used in the present study, along with the hot channel characterization, the coolant temperatures in this channel (Channel 7) are highest in the core at steady state. During the LOEP transient, the computed maximum sodium temperatures for the hot blanket channel are shown in Figure 3.4. Results are shown for both with and without flow redistribution cases (Cases 5 and 6, respectively). Note that the maximum coolant temperature exceeds the saturation temperature (~1200 K) by 80 K when interassembly flow redistribution is suppressed. The maximum coolant temperature in the hot blanket channel is found to be less than 1150 K when the coolant flow is allowed to redistribute during transients.

The computing time on the BNL CDC-7600 machine for Case 1 is 334 CPU seconds for 360 seconds of simulation time, or a ratio of CPU time to simulation time of less than 1.0. For the twelve-channel case, the ratio of CPU time to simulation time was less than two.

Major findings of these calculations for this LOEP event are:

1. The interassembly flow redistribution in the reactor core is the most significant factor in affecting the maximum sodium temperature.

2. The hot channel sodium temperature for both the fuel and blanket assemblies are considerably lower than that obtained by scaling up the corresponding average channel temperatures by appropriate time-invariant hot channel factors.

3. The hot channel sodium temperature is not sensitive to the degree of detailed representation of other assemblies.

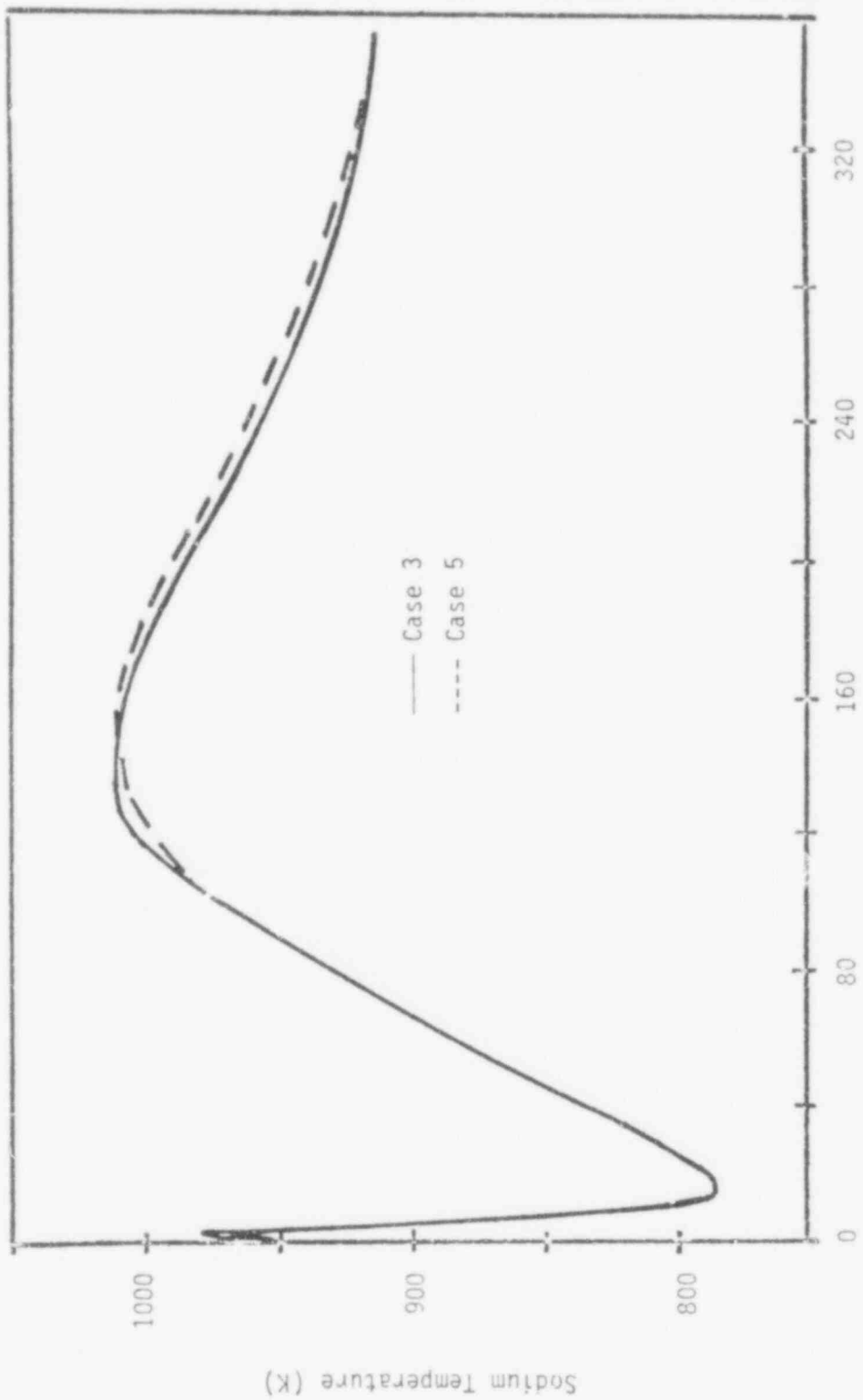

Figure 3.3. Maximum Sodium Temperature in Hot Fuel Channel for Cases 3 and 5.

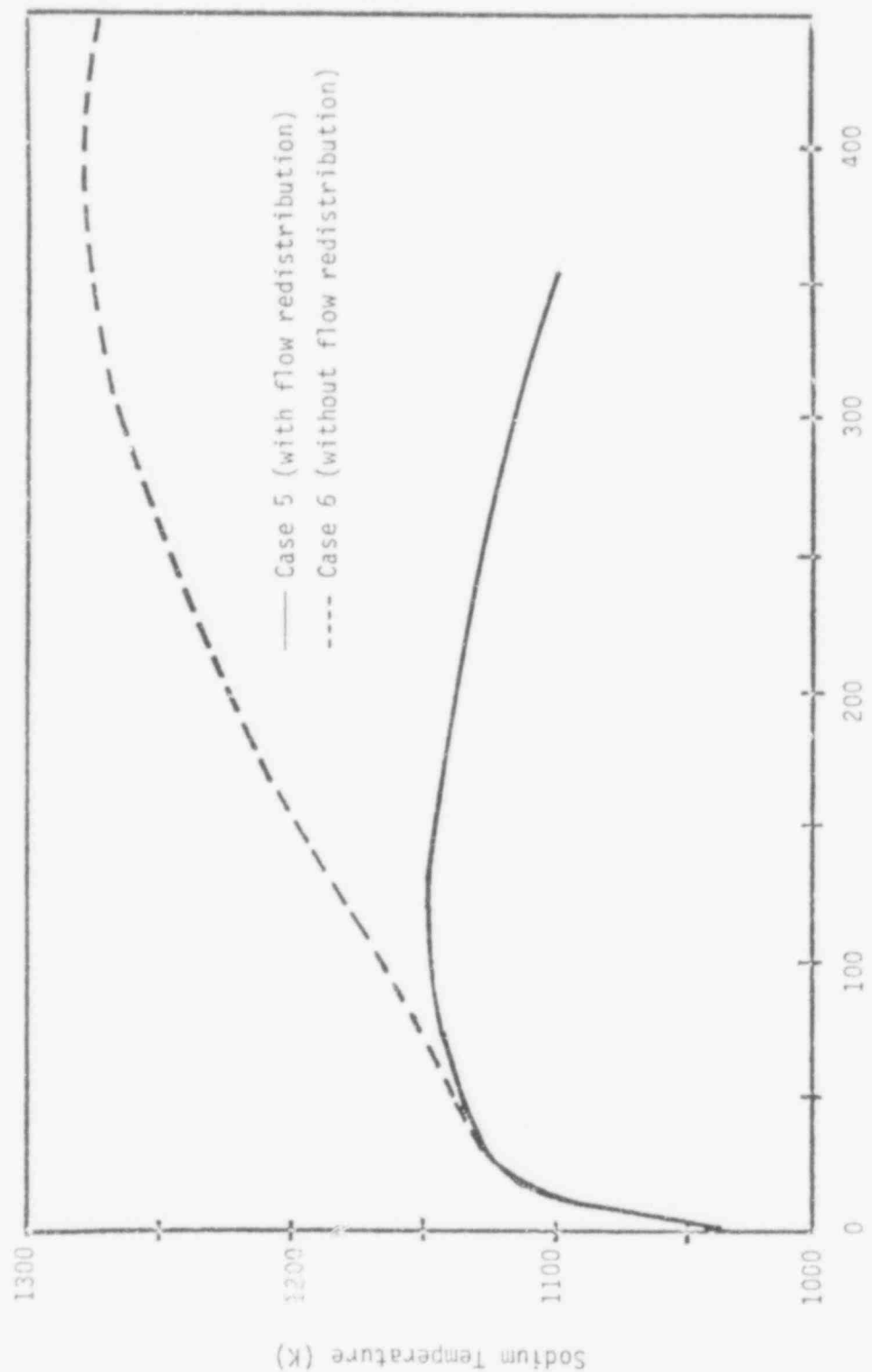

Figure 3.4. Maximum Coolant Temperature in Hot Blanket Channel (Channel 7) for Cases 5 and 6.

4. A minimum of five-channel representation (e.g., one channel each to model explicitly the hot channel in fuel and blanket assemblies, one channel each to model remaining fuel and blanket assemblies and a control rod channel in addition to a bypass channel) of the reactor core is required for adequate prediction of the hot channel temperatures. Additional channels may be utilized for a more complete reactor core temperature mapping.

5. With the interassembly flow redistribution effect included, the maximum hot channel sodium temperatures in the fuel and the blanket assemblies are about 1015 K and 1150 K, respectively. Sodium saturation temperature is about 1200 K.

6. When the interassembly flow redistribution is artifically suppressed, the maximum hot channel sodium temperatures in the fuel and the blanket assemblies would be about 1125 K and 1300 K, respectively. It should be noted that for this calculation, the sodium boiling calculations were not made.

7. The multiple timestep scheme (MTS) used in the SSC-L code permits an efficient usage of the computing machine. On a CDC-7600 machine, the ratio of CPU to problem time for most cases is less than two.

3.1.2 Effect of Decay Heat and Scram-Delay Time (K. E. St.John)

The flow coastdown transient to natural circulation in CRBRP was run for a number of cases in which the decay heat values and the scram time-delays were varied. The scram delay-time is defined as the time elapsed between the initiation of transient and the scram rod insertion. A run matrix was created to attempt parametric studies on the combined effect of scram delay-time and decay heating rates. A total of 15 runs were conducted in which five different scram delay-times were 0.125, 0.375, 0.625, 0.875, and 1.875 seconds from the start of the transient simulation. The simulated decay heat levels were:

1. 125% of the nominal value of fission products decay heating
   110% of the nominal value of transuranics decay heating.

2. 100% of the nominal value for fission product and transuranic decay heating.

3. 75% of the nominal value of fission product decay heating
   90% of the nominal value of transuranic decay heating.

The results obtained from the run matrix were within the range expected. In terms of the coolant temperature at the top of the average fuel channel, it is found that the first peak is dependent on scram times but is insensitive to decay heating levels. The second peak is strongly dependent on the decay heating rates. Figure 3.5 shows the effect of scram time. For the same value of decay heating rates the difference in the peak temperature was 56 K. Figures 3.6 show the effect of the level of decay heating.

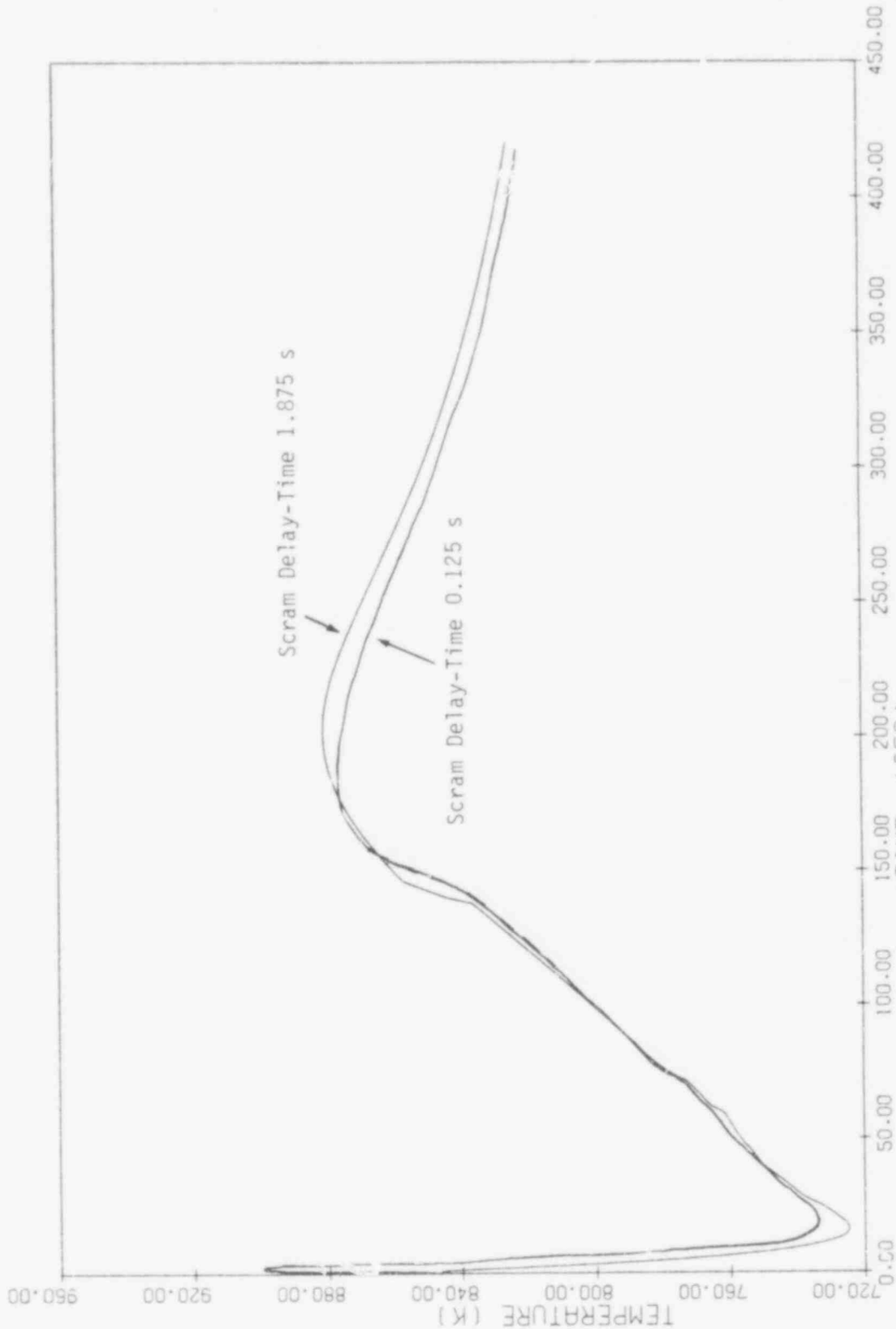

Figure 3.5. The Effect of Scram Delay-Time on Coolant Temperature in Average Fuel Assembly.

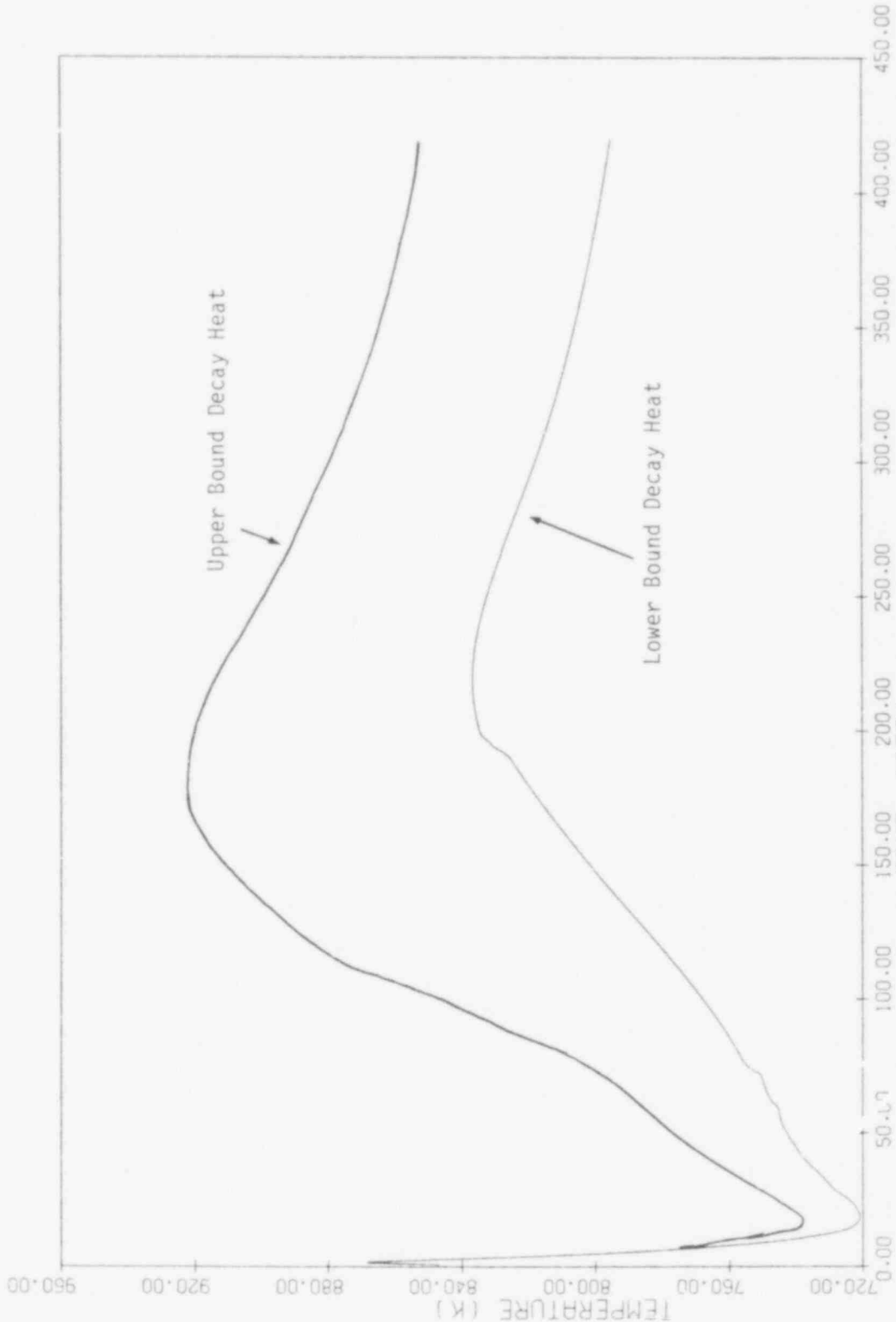

Figure 3.6. The Effect of Uncertainties in After-Heat Values on Coolant Temperature in Average Fuel Assembly.

3.1.3 Sodium Boiling (R. Pyare and T. C. Nepsee)

A single-bubble model for sodium boiling in the reactor core has been described previously (Agrawal, 1978b). The boiling code has been interfaced with the official version of SSC-L and some of the preliminary results for sodium boiling are being presented in this section. The data are taken for the Clinch River Breeder Reactor.

The core of the Clinch River Breeder Reactor is modeled by 4 channels (Case 1 of Table 3.2). The first channel (217) pins represents the average pin in the peak assembly and the second channel consists of all remaining 197 assemblies. The third and fourth channels model radial blanket and control system assemblies, respectively. Bypass channel is also considered in the model as a separate channel.

For the present study, a pipe rupture transient is selected. The break area is the same as the pipe area (0.268 m^2). This represents a double-ended pipe break. The location of rupture is taken at the inlet end of the reactor vessel. The pipe break is initiated at 0 second, and pump trips at 0.125 second. The reactor scram is delayed such that control rods become effective at 0.75 second. The applied reactivity is varied linearly from 0 at 0.75 second to -6$ at 2.75 second. The preliminary results of sodium boiling is represented in Figure 3.7. The formation and collapse of various bubbles seems to continue for a longer period. This calculation is being continued to see if and when boiling is terminated.

3.1.4 Steam Generator Control System (W. L. Weaver III)

During the last quarter, individual models were developed of various elements in the steam generating system which are controlled by the Plant Protection System (PPS) or the Plant Control System (PCS). These elements include, (1) turbine, (2) turbine bypass system, (3) steam generator pressure relief system, (4) main feedwater system, and (5) auxiliary feedwater system. During this quarter, a unified model of these controlled elements was developed. The unified model was made possible by the fact that all of the elements are controlled by varying the positions of valves. The feedwater systems are also controlled by varying the feedwater pump speeds.

The unified model is of the form

$$W(t) = f(W(t), P(t), \alpha_i(t)) \tag{3.1}$$

where

$W(t)$ = time dependent flow rate at interface between controlled element and steam generating system,

$P(t)$ = time dependent pressure at interface between controlled element and steam generating system,

$\alpha_i(t)$ = time dependent parameters describing element, and

$F(W,P,\alpha_i)$ = general non-linear function.

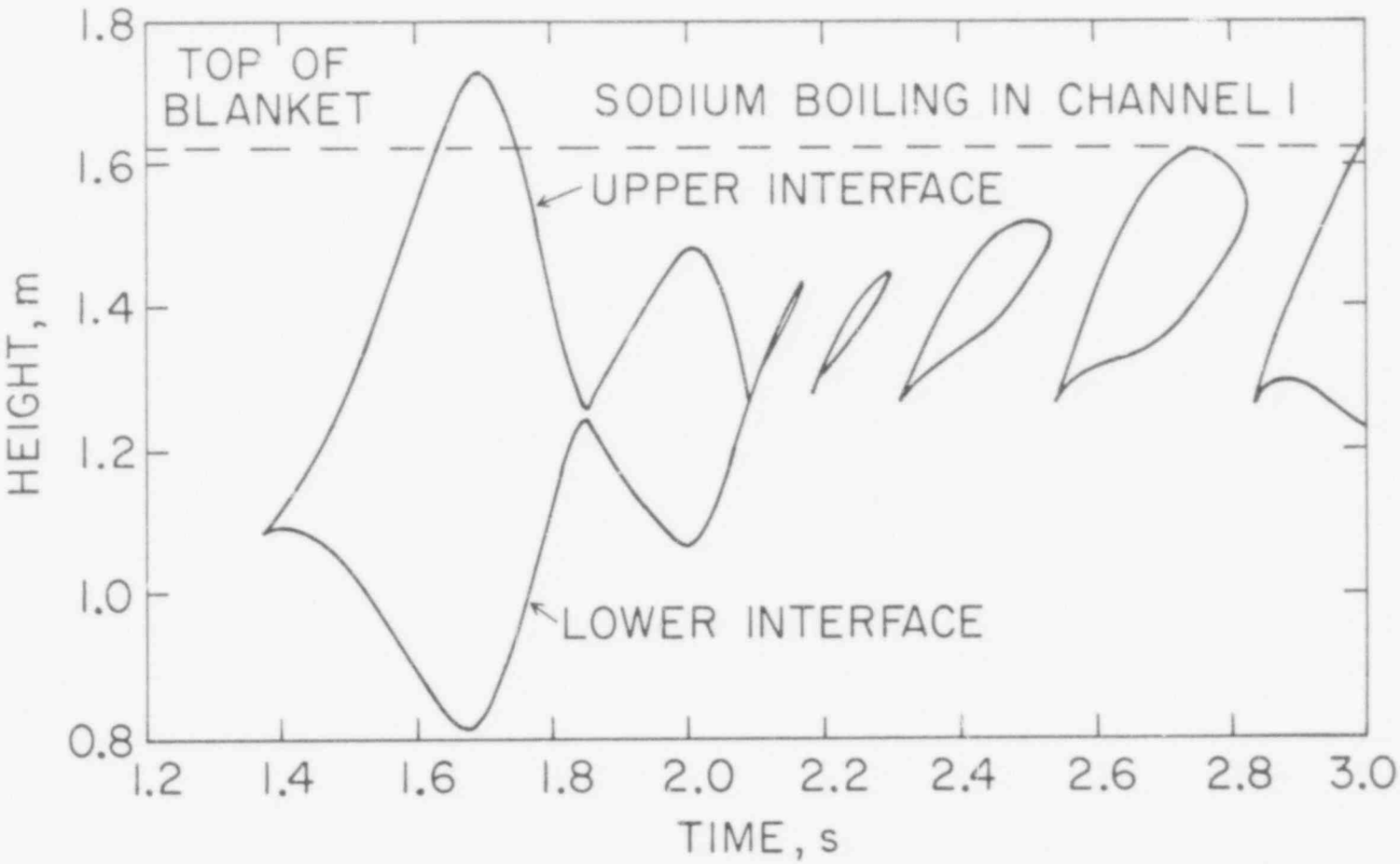

Figure 3.7. Bubble Formation During a Pipe Rupture Transient with Reactor Scram.

The parameters $\alpha_i(t)$ are the controlled variables such as valve position or pump speed. In order to utilize the unified model in the implicit solution algorithm for the steam generator, the flow rate at the interface between the controlled element and the steam generator at the advanced time W^{k+1}, must be expressed as a linear function of the change in the pressure at the interface between the controlled element and the steam generator during the timestep ΔP^{k+1}. This relation is obtained by expanding the non-linear function $f(W, P, \alpha_i)$ in a first order Taylor expansion which yields

$$W^{k+1} = \frac{\left[f(W^k, P^k, \alpha_i^{k+1}) + \frac{\partial f}{\partial P} \Big|^k \Delta P^{k+1} - W^k \frac{\partial f}{\partial W} \Big|^k \right]}{\left[1 - \frac{\partial f}{\partial W} \Big|^k \right]} \tag{3.2}$$

where the values of the parameters at the advanced time, α_i^{k+1}, are supplied by the control system. The form of the general non-linear function $f(W, P, \alpha_i)$ will be given for the various elements.

Turbine

The turbine consists of the turbine control valve and the turbine blade cascade. A quasi-static, single mass velocity flow model is assumed so that the flow rate in the turbine can be determined from the sum of the pressure drops from the turbine inlet to the condenser,

$$P_{TB} + \Delta P_{V,T} + \Delta P_T = P_C \tag{3.3}$$

where

P_{TB} = pressure at inlet of turbine control valve,

$\Delta P_{V,T}$ = pressure drop in turbine control valve,

ΔP_T = pressure drop in turbine blade cascade, and

P_C = pressure in condenser.

Assuming that the flow in blade cascade is choked, the pressure at the inlet of the first stage of the blade cascade can be written as

$$P_{T1} = \Delta P_T + P_C = K_{T1} W_{TB} \tag{3.4}$$

where

K_{T1} = pressure loss coefficient, and

W_{TB} = flow rate in turbine,

The turbine control valve is assumed to be a linear control valve and the flow rate in the valve given by the valve capacity equation for saturated steam (Considine, 1974a) (the correction for steam superheat is very small),

$$C(S) = \frac{W_{TB}}{K P_{TB} (Y_T - 0.148 Y_T^3)} \tag{3.5}$$

$$Y_T = 1.63\sqrt{\frac{\Delta P_{V,T}}{P_{TB}}} \tag{3.6}$$

where

C(S) = position dependent valve capacity,

= $S_T \cdot C(1)$

S_T = normalized valve position,

C(1) = capacity of fully open valve, and

K = constant.

This form of the valve capacity equation covers the region of both choked and unchoked flow in the valve

Substituting for the pressure drop across the valve and rearranging, we obtain

$$W_{TE} = S_T K_{V,T} P_{TB} (Y_T - 0.148Y_T^3) \tag{3.7}$$

$$Y_T = 1.63\sqrt{\frac{P_{TB} - K_{\Gamma 1} W_{TB}}{P_{TB}}} \quad , \text{ and} \tag{3.8}$$

$K_{V,T}$ is a constant.

This relation has the form of the unified model with one parameter, S_T, the turbine control valve position.

Turbine Bypass System

The turbine bypass is used to control the pressure in the steam header whenever the turbine control valve closes during a loss of load on the turbine, and consists of the turbine bypass control valve which is attached directly to the steam header and the piping connecting the valve outlet to the condenser. The model is similar to the turbine except that the pressure drop in the piping is given by

$$\Delta P_{P,B} = K_{BP} W_{BP}^2 \ , \tag{3.9}$$

where

$\Delta P_{P,B}$ = pressure drop in bypass piping,

K_{BP} = pressure loss coefficient, and

W_{BP} = flow rate in bypass.

The bypass valve is also modeled as a linear valve, with the flow rate thru the valve determined from the valve capacity equation for saturated steam. The final result is

$$W_{BP} = S_{BP} K_{V,BP} P_H (Y_{BP} - 0.148 Y_{BP}^3 \tag{3.10}$$

$$Y_{BP} = 1.63\sqrt{\frac{P_H - K_{BP} W_{BP}^2}{P_H}} \tag{3.11}$$

where

S_{BP} = normalized position of bypass valve,

$K_{V,BP}$ = constant, and

P_H = pressure in steam header.

This relation has the form of the unified model with one parameter, S_{BP}, the normalized bypass valve position.

Pressure Relief System

The pressure relief system consists of pressure relief valves which exhaust directly to the atmosphere. The valves are modeled as linear valves and are modeled in exactly the same manner as for the turbine control and turbine bypass valves. The flow rate in the pressure relief system is given

$$W_{PR} = S_{PR} K_{V,PR} P_A (Y_{PR} - 0.148 Y_{PR}^3) \tag{3.12}$$

$$Y_{PR} = 1.63\sqrt{\frac{P_A - P_{ATM}}{P_A}} \tag{3.13}$$

where

S_{PR} = normalized position of pressure relief valve,

$K_{V,PR}$ = pressure relief valve constant,

P_A = pressure at location in steam generator where valve is located, and

P_{ATM} = atmospheric pressure.

This relation has the form of the unified model with one parameter, S_{PR}, the normalized pressure relief valve position.

Main Feedwater Systems

The model of the feedwater system is much more complicated than those described previously because it contains a pump as well as a control valve. The feedwater system consists of the feedwater header, which is the feedwater source, the feedwater pump with the control valve attached directly to the pump discharge nozzle, and the piping which connects the pump to the feedwater header and the control valve outlet to the remainder of the steam generating system. The feedwater flow rate is given by the solution to the momentum equation for the feedwater system where a single mass velocity flow model has been assumed,

$$\left(\frac{L}{A}\right)\frac{dW_F}{dt} = P_{FH} + \Delta P_p - \Delta P_{p,F} - \Delta P_{V,F} - P_{SG} \qquad (3.14)$$

where

$\left(\frac{L}{A}\right)$ = overall inertance of piping in feedwater system,

W_F = feedwater flow rate,

P_{FH} = pressure in feedwater header,

ΔP_p = pressure rise in feedwater pump,

$\Delta P_{p,F}$ = pressure drop in piping in feedwater system,

$\Delta P_{V,F}$ = pressure drop in feedwater control valve, and

P_{SG} = pressure at location in the steam generator where feedwater is added.

Expressing the pressure drop in the piping in terms of a pressure loss coefficient,

$$\Delta P_{p,F} = K_F W_F^2$$

where

K_F = presure loss coefficient.

and the pressure drop across the feedwater control valve in terms of a capacity equation for a linear valve in liquid service, (Considine, 1974b)

$$C(S_F) = \frac{W_F}{K\sqrt{\Delta P_{V,F}}} \quad , \qquad (3.15)$$

where

$C(S_F)$ = position dependent valve capacity, and

S_F = normalized feedwater valve position,

the flow rate in the feedwater system can be written as

$$W_F^{k+1} = W_F^k + \Delta t^{k+1} \left\{ \frac{P_{FH}^{k+1} + \Delta P_p^{k+1} - \left(W_F^{k+1}\right)^2 \left[K_F + \left(\frac{1}{S_F K_{V,F}}\right)^2\right] - P_{SG}^{k+1}}{\left(\frac{L}{A}\right)} \right\} \quad (3.16)$$

where

$K_{V,F}$ = feedwater control valve constant.

The feedwater header pressure is assumed to be a user input constant and the flow squared term is written as,

$$\left(W_F^{k+1}\right)^2 = W_F^k \cdot W_F^{k+1} \quad (3.17)$$

so that the feedwater flow rate can be expressed in the form of the unified model as,

$$W_F^{k+1} = \frac{W_F + \frac{\Delta t}{(L/A)} \left\{ P_{FH}^{k+1} + \Delta P_p^{k+1} - P_{SG}^{k+1} \right\}}{\left\{ 1 - W_F^k \left[K_F + \left(\frac{1}{K_{V,F} S_p} \right)^2 \right] \cdot \frac{\Delta t}{(L/A)} \right\}} \quad (3.18)$$

with two parameters, S_F, the feedwater control valve position, and ΔP_p^{k+1}, the feedwater pump pressure rise.

The pressure rise across the feedwater pump can be found from the homologous pump characteristics for the feedwater pump in terms of the feedwater flow rate and feedwater pump speed.

The pump speed is determined from the momentum equation for the rotating mass consisting of pump impeller, shaft, and motor armature,

$$I \frac{d\omega}{dt} = \tau_m - \tau_f(\omega) - \tau_{hy}(\omega, W) \quad (3.19)$$

where

I = moment of inertia of rotating mass,

ω = angular speed of pump,

τ_m = motor torque,

$\tau_f(\omega)$ = frictional torque, and

$\tau_{hy}(\omega, W)$ = hydraulic torque.

The motor torque is generated by the drive motor and computed by the pump controller. The pump speed is found implicitly from the momentum equation by expanding the torques in first order Taylor expansions, to give

$$\omega^{k+1} - \omega^k = A_p + B_p \left(W^{k+1} - W^k\right) \quad (3.20)$$

where

$$A_p = \frac{\tau_m^{k+1} - \tau_f^k - \tau_{hy}^k}{\frac{\Delta t}{I} + \frac{\partial \tau_f}{\partial \omega} + \frac{\partial \tau_{hy}}{\partial \omega}} \text{, and} \tag{3.21}$$

$$B_p = \frac{-\left(\frac{\partial \tau_{hy}}{\partial W}\right)}{\frac{\Delta t}{I} + \frac{\partial \tau_f}{\partial \omega} + \frac{\partial \tau_{hy}}{\partial \omega}} \text{.} \tag{3.22}$$

The pump pressure rise is then given by

$$\Delta P_p^{k+1} = \rho\ g\ H\ (\omega^{k+1}, W^{k+1})$$

$$= \rho^k\ g \left[H(\omega^k, W^k) + \frac{\partial H}{\partial \omega} (\omega^{k+1} - \omega^k) + \frac{\partial H}{\partial W} (W^{k+1} - W^k) \right] \tag{3.23}$$

where the homologous pump head characteristic $H(\omega^{k+1}, W^{k+1})$ has been expressed in terms of the known values at the beginning of the time step by means of a first order Taylor expansion. The pump speed is eliminated from this relation to give,

$$\Delta P_p^{k+1} = C_p + D_p\ (W^{k+1} - W^k) \tag{3.24}$$

where

$$C_p = \rho^k\ g \left[H^k + \frac{\partial H}{\partial \omega} A_p \right] \text{, and} \tag{3.25}$$

$$D_p = \rho^k\ g \left[B_p \frac{\partial H}{\partial \omega} + \frac{\partial H}{\partial W} \right] \text{.} \tag{3.26}$$

The pump pressure rise is then substituted into the equation for the feedwater flow rate, Equation (3.18), which yields,

$$W_F^{k+1} = A_F + B_F\ \Delta P_{SG}^{k+1} \tag{3.27}$$

where

$$A_F = \frac{W_F^k \left[1 - \frac{\Delta t}{(L/A)} D_p \right] + \frac{\Delta t}{(L/A)} \left[P_{FH}^{k+1} - P_{SG}^k + C_p \right]}{1 - \frac{\Delta t}{(L/A)} \left\{ D_p - W_F^k \cdot \left[K_F + \frac{1}{K_{V,F}\ S_F} \right]^2 \right\}} \text{, and} \tag{3.28}$$

$$B_F = \frac{-\left[\frac{\Delta t}{(L/A)}\right]}{1 - \frac{\Delta t}{(L/A)}\left\{D_p^{-} - W_F^k\left[K_F + \left(\frac{1}{K_{V,F}\, S_F}\right)^2\right]\right\}} \qquad (3.29)$$

This relation can be used directly since it is a linear relation and has the form of the unified model with two parameters, S_F, the feedwater control valve position, and τ_m the feedwater pump drive motor torque. These two parameters are computed by the PPS/PCS subroutines.

Auxiliary Feedwater System

The auxiliary feedwater system is modeled in exactly the same manner as the main feedwater system. However, the auxiliary feedwater pump may be a turbine driven pump rather than a motor driven pump, in which case the drive motor torque is replaced by the turbine torque. The auxiliary feedwater turbine is modeled in the same manner as the main turbine.

3.1.5 Steam Tables Simplifications (W. L. Weaver III and G. J. Van Tuyle)

The steam tables routines compute the various transport properties, conductivity, specific heat, viscosity, surface tension, etc., as well as the fluid density and temperature as a function of pressure and enthalpy for the water and steam phases. A check was made in each property subroutine to verify that the enthalpy and pressure input into the subroutine for a liquid property were in the liquid region and vice versa. If the input properties were in the wrong phase region, an error message was generated and the property computed at the saturation line for the phase region specified by the property routine. Their checks are very time consuming because of the large number of times that the property routines are called during each timestep, and were redundant since the same check was being made to determine which property routine was to be called. The checks in the individual property routines have been removed.

The thermohydraulic properties, density and temperature, were calculated by a master subroutine which determined the phase region from the input pressure and enthalpy and called the individual property subroutines. The calculation of the temperature is only needed during the computation of the surface heat fluxes in the heat exchangers so that the master routine was modified to compute the temperature only when needed. The removal of the check on the phase region by the individual property routine and by eliminating the extraneous calculation of the fluid temperatures reduced the CPU time per timestep by a factor of approximately 3, from 4 m sec per node per timestep to 1.2 m sec per node per timestep.

Functional fit steam tables, as provided by L. Agee, were coded into function subprograms form. These tables have a wider range of applicability than the steam tables currently in the SSC-L package, and because of a quirk in the usage of one of the functions, may provide a computational advantage as well. Both functions and function derivatives have been verified outside the SSC package. However, because of other projects of higher priority, the new steam tables have not been fully implemented and tested in SSC-L at this time.

3.1.6 Plant Protection and Control System (M. Khatib-Rahbar and F. S. Srinivasan)

The work during this quarter was directed toward debugging and testing of the combined PPS/PCS and the SSC-L model. In addition, a meeting was held with the Nuclear Regulatory Commission staff members to discuss the program on PPS/PCS and some of the preliminary results.

Several operational transients have been simulated to check the interfacing between the PPS/PCS model and the remainder of the code. As an example, transient results for a 10% ramp change in load demand in 40 s are shown in Figures 3.8 through 3.13.

Figure 3.8 shows the transient forcing function as a function of time. It is observed the load demand is reduced from 100% to 90% in 40 s and held constant thereafter. The response of the individual controllers are seen from the control rod position (Figure 3.9) and motor torque (Figure 3.11) time responses causing a reduction in the reactor power level (Figure 3.10), pump speed (Figure 3.11) and thereby the sodium flow rate (Figure 3.12).

Figure 3.13 shows the CPU comparison for this transient and it is observed that the PPS/PCS running time is quite reasonable as compared to the rest of the code.

3.1.7 Heat Transport System (I. K. Madni and E. G. Cazzoli)

Pump characteristics were extended to include both the HAN and HVN curves during steady-state calculations. Corresponding changes were also made to the head polynomial equation to be solved for pump speed. Pipe break computations were improved through the inclusion of an iteration logic to obtain a converged jet discharge velocity at the start of the transient.

In June, 1978, a topical report describing the sodium pump model in SSC-L (Madni, 1978) was prepared and published. A few errors had gone unnoticed in Tables A.I and A. II of the report. These tables listed the complete pump head and torque characteristic coefficients. The errors have been removed and the corrected tables are reproduced in this report as Table 3.4.

3.1.8 Code Update (R. J. Kennett)

A substantial programming effort was required during this quarter to incorporate the PPS/PCS systems into SSC-L. Modifications were required to the transient input reader and data management routines to handle the data for these new modules.

During this quarter a series of changes were made to the code to aid program debugging and to improve the output capabilities.

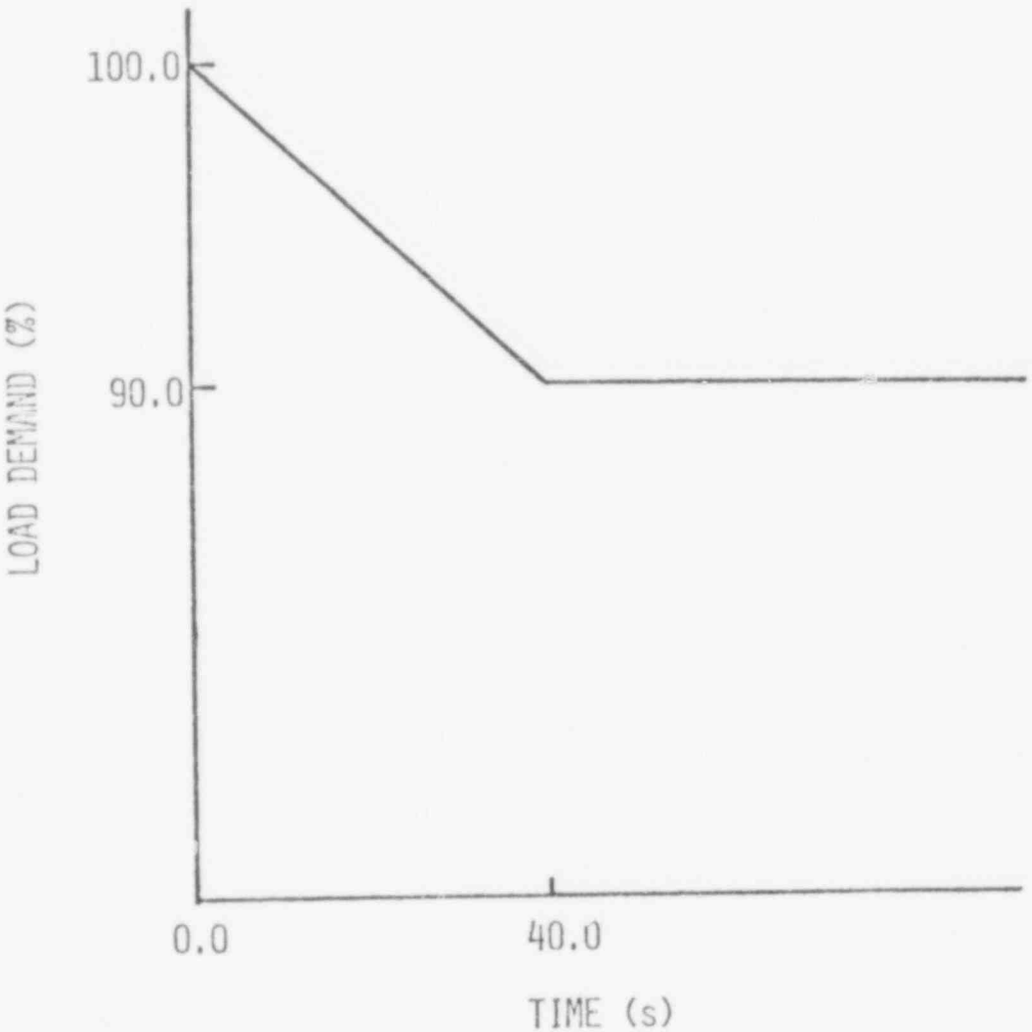

Figure 3.8. Transient Forcing Function

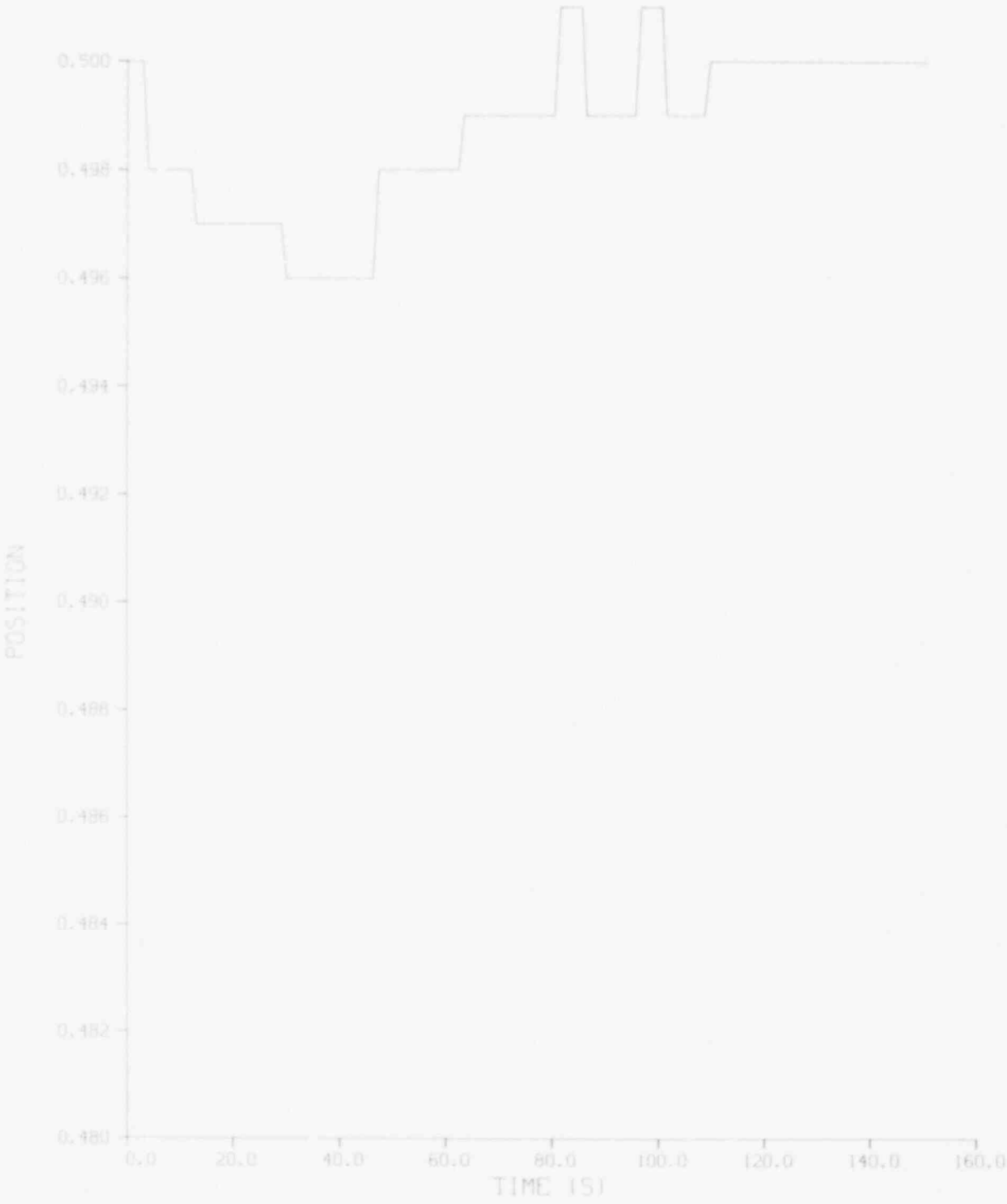

Figure 3.9. Fractional Withdrawal of the Primary Control Rod (Fine Regulating Rod).

Figure 3.10. Neutron Flux Amplitude.

Figure 3.11. Drive Motor Fractional Torque.

Figure 3.12. Fractional Sodium Flow in the Primary Circuit.

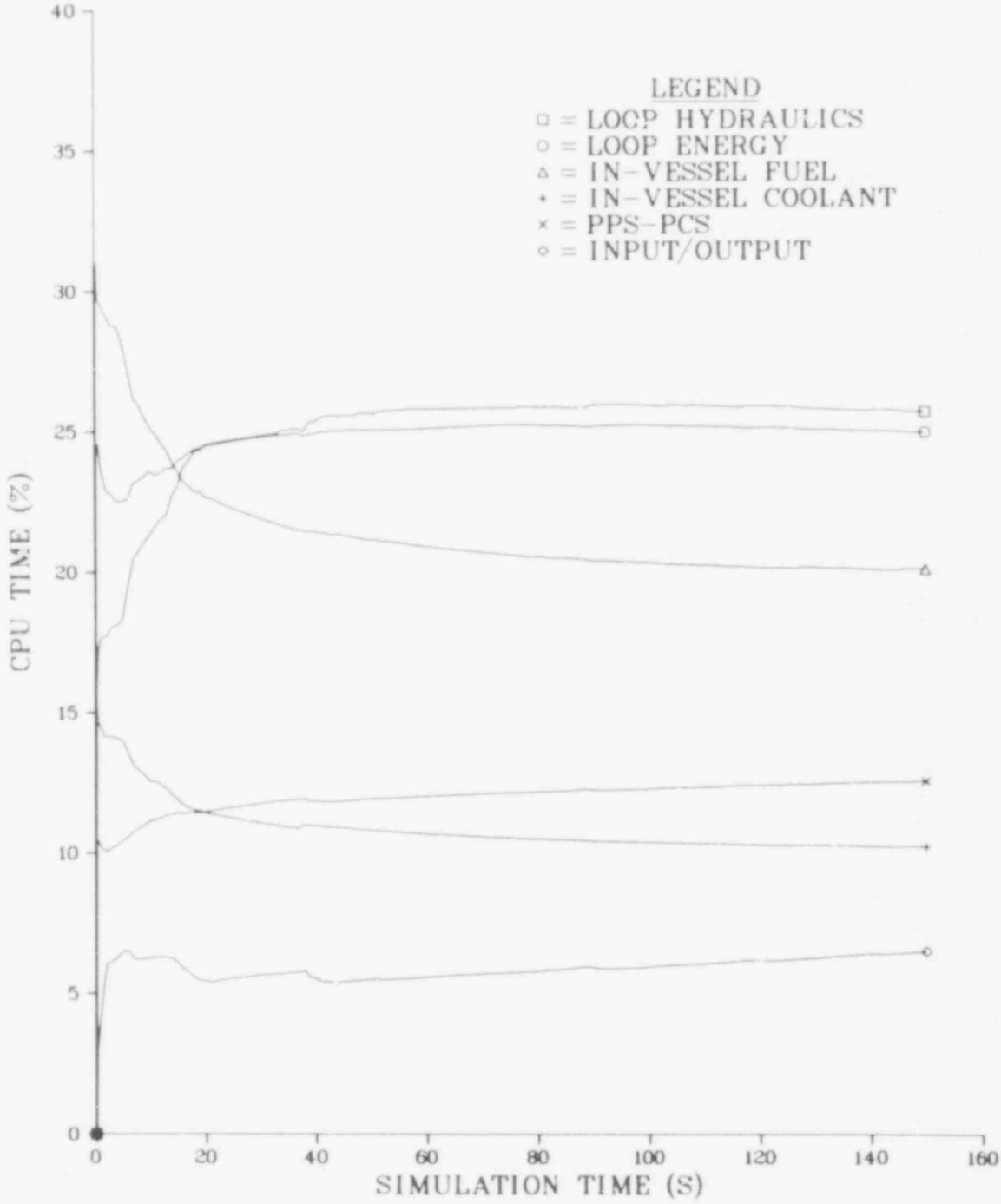

479 276 Figure 3.13. Comparisons of Computer Running Time.

Table 3.4 Homologous head and torque polynomial coefficients (H,B≡head or torque curve; A or V≡division by α^2 or ν^2; N,D,T or R≡normal, energy dissipation, turbine, or reverse pump region)

(I) Curves \ Coeff.	c_0	c_1	c_2	c_3	c_4	c_5
1 HVN	−0.556	0.85376	0.82906	−3.7106	7.0593	−3.4776
2 HAN+HAD	1.2897	−0.061907	0.17327	−0.57294	0.033762	0.13865
3 HVD	0.69189	0.43961	0.68459	−0.24701	0.63156	−0.20833
4 HVT	0.69209	−0.46132	0.92592	−0.4308	0.50845	−0.22436
5 HAT	0.63405	0.20178	−0.30242	0.76603	−0.48077	0.19231
6 HAR	0.63405	0.14665	−4.1896	−2.4828	0.89730	0.0
7 HVR	−0.556	0.66362	−0.086081	−0.93928	−0.57381	0.0
1 BVN	−0.37069	0.41741	3.8511	−7.6752	7.0695	−2.2917
2 BAN+BAD	0.44652	0.5065	0.59643	−0.64055	−0.025531	0.11531
3 BVD	0.8658	0.28437	−0.22348	0.45083	−0.70586	0.21562
4 BVT	0.86533	−0.60816	3.1497	−9.3647	10.418	−4.0064
5 BAT	−0.68468	1.8495	0.96871	−8.9653	12.045	−4.7546
6 BAR	−0.384	2.0342	−0.95477	−0.42286	0.0	0.0
7 BVR	−0.372	2.3716	−0.56147	0.0	0.0	0.0

3.2 SSC-P (I. K. Madni)

3.2.1 Initialization (I. K. Madni and S. F. Carter)

During this reporting period, the steady-state code was successfully debugged and a converged solution was obtained. Input data and individual modules were upgraded and modified. The steady-state results are now, in general, consistent with known and expected PHENIX operating values. Some of the modifications are described below.

Level Calculations

For the hot pool design we can write, from static balance

$$P_{Xin} = P_{gas} + \rho_H g(Z_{HP} - Z_{Xin}) \tag{3.30}$$

$$P_{Xo} = P_{gas} + \rho_C g(Z_{CP} - Z_{Xo}) \tag{3.31}$$

Subtracting Equation (3.31) from Equation (3.30) and rearranging yields

$$Z_{CP} = \left[\rho_H(Z_{HP} - Z_{Xin}) - \frac{\Delta P_X}{g} + \rho_C Z_{Xo}\right]/\rho_C \tag{3.32}$$

Knowing Z_{HP}, ΔP_X and IHX elevations, the cold pool level Z_{CP} is calculated from Equation (3.32). ΔP_X comprises both the losses due to friction, turning, area expansion and contraction effects, as well as the gravity gain as the coolant moves downward in the IHX. With this definition, the code calculates a level difference between pools equal to 66.405 cm. The volume of cover gas is obtained simply as

$$V_{gas} = (Z_{tank} - Z_{HP})A_{hg} + (Z_{tank} - Z_{CP})A_{cg} \tag{3.33}$$

where A_{hg}, A_{cg} are, respectively, the areas of hot pool and cold pool in contact with the cover gas.

Check Valve

The check valve equation during steady-state has been modified to

$$\Delta P_{CP} = \frac{KW|W|}{\rho_{CP}} + \rho g \Delta Z_{CV} \tag{3.34}$$

The extra term describes gravity loss or gain in the valve. It will be zero if the valve is placed horizontally (through user-input ΔZ_{CV}).

Pumps

For the PHENIX primary pumps, the specific speed, N_S, is calculated as 35.92 (S.I. units), and for the secondary pumps, N_S = 36.67. Since the pump model in SSC-L is based on data for N_S = 35, no changes are proposed for the characteristic coefficients.

External Bypass

The code models external bypass flow, a small fraction of the total pump flow that leaks down from the core inlet plenum and up between the outer baffle and the tank wall. With known core flow and bypass fraction, the code calculates the loss coefficient accounting for all losses in the external bypass as

$$K_{BP} = (\Delta P_{BP} - \rho_c g\ Z_{BPo})\rho_c/(W_{BP}|W_{BP}|) \qquad (3.35)$$

K_{BP} is held constant during transient computations.

Cold Pool

The expression for pressure drop in the cold pool has a term added to account for losses occurring as the fluid turns upward in the annulus towards pump inlet. The annulus is present in the PHENIX design and may or may not be present in other designs. Its purpose seems to be to minimize the impact of cold pool stratification (during IHX under-cooling events) on the inlet temperature to the core.

Barrier Heat Transfer

A study was made to evaluate the sensitivity of barrier overall heat transfer coefficients to temperature, e.g., U_{hm2} to T_{m2} and T_{HP}, and an option has been added to the code that allows the user to specify U_{hm2} and U_{cm2}, bypassing UBRRIU altogether. These coefficients would then remain constant during transient computations.

3.2.2 Transient (I. K. Madni and E. G. Uzzoli)

Model equations describing transient primary system hydraulics for the hot pool concept have been formulated. The equations, logic, parameter definitions and names, etc., have been set up for programming. More PHENIX data relevant to transient computations is urgently needed.

3.3 SSC-S Code (W. L. Weaver III)

3.3.1 Identification of Areas of Developmental Effort (W. L. Weaver III and G. J. Van Tuyle)

One accomplishment during this quarter was to separate the various tasks and subtasks outlined in the work plan for the development of the SSC-S Code (Weaver, 1978) into two main areas of effort. These two areas are the

in-vessel portions of the plant and the balance of plant. The two areas are natural divisions because of the geometric arrangement of the plant which is reflected in the calculational aspects of the simulation. As a result of the identification of major areas of effort, personnel have been assigned prime responsibility for these areas of the developmental effort.

3.3.2 In-Vessel Model (G. J. Van Tuyle)

The in-vessel model to be used in SSC-S was given preliminary consideration. Discussions with Professor John E. Meyer of M.I.T. revealed the possibility of significant inter-assembly radial heat transfer in EBR-II, under certain flow conditions. Consideration of this and other modeling efforts indicate possible advantages in loading S-type module into the extant SSC-L package, rather than creating a stand-alone SSC-S.

3.3.3 Auxiliary Feedwater System (W. L. Weaver III)

The second milestone in the development of the SSC-S code was satisfied during the quarter with the development of a model of the auxiliary feedwater system. This system will be needed to replace the fluid lost by the steam generating system whenever the reactor generated decay heat as well as the heat transferred from the system components to the sodium coolant is dissipated to the atmosphere by venting of the steam generated in the steam generator. The constant enthalpy auxiliary feedwater will be supplied from a large water tank. The hydraulic model of the auxiliary feedwater system which was developed for the SSC-L code and which is described in this quarterly report will be utilized in the SSC-S code to calculate the auxiliary feedwater flow rate. If the auxiliary feedwater pump is a turbine driven pump, rather than electrically driven pump, the drive motor torque in the pump speed equation will be replaced by the turbine torque. The turbine torque will be calculated from the homologous torque curves for the turbine as a function of turbine speed and turbine flow rate where flow rate thru the auxiliary turbine will be computed in the same manner as the flow rate in the main turbine.

PUBLICATIONS:

The following is a list of publications during the current reporting period from this activity:

AGRAWAL, A. K., et al., "Users' Manual for the SSC-L Code," Brookhaven National Laboratory, BNL-NUREG-50914 (October 1978).

GUPPY, J. G., and AGRAWAL, A. K., "SSC-L Simulation of System Transients in CRBRP," Brookhaven National Laboratory, BNL-NUREG-25100 (November 1978).

GUPPY, J. G., and AGRAWAL, A. K., Confirmatory Simulation of Safety and Operational Transients in LMFBR Systems," Paper presented at the International Meeting on Nuclear Power Reactor Safety, October 16-19, 1978, Brussels, Belgium.

MEYER, J. E., "Some Physical and Numerical Considerations for the SSC-S Code," Brookhaven National Laboratory, BNL-NUREG-50913 (November 1978).

ST.JOHN, K. E., AGRAWAL, A. K. and GUPPY, J. G., "A Comparison Between SSC-L and BRENDA System Codes," Brookhaven National Laboratory, BNL-NUREG-25099 (October 1978).

REFERENCES

AGRAWAL, A. K., et al., (1978a), "SSC Code Development" in Reactor Safety Research Programs Quarterly Progress Report, July 1-September 30, 1978, Brookhaven National Laboratory, NUREG/CR-05013, BNL-NUREG-50931, pp. 118-137 (November 1978).

GUPPY, J. G., and AGRAWAL, A. K., (1978), "SSC-L Simulation of System Transients in CRBRP," Brookhaven National Laboratory, BNL-NUREG-25100 (November 1978).

WEAVER, W. L. III, and AGRAWAL, A. K., (1978), "A Work Plan for the Development of SSC-S," Brookhaven National Laboratory, BNL-NUREG-24609, (June 1978).

CONSIDINE, D. M., (ed.), (1974a), Process Instruments and Controls Handbook, McGraw-Hill, pp. 19-48.

CONSIDINE, D. M., (ed.), (1974b), Process Instruments and Controls Handbook, McGraw-Hill, pp. 19-47.

4. SSC Code Validation (A. K. Agrawal and R. J. Cerbone)

The SSC Validation work during this quarter covers the following areas

4.1 Intercomparison of SSC-L and IANUS

4.2 Analyses of Thermohydraulic Experiments

4.3 Intercomparison of SSC-L with BRENDA

4.1 Intercomparison of SSC-L with IANUS (J. W. Yang)

Comparison between SSC-L (Agrawal 1978a) and IANUS (Wolfe, 1976) continued as part of the preparation for the pre-analysis of the pre-operational tests to be conducted as part of the FFTF startup program. Since these tests, coupled to the planned natural circulation tests, will play a dominant role in the SSC Verification program, it was essential that this work proceed as quickly as possible. During this quarter, simulation and partial testing for the primary loop of FFTF was completed. The loss of electric power followed by scram was calculated using SSC-L and IANUS. Comparisons between the results obtained with each code are reasonably close; differences remain to be resolved.

4.1.1 SSC Modeling of FFTF

In order to provide a consistent basis of comparison with IANUS, only three channels were used. These are a hot channel, average channel and a bypass channel. Recall that IANUS is a single channel code while SSC is a multi-channel code. One fuel assembly was selected to represent the "hot channel" and the remaining 75 assemblies are grouped together as the "average" channel. The power ratio of the hot to average channel is taken 1.592 while the flow ratio is 0.892. The ratios were determined such that the SSC-L calculated enthalpy agreed with the IANUS calculation using a 1.79 hot channel factor. The selection of the SSC channels is given in Table 4.1 where approximately 82% of the coolant flow passes through the fuel subassemblies which generate about 95% of the total power. The bypass channel then includes all other coolant paths in the core. It is characterized by the remainder of total flow and power values.

Table 4.1

Selection of Channels for SSC-L Analysis

	Number of Assemblies	Fraction of Flow	Fraction of Power
Hot Channel	1	0.009625	0.01986
Average Channel	75	0.80935	0.93207
Bypass Channel	--	0.181025	0.04807

4.1.2 Steady State Calculations

In order to provide a consistent basis of comparison between IANUS and SSC-L, a great deal of effort was devoted to preparing the input data. The input data then underwent further checking provided by the steady state comparisons between the two codes. The input data requirements for SSC-L are different from IANUS, because of the degree of detail available in SSC-L to model the reactor. In addition, the two codes have vastly different code structures. All the input data used in SSC-L were obtained from design and operation information used in the IANUS (Wolfe, 1976) Code. Loss coefficients in the loop system were computed according to the correlations given by Wolfe (1976). Using the input data, a steady-state condition was established for the SSC-L code. Comparison for the steady state thermohydraulics indicates good agreement between the two codes. The pump performance, pressure drop and temperature rise of the coolant in various components are shown in Table 4.2. The overall good agreement lends confidence in the consistency of the input data for the primary heat transport loop.

Table 4.2

Comparison of Steady-State Coolant Dynamics Predicted by SSC-L and IANUS

	IANUS	SSC-L
Pump		
Head, m	146.9	147.4
rpm	1088.5	1090.6
p, psi	170.9	170.6
Q, gpm	14304.8	14353.1
Pressure Drop		
Vessel	134.5	134.4
IHX*	9.27	9.27
Check Valve*	9.53	9.55
Vessel to Pump	1.04	1.08
Pump to Vessel	35.4	35.1
Temperature Rise, K		
Vessel	143.5	141.7
Core Hot Channel	295.1	293.1
Core Ave. Channel	164.7	163.3
IHX (Primary)	143.3	143.8
IHX (Secondary)	143.3	142.6

*Included in Pump to Vessel Pressure Drop

4.1.3 Transient Calculations

The transient flow and power are the most important variables affecting the transient thermohydraulic behavior of the entire plant. Hence, it was essential that the transient power and flow used by SSC-L and IANUS agree.

Figure 4.1 shows comparisons between the two codes in predicting the transient flow and power due to the pump coastdown and scram. Comparisons of the transient flow indicate good agreement up to about 150 seconds. It should be noted that so far the immediate heat transport loop and the DHX have not been modeled. These will have a major impact on the overall calculations beyond, say, one hundred seconds. The transient flow computation includes not only the pump model but also includes the hydraulics of the entire primary loop and vessel. Thus, the good agreement indicates consistency between the two codes for computing the hydraulics in the two codes. Agreement between calculated transient powers, however, was obtained by adjusting the scram rod reactivity insertion rate in SSC-L to match the fission power response to that obtained with IANUS. From the good agreement obtained for the steady-state conditions coupled to the good agreement on transient flow and power, a basis for comparison of the transient computations has been demonstrated.

SSC-L predicted coolant temperatures at the top of the active fuel region for both the hot and average channel are shown in Figure 4.2. It should be pointed out that, through the verification effort, certain bugs were discovered in the SSC-L code. In the present calculations, the transient effect of the associated hexcan structure was not computed.

Figures 4.3 and 4.4 illustrate detailed comparisons of the transient coolant temperature of the hot and average channel, respectively. There are differences between the shape of the temperature curves as predicted by SSC-L and IANUS. A broader peak developed at a later time in the transient is calculated by SSC-L. The difference may be the interaction with fuel rod and structure. It is noted, once again, that the lack of IHTS and DHX in the present SSC-L calculations makes more direct comparison between the two codes difficult.

In addition to the coolant dynamics in the vessel, transient results of other components were also examined. For example, in the study of IHX performance, it was found that the transient temperature distribution strongly depends on the number of nodes used in the model. A detailed sensitivity study of the IHX should, therefore, be performed.

4.1.4 Conclusion from Analyses to Date

Code verification is a continuing process in which experience from the verification process is fed back into the code development. The intercomparison of SSC-L and IANUS in predicting the steady state and transient response of FFTF is only a first step in the SSC-L verification process. The conclusions to be drawn from these comparisons to date are:

1. SSC-L and IANUS prediction of FFTF hydraulics are in good agreement. There is overall consistency between the two codes.

2. Both codes predict essentially the same steady state primary loop operating conditions.

3. Both codes predict essentially the same temperature distributions in the primary loop.

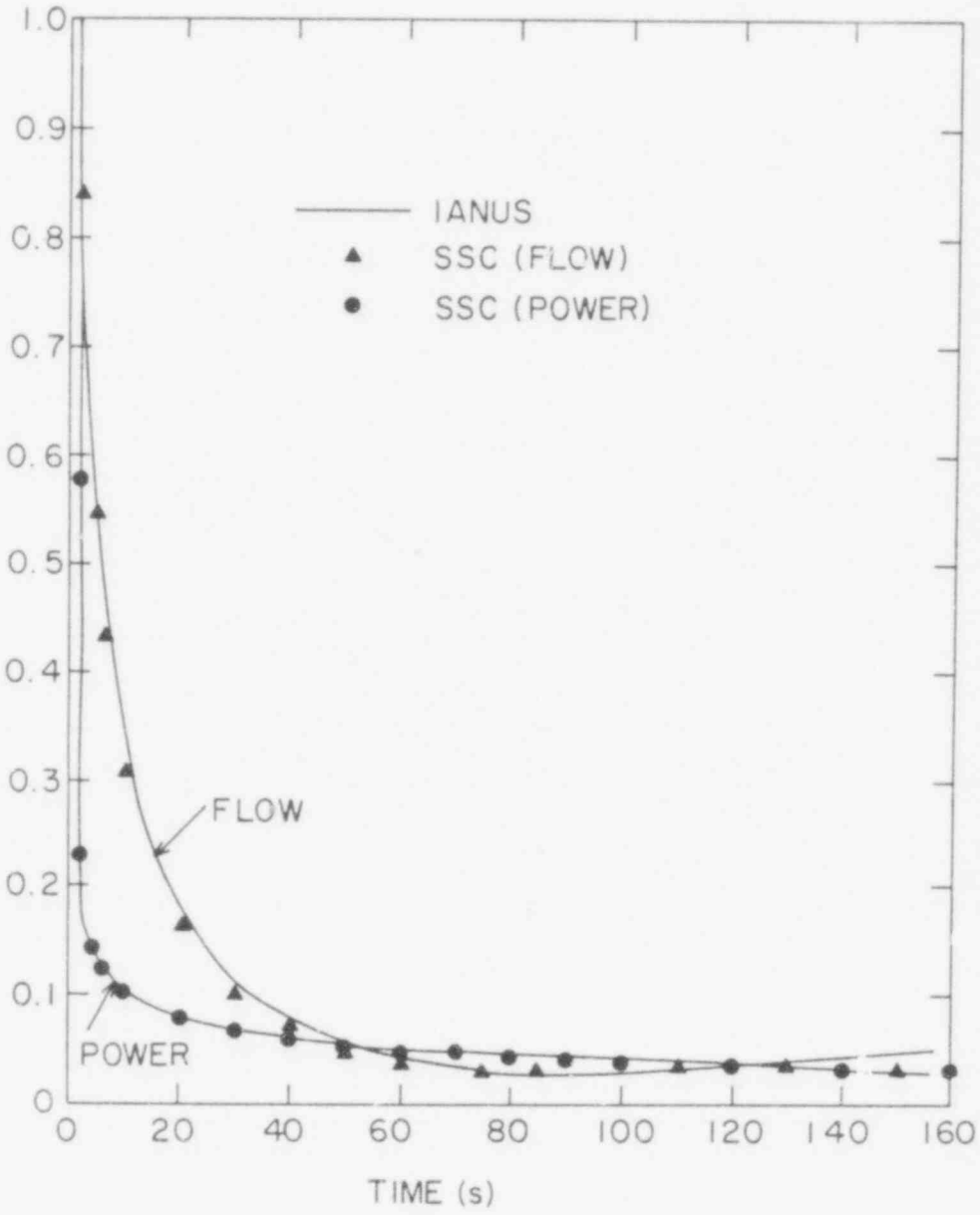

Figure 4.1. Comparisons of Transient Flow and Power Predicted by IANUS and SSC-L.

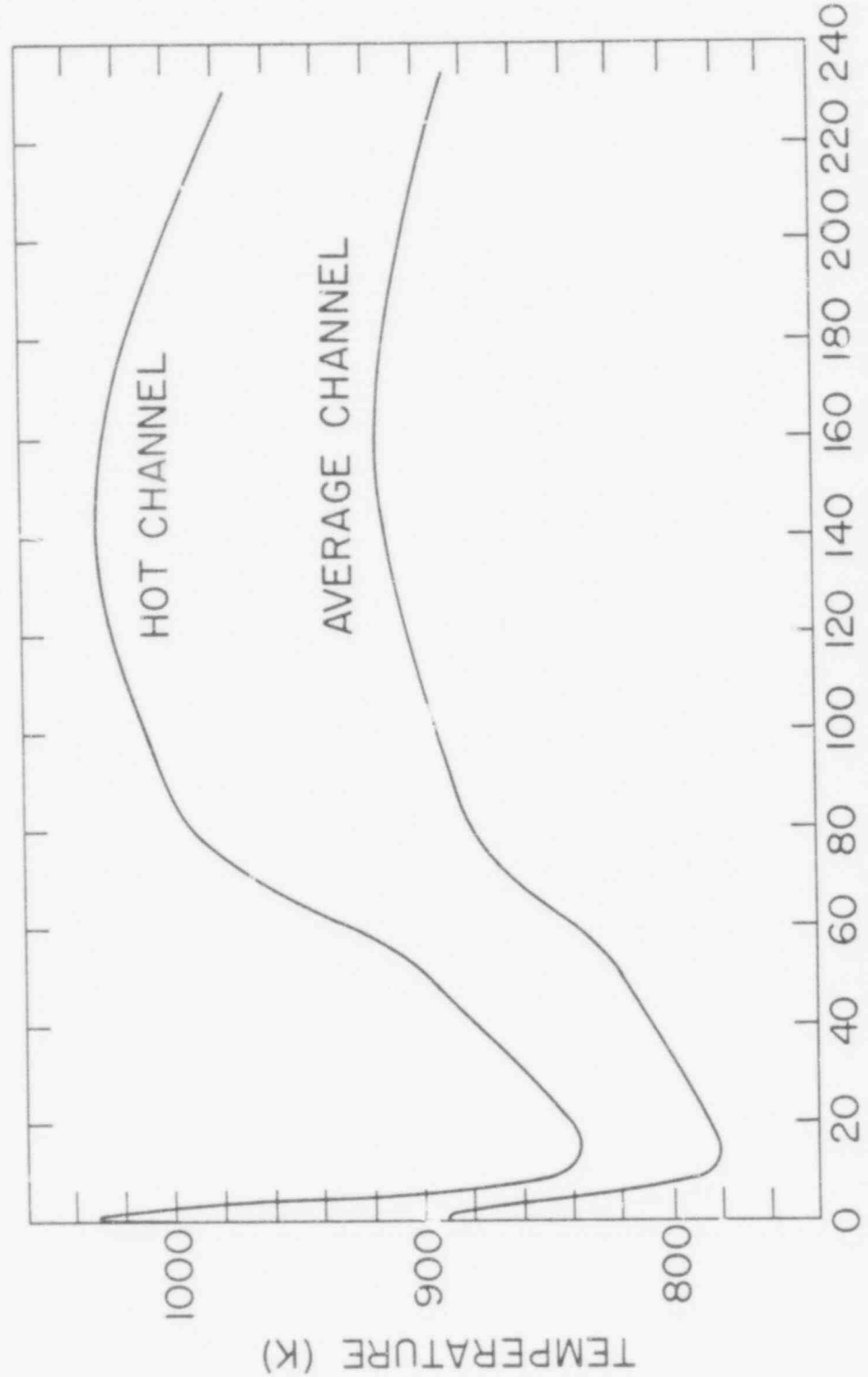

Figure 4.2. SSC-L Predicted Transient Temperature at the Top of Active Fuel Region.

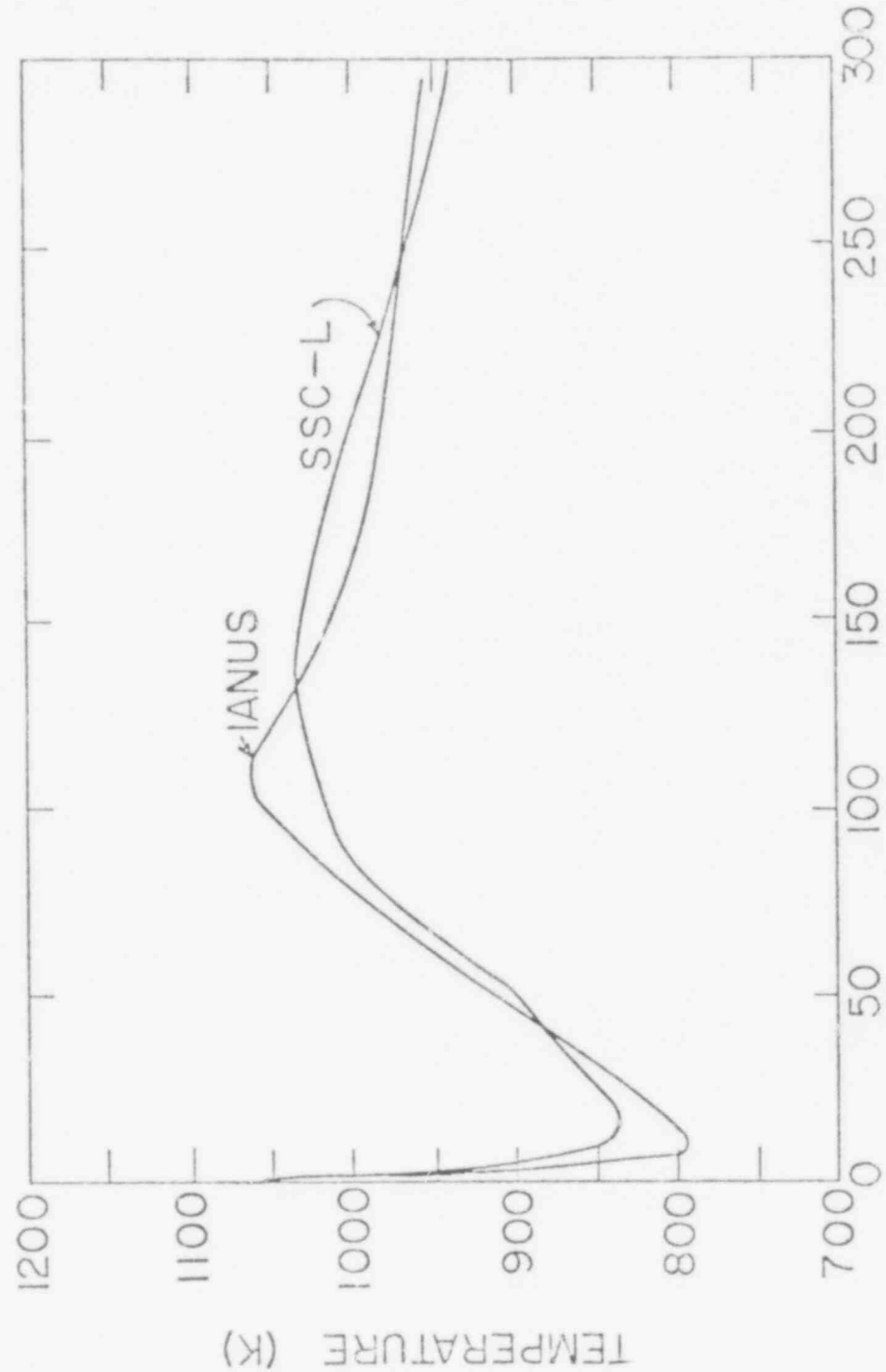

Figure 4.3. Comparison of SSC-L and IANUS Predictions of Coolant Temperature at the Top of Active Fuel Region of the Hot Channel.

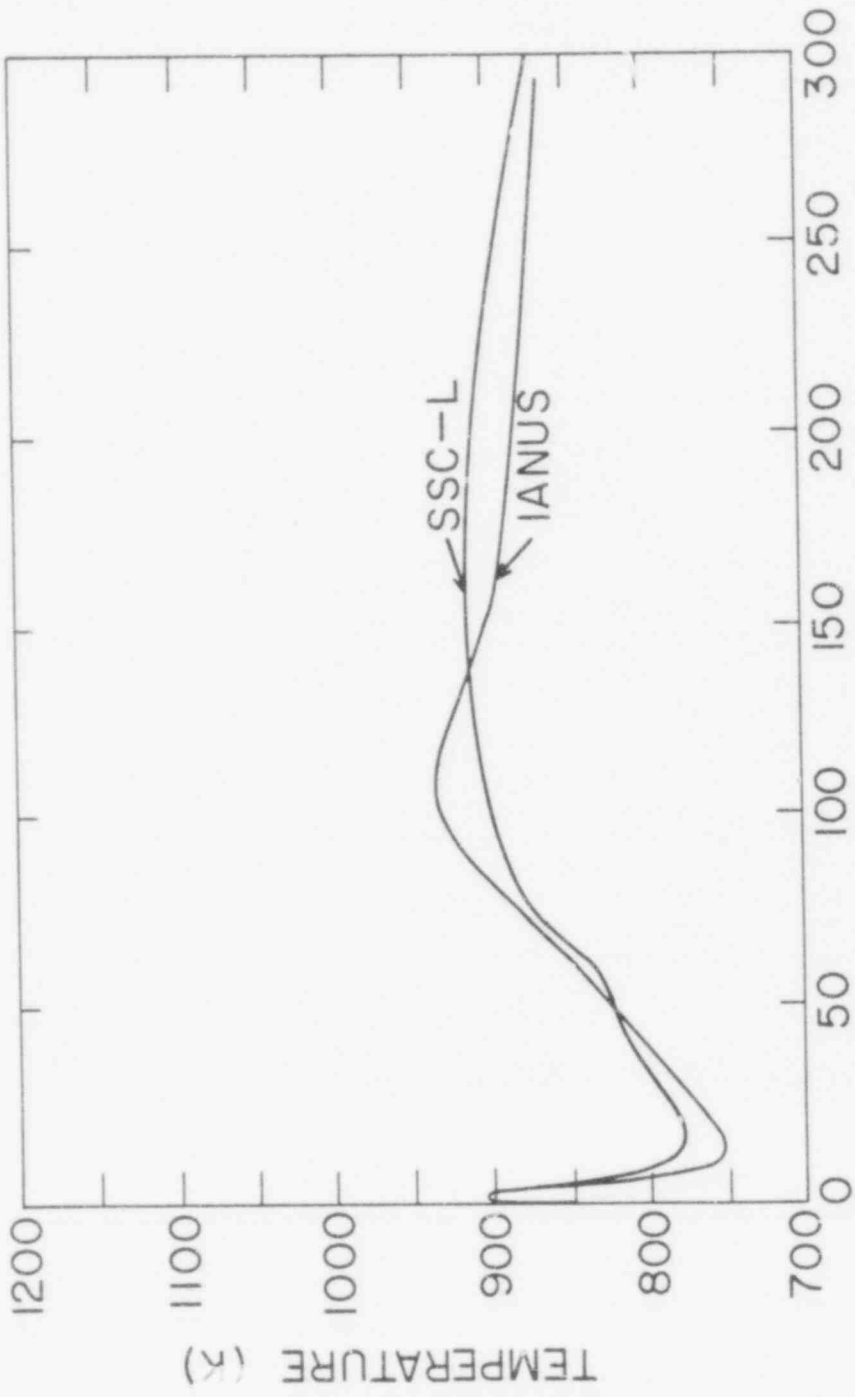

Figure 4.4. Comparison of SSC-L and IANUS Predictions of Coolant Temperature at the Top of Active Fuel Region of the Average Channel.

4. In the transient analyses, temperature time profiles from both codes agree. However, the SSC predicted peak temperature is approximately 50 K lower and occurs about 50 seconds later into the transient. This difference could be due to a number of reasons. Perhaps the two most significant ones are (1) the lack of IHTS and DHX models and (2) the heat loss to structure in the fuel assemblies.

4.2 Analysis of Thermohydraulic Experiments (D. Majumdar and H. Ludewig)

4.2.1 FFTF Instrumentation

The report on the adequacy of FFTF instruments to provide relevart data for SSC-L verification has undergone extensive review and revision. A draft report will be issued by February 15, 1979.

4.3 Intercomparison of SSC-L with BRENDA (K. E. St.John, A. K. Agrawal and J. G. Guppy)

A set of calculations was performed with the SSC-L code (Agrawal, 1978a) so that a direct comparison of results obtained from the BRENDA code (Hetrick, 1978) could be made. The transient chosen was a step insertion of 10¢ of positive reactivity at time t = 0 in the Clinch River Breeder Reactor Plant. This plant was assumed to be operating at nominal steady state design conditions (full-power and full-flow) with the fuel at the end of equilibrium cycle conditions. The SSC-L results were reported during the last progress report (Agrawal, 1978b). Their comparisons with BRENDA is reported here. More details are included in a separate report (St.John, 1978).

The transient simulated is the step addition of 10¢ of positive reactivity in CRBRP. The only reactivity feedback mechanism utilized for this comparison was the Doppler effect. Table 4.3 gives a summary of the key steady-state parameters used by the two codes. Figure 4.5 shows a comparison of the computed fission power. In both cases, the actual power is normalized to its value at time t = 0. In the case of BRENDA, this curve also represents normalized reactor power. The reactor power from SSC-L can be obtained by adding the contribution from fission products, which remains essentially unchanged, to the fission term, as shown in the previous sections.

Figure 4.6 shows the primary sodium flow rate in each of the three physical loops present in CRBRP. Both codes predict the same shape of the plant response, BRENDA, however predicts a slightly higher (0.22%) value for the whole curve. This is a consequence of a slight runs-match at steady-state. The shape of the curve is due to change in sodium density. As the reactor power increases, the temperature of the sodium leaving the vessel increases, hence, the sodium density decreases.

Figures 4.7 and 4.8 show the primary sodium temperatures at the inlet and outlet of the intermediate heat exchanger, respectively. The BRENDA code prediction is slightly higher than SSC-L as a result of slight difference in the pre-transient values.

Table 4.3

Summary of Key Steady-State Parameters Used to Characterize CRBRP

PARAMETERS	SSC-L	BRENDA
Power per Steam Generator, MW	325	325
Number of Loops	3	3
Reactor Power, MW	968.4	975.06
Flow Rates:		
Primary Sodium per Loop, kg/s	1741.3	1745.0
Intermediate Sodium per Loop, kg/s	1610.2	1614.0
Feedwater per Loop, kg/s	139.68	140.6
Turbine Steam, kg/s	419.04	421.8
Temperatures:		
Reactor Inlet, K	655	661
Reactor Outlet, K	801	808

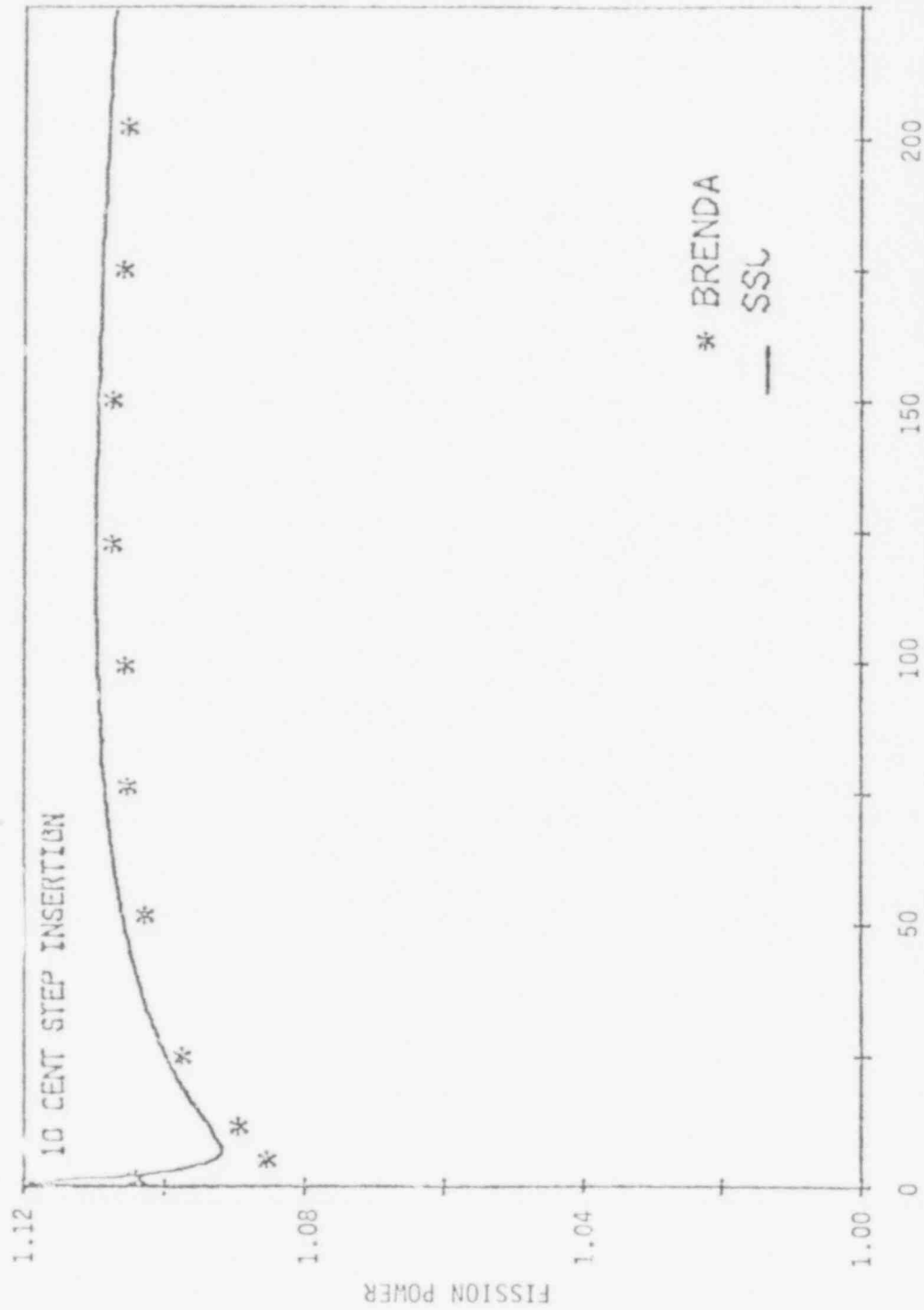

Figure 4.5 Normalized Fission Power

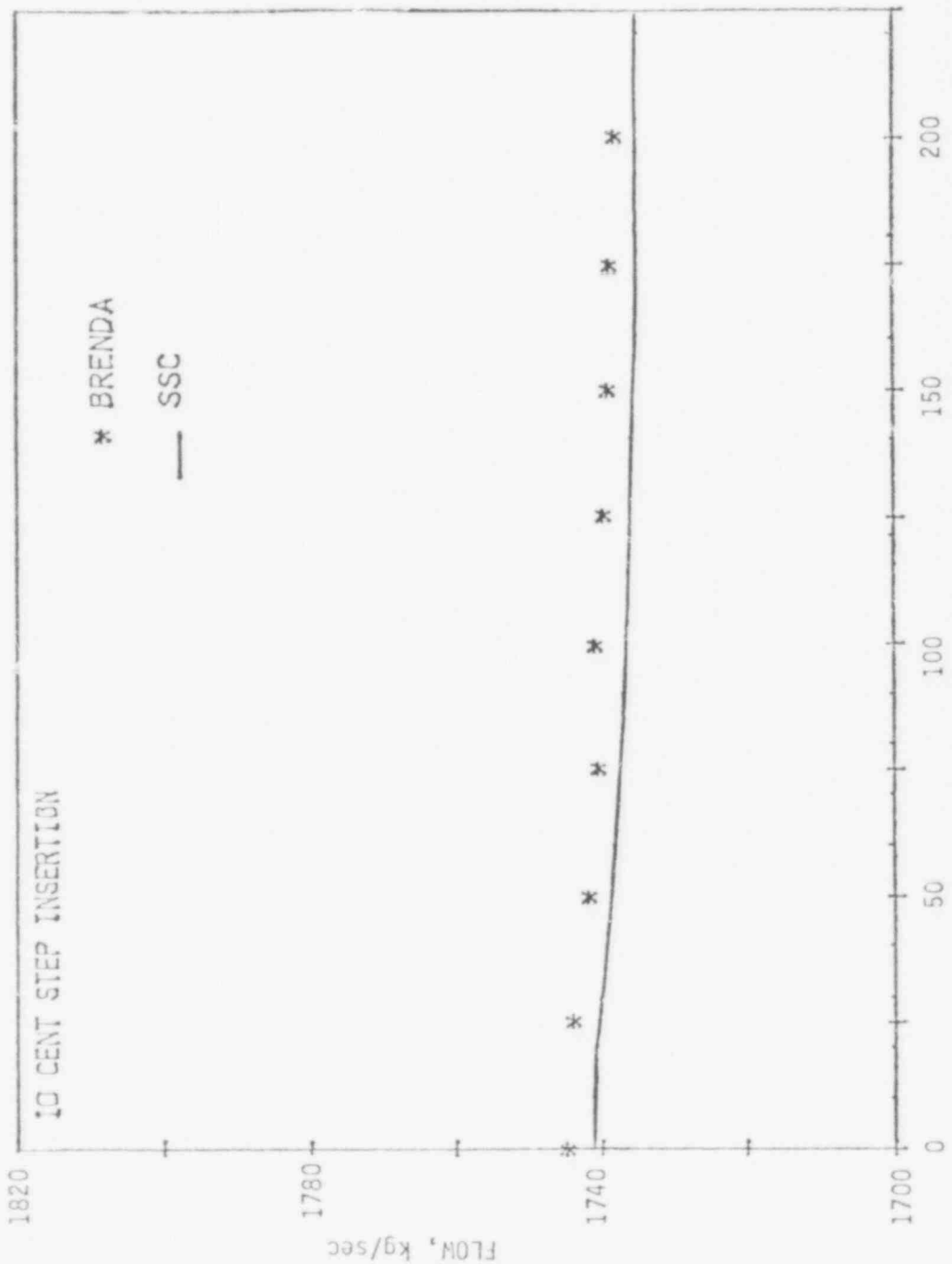

Figure 4.6. Primary Sodium Flow Rate per Loop

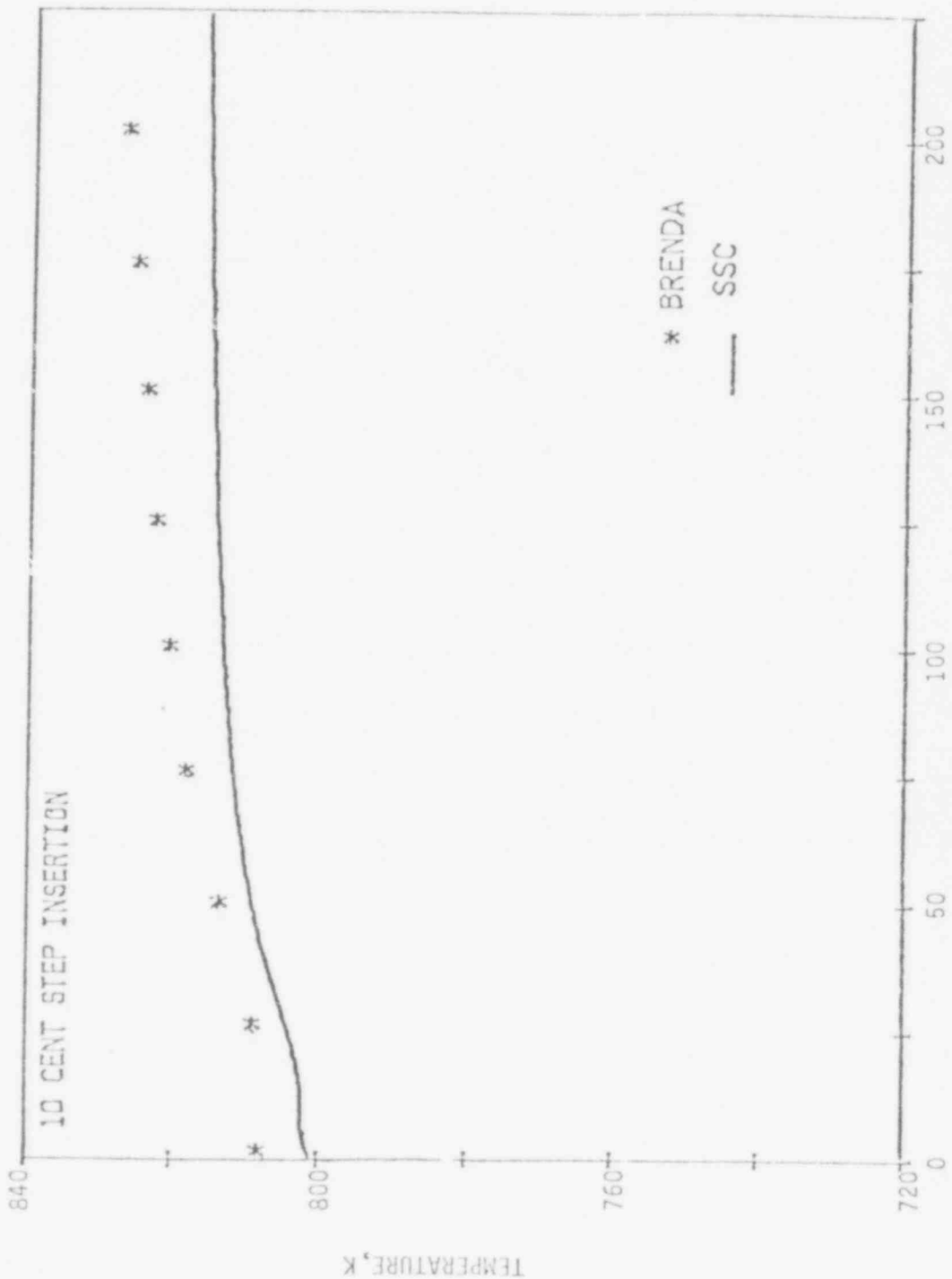

Figure 4.7. Primary Sodium Temperature at IHX Inlet

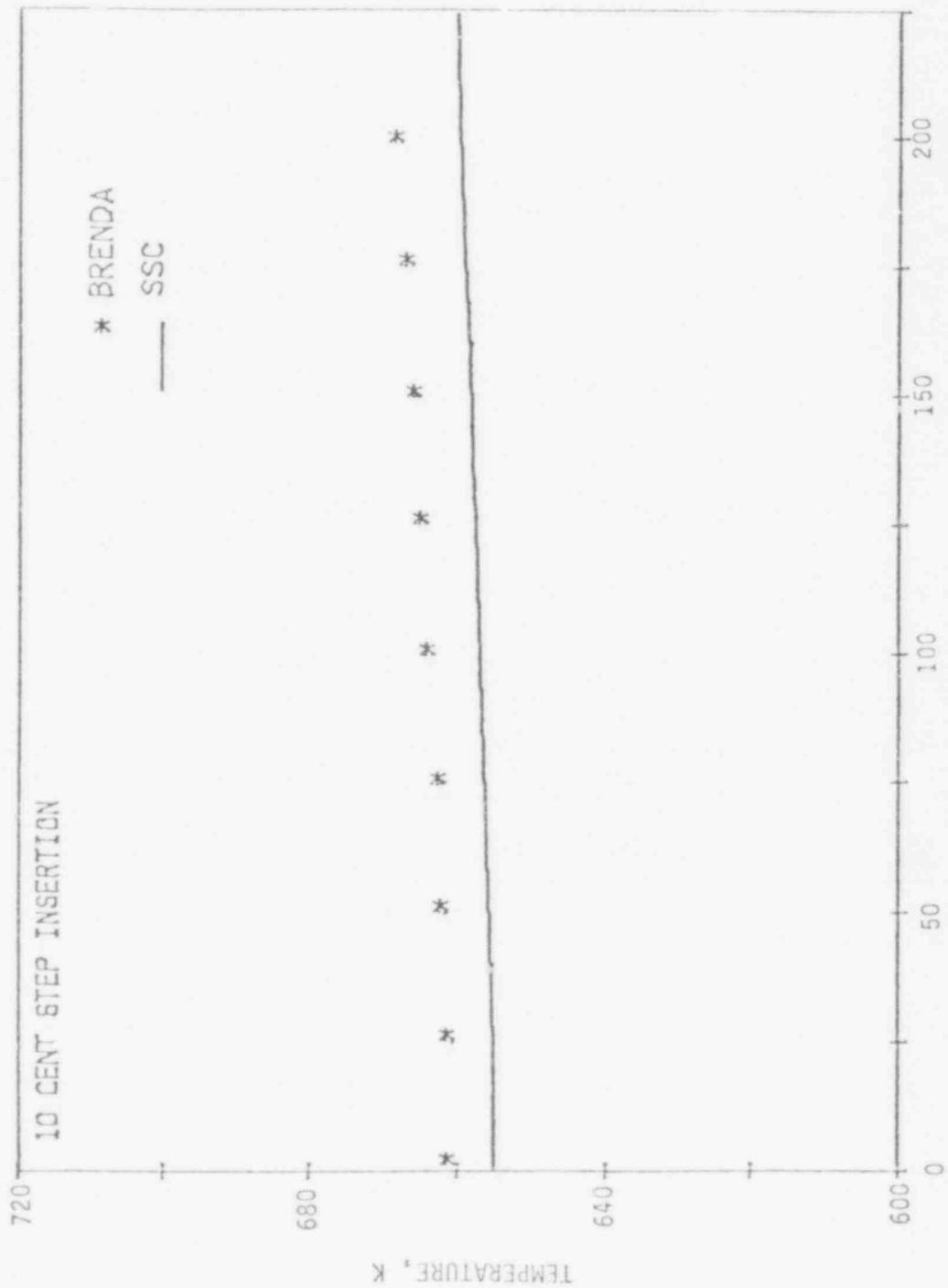

Figure 4.8. Primary Sodium Temperature at IHX Outlet

The two codes, BRENDA and SSC-L, produced results which in almost all cases compared well. The response of the plant predicted by the codes is identical in shape, though shifted slightly in absolute value, of the parameter being compared. The difference in the absolute values is due to slight difference in steady-state values.

PUBLICATIONS:

The following is a list of publications during the current reporting period from this activity:

ST.JOHN, K. E., AGRAWAL, A. K., and GUPPY, J. G., "A Comparison Between SSC-L and BRENDA System Codes," Brookhaven National Laboraotry, BNL-NUREG-25099 (October 1978).

YANG, J. W., "Comparative Studies of FFTF Upper-Plenum Mixing and Stratification," Trans. Am. Nucl. Soc. Vol. 30, p. 535 (1978).

YANG, J. W., "Comparative Studies on LMFBR Systems Codes: Part 2, FFTF Upper-Plenum Mixing and Stratification," Brookhaven National Laboratory, BNL-NUREG-24856-R (October 1978).

REFERENCES

AGRAWAL, A. K., et al., (1978a), "An Advanced Thermohydraulic Simulation Code for Transients in LMFBRs (SSC-L Code)," Brookhaven National Laboratory, BNL-NUREG-50773 (February 1978).

AGRAWAL, A. K., et al., (1978b), "SSC Code Validation" in Reactor Safety Research Programs Quarterly Progress Report, July 1-September 30, 1978, Brookhaven National Laboratory, NUREG/CR-05013, BNL-NUREG-50931, pp. 138-149 (November 1978).

HETRICK, D. L., and SOWER, G. W., (1978), "BRENDA, A Dynamic Simulator for Sodium-Cooled Fast Reactor Power Plant," NUREG/CR-0244 (July 1978).

ST.JOHN, K. E., AGRAWAL, A. K., and GUPPY, J. G., (1978), "A Comparison Between SSC-L and BRENDA System Codes," Brookhaven National Laboratory, BNL-NUREG-25099 (October 1978).

WOLFE, C. F., (1976), "IANUS - Application Information, WARD-FPC-1253 (Proprietary), Rev. 1, (May 1976).

III. LIGHT WATER REACTOR SAFETY

SUMMARY

An Interim Milestone Report on the analytical work to model the nonequilibrium vapor generation in flashing flows was completed. The results compare well with the experimental data of Reocreux for void fractions below 0.3. Observations on the onset of the vapor generation as related to mass flux seem to be opposite to the well-known relations observed for vapor condensation in supersonic nozzles.

A second set of flashing experiments were performed with TS-2. In these tests, in addition to the pressure distributions along the nozzle, photographic observations of the flashing regimes at the exit of the test section were also recorded. The data reported show that the reproducibility of the results is very good. In these series of tests, we also studied the effects of the various flow parameters, i.e., inlet pressure, inlet subcooling, mass flux, and exit pressure or condensing tank pressure on the pressure distributions and flashing regimes.

In one set of experiments, the onset of flashing was moved upstream of the throat. The pressure distributions recorded under this condition are representative of a supercritical flow in the nozzle.

The single channel γ densitometer with the traversing mechanism was installed and debugged in preparation of the void fraction distribution measurements.

Improvements have been made in the THOR description of the quench front velocity to better match both low pressure and high pressure minimum stable film boiling temperature. The THOR input description was improved and a new pseudo-restart capability was added. THOR calculations of the Semiscale downcomer lower plenum assembly behavior were extended showing good comparison with core and break flows but much larger voiding in the lower plenum than actually measured. Continuation of the effort to resolve the numerical instability in the N-zone hydraulics module revealed that the incomplete and complete linearization methods produced essentially the same results. Reformulation with smooth transitions in drift flux across flow regime boundaries without the need for description of derivatives at the boundaries was undertaken.

This is the first quarterly report for the second fiscal year of the RSR program. Complete data are included in the first annual report which is to be issued in the near future.

In the experimental area, additional slow straining systems are being constructed and the tensile specimen design has been modified. Pressurized capsule specimens are being fabricated and will provide a stress pattern similar to a dented tube.

Five heats of material have shown cracking at the two highest temperatures and results at 325°C are expected soon, judging from curves through the first points.

The slow straining test has produced intergranular cracking at 365°C, 345°C and 325°C. A test is currently in progress at 290°C with a strain rate of 5×10^{-8} sec^{-1}.

Controlled potential tests at 365°C have reduced the time to failure of specimens held at 40 mV to 160 mV negative to the open circuit potential.

Specimens have been cracked under a cyclic load in 365°C pure water with frequencies of 10^{-3} Hz, 10^{-2} Hz and 10^{-1} Hz.

1. Light Water Reactor Thermal/Hydraulic Development Program (N. Abuaf and O. C. Jones, Jr.)

1.1 Analytical Modeling (B.J.C. Wu)

1.1.1 Effects of Pressure Change

An Interim Milestone Report on the analytical work (Saha 1977a,b,c,d and Wu 1978) to model the nonequilibrium vapor generation in flashing flows has been completed. Results of comparison of this model with the experiments of Reocreux (1974) indicate that:

(a) the model worked well for void fractions below about 0.3, above this value, it seemed to underestimate the vapor generation rate,

(b) higher superheat values--or higher ($p_{sat} - p$), the difference between the saturation and actual liquid pressures--were reached at the point of net vapor generation (NVG) for low mass fluxes, and vice versa, and

(c) the "rate constant" C_r, which is proportional to the cube root of the bubble concentration and incorporates the constant factors in the heat transfer coefficient and interfacial area density function used, was found to increase with the mass flux.

Result (b) implies that the value of superheat at NVG decreases with increasing depressurization rate, which is proportional to the cube of the mass flux. This trend, also observed by Seynhaeve (1976), is opposite to the well-known critical supercooling vs. cooling rate relationship first noticed by Oswatitsch (1942) for supersonic nozzle flows with vapor condensation. If C_r is taken to be a measure of the bubble concentration, then results (c) and (b) indicate that a greater number of bubbles are produced when net vapor generation occurs at a low superheat value. This seems to suggest that the controlling driving potential for bubble production may not be the liquid superheat, in contrast to the case of nozzle flows with condensation, where vapor supercooling plays a dominant role. In the past quarter, work was initiated to investigate possible mechanisms of bubble formation in which the rate-limiting step is the detachment from surface sites and entrainment in the flow rather than the growth to the critical size commonly assumed in nucleation theories.

1.2 Test Sections and Seal Development (W. J. Leonhardt and J. H. Klein)

Test Section 2 (TS-2) was operated in the flashing facility during much of this quarter with temperatures reaching 150°C and flow rates up to 850 ℓ/min. The test section operated without any problems, and the slight deformation, reported last quarter (Leonhardt 1978), remained unchanged. After some investigation, it was determined that the deformation occurred

because of inadequate allowance for thermal expansion between the test section and the gamma densitometer traversing mechanism, a situation which has been corrected.

Development of the probe seal for TS-3 has resulted in the following conclusions:

a) No suitable material appears to exist to allow an inflatable/deflatable seal design to function. Therefore, this design concept has been abandoned.

b) Of the nine design concepts examined in detail, six have also been rejected due to lack of suitable materials.

c) A static seal design concept is currently being pursued, which does not appear to have the same drawbacks as the previous concepts. A suitable test fixture is being constructed for further evaluation of this design.

1.3 Global Densitometer (W. J. Leonhardt and N. Abuaf)

The single channel gamma densitometer has been made operational and has been installed on TS-2. Currently, calibration runs are being performed.

The observations regarding neutron activation of a Scandium impurity described in the previous quarterly report have now been confirmed by Harwell (Isotope Sales Division). This is apparently the first time such observations have been made. On this basis, an ultra-purified Thulium source material was obtained from Iowa State University and has been found through our activation analysis to possess a 700 fold reduction in the Scandium levels compared with material of our other suppliers. It is the Scandium which causes the 1.12 MeV radiation which in turn requires excessive shielding. There is some uncertainty as to the source of the Scandium since both two independent vendors and Harwell reported pre-radiation contamination levels of less than 0.5 ppm Scandium. Post irradiation levels of $\sim$ 80 ppm were found at BNL and confirmed independently by Harwell. Further testing is being undertaken to insure no further difficulties appear at higher source intensities (longer activation times).

1.4 Flashing Experiments (G. A. Zimmer, B.J.C. Wu, W. J. Leonhardt J. H. Klein, and N. Abuaf)

A second set of flashing experiments were performed, and pressure distributions along the converging diverging nozzle were recorded. In addition to the pressure measurements, the flashing regimes, under a variety of inlet conditions and flow rates, were also recorded photographically by means of a flash and a still camera arrangement located downstream of the test section outlet. A list of the runs performed with their inlet conditions and mass flow rates are presented in Table (1.1). The typical effects observed are summarized below.

TABLE I

SUMMARY OF EXPERIMENTAL CONDITIONS

A. COLD & HOT CALIBRATION				B. FLASHING EXPERIMENTS							
Run No	p_{in}(kPa)	T_{in}(^{o}C)	G Mg/m^{2}sec	Run No	p_{in}(kPa)	T_{in}(^{o}C)	G Mg/m^{2}sec	Run No	p_{in}(kPa)	T_{in}(^{o}C)	G Mg/m^{2}sec
1	-----	----	----	20	278.5	98.3	4.90	48	185.5	99.8	3.04
2	369.7	26.4	1.56	21	393.0	100.6	6.01	49	144.1	99.4	[illegible]
3	388.2	26.8	3.13	22	169.6	100.2	3.04	50	140.0	99.9	[illegible]
4	360.0	27.2	4.71	23	130.3	99.4	1.81	51	-----	-----	----
5	349.7	27.6	6.28	24	160.0	98.0	3.05	52	394.4	123.5	4.45
6	679.5	27.7	7.01	25	246.8	97.4	4.52	53	399.9	123.6	4.43
7	688.5	27.3	6.30	26	386.1	97.8	6.02	54	553.0	123.5	5.96
8	692.6	26.9	4.71	27	326.1	130.0	2.95	55	295.8	123.8	2.99
9	696.0	27.1	3.13	28	555.4	131.7	5.90	56	261.3	123.5	2.20
10	708.4	27.0	1.56	29	488.2	123.5	5.77	57	262.0	123.2	2.01
11	685.7	27.7	6.26	30	375.1	125.1	4.47	58	257.2	123.1	2.9[illegible]
..	1029.2	29.2	7.01	31	-----	-----	----	59	257.2	123.3	2.94
13	1027.9	29.4	7.88	35	287.5	99.4	4.96	60	266.8	126.1	2.90
14	335.3	23.0	6.25	37	295.8	100.3	4.94	61	261.3	124.2	2.95
15	346.3	22.9	4.74	38	117.2	100.3	2.05	63	769.5	148.5	5.81
16	364.2	66.3	3.08	39	136.5	100.5	2.25	64	626.0	148.8	4.36
17	365.5	64.1	1.56	40	167.5	100.3	3.02	65	----	----	----
18	-----	----	----	41	249.6	100.2	4.54	66	525.4	148.8	2.90
19	336.0	94.4	5.49	42	193.7	99.6	3.79	67	503.3	149.2	2.18
32	326.4	11.6	4.71	43	286.8	100.2	4.97	68	393.0	143.9	1.21
33	314.0	11.9	6.29	44	283.4	99.9	4.50	69	396.4	144.6	1.19
34	333.9	12.3	3.15	45	324.1	100.1	4.97				
36	292.0	69.0	3.08	46	-----	100.2	3.79				
62	697.8	148.6	2.29	47	-----	-----	----				

1.4.1 Reproducibility Studies

To compare our present results to the results obtained in the first set of experiments, reported in the last quarterly (Abuaf 1978), and to check the repeatability of the data, several runs were performed at nearly identical inlet conditions and flow rates. Figure (1.1) shows the comparison between the pressure distributions obtained in the two sets of experiments for p_{in} = 168 kPa, T_{in} = 100°C, and mass flux of 3.03×10^3 kg/m^{2}sec. Experiments were also performed at a higher mass flux 4.45×10^3 kg/m^{2}sec and T_{in} = 153°C and p_{in} = 396 kPa. Figure (1.2) depicts the pressure distributions for these latter cases, i.e., Exps. 52 and 53. The results at these mass fluxes are reproducible to within less than 2 percent.

1.4.2 Effect of Back Pressure on the Flashing Regime

Flashing was initiated with the condensing tank liquid level (defined as the location of the free surface below the top of the tank) equal to zero, i.e., an almost solid loop condition (Fig. 1.3, Exp. 35). Decreasing the condensing tank liquid level, i.e., increasing the size of the steam cavity in the condensing tank changed the flashing conditions and the pressure distributions drastically (Exp. 37) although the flow rate and inlet conditions were held constant. The photographic observations of these experiments are presented in Fig. (1.4). One observes that for flashing under an almost solid system, the bubble sizes formed are minute and their number density is very large (Fig. 1.4a). Increasing the vapor bubble at the condensing tank increases the vapor generation as seen in Fig. (1.4b) and (1.4c). However, this drastic difference in appearance observed between Exp. 37 and 43 (Fig. 1.4b and 1.4c) does not noticeably affect the pressure distributions as seen in Fig. (1.3).

1.4.3 Parametric Effects

The effects of the flow parameters, inlet pressure p_{in}, inlet temperature T_{in} and mass flux on the flashing regimes and pressure distributions were also investigated. Figures (1.5), (1.6), (1.7), (1.8), (1.9), and (1.10) present the results for the cases where p_{in} and T_{in} were kept constant, and the mass flux was varied. Figures (1.5) and (1.6) (Exp. 49 and 50) correspond to the onset of flashing in the nozzle. The pressure distribution in the converging part follows very closely the single phase calibration. Downstream of the throat, the vapor generation presents itself as a deviation in the pressure distribution. This is followed by a sudden pressure increase caused by the sudden collapse of the bubbles and a pressure recovery typical of single phase flows. In Fig. (1.6), we see the photographic observations for these two cases. The appearance of bubbles seemed to be intermittent in Exp. 50, but this fact was not observed in the pressure measurement due to our long averaging time. Figure (1.7) represents similar results for p_{in} = 284 kPa, T_{in} = 100°C and mass fluxes of 4.97×10^3 (Exp 43) and 4.50×10^3. Here, with higher mass fluxes, the

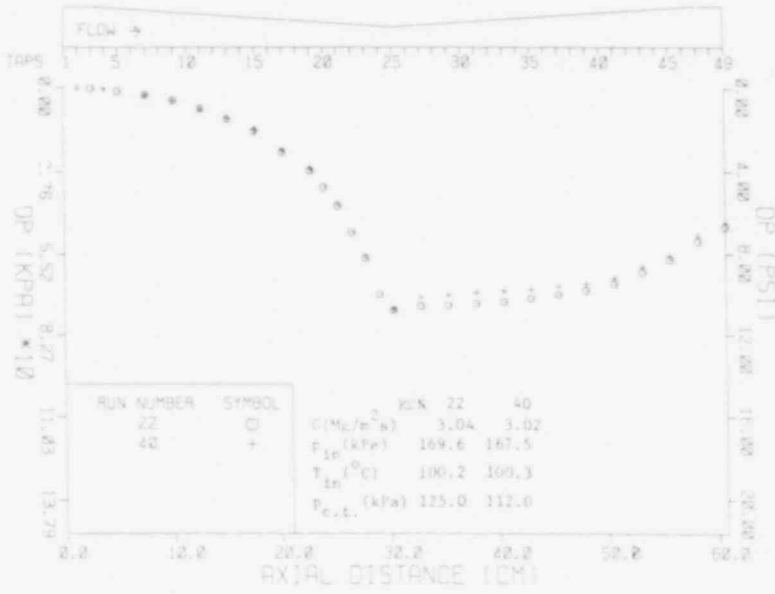

Figure (1.1) - Comparison of pressure distribution in two experiments to show the reproducibility of the results at low mass fluxes $G = 3.03 \times 10^3$ kg/m^2 sec (BNL Neg. No [illegible]-79).

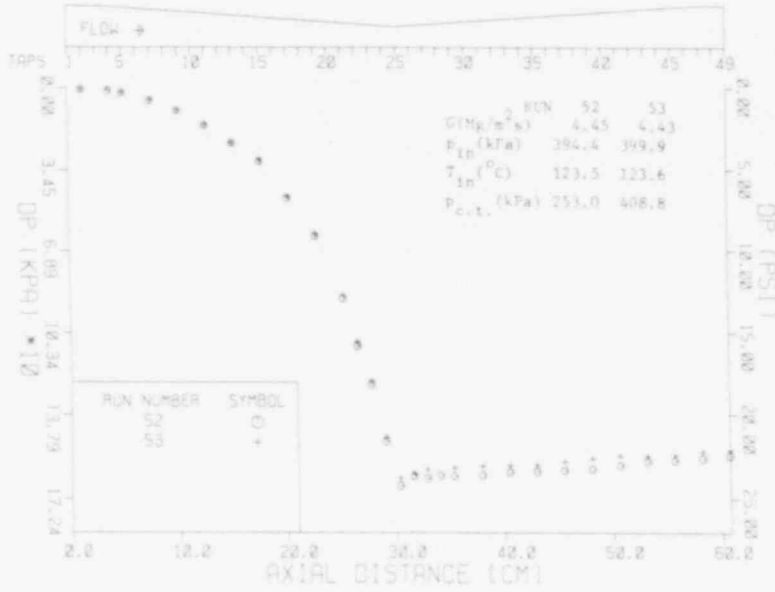

Figure (1.2) - Comparison of pressure distributions in two experiments to show the reproducibility of the results at high mass flux $G = 4.45 \times 10^3$ kg/m^2 sec (BNL Neg. No 1-724-79)

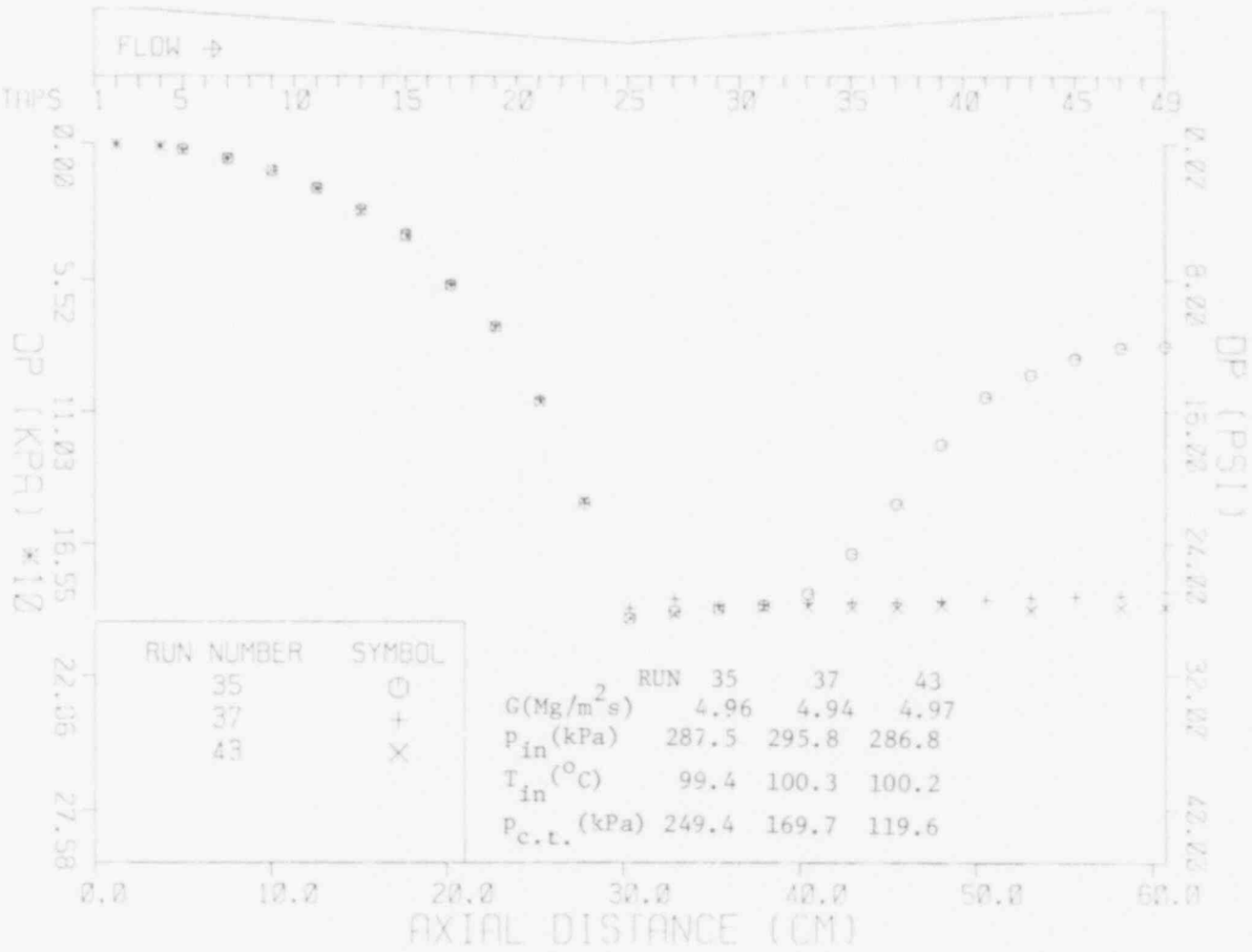

Figure (1.3) - Pressure distributions showing the effect of condensing tank back pressure for identical nozzle inlet conditions (BNL Neg. No 1-728-79).

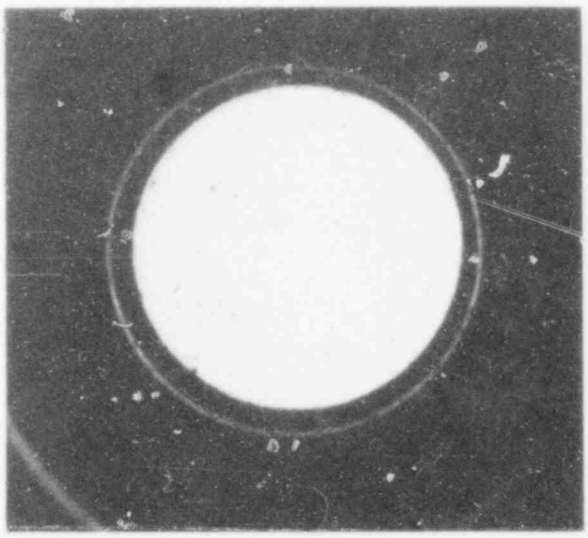

A. RUN NO. 35

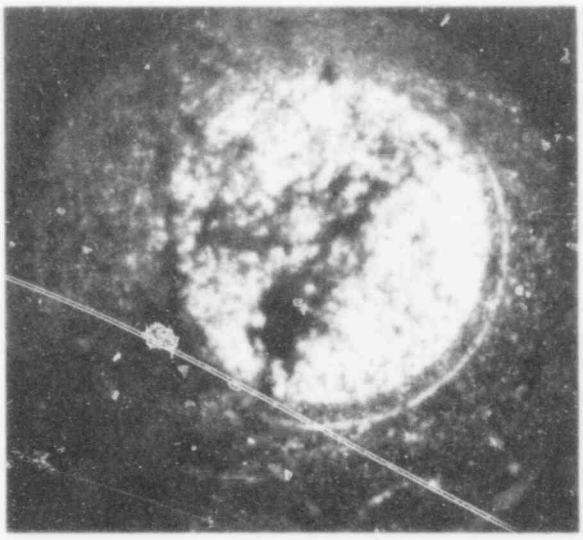

B. RUN NO. 37

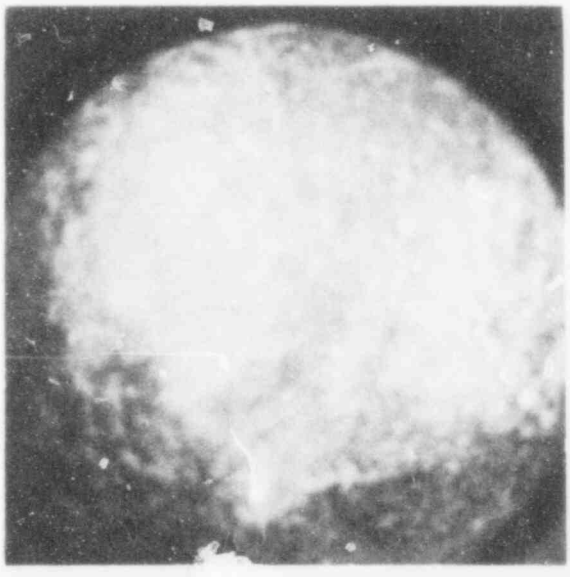

SCALE 1:1

C. RUN NO. 43

Figure (1.4) - Photographic observations for the experimental conditions presented in Fig. (1.3) (BNL Neg. No 1-919-79).

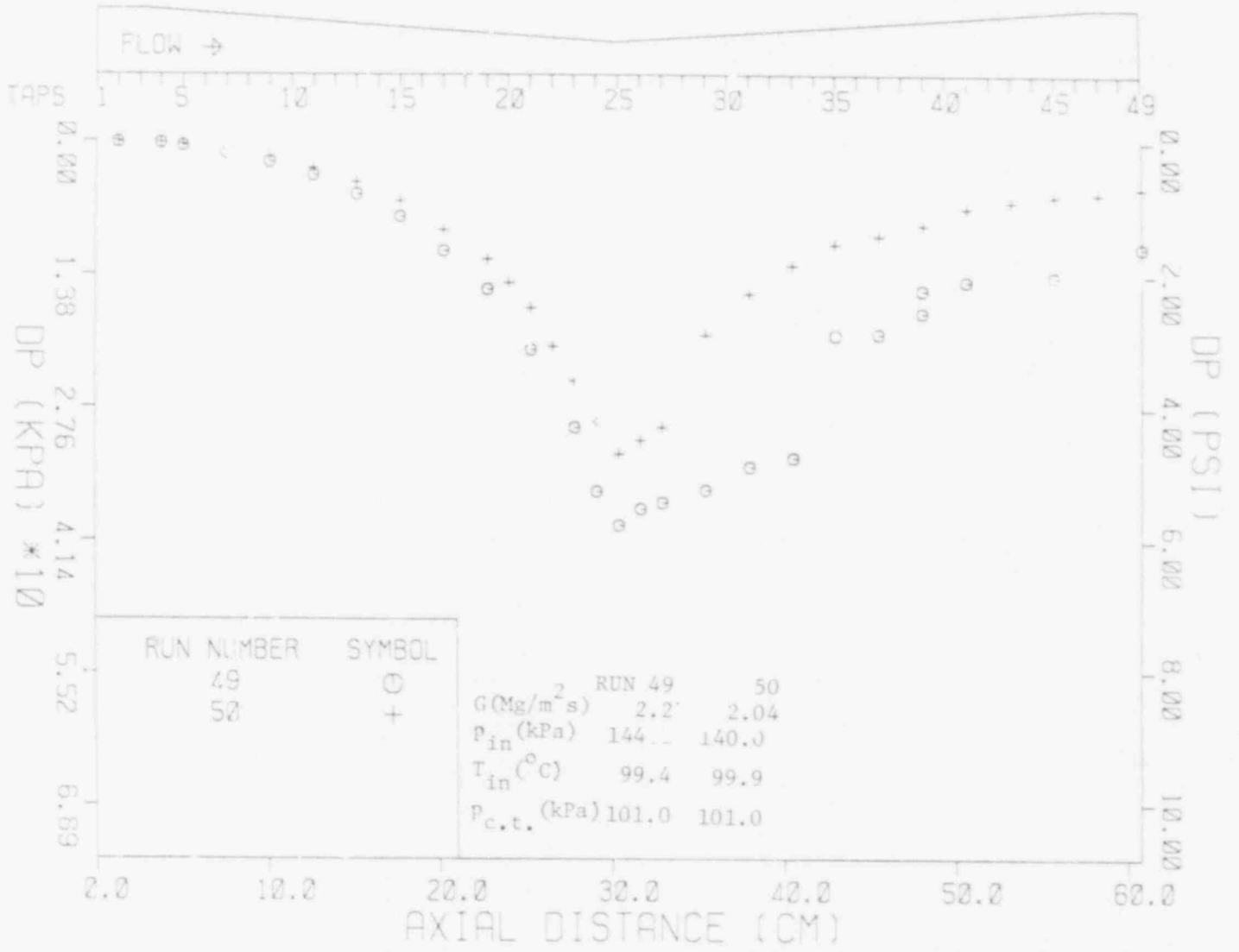

Figure (1.5) - Effect of mass flux on pressure distributions for identical nozzle inlet conditions which are close to the onset of flashing in the test section (BNL Neg. No 1-727-79).

SCALE 1:1

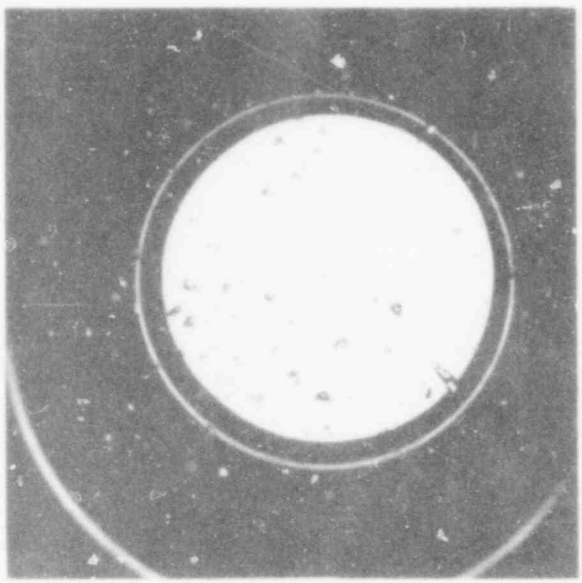

RUN NO. 49

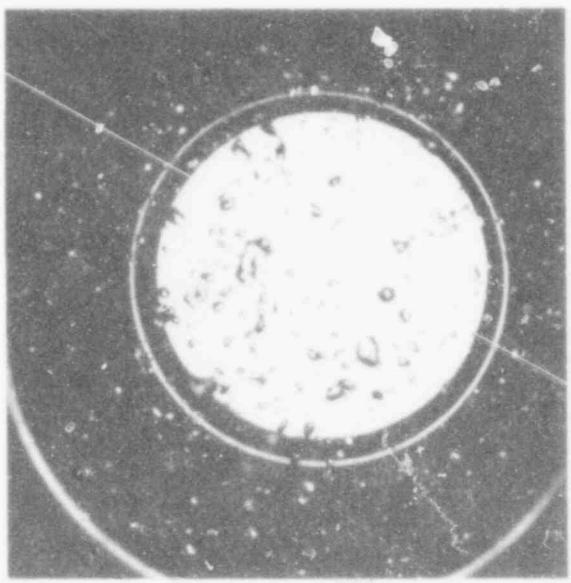

RUN NO. 49

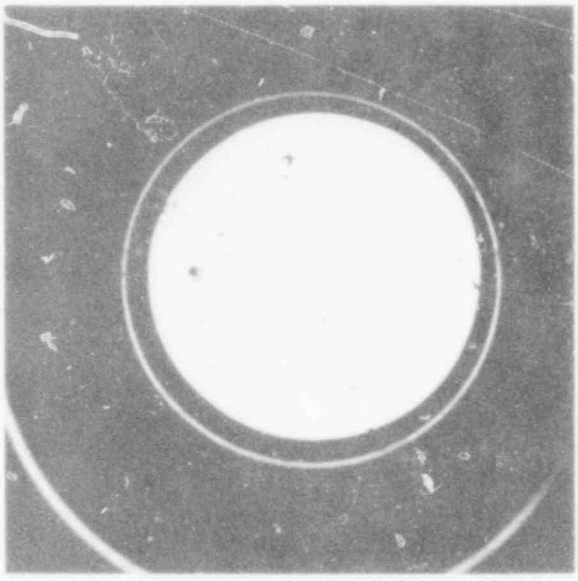

RUN NO. 50

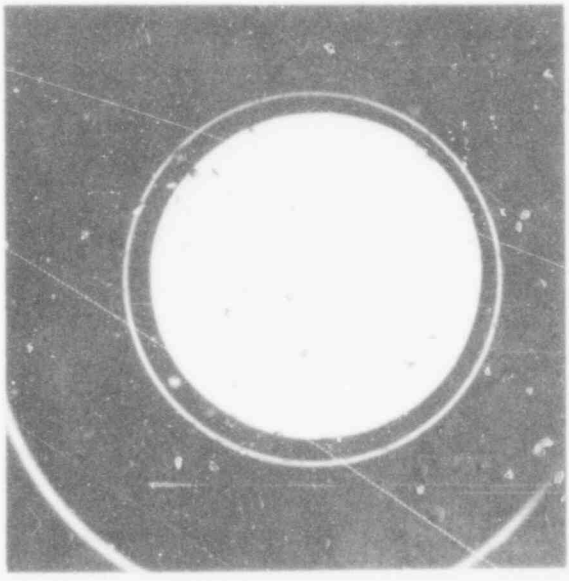

RUN NO. 50

Figure (7.6) - Photographic observations for the experimental conditions presented in Fig. (1.5) (BNL Neg. No 1-922-79).

flashing appears more pronounced, and the pressure downstream of the throat appears to remain constant. Figure (1.8) depicts a similar G-variation for a T_{in} = 123°C and p_{in} = 260 kPa, from onset of flashing (Exp. 57) at 2.01 x 10^3 kg/m^2sec, to violent flashing at 2.95 x 10^3 kg/m^2sec (Exp. 61). The photographic observations for Exps. 57 and 61 are presented in Fig. (1.9).

The next set of figures represent the effect of the nozzle inlet temperature while a constant inlet subcooling is maintained by a corresponding variation of the inlet pressure. Figure (1.10) represents these results for Exp. 67 (T_{in} = 149.2°C, p_{in} = 503.3 kPa) Exp. 56 (T_{in} = 123.5°C, p_{in} = 136.5 kPa) while the mass flux is 2.20 x 10^3 kg/m^2sec for the experimental conditions close to the onset of flashing. The photographic observations for Exps. 39 and 56 are presented in Fig. (1.11). One observes that the effect of inlet temperature is small as long as the inlet pressure is adjusted for constant subcooling at the inlet. The same observation will be valid for the following results. Figures (1.12), (1.13), (1.14) show similar results for progressively higher mass fluxes, and Fig. (1.15) show photographic observations for Exp. 55 and 52 (Fig. 1.15).

A slight variation of the inlet pressure is observed to have an effect on the pressure distributions and flashing regimes for the same inlet temperatures and mass fluxes. This dependence and sensitivity seems to be more pronounced at low mass fluxes; Fig. (1.16) presents the results for Exp. 55 (T_{in} = 123.8°C, G = 2.99 x 10^3 kg/m^2sec, p_{in} = 296 kPa) and Exp. 58 (T_{in} = 123.1°C, G = 2.96 x 10^3 kg/m^2sec, and p_{in} = 257.2 kPa).* Figure (1.17) for Exps. 22 and 48 and Fig. (1.18) for Exps. 45, 37, and 43 show correspondingly smaller differences in the pressure distribution as a result of smaller variations in p_{in}.

1.4.4 Flashing Upstream of the Throat

In all the experiments presented above, flashing occurred in the vicinity of the throat. By changing and controlling the flow conditions, we were able to obtain almost saturation conditions at the inlet of the test section. The pressure distribution recorded under this condition is presented in Fig. (1.19). Flashing started around pressure tap #13, (15 cm upstream of the throat) where the distribution deviates from the single phase calibration. The continuous pressure decrease in the converging, as well as the diverging sections of the nozzle, is reminiscent of the supercritical flows in supersonic nozzles in classical gasdynamics. The onset of flashing, which is accompanied with a strong deviation in the pressure distribution as compared to the single phase calibration, is depicted in

---

*Note that in these two experiments, the condensing tank pressure also varied from 174 kPa (Exp. 58) to 251 kPa (Exp. 55).

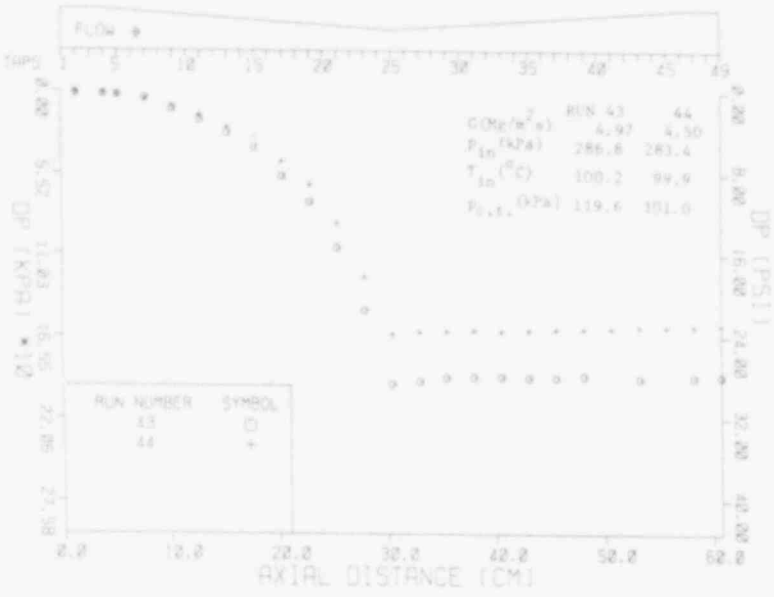

Figure (1.7) - Effect of mass flux on the pressure distribution in the test section (BNL Neg. No 1-723-79).

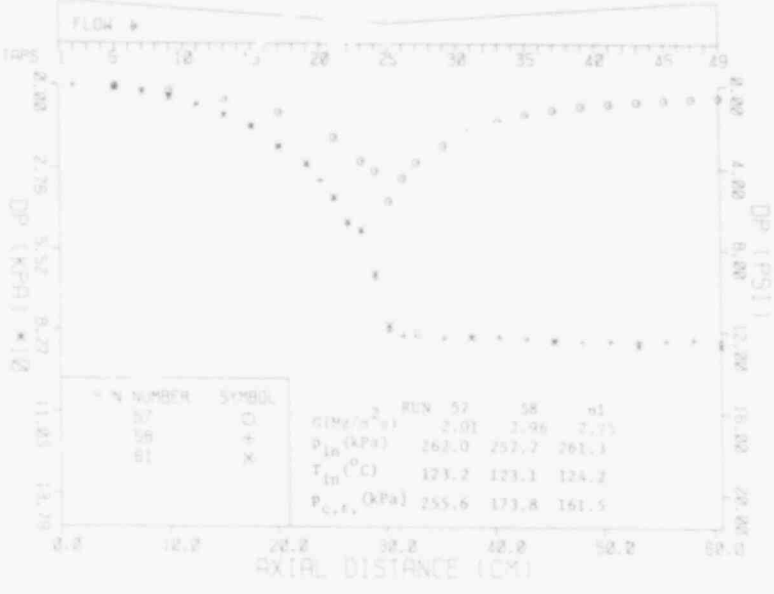

Figure (1.8) - Effect of mass flux on the pressure distribution in the test section (BNL Neg. No 1-722-79).

479 307

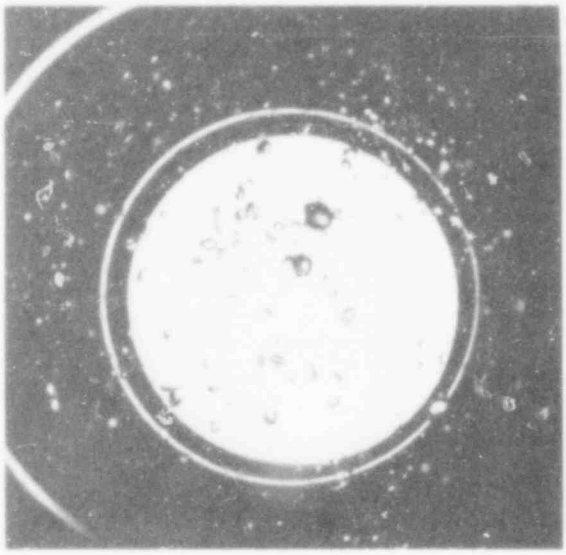

RUN NO. 57

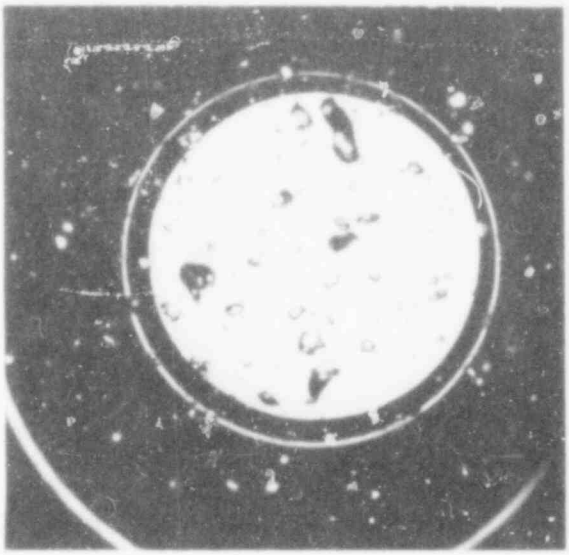

RUN NO. 57

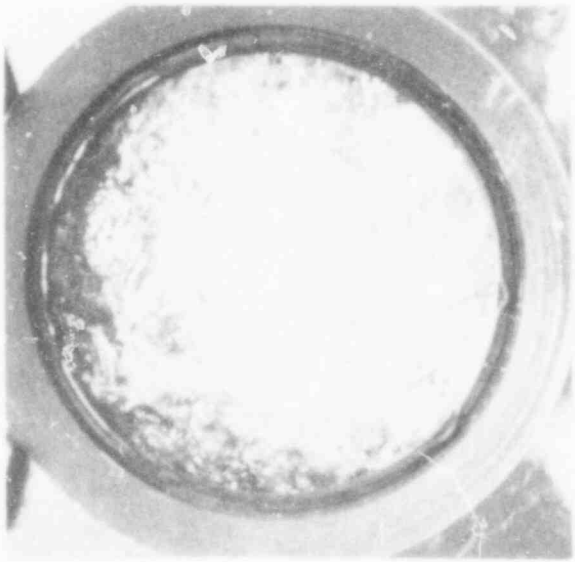

SCALE 1:1

RUN NO. 61

Figure (1.9) - Photographic observations for the experimental conditions presented in Fig. (1.8) (BNL Neg. No 1-918-79).

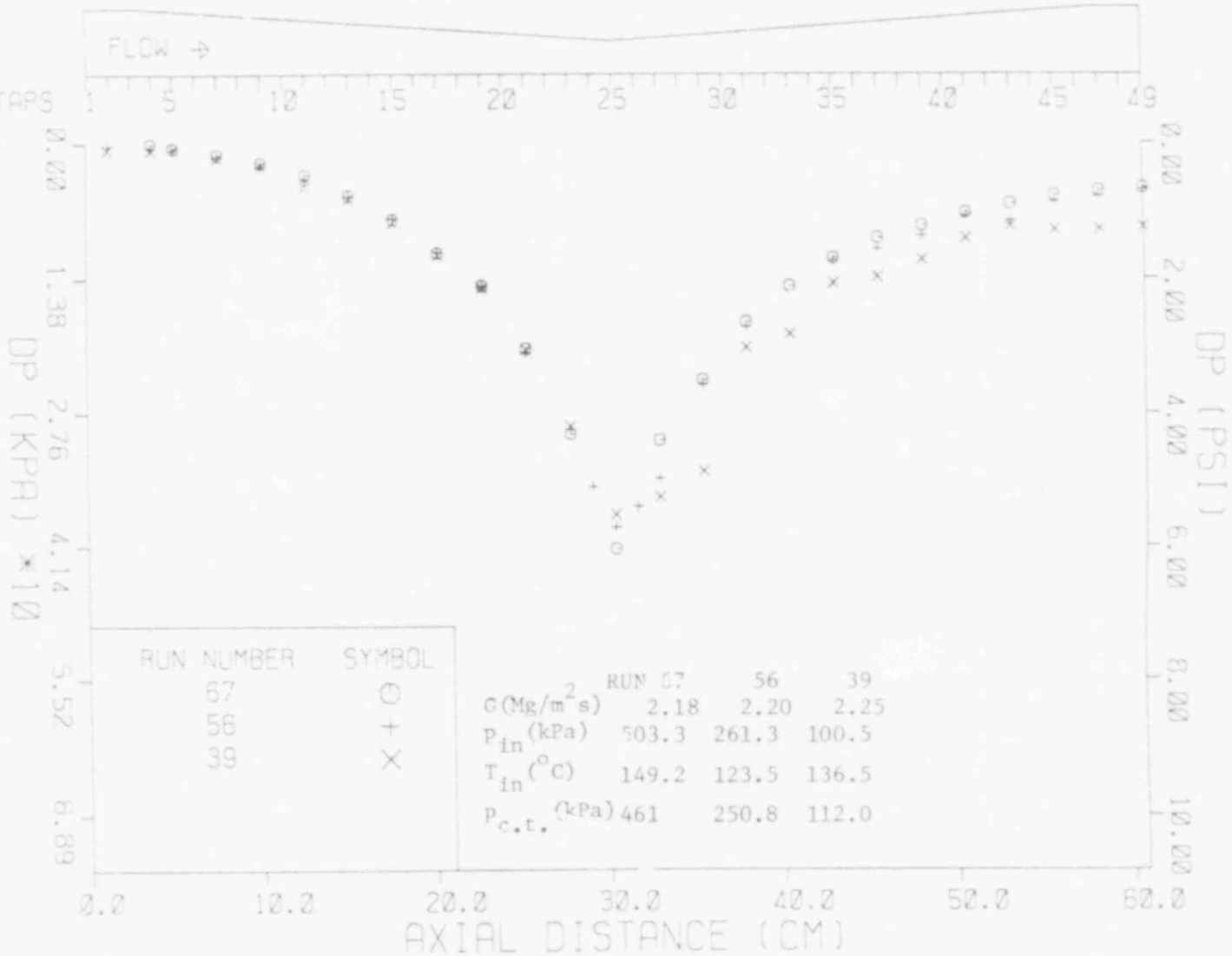

Figure (1.10) - Effect of nozzle inlet temperature on the pressure distribution in the test section (BNL Neg. No 1-726-79).

SCALE 1:1

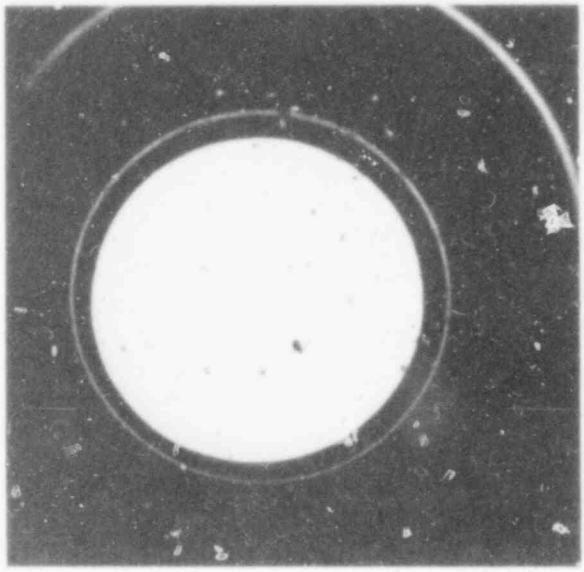

RUN NO. 56

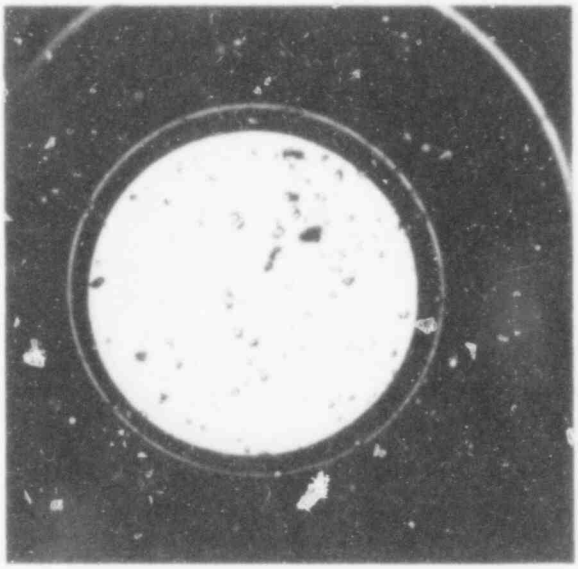

RUN NO. 56

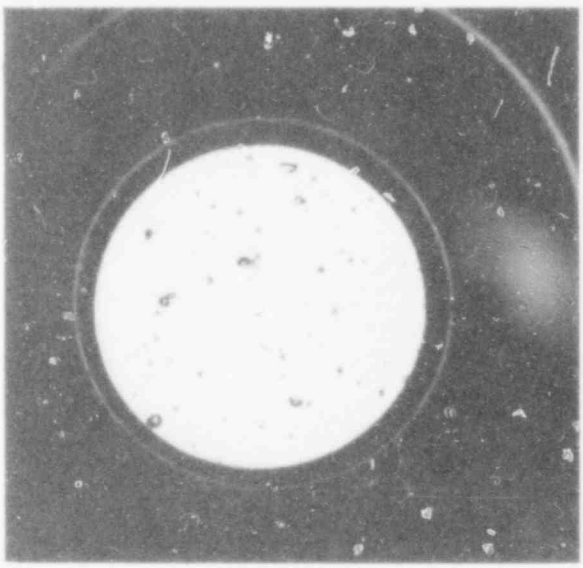

RUN NO. 39

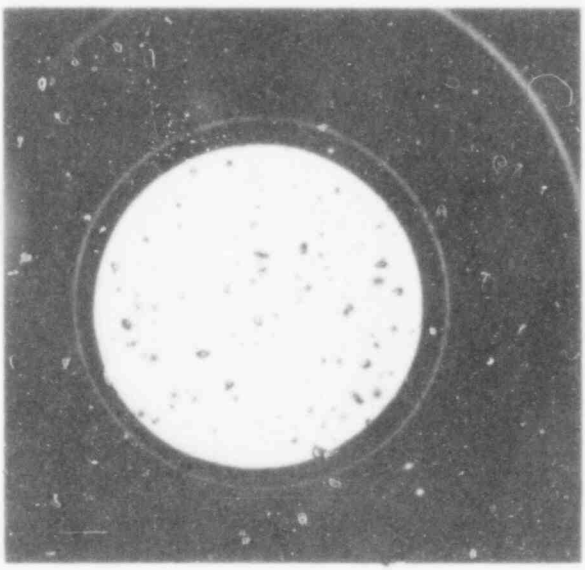

RUN NO. 39

Figure .11) - Photographic observations for experimental conditions presented in Fig. (1.10) (BNL Neg. No 1-921-79).

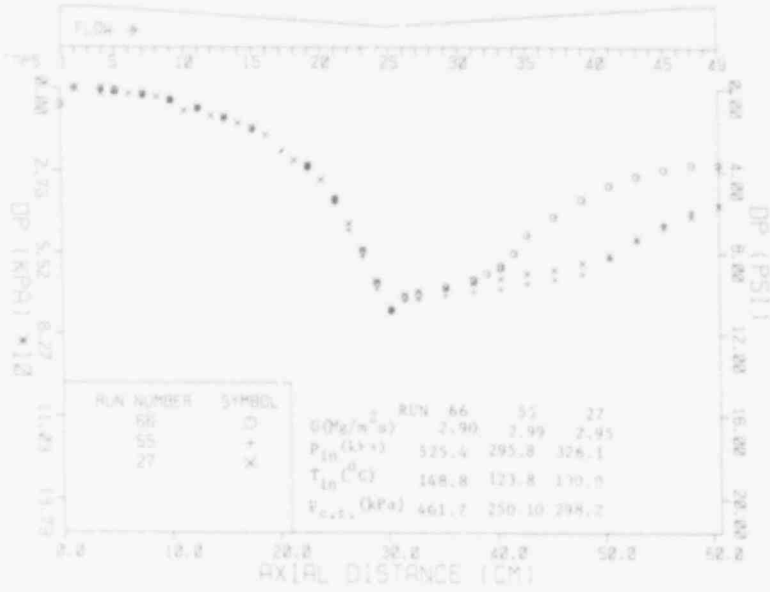

Figure (1.12) - Effect of nozzle inlet temperature on the pressure distribution in the nozzle (BNL Neg. No 1-721-79).

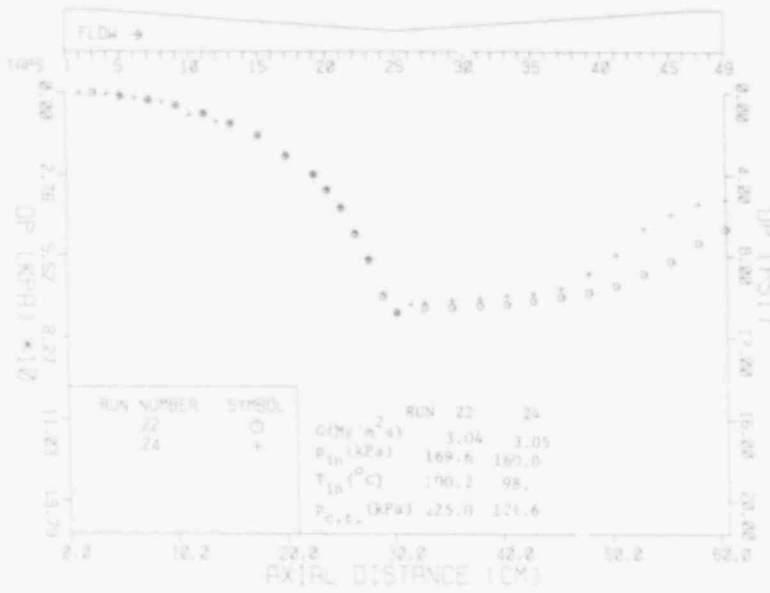

Figure (1.13) - Effect of nozzle inlet temperature on the pressure distribution in the nozzle (BNL Neg. No 1-720-79).

479 311

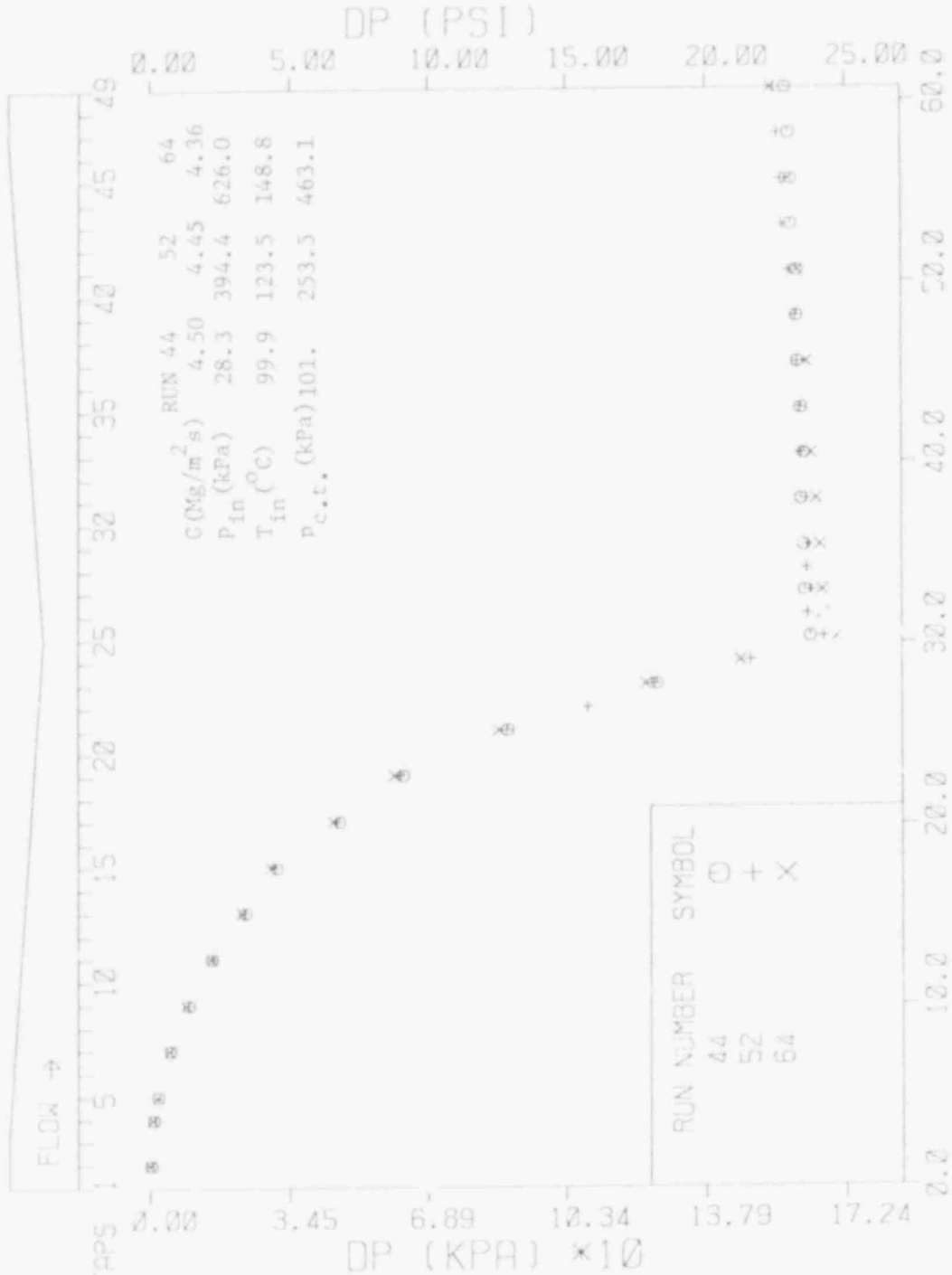

Figure (I.14) - Effect of nozzle inlet temperature on the pressure distribution in the nozzle (BNL Neg. No 1-725-79).

SCALE 1:1

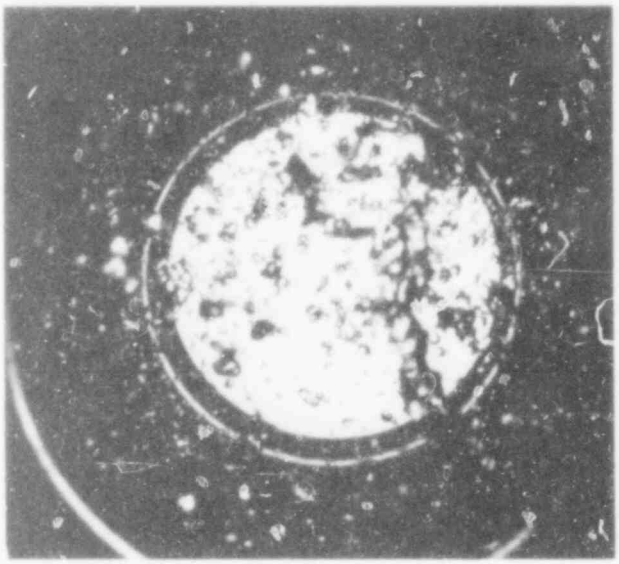

RUN NO. 55

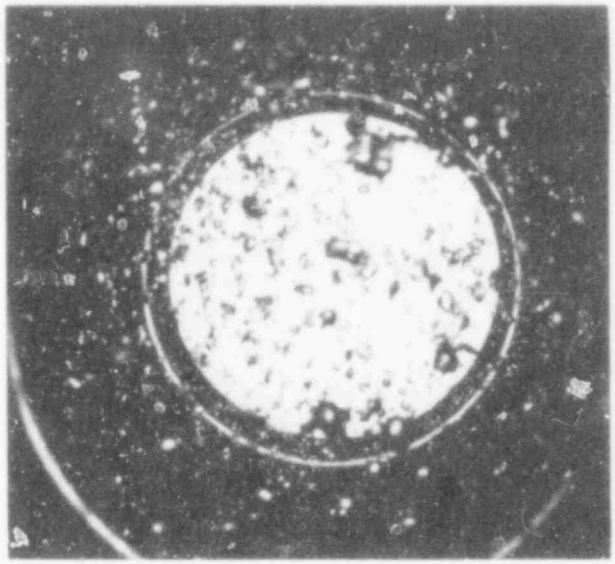

RUN NO. 55

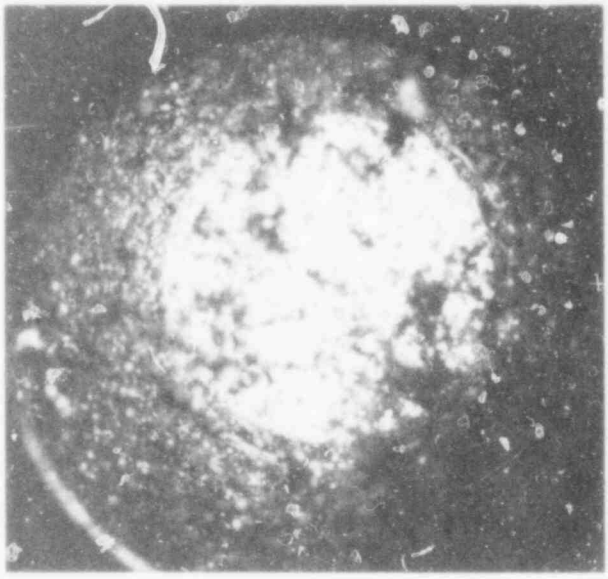

RUN NO. 52

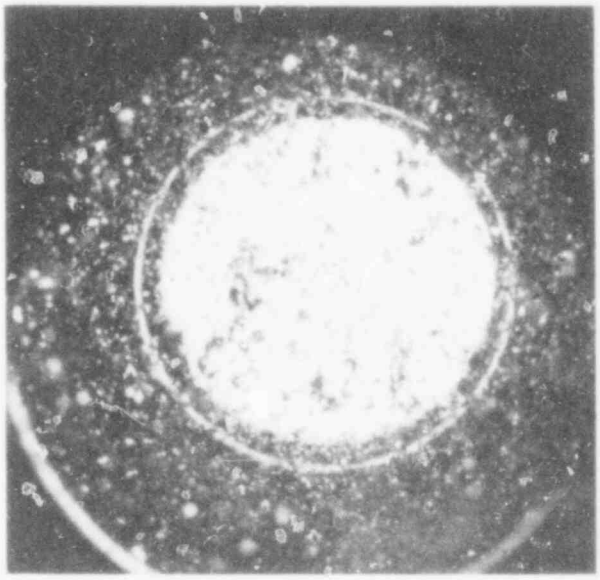

RUN NO. 52

Figure (1.15) - Photographic observation for experimental conditions presented in Figs. (1.12) and (1.14) (BNL Neg No. 1-920-79).

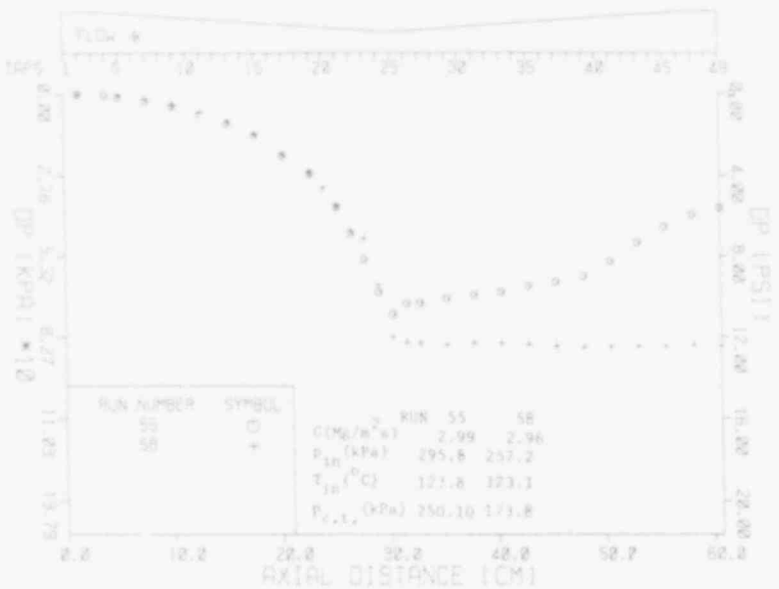

Figure (1.16) - Effect of nozzle inlet pressure at constant subcooling on the pressure distributions in the test section (BNL Neg. No 1-719-79).

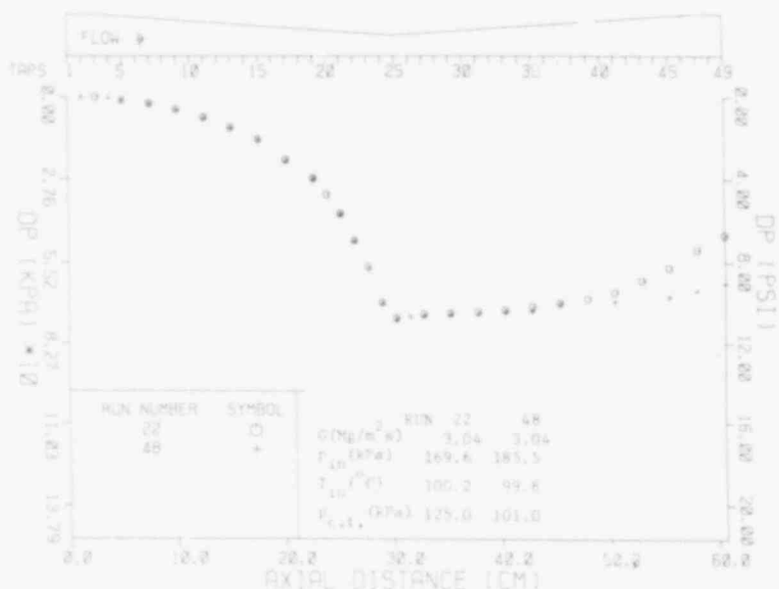

Figure (1.17) - Effect of nozzle inlet pressure at constant subcooling on the pressure distributions in the test section (BNL Neg. No 1-718-79).

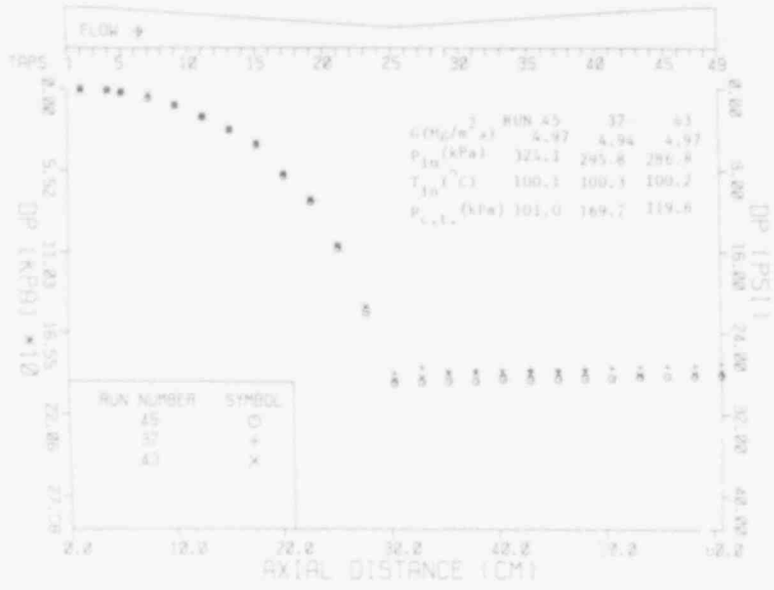

Figure (1.18) - Effect of nozzle inlet pressure at constant subcooling on the pressure distributions in the test section (BNL Neg. No 1-717-79).

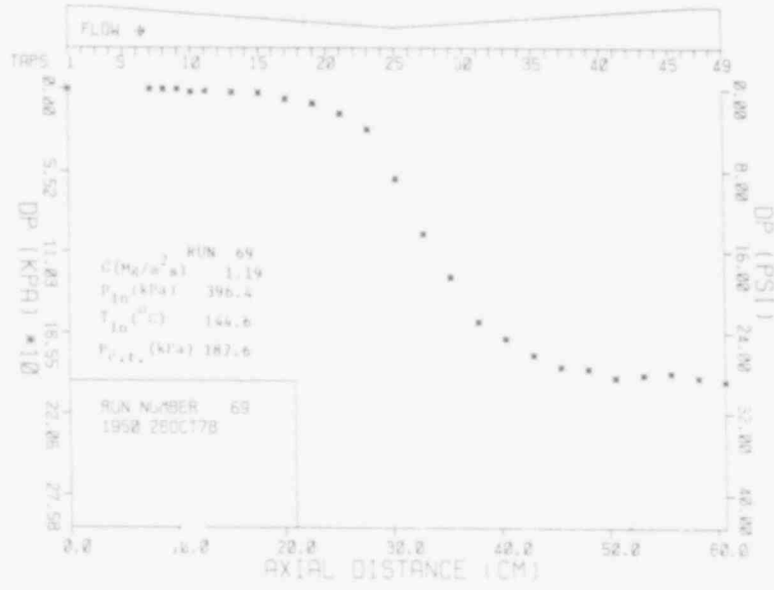

Figure (1.19) - Pressure distributions in the test section while the flashing onset is upstream of the nozzle throat (BNL Neg. No 1-716-79).

Fig. (1.20). This pressure distribution plot nondimensionalized with the inlet kinetic energy of the flow provides a very accurate way of determining the onset of vapor generation.

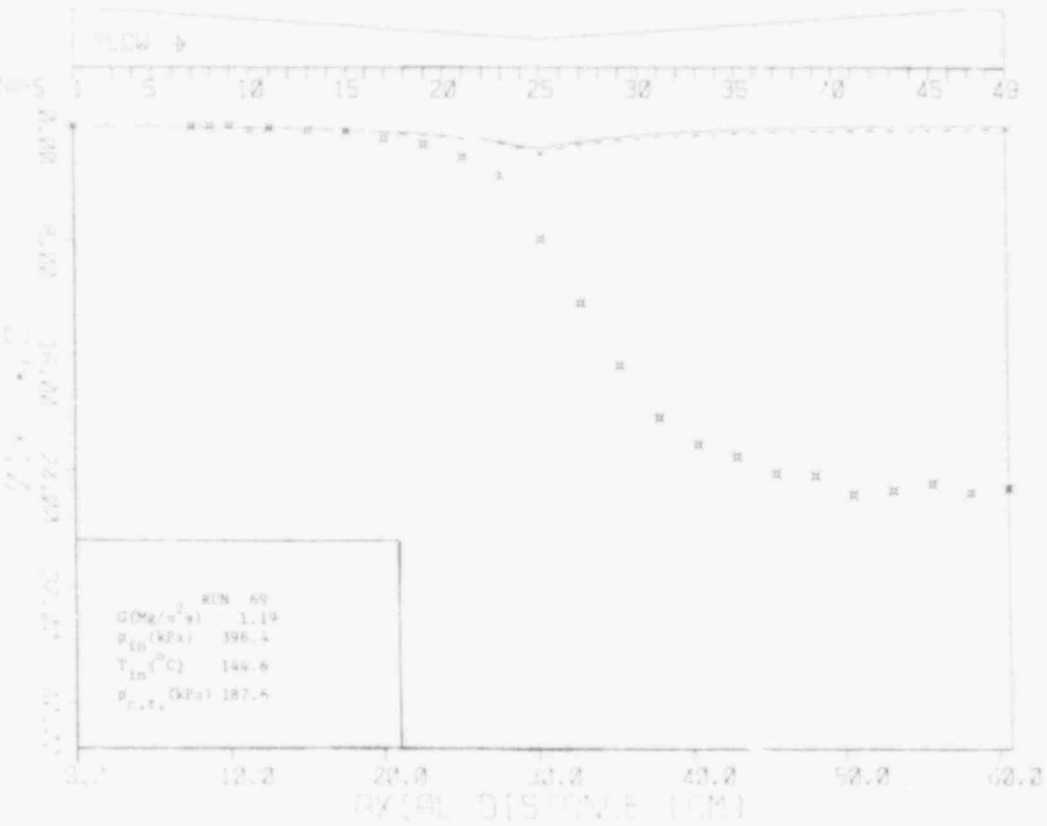

Figure (1.20) - Nondimensional pressure distribution $DP^* = DP/\frac{1}{2}\rho V_{in}^2$, in the test section, while the flashing onset is upstream of the nozzle throat. (No BNL Neg. No).

REFERENCES

ABUAF, N., "Reactor Safety Research Programs: Quarterly Progress Report for the period July-September 1978," BNL-NUREG-50931, p.160 (1978).

LEONHARDT, [illegible] and KLEIN, J. H., "Reactor Safety Research Programs: Quarterly Progress Report for the period July-September 1978," BNL-NUREG-50931, p.154 (1978).

OSWATITSCH, K., "Kondensationserscheinungen in Überschalldüsen," Z. angew. Math. Mech. 22, 1 (1942).

REOCREUX, M., "Contribution a l'Etude des debits critiques en ecoulement diphasique eau-vapeur," PhD. Thesis, University Scientifique et Medicale de Grenoble, France (1974).

SAHA, P., "Reactor Safety Research Programs: Quarterly Progress Report for the period January-March 1977," BNL-NUREG-50661, p. 144 (1977a).

SAHA, P., "Reactor Safety Research Programs: Quarterly Progress Report for the period April-June 1977," BNL-NUREG-50683, p. 145 (1977b).

SAHA, P., "Reactor Safety Research Programs: Quarterly Progress Report for the period July-September 1977, BNL-NUREG-50747, p. 169 (1977c).

SAHA, P., "Reactor Safety Research Programs: Quarterly Progress Report for the period October-December 1977, BNL-NUREG-50785, p. 169 (1977d).

SEYNHAEVE, J. M., GIOT, M. M., and FRITTE, A. A., "Nonequilibrium Effects on Critical Flow Rates at Low Qualities," paper presented at the Specialists' Meeting on Transient Two-Phase Flow, Toronto, August 3-4, 1976. OECD Nuclear Energy Agency Committe on the Safety of Nuclear Installations.

WU, B.J.C., "Reactor Safety Research Programs: Quarterly Progress Report for the period July-September 1978," BNL-NUREG-50931, p.153(1978).

2. THOR CODE DEVELOPMENT (W. Wulff, P. Saha, and O.C. Jones, Jr.)

The general objectives of the THOR Code Development Program is to produce an advanced computer code for the prediction of accident-induced thermohydraulic transients in water-cooled nuclear reactors.

The primary objectives are:

1. The model should include the effects of thermal nonequilibrium, as well as unequal velocities between the vapor and liquid phases.

2. The reactor components should be modeled to include the specific characteristics of each component.

3. The axial variation of the transient fission power must be modeled.

4. The program should include the capability for an initial steady-state computation.

5. The code structure should be modular, permitting its application to different system configurations, as well as providing for ready improvement of individual component and process subroutines.

6. The code should be executing rapidly, for instance, for frequent application in parametric studies.

The objectives itemized above and their implementation represent a significant and major departure from all other previous or currently developed thermal hydraulic codes such as RELAP or TRAC. These are invariably discrete paameter codes written around a standardized unit cell to which the appropriate base-level field equations are directly applied in generally semi-implicit numerical forms. Thus, once the numerical scheme has been identified and coded, simple calculations follow almost immediately. Additional levels of sophistication may then be added as is deemed necessary to appropriately describe the geometry and processes involved.

A single component may require many numerical cells to adequately describe its thermohydraulic behavior. On the other hand, THOR represents a single component as a single, lumped, integral entity where considerable detail, even on the most basic, simplistic level, is required. The modeler is thus able to take advantage of simplifications inherent in the individual component to adequately describe the behavior of each as a single entity. In addition, where multiple flow regimes may exist within a component, the modeler can accomodate these in his development while still allowing the module to shed complicacy as the number of regimes decreases. Thus, the equivalence of a variable fine mesh grid is achieved in principle, on a component-wide basis, without the associated complicacy.

Another major difference is the built-in ability of THOR components to handle, in fact to track, sharp discontinuities in hydraulic or thermal behavior. Thus, a demarcation between a region of all vapor and a high density two-phase mixture, such as occurs in the pressurizer, accumulator, core and steam

generator, is automatically accounted for through appropriate logic, coupled with correct application of the lumped zone and shock balance equations. Tracking of regime interfaces in general and of mixture levels are important for approximating flow parameters effectively by profile functions, and for coupling the hydraulics with fuel element conduction during the reflood period.

An extremely important feature of lumped-parameter modeling with regime interface tracking is that the boundary conditions at every computational cell are continuous with respect to time, even when sharp discontinuities (levels) pass through stationary (Eulerian) component interfaces. This is accomplished with the application of moving regime boundaries which serve simultaneously as boundaries of computational cells (W. Wulff, 1978) with appropriate creation or destruction of zones as required. Discontinuous boundary conditions on a Eulerian finite difference mesh grid frequently produce computational instabilities.

One major short-term disadvantage exists, however, when comparing THOR with other codes. While codes being developed using a discrete cell description can begin to calculate almost immediately and further developed by intensive efforts at improvements, little can be accomplished with the THOR system beyond simple calculations until the complete component module descriptions have been developed following complete spatial integration of the field equations. This requires a thorough analysis of the component resulting in different systems of differential and algebraic equations for each component, different numerical descriptions, and different problems with accuracy, convergence, and stability. The "up-front" investment prior to first credible results is thus seen to be considerable in contrast with other codes. Once developed, however, the payoff potential is expected to be much more rapidly realized.

To achieve these objectives, individual lumped-parameter models have been developed for the components of the reactor system. Discrete-parameter modeling is being used for predicting the choked flow through the break during a Loss of Coolant Accident. A semi-implicit integration scheme is being employed for the ordinary and partial differential equations of lumped and discrete parameter modeling, respectively.

Work toward achieving the above objectives has been described in previous quarterly progress reports (e.g. Wulff, Saha, and Jones, 1978), particularly the formulation of lumped-parameter models for nonhomogeneous nonequilibrium flow in reactor components, process models for vapor drift in gravity-dominated flow channels, nonequilibrium mass transfer for condensation and evaporation, a model for critical break flow, and a model for one-dimensional neutron kinetics. The THOR-1 code structure has been completed, and all PWR reactor component modules are interfaced with the operating system. Developmental verification of component subassemblies has begun in THOR-1 with considerable success.

Progress achieved during the reporting period from October 1 through December 1978 is presented below.

2.1 Component Modeling

2.1.1 Core, Steam Generator and Pressurizer Subassemblies (J. Jo, J.M. Kaufman, R. Krasny, S. Lekach, C. Ruger, and P. Saha)

Work on these subassemblies continued as required when problems were encountered in system calculations. All were upgraded to be compatible with the improved operating system input routines.

2.1.2 Discrete Heated Channel (J.M. Kaufman and S.V. Lekach)

Work is being done on a discrete heated channel with wall heat conduction. This will then provide a bench mark to test the lumped parameter model for core. Presently the discrete heated channel model is being applied to the Combustion Engineering blowdown problem. A satisfactory steady state has been reached and investigation of the transient is now taking place.

2.2 Process Modeling

2.2.1 Quench Front Propagation Velocity (W. Wulff)

Overview

The code module for the prediction of the quench front propagation velocity as described in Volume 2 of the TRAC-P1 (PWR) report (W. Wulff, D.C. Jones, Jr. et al. 1978) has been tested by comparing the code predictions with experimental data (A.W. Bennett et al. 1966). The experimental data were obtained with a falling quench front on the outside of an electrically heated, hollow tube, and in steam-water systems in the pressure range from 7 to 70 bar. The data were used to assess the quench front velocity prediction as a function of pressure. The results of the comparison are shown in Figure 2.1.

Summary of Primary Results

The system pressure affects the quench front propagation velocity through the dependence of fluid properties and of the heat transfer coefficient on pressure. The heat transfer coefficient $h_\ell(T_W)$ as a function of the clad surface temperature is expressed in terms of three key temperatures and three corresponding heat transfer coefficients. These are the saturation temperature T_{sat} the temperature T_{CHF} at the critical heat flux, the minimum stable film boiling temperature T_{MSFB}, and the heat transfer coefficients h_{1p}, h_{CHF} and h_{MSFB} for single phase flow, critical heat flux and minimum stable film boiling, respectively. Of these six key parameters, the minimum stable film boiling temperature $T_{MSFB}(p)$ as a function of pressure p is the most difficult one to predict. T_{MSFB} affects the prediction of the quench front propagation velocity primarily through the calculation of the heat transfer coefficient h_{CHF} at critical heat flux (Ishii, 1975)

$$h_{CHF} = (h_{CHF})_o \, K_1 \qquad (1)$$

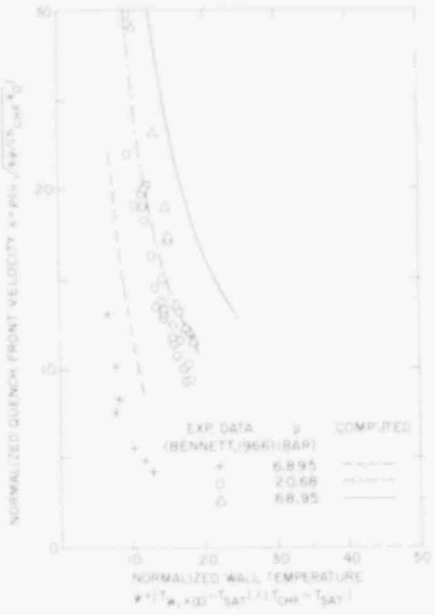

Figure 2.1 Summary of quent front propagation results

where $$K_1 = 1 + \frac{\rho_\ell c_{p,\ell}}{\rho_v h_{fg}} \; 0.05 \; (T_{MSFB} - T_{sat}) + 1.1 \; (T_{sat} - T_\ell) \quad . \qquad (2)$$

Here (h_{CHF}) is the standard burnout heat transfer coefficient. The symbols , c , and h represent density, specific heat, and latent heat of evaporation, respectively. Subscripts and v designate liquid and vapor, respectively.

Three methods have been used to predict $T_{MSFB}(p)$. Firstly, the method given by Henry (1974) was found to produce good values of T_{MSFB} for low pressures between 1 and 2 bar but excessively high values at higher pressures. A few select values of the fluid-clad contact temperature (T_{MSFB}) , which is slightly below T_{MSFB}, are presented in the following table to show that the minimum stable film boiling temperature T_{MSFB} as computed after Henry (1974) exceeds the critical temperature of water T_{cr} = 374° C for relatively low pressures.

Contact Temperature at Minimum Stable Film Boiling
(Henry, 1974)

p (bar)	$(T_{MSFB})_i$ (°C)
1	184
10	649
20	921
40	1,219
70	1,316

This method has been discarded.

The second method used was given by Andreoni and is described in Volume 2 of the THOR-1 (PWR) report (W. Wulff, O.C. Jones, Jr. et al., 1978):

$$T_{MSFB} = T_{MS} - T_f \sqrt{\frac{(\rho\ c_p\ k)_\ell}{(\rho\ c_p\ k)_w}} \qquad (3)$$

$$T_{MS} = 647.2^{o}K - 0.234^{o}K/bar\ [221.2\ bar - p] \qquad (4)$$

Here k stands for the thermal conductivity and the subscript w designates clad properties. These expressions yield values for T_{MSFB} which are too high at low pressures, and consequently, the K_1 values according to Eq. (2) are too high as well. Therefore, this method has also been discarded.

Bennett et al. (1966) inferred the minimum stable film boiling temperature from the quench experiments and tabulated the results. A polynomial curve fit through the tabulated data yields for stainless steel tubes

$$T_{MSFB} = \left\{515.5 + p^{*}\ [131.35 + p^{*}\ (-49.7 + 7.35\ p^{*})]\right\}^{o}K\ , \qquad (5)$$

where $p^{*} = (p-5\ bar)/20\ bar$. This expression gives values in agreement with pool boiling data at low pressures but values slightly larger than the results from Equation 3 at high pressures. Equation 5 has been used to calculate the results in Figure 2.1.

The minimum stable film boiling temperature T_{MSFB} enters also the calculation of the mean thermal boundary layer thickness δ in the clad. Two methods have been employed to estimate this mean thickness δ. Firstly, a cubic profile was used for the lateral temperature distribution T(y) in the clad. This cubic profile satisfies

$$\left.\begin{aligned} &\text{at } y = \delta: \quad \partial T/\partial y = 0 \\ &\qquad\qquad \partial^2 T/\partial y^2 = 0 \\ &\qquad\qquad T = T_{w,+\infty} \quad \text{for } \delta < s \\ &\text{at } y = 0: \quad \partial T/\partial y = \bar{h}_c/k_w\ (T_o - T_\ell)\ , \end{aligned}\right\} \qquad (6)$$

where $T_{w,+\infty}$ designated the downstream wall temperature, T_o designates the mean surface temperature $T_{sat} < T_o < T_{w,+\infty}$, and s stands for the clad thickness. The cubic profile yields for $\delta < s$ the thickness

$$\delta = (3k_w/\bar{h}_c)\ (T_{w,\infty} - T_o)\ /\ (T_o - T_\ell) \qquad (7)$$

and for $\delta > s$ it yields the back wall temperature T(s). The application of Equation 7 is sensitive to the choice of the average film coefficient h_c and the mean surface temperature T_o.

A second method has been used earlier by Ishii (1975) who set

$$\delta = \pi\alpha\tau \quad , \quad \tau = \frac{\varepsilon}{u} \left(T_{w,+\infty} - T_{CHF}\right) / \left(T_{MSFB} - T_{CHF}\right) \quad . \qquad (8)$$

Here α, ε and u represent the thermal diffusivity of the clad material, the sputtering length and the quench front propagation velocity u, respectively. Using the simplified analysis of Ishii (1975) one can compute an estimate of u and ε and evaluate δ according to Equation 8. However, better estimates for the penetration thickness δ are

$$\delta = 12\alpha\tau \qquad \text{for sudden change of surface temperature, and} \qquad (9)$$

$$\delta = 6\alpha\tau \qquad \text{for suddenly imposed, fixed surface heat flux.} \qquad (10)$$

Equations 7 and 10 yield approximately the same penetration thicknesses if $T_o = T_{CHF}$ is chosen but the trend of quench front propagation velocity $u(T_{w,+\infty})$ as a function of wall temperature agrees better with experimental data if Equations 9 and 10 are used. Equations 7 and 10, however, give velocities u which are greater than experimentally obtained velocities. Therefore, Equation 9 was used to produce the comparison in Figure 2.1.

Future Efforts:

The data comparison is to be extended to the regime of thermally thin clad walls which is important for low propagation velocities and high wall temperatures.

2.3 System Modeling

2.3.1 Discrete Parameter Model (S.V. Lekach)

During the past quarter the discrete parameter model, including choking, was converted from a (h_m, p, v_m, c) basis for the solution vector at every node to a (h_m, p, G_m, c) vector solution. The conversion is done in a subroutine producing an exact conversion prior to the differencing.

2.3.2 THOR Operating System (S.V. Lekach)

The set of linear algebraic equations produced by the different modules in THOR can now be solved by either a standard, FORTRAN-written, linear equation solver (GELG) or by two CDC COMPASS language-written routines (DEC/SOL). The routines are set up such that no change in THOR coding is required. The DEC/SOL set is so optimized that it is capable of reducing the typical system computation times by 40-80%

2.3.3 Input Description (R. Krasny)

A user-oriented input routine was installed into the system. The code now reads the input information from an input file. In addition, another routine was written to output a pseudo-restart file which conforms to the input file format. It is intended that this capability can be used to save a particular set of steady-state data for use in starting arbitrary transients from the given conditions. However, this facility cannot be used for a genuine transient restart because some information (e.g. derivatives) is not saved.

2.4 Developmental Verification

2.4.1 USNRC Standard Problem No. 8 (D.I. Garber and C.J. Ruger)

During the present quarter effort has been directed at obtaining the steady state for the entire system configured to represent Standard Problem No. This exercise utilizes 30 THOR components and serves as a general "shake-out" of the THOR system and components. A number of problems have been identified and corrected.

The steady-state computation begins with the system variables initialized, the pressurizer decoupled from the main system body, and a fixed pressure drop representing the pump. A constant heat transfer coefficient is currently being used in the steam generator. The time step size is initially small, the computation commences with ever increasing time step sizes. When the system has relaxed somewhat, the homologous curve pump model replaces the fixed pressure drop pump representation. This system using the pump motor control curve will attain a steady-state asymptote. When the system with pump is relaxed and conditions around the surge line are a reasonable match, the pressurizer is connected to the system. Problems which are presently being addressed arise at low flow rates in the pressurizer and when sub-cooled liquid flows into the pressurizer. The CPU time per time step for the entire system has been found to be approximately 0.8 seconds/step.

2.4.2 Downcomer/Lower Plenum Subassembly (U.S. Rohatgi, L. Slatest, and P. Saha)

The work on downcomer subassembly consisting of two cold leg pipes, downcomer, and lower plenum was continued. The composite profile functions in the downcomer model were slightly changed to account for flow reversal more accurately. This improvement allowed the computation to proceed to 40 seconds of transient. The details of this subassembly and the boundary conditions used has been described in the previous quarterly. Some of the results are shown in Figures 2.2 to 2.4. Figures 2.2 and 2.3 show the comparison between experimental mass flow rates at the junction of lower plenum and core, and at the break with the predicted values and it is good. However, the comparison of average density in the lower plenum with the experimentally obtained density by a single diagonal beam is not very good. The model predicts the voiding much too soon. This could be explained by the homogeneous model for the lower plenum.

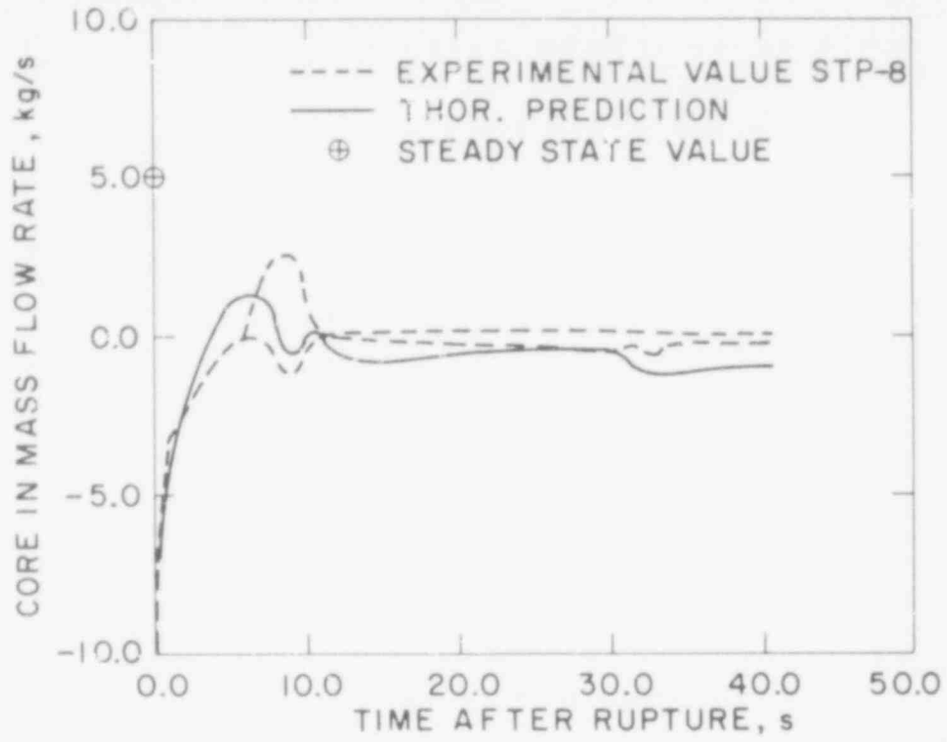

Figure 2.2 Mass flow rate at the junction of the lower plenum and core

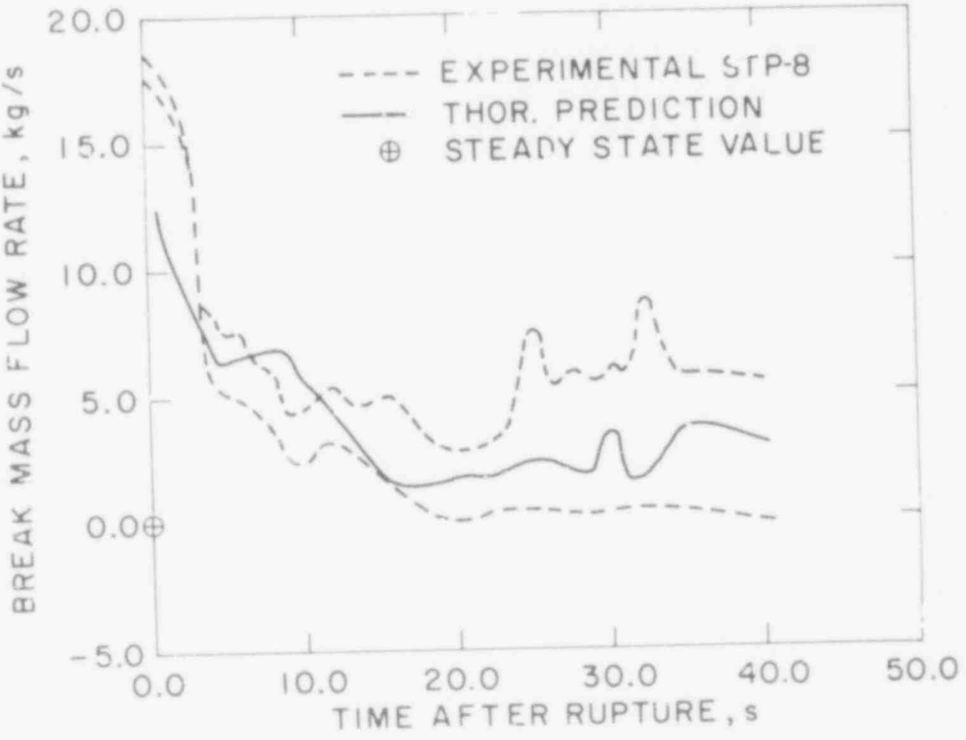

Figure 2.3 Mass flow in borken cold leg 1.03 m from the vessel

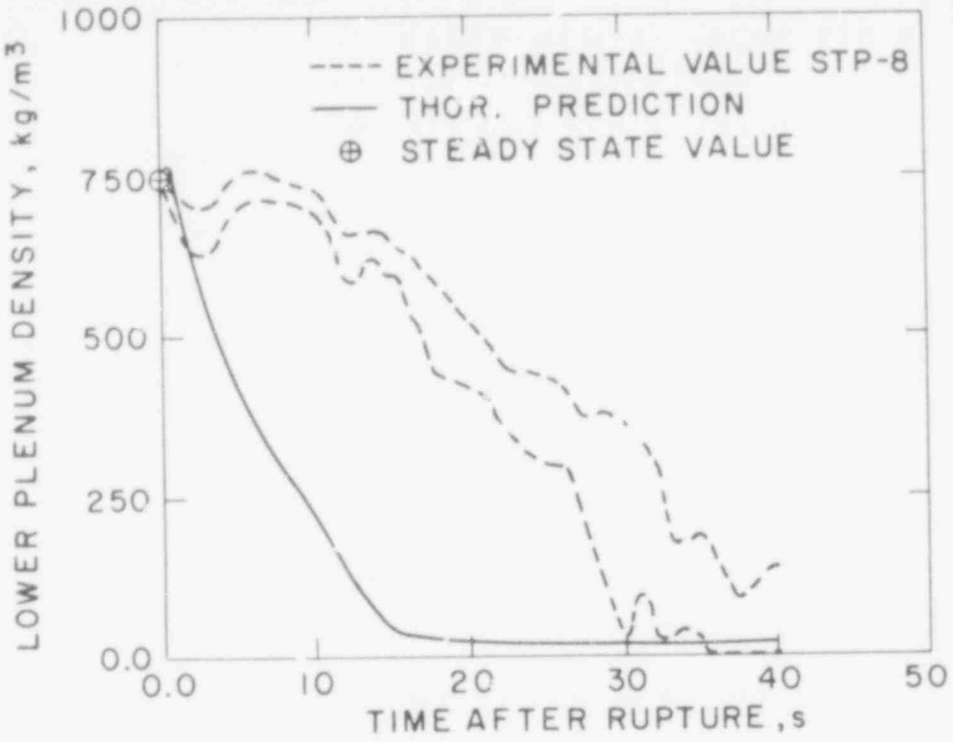

Figure 2.4 Density in the lower plenum as predicted by THOR and as measured by a diagonal densitometer beam.

As is seen from Figure 2.2 the flow is coming into the lower plenum at core inlet, and an absence of drift will mean that the vapor velocity is larger than it should be. This, coupled with the reverse effect at the junction of the lower plenum and downcomer, increases the voiding in the lower plenum.

2.5 Numerical and Analytical Modeling of the N-zone Stability Problem

The previous quarterly (Eisenhart, 1978) gave an overview to the current ideas on the mathematical problems involved in the N-zone stability question of a THOR heated channel. During this quarter a new set of difference analogues was derived and is currently being implemented into an experimental stand alone program. Also, a different approach (continuity across the zone interfaces) to the physical modelling was also pursued. This later approach is a modification of one previously attempted with the expectation of circumventing the difficulties encountered and eliminating the need of detailed knowledge of drift near the interface.

2.5.1 A New Finite Differencing (L.D. Eisenhart)

A semi-implicit technique requires some level of approximation to obtain linearization in order to formulate a linear coefficient matrix at each time step. The most common technique is the linear Taylor approximation:

$$f(t_{j+1})\, g(t_{j+1}) \quad f(t_{j+1})g(t_j) + f(t_j)\, g(t_{j+1}) - f(t_j)\, g(t_j) \qquad (11)$$

alternatively noted

$$f_{j+1}\, g_{j+1} = f_{j+1}\, g_j + f_j g_{j+1} - f_j g_j \tag{12}$$

However, Equation 12 has been less understood when f (or g) is a derivative of a basic variable, e.g. position, enthalpy, or flow. Earlier THOR work used the less than linear approximation of Equation 13.

$$\frac{\partial A_{j+1}}{\partial t}\, g_{j+1} \approx \frac{\partial A_{j+1}}{\partial t}\, g_j \approx \left(\frac{A_{j+1} - A_j}{\Delta t_j}\right) g_j \tag{13}$$

Equation 13 can be derived from Equation 12 with the addition of two more assumptions:

$$\text{a)} \quad \left(g_{j+1}\right) - g_j \frac{\partial A_j}{\partial t} = O(\epsilon) \tag{14}$$

$$\text{b)} \quad \frac{\partial A_{j+1}}{\partial t} = (A_{j+1} - A_j)\ /\Delta t \tag{15}$$

Ignoring the terms in assumption a) will lead to a difference scheme that, regretfully, is of order 0 (const.) rather than (Δt). If, instead assumption is relaxed, Equation 13 is replaced by

$$\frac{\partial A_{j+1}}{\partial t}\, g_{j+1} \approx \frac{A_{j+1} - A_j}{\Delta t_j}\, g_j + \frac{A_j - A_{j-1}}{\Delta t_{j-1}} \left(g_{j+1} - g_j\right) \tag{16}$$

A set of multizone heated channel finite difference equations was then derived using Equations 12 and 16 rather than Equations 12 and 13 as was done previously. Although, this should enhance the approximation properties of the discretized ODE's in the system, it does nothing to relax the stiffness of the associated algebraic conditions. Specifically, the interface equation relating the jump in momentum given by

$$G_{2i-1} - G_{2i-2} = \dot{Z}_i \left(\rho_{2i-1} - \rho_{2i-2}\right) \tag{17}$$

is unchanged by this new differencing method since the density (ρ) is not a primary variable. In either case, the difference analogue to Equation 17 is

$$\Delta t_j \left(G_{2i-1}^{j+1} - G_{2i-2}^{j+1}\right) = \left(Z_i^{j+1} - Z_i^j\right) \left(\rho_{2i-1}^j - \rho_{2i-2}^j\right) \tag{18}$$

It was noted that in other differencing schemes the first order time difference Equation 15 is assumed to be the derivative at some point t_j^* where $t_j < t_j^* < t_{j+1}$. Usually t_j^* is chosen as the midpoint. Alternatively, Equation 15 is replaced by

$$1/2 \left[f_{j+1} + \quad_j\right] = \left[A_{j+1} - A_j\right] /\Delta t_j \tag{19}$$

where $f(t) = dA(t)/dt$ in order to express all terms as variables evaluated at the discrete time points t_j. Thus f_{j+1} is given trivially by

$$f_{j+1} = \frac{2}{\Delta t_j}\left[A_{j+1} - A_j\right] - f_j \tag{20}$$

The only extra condition necessary is $f_o(=f(o))$. But this is also trivial since all transients are initiated from some steady state condition where $f_o=0$ Substituting Equation 20 into Equation 12 gives

$$g_{j+1}\, f_{j+1} = g_{j+1}\, f_j + \frac{2}{\Delta t_j} g_j\, A_{j+1} - \frac{2}{\Delta t_j} g_j\, A_j - 2\, g_j\, f_j \tag{21}$$

which is directly usable in a semi-implicit scheme when f(t) is the first derivative of a function A(t).

Again, a set of finite difference equations was derived now using Equations 12 and 16. However, due to the assumption of Equation 19 even the algebraic balance equations such as the momentum jump across the moving interface

$$G_{2i-1} - G_{2i-2} = U_i\left[\rho_{2i-1} - \rho_{2i-2}\right] \quad \text{where } U = dZ/dt \tag{22}$$

were also changed. After some modest algebra, we obtain Equation 23.

$$\Delta t_j\left(G_{2i-1}^{j+1} - G_{2i-2}^{j+1}\right) - 2\left(\rho_{2i-1}^{j} - \rho_{2i-2}^{j}\right) Z_i^{j+1}$$

$$= -\left(\rho_{2i-1}^{j} - \rho_{2i-2}^{j}\right)\left[2Z_i^j + \Delta t_i\, U_i^j\right] \tag{23}$$

it should be noted that as $\Delta t_j \to 0$ the effect of this assumption (i.e. the placement of point in time of $(A_{j+1}-A_j)/\Delta t_j$ denoted by Equation 19 this assumption Equation 19 goes to zero as is physically expected. This behavior in the limit of $\Delta t_j \to 0$ is the same as the behavior of the previous schemes (e.g. Equation 18). However, for small but positive Δt_j as is truly encountered in computations, the stiffness of the equations should be altered. These difference equations are currently being implemented into an existing small test program. Their impact will be analyzed and reported during the next quarter. Also, some adjustments to the instantaneous linear profile assumptions will also be investigated.

2.5.2 Continuous Drift Flux Model (J.H. Jo)

It seems that one of the possible sources of instability in the basic physical model is the jump equations that account for the discontinuous change of certain variables, particularly the drift flux, across an interface. Therefore, it was hypothesized that one might be able to alleviate this difficulty

if the incerface jump equations could be avoided. This approach is similar to that examined previously (Rugei, 1977) except that v_{gj} derivatives are not required. This approach assumes a continuous change of v_{gj} across the interface while the linear profile of c still requires uniform v_{gj} within the flow regime. The resultant v_{gj} distribution in a flow regime is shown in Figure 2.5.

An attempt was made to reformulate the integrated lump equations based on this distribution. The terms involving v_{gj} can now be integrated as follows. First,

$$\int_{Z_1}^{Z_2} \frac{\partial}{\partial Z} \left(\frac{c}{1-c} \rho v_{gm}^2 \right) dZ = \frac{c}{1-c} \rho v_{gm}^2 \Big]_{Z_1}^{Z_2} \tag{24}$$

which represents no changes from the original formulation. Also, using the product rule, (25)

$$\int_{Z_1}^{Z_2} \frac{1}{\rho} \frac{\partial}{\partial Z} \left\{ \rho v_{gm} (h-h_\ell) \right\} dZ = \frac{1}{\rho} \rho_\ell v_{gj} (h-h_\ell) \Big]_{Z_1}^{Z_2} - \int_{Z_1}^{Z_2} \rho v_{gm} (h-h_\ell) \frac{\partial(1/\rho)}{\partial Z} dZ$$

which may be rearranged to yield (since $1/\rho$ is linear),

$$= \frac{1}{\rho} \rho_\ell v_{gj} (h-h_\ell) \Big]_{Z_1}^{Z_2} - \frac{\partial(1/\rho)}{\partial Z} \int_{Z_1}^{Z_2} \rho_\ell v_{gj} (h-n_\ell) dZ. \tag{26}$$

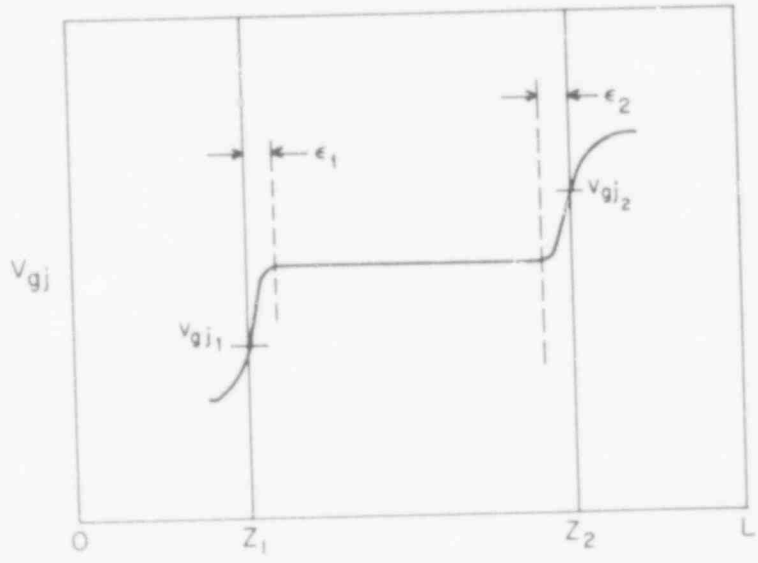

Figure 2.5 Drift flux distribution in a flow regime

479 321

In terms of the layer thickness ε_1 and ε_2, we then have

$$= v_{gm} (h-h_\ell)\Big]_{Z_1}^{Z_2} - \frac{\partial(1/\rho)}{\partial Z} \left[\int_{Z_1}^{Z_1+\varepsilon_1} \rho_\ell v_{gj} (h-h_\ell)\, dZ \right.$$

$$\left. + \int_{Z_1+\varepsilon_1}^{Z_2-\varepsilon_2} \rho_\ell v_{gj} (h-h_\ell)\, dZ + \int_{Z_2-\varepsilon_2}^{Z_2} \rho_\ell v_{gj} (h-h_\ell)\, dZ \right] \qquad (27)$$

As ε_1, ε_2 independently approach to zero, the first and third terms within the brackets vanish since the integrands are finite and the second term, since ρ_ℓ and v_{gj} are considered constant in $(Z_1+\varepsilon_1, Z_2-\varepsilon_2)$, becomes

$$\lim_{\varepsilon_1,\varepsilon_2 \to 0} \int_{Z_1+\varepsilon_1}^{Z_2-\varepsilon_2} \rho_\ell v_{gj} (h-h_\ell)\, dZ \qquad (28)$$

$$= \langle \rho_\ell v_{gj} \rangle (\langle h \rangle - h_\ell) (Z_2-Z_1)$$

The resultant expression for the integration is

$$\int_{Z_1}^{Z_2} \frac{1}{\rho} \frac{\partial}{\partial Z} \left\{ \rho v_{gm} (h-h_\ell) \right\} dZ = \frac{1}{\rho_2} (\rho_\ell v_{gj})_2 (h_2-h_\ell) - \frac{1}{\rho_1} (\rho_\ell v_{gj})_1 (h_1-h_\ell)$$

$$- \langle \rho_\ell v_{gj} \rangle (\langle h \rangle - h_\ell) (Z_2-Z_1) \frac{\partial(1/\rho)}{\partial Z} \qquad (29)$$

which may be compared with the discontinuous result given in Volume 3 of the THOR-1 (PWR) report (W. Wulff, O.C. Jones, Jr. et al., 1978). It is seen that the two differ in that the new expression involves the difference of v_{gj} at both ends while the old one treats them as identical.

In the process, the same assumptions were used for the linear $1/\rho$ profile and uniform ρ_ℓ, h_ℓ, v_{gj}, etc. within the regime.

Similarly;

$$\int_{Z_1}^{Z_2} \frac{1}{\rho} \frac{\partial}{\partial Z} (\rho c\, v_{gm})\, dZ = \frac{1}{\rho} \rho c\, v_{gm} \Big]_{Z_1}^{Z_2} - \int_{Z_1}^{Z_2} \rho c\, v_{gm} \frac{\partial (1/\rho)}{\partial Z}\, dZ$$

$$= c\, v_{gm} \Big]_{Z_1}^{Z_2} - \frac{\partial (1/\rho)}{\partial Z} \rho_\ell\, v_{gj} \langle c \rangle (Z_2 - Z_1) \qquad (30)$$

The implication is that integration has been completed without the discontinuity of v_{gj} across the interface while preserving the uniform v_{gj} and the result does not depend on the arbitrary slope across interfaces. However, it was later found that this approach does not provide mass conservation across the flow regime (mass is still conserved across interfaces, though), because linear profile of c requires uniform v_{gj} not only within the flow regime but at both boundaries as well.

REFERENCES

BENNETT, A.W. et al., (1966) The Wetting of Hot Surfaces by Water in a Steam Environment at High Pressure, AERE-R5146, 1966.

EISENHART, L. (1978) THOR Code Development, Reactor Safety Research Programs, Quarterly Progress Report, July 1 - September 30, 1978, BNL-NUREG-50931, 1978.

HENRY, R.E. (1974) A Correlation for Minimum Film Boiling Temperature, AiChe. Symposium Series, Vol. 70, Nr. 138, pp. 81-90, 1974.

ISHII, M. (1975) Study on Emergency Core Cooling, J. British Nuclear Energy Society, Vol. 14, No. 3, pp. 237-242, 1975.

WULFF, W. JONES, O.C., Jr. et al., (1978) THOR-1 (PWR) Code for Predicting the Thermal Hydraulic Behavior of Nuclear Reactor Systems, Vol. 2, Vol. 3, Process Modeling and Verification, Informal Report, BNL-NUREG-24760, 1978.

RUGER, C. (1977) THOR Code Development, Reactor Safety Research Programs, Quarterly Progress Report, July 1 - Sept. 20, 1978, BNL-NUREG-50931, 1978.

4. Stress Corrosion Cracking of PWR Steam Generator Tubing

(D. van Rooyen)

4.1 Laboratory and Apparatus

As reported in the last quarterly report, all equipment is installed and operating, but results have prompted us to build additional test facilities and modify some of the test procedures. Specifically, more slow strain rate testing is planned, the constant stress method was improved, and slow strain specimens were added to eliminate the need to flatten tubes.

The one slow strain apparatus that has been operating provided some very useful information for material which may be experiencing conditions similar to active denting. This testing, especially at the lower temperature where very low strain rates are needed to induce cracking, requires a fairly long exposure time. Therefore, to examine a sufficient number of materials and test conditions, it has become necessary to build additional slow straining equipment. The second unit will be completed before March and components for the third unit have been ordered.

There has been some concern regarding the amount of cold working the specimens received as a result of flattening the tube sections before cutting into plate tensile pieces. Tensile specimens have been prepared from the tube sections without any rolling and special grips have been designed to hold the semicircular ends. These specimens will be tested and compared to the plate type which have been used to date, to ensure that the slight degree of cold work did not influence the conclusions drawn.

Capsules (Fig. 1) have been designed and fabricated to provide a specimen with a stress pattern similar to that of a dented tube. These capsules will be placed in an autoclave and the stress in the gauge section will be controlled by the difference of the vapor pressure of the solution and the gas pressure in the tube. The gas pressure inside the tubes will be held constant to simulate a condition where denting has stopped or the pressure will be slowly increased to provide the continuously increasing strain a tube would experience in an active denting condition. Time to failure will also be recorded by a contacting pressure gauge monitoring the internal pressure. This test is being done to conform to the "different stress types" item in the proposed schedule of the research.

4.2 Results

Table 1 shows the five heats, of production type material, that have cracked both at 365°C and 345°C. The exposure time of the U-bend specimens at 325°C is now 20 weeks and we are expecting to see some results from that test very shortly.

The previous report listed the N_2 content of materials which have cracked as U-bends. The results of analysis on the heats which have not cracked have now been received and the results are summarized in Table 2. This is a very small sampling for any decisions on the effect of N_2, but it can be seen that the free N_2 content of the uncracked materials is ~30% to 60% higher than the slowest cracking material. More data will be obtained with N_2.

Figure 2 is a family of stress strain curves for heat #4 in D.I. H_2O with a strain rate of $\sim 10^{-7}$ sec^{-1}. It can be seen from Table 3 that the crack propagation rate diminishes with temperature to the extent that very little intergranular SCC occurs at 325°C with a strain rate of 10^{-7} sec^{-1}. The 325°C test was repeated with a strain rate of 10^{-8} sec^{-1}, and Figure 3 shows the comparison of the two strain rates. A test at 290°C with a strain rate of 10^{-8} sec^{-1} is now in progress.

Controlled potential studies are continuing with heat #5 in 365°C simulated primary water. Five of the six specimens in the series have now shown accelerated cracking as compared to U-bends of the same material in D.I. H_2O. The only specimen still uncracked (see Table 4) is one being held 200 mV cathodic to the corrosion potential. A point of interest is that the specimen at the open circuit potential cracked in 40 to 45 days whereas this material generally cracks in 10 weeks in D.I. water. During the test, specimens which have cracked are replaced with new specimens to determine the scatter in failure time. The first replacement specimen to crack was in the -120 mV position. This was the first specimen to crack in the initial series, however, as shown in Table 4, the difference in failure time is quite large.

Constant stress tests on a series of 5 C-ring specimens from heat #2 are in progress. The specimens are stressed to 130% y.s. and exposed to 365°C D.I. water. There has been no indication of failure after 4 weeks.

Cyclic load tests using a sinusoidal wave form and a stress of 110% to 130% of the yield strength have shown accelerated cracking of the plate tensile specimens. Table 5 shows that although the frequency was varied from 10^{-3} Hz to 10^{-2} Hz and 10^{-1} Hz the time to failure remained relatively constant at 13 to 15 days. The next series of testing will explore the effect of increased load range using the same wave form and frequencies. Also, it is necessary to find out if cyclic stress will cause cracking in materials that do not fail as U-bends and after treatment at 700°C, which increases resistance to SCC.

TABLE I SPECIMENS FAILED IN D.I. H_2O

Heat No.	Specimen No.	Specimen Type	Heat Treatment	Test Temp. (°C)	Time to Failure (WEEKS)
2	0-5	Tube U-bend	As Received	365	2 to 4
2	0-6	" " "	" "	365	2 to 4
2	0-8	" " "	" "	365	0 to 2
2	1-3	" " "	" " + Pickled	365	2 to 4
2	1-4	" " "	" " + Pickled	365	0 to 2
2	10-4	" " "	15 min. in H_2 @ 1775°F	365	6 to 8
2	11-3	" " "	" " " " " " +Pickle	365	0 to 2
2	0-10	" " "	As Received	345	10 to 12
2	1-7	" " "	" " + Pickled	345	12 to 14
4	0-6	Tube U-bend	As Received	365	10 to 12
4	0-7	" " "	" "	365	10 to 12
4	1-3	" " "	" " + Pickled	345	12 to 14
4	1-4	" " "	" " + Pickled	345	6 to 8
5	0-1	Tube U-bend	As Received	365	8 to 10
5	0-5	" " "	" "	365	10 to 12
5	0-6	" " "	" "	365	16 to 18
5	0-7	" " "	" "	365	16 to 18
5	1-1	" " "	" " + Pickled	365	8 to 10
5	0-14	" " "	As Received	345	12 to 14
5	1-7	" " "	" " + Pickled	345	10 to 12
5	1-8	" " "	" " + Pickled	345	14 to 16
6	0-1	Tube U-bend	As Received(unannealed)	365	0 to 2
6	0-2	" " "	" " "	365	0 to 2
6	C7 & C8	C-Rings*	" " "	365	0 to 2
6	C9 & C10	C-Rings**	" " "	365	0 to 2
6	C11 & C12	C-Rings*	" " "	345	0 to 2
6	C13 & C14	C-Rings**	" " "	345	0 to 2
6	C1,C2 & C3	C-Rings*	" " "	290	0 to 9
6	C4,C5 & C6	C-Rings**	" " "	290	0 to 9
10	1-1	Tube U-bend	As Received + Pickled	365	2 to 4
10	1-2	" " "	" " " "	365	0 to 2
10	1-5	" " "	" " " "	345	6 to 8
10	1-6	" " "	" " " "	345	2 to 4
11	0-2	Tube U-bend	As Received	365	12 to 14
11	1-1	" " "	" " + Pickled	365	2 to 4
11	1-2	" " "	" " + Pickled	365	4 to 6
11	1-5	" " "	" " " "	345	12 to 14
12	0-1	Tube U-bend	As Received(cold worked)	365	0 to 2
12	0-2	" " "	" " " "	365	0 to 2
12	0-3	" " "	" " " "	365	0 to 2
12	C1 & C2	C-Rings*	" " " "	365	0 to 2
12	C3 & C4	C-Rings**	" " " "	365	0 to 2
12	C10	C-Rings*	" " " "	345	4 to 6
12	C11 & C12	C-Rings**	" " " "	345	4 to 6

*Stressed to 95% Y.S.
**Stressed to 110% Y.S.

TABLE 2 Nitrogen Content and Average Failure Times of Inconel 600

Heat #	Wt % N_2		Av. Failure Time of U-bend in 365°C D.I. H_2O (WEEKS)
	Fixed	Free	
2	.0068	.0042	2.2
4	.0030	.0052	11.
5	.0034	.0044	12.6
10	.0063	.0047	2.
11	.0089	.0021	4.
3	.0073	.0067	No Cracks After 20 wks.
13	.0058	.0082	

TABLE 3 C.E.R.T. RESULTS

Identification	Test Temp. (°C)	Heat Treatment of "as received" Material	Strain Rate (Sec^{-1})	% Strain at Max. Stress	% of Fracture Face Area Showing I.G.S.C.C.	Time to Failure in C.E.R.T. (Days)	Time** to Failure as U-bends (Weeks)
Heat #2	365	None	2.8×10^{-7}	10	71	7	<2 to 4
" #2	365	20 hrs in Ar @ 700°C	3.0×10^{-7}	32	2	12	>16
" #4	365	None	7.6×10^{-7}	7	60	6	10 to 12
" #4	345	None	3.0×10^{-7}	16	39	8	>16
" #4	325	None	2.9×10^{-7}	32	1.5	16	>10
" #4	325	None	3.9×10^{-8}	8	57	32	>10
" #5	365	None	2.0×10^{-6}	34	<1.	2	8 to 18
" #5	365	None	6.4×10^{-8}	*	10 mil deep crack	-	8 to 18

*Specimen pulled to 6.5% strain then the test accidently shut down.

** In 365°C H_2O.

TABLE 4 SCC Results of the Controlled Potential Tests After the 7th 4-day Exposure

Specimen	Potential*	Results	Time at Controlled Potential (days)
#1-1	Open circuit	IGC** in the 9th exposure	36
#2-1	-40 mV	IGC in the 5th exposure	20
#3-1	-80 mV	IGC in the 6th exposure	24
#4-1	-120 mV	IGC in the 2nd exposure	8
#5-1	-160 mV	IGC in the 4th exposure	16
#6-1	-200 mV	No cracking	
#4-2	-120 mV	IGC in the 11th exposure	36

*Approximate values except #6 case

**Intergranular Cracking

TABLE 5 Cyclic Load Tests at 365°C in D.I. H_2O

Test	Frequency	Results
#1	10^{-1} Hz	1) failed after 123041 cycles 2) IGC* 3) 17.2% elongation
#2	10^{-2} Hz	1) failed after 11570 cycles 2) IGC 3) 18.7% elongation
#3	10^{-3} Hz	1) failed after 1295 cycles 2) IGC 3) 18.4% elongation

*Intergranular Cracking.

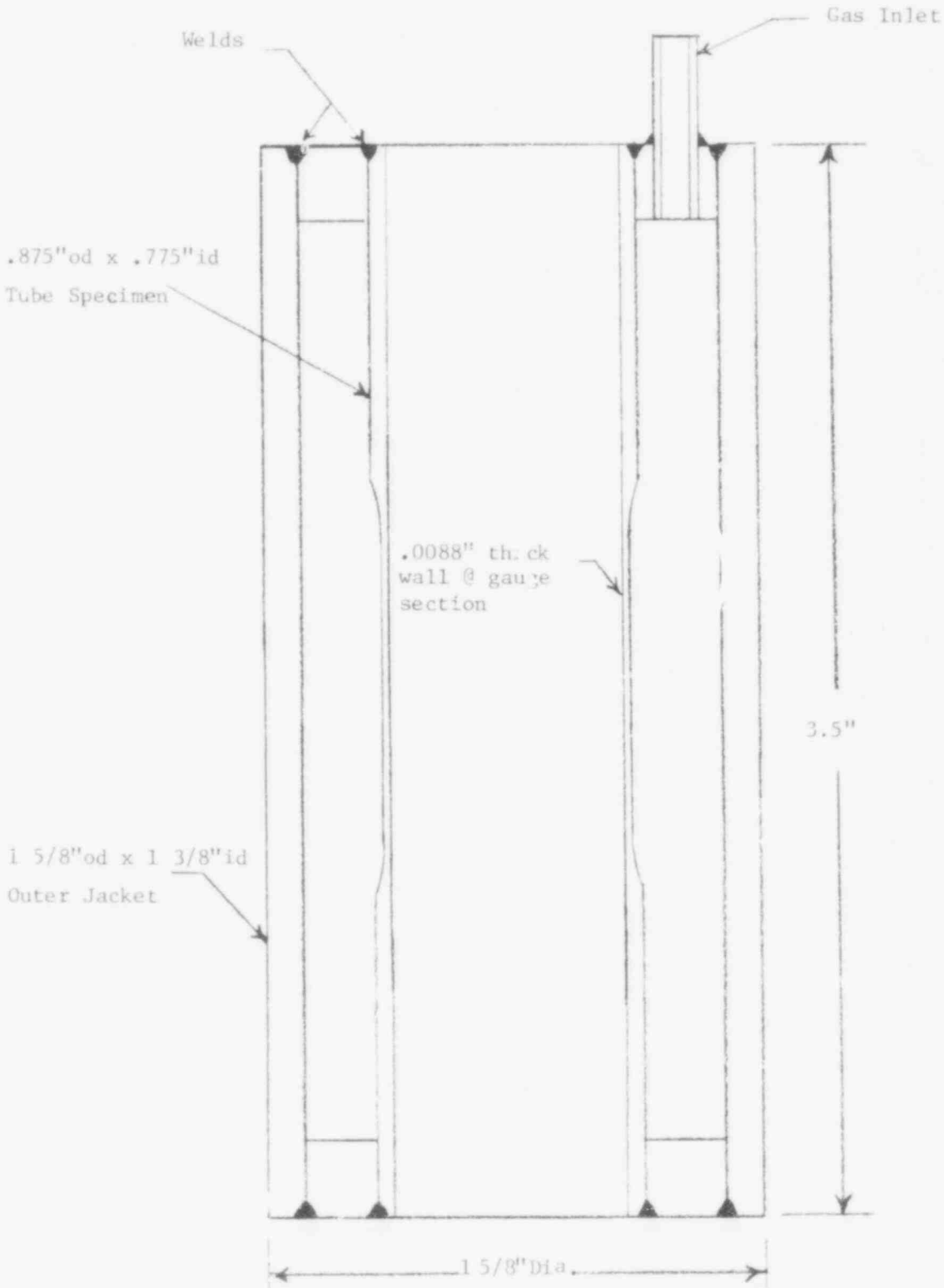

Fig. 1 Pressurized Capsule Specimen

339

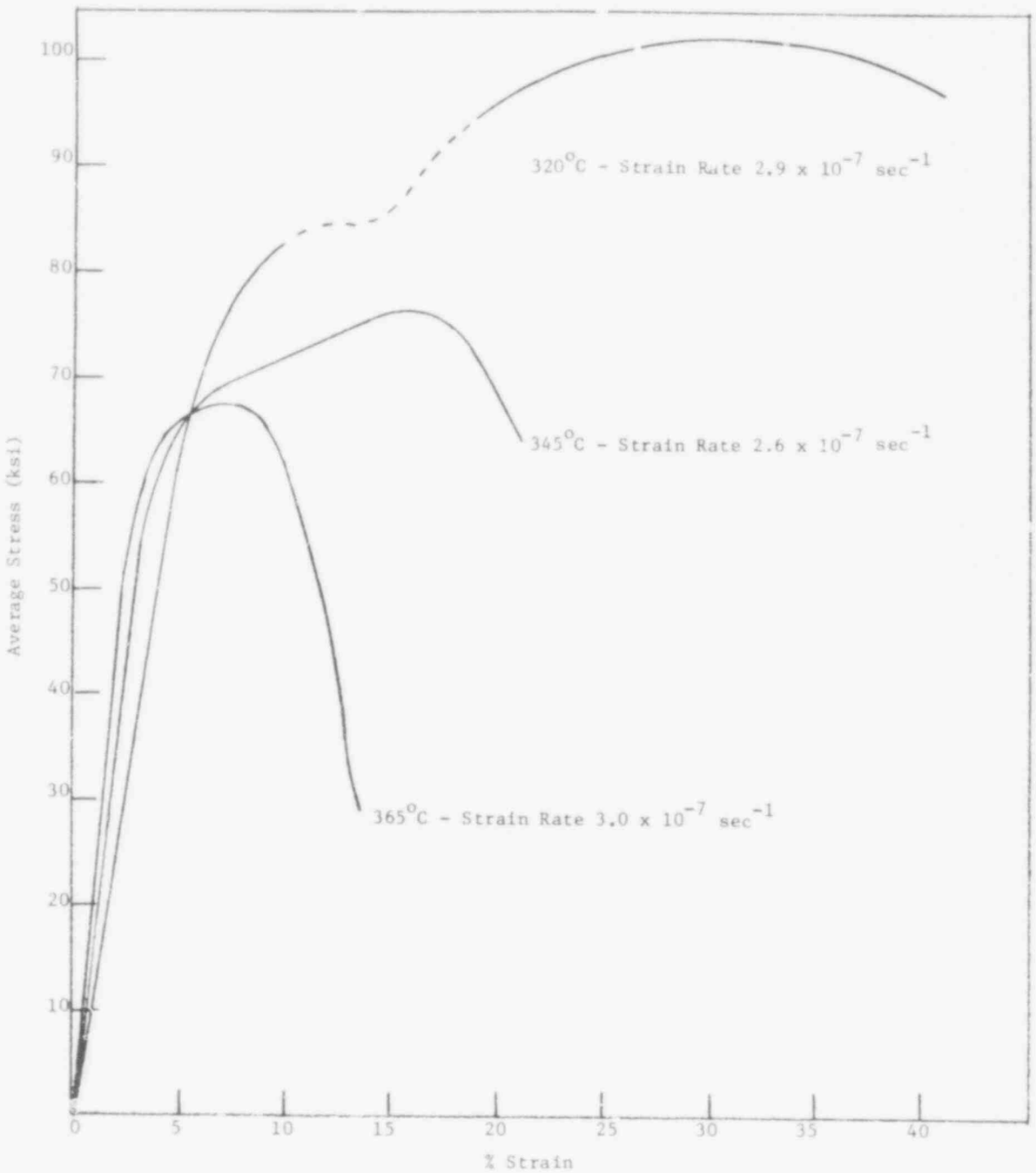

Fig. 2 Stress-Strain Curve for Heat #4 in D.I. H_2O

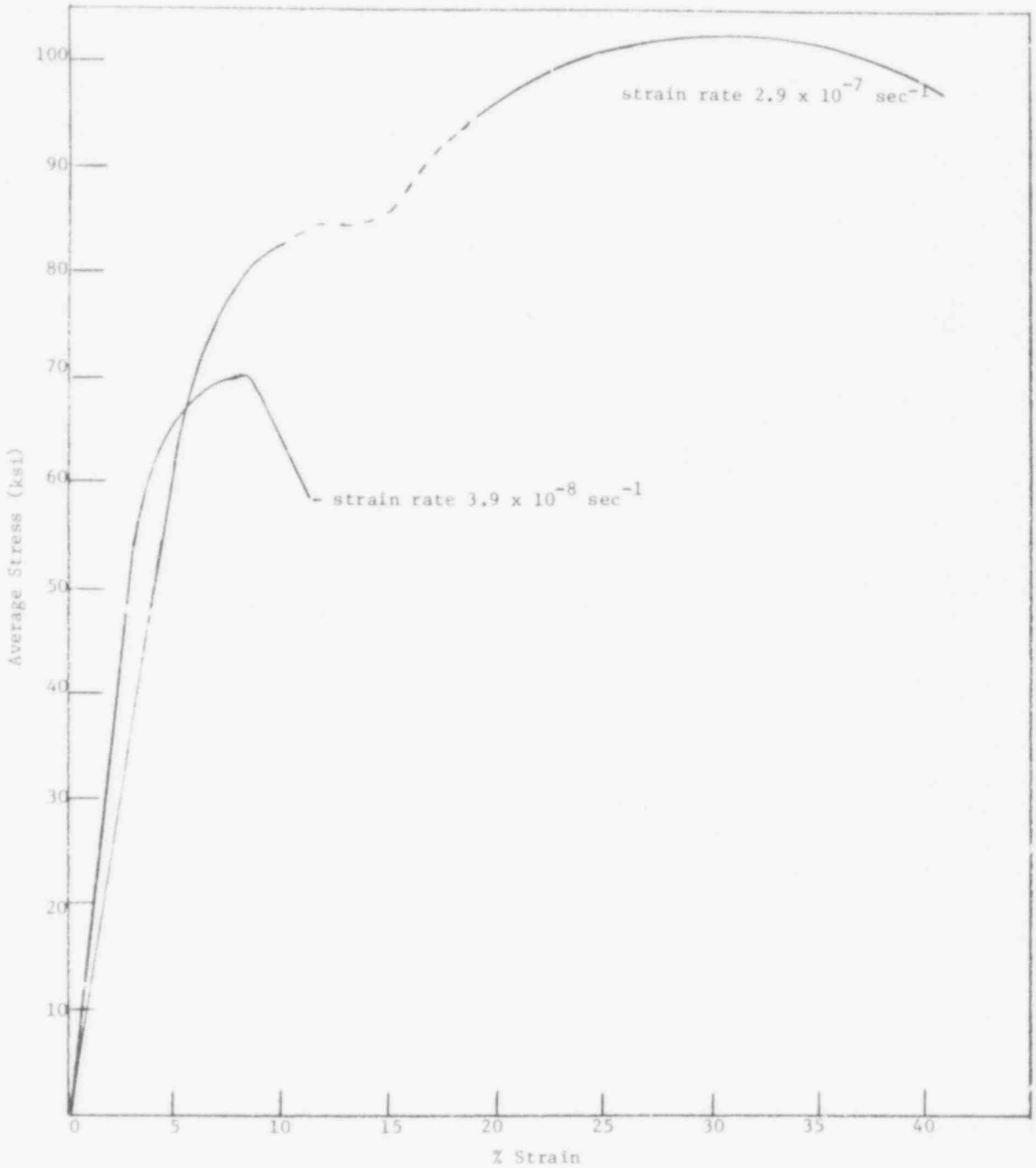

Fig. 3 Stress-Strain Curve for Heat #4 in D.I. H_2O at 320°C